



**HAL**  
open science

# Investigation of dynamic fracture of elastomers : On the role played by viscoelasticity

Vasudevan Kamasamudram

► **To cite this version:**

Vasudevan Kamasamudram. Investigation of dynamic fracture of elastomers : On the role played by viscoelasticity. Solid mechanics [physics.class-ph]. École centrale de Nantes, 2021. English. NNT : 2021ECDN0048 . tel-03663421

**HAL Id: tel-03663421**

**<https://theses.hal.science/tel-03663421>**

Submitted on 10 May 2022

**HAL** is a multi-disciplinary open access archive for the deposit and dissemination of scientific research documents, whether they are published or not. The documents may come from teaching and research institutions in France or abroad, or from public or private research centers.

L'archive ouverte pluridisciplinaire **HAL**, est destinée au dépôt et à la diffusion de documents scientifiques de niveau recherche, publiés ou non, émanant des établissements d'enseignement et de recherche français ou étrangers, des laboratoires publics ou privés.



# THÈSE DE DOCTORAT DE

L'ÉCOLE CENTRALE DE NANTES

ÉCOLE DOCTORALE N°602

*Sciences pour l'Ingénieur*

Spécialité : *Mécanique des Solides, des matériaux, des structures et des surfaces*  
par

**Vasudevan KAMASAMUDRAM**

## **Investigation of dynamic fracture of elastomers: On the role played by viscoelasticity**

Thèse présentée et soutenue à l'École Centrale de Nantes, le 9 Décembre 2021

Unité de recherche : UMR 6183, Institut de Recherche en Génie Civil et Mécanique (GeM)

### **Rapporteurs avant soutenance:**

Rafael ESTEVEZ    Professeur des universités, INP de Grenoble Alpes, Saint-Martin d'Hères  
Patrice HAURET    Ingénieur de recherche HDR, MICHELIN, Chamalieres

### **Composition du Jury :**

Président :	Patrick LE TALLEC	Professeur, École Polytechnique, CNRS
Examineurs :	Julie DIANI	Directrice de recherche, École Polytechnique, CNRS
	Gergely MOLNAR	Chargé de recherche, INSA Lyon
	Vito RUBINO	Chargé de recherche, California Institute of Technology, USA
Directeur de thèse :	Michel CORET	Professeur des universités, École Centrale de Nantes
Co-directeur de thèse:	Nicolas MOËS	Professeur des universités, École Centrale de Nantes

*Investigation of dynamic fracture of elastomers:  
On the role played by viscoelasticity*

*Vasudevan Kamasamudram*



# Acknowledgements

I thank several people - the ones that were almost finished with their work when I was starting, the ones that were already there, the ones that started with me, the ones that started after me.

In the first category, I thank Thomas Corre for various discussions that we had at the beginning of my thesis and for a nice transition.

In the next category comes Baptiste Reyne, with whom I had the chance to have some very nice discussions about several topics in Mechanics. Tauno Tiirats introduced me to Abaqus and helped in efficiently linking the subroutines written in C++ with Abaqus. Not to miss in here are George Jagite and Erwan Grelier.

Next, the people who started their PhDs with me - Elie Eid, who happened to work on dynamic fracture as well and his thesis defended itself successfully the day after mine. Raphaël Langlois (aka hungry) and Adrien Vinel, with whom I did not have several overlapping areas of interest at work, but had several common interests in comedy. Raphaël also introduced me to cheese and brought in several varieties of cheese for my after defense. Not to forget Paris Mulye for interesting conversations about his and my works during the first quarantine (for those people in future, yes the covid was during our thesis) and later on as well.

The people who started after me and shared an office with me - Pauline Bourda, a fellow fan of The Office, for various discussions and for nice presents on my farewell. Shaoqi Wu, for some interesting discussions on several topics.

On the other front, I'd thank Erwan Verron for our discussions regarding viscoelastic models (the details of which I couldn't unfortunately develop further) and other aspects, Julien Réthoré for his invaluable comments during my CSI meetings. Also, my supervisors Michel Coret and Nicolas Moës for giving me this opportunity and putting up with me for the three years.

The readers of this thesis, should they wish, can read the citations as *that's what (s)he said*, as Micheal Scott, the Regional Manager of Dunder Mifflin, Scranton, would do. The template used in this thesis was developed by Baptiste Reyne and can be found at <https://gitlab.com/breyne/latex-two-thirds>.

# Contents

	<b>1</b>
<b>I Literature review</b>	<b>4</b>
<b>1 Introduction to fracture mechanics</b>	<b>5</b>
1.1 Introduction . . . . .	6
1.2 Crack Propagation condition . . . . .	7
1.3 Weakly Nonlinear Theory of fracture . . . . .	11
1.4 Crack tip fields in elastomers . . . . .	12
1.5 Transonic cracks . . . . .	13
<b>2 Experimental and theoretical studies</b>	<b>15</b>
2.1 Early studies . . . . .	16
2.2 'Instabilities' in dynamic fracture . . . . .	17
2.3 Fracture of elastomers . . . . .	18
2.4 Experimental and theoretical studies on polymer fracture . . . . .	19
2.5 Energy release rate through integrals . . . . .	22
<b>3 Polymers</b>	<b>28</b>
3.1 Elastomers . . . . .	29
3.2 Nonlinear elasticity . . . . .	29
3.3 viscoelasticity . . . . .	32
<b>II Experiments</b>	<b>36</b>
<b>4 Fracture of polyurethane</b>	<b>37</b>
4.1 Experimental setup . . . . .	38
4.2 Procedure . . . . .	38
4.3 Results . . . . .	39
4.4 Complex geometry and crack path . . . . .	41
4.5 Comparison with literature . . . . .	42
<b>5 Additional experiments</b>	<b>45</b>
5.1 Results of 20 mm and 60 mm samples . . . . .	46
5.2 Other experiments on the 40 mm specimen . . . . .	48
5.3 Samples of another batch (Batch 2) . . . . .	49
5.4 Temperature measurements . . . . .	50
5.5 Discussion . . . . .	52
<b>6 Revisiting the fracture experiments</b>	<b>55</b>
6.1 Displacement, Velocity and Strain fields . . . . .	57
6.2 Observations on the variation of surface roughness . . . . .	58
6.3 Discussion . . . . .	62

<b>III</b>	<b>Simulations</b>	<b>64</b>
<b>7</b>	<b>The role of viscoelasticity in the bulk</b>	<b>65</b>
7.1	Using momentum balance . . . . .	67
7.2	Using the cracks speed as an input . . . . .	71
7.3	Discussions . . . . .	78
<b>8</b>	<b>Cohesive zone model</b>	<b>82</b>
8.1	Bulk material . . . . .	85
8.2	Rate independent cohesive zone model . . . . .	85
8.3	Viscous Cohesive zone model . . . . .	88
8.4	Finite Element Implementation . . . . .	90
8.5	Crack speeds prediction and traction - separation relations . . . . .	94
8.6	Discussions . . . . .	98
<b>9</b>	<b>Finite Viscoelastic model</b>	<b>103</b>
9.1	Thermodynamics . . . . .	104
9.2	Integration of the evolution equation . . . . .	105
9.3	Plane stress formulation . . . . .	106
9.4	Model checks . . . . .	112
9.5	Application of FV model to the experiments . . . . .	116
9.6	Energy budget in viscoelastodynamic fracture . . . . .	123
9.7	Discussions . . . . .	128
<b>A</b>	<b>Plane stress version of Finite linear viscoelastic model</b>	<b>143</b>
A.1	Time integration . . . . .	147
A.2	Computation of tangent . . . . .	148
<b>B</b>	<b>Additional results for Finite viscoelastic model</b>	<b>149</b>
B.1	Stress components for the hyperelastic case . . . . .	150
B.2	Comparison of relaxation tests between FLV and FV . . . . .	150
<b>C</b>	<b>C++ implementation of the UMAT</b>	<b>154</b>



# General introduction

Elastomers are the materials that are capable of undergoing large deformations reversibly. Compared to brittle solids, high speed crack propagation (high speed when compared to the corresponding wave speeds) in these materials happen at large strain levels. When a membrane made of elastomer is stretched and a crack is introduced, the crack propagates with a speed that depends on the stretch level. These types of experiments were widely performed in the literature on the specimen in pure shear geometry. The output of these experiments are the crack speeds. The crack speeds are usually correlated with the energy release rate, which is measured using the specimen geometry and the applied stretch, using a constitutive model. In some experiments performed like above, it was observed that the crack speeds exceeded the shear wave speed (computed from the hyperelastic material parameters) of the material. Such cracks are called Transonic cracks.

Linear Elastic Fracture Mechanics (LEFM) bounds the speed of the cracks from the above by the corresponding wave speeds depending on the mode of propagation. For the cracks that propagate in opening mode, the limiting speed is the Rayleigh wave speed. However, for the propagation under in-plane shear loading, the cracks were observed to propagate at speeds that exceed the shear wave speed. The theory of LEFM was later extended to include the description of such cracks. Also, during the cracks propagation in this regime, shock fronts that travel along with the crack tip were observed in the experiments. In the case of aforementioned transonic crack propagation in elastomers, no reports of such shock-fronts in the material exist. Instead, it is remarked in the literature that for the cracks that propagate in this regime, the crack faces (crack opening) are wedge-shaped as opposed to being parabolic-shaped in the subsonic regime. No specific mention about the shock front in the material was made.

Some studies attribute the existence of Transonic cracks in elastomers to the hyperelastic stiffening of the material. They hypothesize that the hyperelastic stiffening increases the wave speed locally near the tip allowing the cracks to propagate at Transonic speeds. Other studies attribute the observation of Transonic cracks to the viscoelastic stiffening of the material. To the author's knowledge, no study exists that evaluates the two hypotheses to conclusively determine if either of these phenomena are responsible for the crack propagation in transonic regime.

In the experiments performed in literature on natural rubber, it was observed that the crack speeds became independent of the specimen geometry in the transonic regime. More precisely, it was observed that when the specimen of different geometries are subjected to the same stretch level, the crack speeds do not change from one specimen to the other when propagating in the transonic regime. When the crack speeds are smaller, the crack speed dependence on the specimen size was reported to be seen. Whether this observation holds for all the materials is not clear. Also, to the author's knowledge, no studies exist that examine the necessary ingredients to investigate this phenomenon using the Finite element method.

The energy partition during the fracture of elastomers is also of interest. Some part of the energy stored in the body is dissipated by the viscoelastic effects of the material and some at the tip, in the fracture process zone. However, to the author's knowledge, how these energies compare with each other is not known.

Also, the viscoelastic dissipation in the bulk leads to a raise in the temperature of the material, which in turn affects the viscoelastic properties of the material. This leads to a fully coupled thermomechanical problem.

This thesis is divided into three parts. The first part begins by introducing the basic notions of Linear Elastic Fracture Mechanics, followed by a brief description of the experimental and theoretical studies on elastomer fracture. The next part of this thesis describes the experiments performed on the pure shear samples of polyurethane. Chapter 4 describes the experiments performed in literature on polyurethane samples one one geometry. Chapter 5 describes the additional experiments performed by the current author on samples of different geometries. Chapter 6 presents additional results and observations from the experiments performed in the literature. The other part involves performing FE simulations to understand and predict the results obtained from the experiments. Chapter 7 examines the hypotheses of hyperelastic and viscoelastic stiffening using the data obtained from experiments. Chapter 8 describes a rate dependent cohesive zone to predict the crack speeds. Chapter 9 describes the plane stress version of the Finite viscoelastic model and the analysis of the energy expenditure during the dynamic fracture.

PART I  
**LITERATURE REVIEW**

# INTRODUCTION TO FRACTURE MECHANICS



---

This chapter introduces the notion of Linear Elastic Fracture Mechanics and the asymptotic crack tip fields in the case of a stationary and a moving crack. Different loading modes and the notion of limiting speeds in different modes will be discussed. Different criterion to predict crack propagation will be described. The extension of LEFM to moderate to large deformations will be described as well. It ends with a brief discussion on the notion of Transonic cracks.

---

### CONTENTS

1.1	Introduction . . . . .	6
1.2	Crack Propagation condition . . . . .	7
1.2.1	Energy flux integral . . . . .	8
1.2.2	Propagation direction . . . . .	10
1.3	Weakly Nonlinear Theory of fracture . . . . .	11
1.4	Crack tip fields in elastomers . . . . .	12
1.5	Transonic cracks . . . . .	13

## 1.1 INTRODUCTION

Early analysis of cracks can be attributed to the studies of Inglis (Inglis, 1913), Griffith (Griffith, 1921) and Irwin (Irwin, 1957). Inglis studied the problem of an elliptic hole in a plate and determined the stress concentration factor arising from the elliptical corners of the plate. The stress concentration factor was seen to depend inversely on the radius of curvature of the elliptical edge. As the aspect ratio of the ellipse is increased, the ellipse tends to a crack with the radius of the corners tending to zero. The stresses hence tend to become singular as the limit of a crack is reached. Westergaard used complex analysis to develop the variation of stresses in a plate under plane stress and plane strain assumptions. Irwin later used this method to develop the expression of stresses in the vicinity of the crack tip. This led to the definition of Stress Intensity Factor as the quantity that describes the amplitude of the stress singularity at the crack tip. Griffith arrived at a criterion for the propagation of crack in a medium. He stated that the crack will propagate in a medium when the rate of increase in the surface energy because of crack propagation is offset by the rate of decrease in the potential energy of the body under the external loading as a consequence of crack growth. Irwin developed a relation between the Stress Intensity Factor (SIF) and the energy criterion of Griffith.

The study of propagation of cracks under small strains in a linear elastic material comes under the umbrella of Linear Elastic Fracture Mechanics (LEFM). In this section, a brief review will be made about the theory and some results of LEFM.

### LINEAR ELASTIC FRACTURE MECHANICS (LEFM)

The study of simple crack in a linear elastic material has been performed by a number of researchers. An exhaustive discussion on the theory can be found in (Anderson, 2017) and when the dynamic effects are included in (Freund, 1990; Broberg, 1999). The theory of LEFM states that the state of stresses at the crack tip are singular and the near tip variation of displacement, stress and strain fields are universal. The effect of external loading and geometry are introduced through a quantity called Stress Intensity Factor (SIF),  $K = \lim_{r \rightarrow 0} \sigma \sqrt{2\pi r}$ .

The hypothesis of LEFM are as follows.

- The material behaves linearly and is elastic. Homogeneity and isotropy are also assumed.
- The failure and inelastic processes occur in a very small zone near the tip. This is called *The hypothesis of Small Scale Yielding*.
- The analysis is restricted to simple cracks. Events such as branching are discounted.

For a simple crack in a material, three modes of crack propagation can be defined based on the external loading. They can be seen in the figure 1.3. In mode-I, also called *the opening mode*, the crack faces open perpendicular to the crack path. The shear stresses are zero along the line of symmetry. Mode-II is characterized by the in-plane shear loading along the crack propagation direction. In mode-III, also called *the tearing mode*, the crack faces open perpendicular to the plane of crack propagation.

Using the notion of SIF developed by Irwin, and the small scale yielding hypothesis, the stress state in the vicinity of crack tip can be expressed in terms of

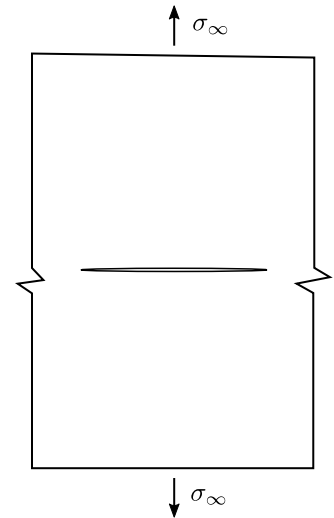


Figure 1.1: A body with a crack.

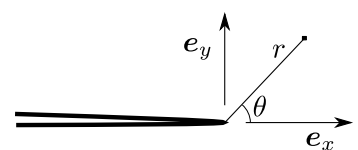


Figure 1.2: Polar coordinates centered at the crack tip.

the SIFs in three modes as (Anderson, 2017)

$$\sigma_{ij} = \frac{K_I}{\sqrt{2\pi r}} \Sigma_{ij}^I(\theta) + \frac{K_{II}}{\sqrt{2\pi r}} \Sigma_{ij}^{II}(\theta) + \frac{K_{III}}{\sqrt{2\pi r}} \Sigma_{ij}^{III}(\theta) \delta_{j3} \quad (\text{no sum on } j) \quad (1.1)$$

where  $K$  denotes the SIF in the corresponding mode as indicated by the subscript.  $\Sigma^i$ s determine the angular dependence of the stress distribution. Owing to the linearity of the material and small strains, principle of superposition has been used.  $\delta$  denotes the Kronecker delta and equals to 1 when  $j = 3$  or to 0 otherwise.

The hypothesis of small scale yielding implies that the fracture processes occur at regions that are very close to the tip. The region where the stress distribution is dominated by the singularity lies outside the the region where the fracture processes occur.

### Dynamic case

When inertial effects are included, the asymptotic crack tip fields have the same singularity as in the static case, but the angular dependence is now a function of crack speed as well. Hence, the equation 1.1 now becomes (Freund, 1990)

$$\sigma_{ij} = \frac{K_I}{\sqrt{2\pi r}} \Sigma_{ij}^I(\theta, v) + \frac{K_{II}}{\sqrt{2\pi r}} \Sigma_{ij}^{II}(\theta, v) + \frac{K_{III}}{\sqrt{2\pi r}} \Sigma_{ij}^{III}(\theta, v) \delta_{j3} \quad (\text{no sum on } j) \quad (1.2)$$

At a distance  $r$  from the tip, the displacement field varies as  $\sqrt{r}$  and hence, the particle velocity is proportional to  $vK_I/E\sqrt{r}$ . So, the kinetic energy density varies as

$$K \sim \frac{\rho v^2}{2} \frac{K_I^2}{rE^2}, \quad (1.3)$$

where  $\rho$  and  $E$  are the density and the Young's modulus, respectively. The strain energy density can be seen to vary with  $r$  as

$$U \sim \frac{1}{2} \frac{K_I^2}{rE}. \quad (1.4)$$

The ratio of these two energy densities can be seen to be

$$\frac{K}{U} \sim \frac{v^2}{E/\rho}. \quad (1.5)$$

The ratio is independent of  $r$  and so, it can be seen that the inertial effects may not be important in studying the problem as long as the crack speeds remain less than about  $\frac{1}{3}$ rd of the elastic wave speed  $\left(\sqrt{E/\rho}\right)$ .

The introduction of inertial effects results in the notion of the limiting speed for the crack. It will be shown in the following section that the *Energy release rate*,  $G$  changes its sign as the crack speed passes the Rayleigh wave speed ( $c_R$ ). Since a positive value of  $G$  is necessary for the crack to propagate,  $c_R$  is the upper bound on the crack speed (Freund, 1990).

## 1.2 CRACK PROPAGATION CONDITION

To predict the propagation of a crack in a body, an additional relation is needed along with the constitutive model that describes the behavior of the bulk material. The additional relation is in terms of a propagation criterion. As mentioned earlier,

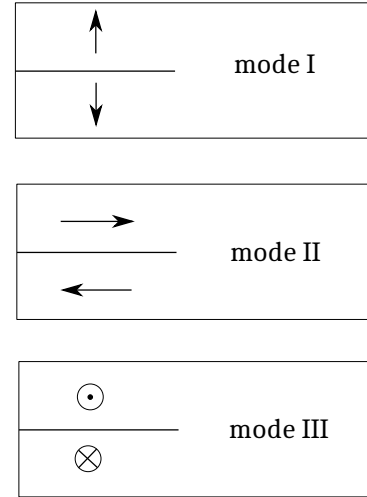


Figure 1.3: Opening mode (I), Shear mode (II) and Anti-plane shear mode (III).

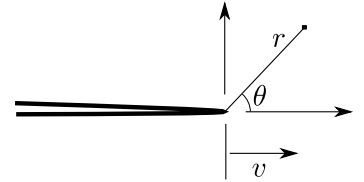


Figure 1.4: Polar coordinates centered at the crack tip.

(Griffith, 1921) established a crack propagation criterion based on the energy balance of the system. Formally, the Griffith's criterion can be stated as follows. Denoting the total mechanical energy of the structure as  $\Pi$ , the *Energy Release Rate*,  $G$  can be defined to be

$$G = -\frac{\partial \Pi}{\partial A} \quad (1.6)$$

where  $A$  denotes the area of the crack surface. Defining the fracture energy  $\gamma$  to be the energy required to create a unit surface area of the crack, Griffith's criterion can be expressed as

$$G < \gamma, \quad \text{Crack does not propagate.}$$

$$G = \gamma, \quad \text{Crack may propagate.}$$

In other words, the crack propagates in the body if the loss of potential energy of the bulk material equals to the increase in surface energy resulting from the crack growth. Griffith's criterion can also be seen to imply that the equilibrium crack length is the one that minimizes the total energy of the system,  $E := \Pi + \gamma A$ .

In quasi static case, the relation between the Energy release rate and the SIF has been obtained in Irwin (1957) to be

$$G = \frac{K_I^2}{E} \quad (1.7)$$

where  $E$  is the Young's modulus of the material.

The energy release rate,  $G$ , can also be related to the J-integral proposed by (J R Rice, 1968) using the Eshelby stress tensor (Eshelby, 1956) as

$$J = \mathbf{e}_1 \cdot \int_{\Gamma} (\rho_0 \psi \mathbf{I} - \boldsymbol{\sigma} \cdot \nabla \mathbf{u}) \cdot \mathbf{n}_0 \, dS, \quad (1.8)$$

where  $\psi$  is the energy density,  $\boldsymbol{\sigma}$  is the stress tensor and  $\nabla \mathbf{u}$  denotes the displacement gradient. For a crack in linear elastic material and under quasi-static loading conditions, it has been proved that  $J = G$ . The path independence of the contour integral can be used to obtain the  $G$  from far field quantities. The relation in the equation 1.7 can then be used to obtain the SIF from far field measurements.

The crack propagation condition expressed above in terms of the energy release rate can also be expressed in terms of the SIF. Using the relation between the  $G$  and SIF, the propagation condition can be expressed to be (in the case of a pure mode-I loading)

$$K_I = K_{\text{crit}}, \quad (1.9)$$

where  $K_{\text{crit}}$  can be expressed in terms of  $\gamma$ .

### 1.2.1 Energy flux integral

The expression for the net energy flux through a contour  $\Gamma$  moving at a speed  $v$  along with the tip has been arrived at by (Freund, 1990). By taking a dot product of the momentum equation with velocity and using the divergence theorem in space and time, the expression for the energy flux through  $\Gamma$  has been obtained as

$$F(\Gamma) = \int_{\Gamma} [(U + K)v n_1 + \mathbf{v} \cdot \boldsymbol{\sigma} \mathbf{n}] \, dS, \quad (1.10)$$

where  $U = \int_{-\infty}^t \sigma_{ij} \frac{\partial^2 u_i}{\partial t \partial x_j} \, dt$  is the stress work density. In the case of elastic material, stress work density can be seen to be equal to the strain energy density, since

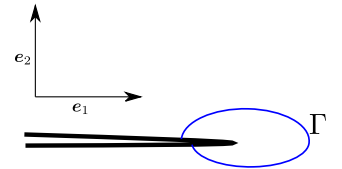


Figure 1.5: Contour  $\Gamma$  surrounding the tip.

$\sigma_{ij} = \frac{\partial W}{\partial \epsilon_{ij}}$ . It can be seen (in the later sections) that the flux integral in the above equation is contour independent as long as steady state conditions prevail regardless of the material behavior.

The dynamic energy release rate can be defined using the definition of flux integral to be

$$G = \lim_{\Gamma \rightarrow 0} \left\{ \frac{F(\Gamma)}{v} \right\} \quad (1.11)$$

The value of the energy flux integral is independent of the shape of the contour as the contour is shrunk to the tip. Hence, a contour that looks like in figure 1.6 has been used where to shrink to the tip by first letting  $\delta_2 \rightarrow 0$  and then  $\delta_1 \rightarrow 0$ . Using the asymptotic crack tip fields, the energy release rate has been obtained to be (Freund, 1990)

$$G = \frac{1-v^2}{E} \left( A_I(v)K_I^2 + A_{II}(v)K_{II}^2 \right) + \frac{1}{2\mu} A_{III}(v)K_{III}^2 \quad (1.12)$$

where

$$A_I = \frac{v^2 \alpha_d}{(1-v)c_s^2 D}, \quad A_{II} = \frac{v^2 \alpha_s}{(1-v)c_s^2 D}, \quad A_{III} = \frac{1}{\alpha_s}. \quad (1.13)$$

$$D = 4\alpha_d \alpha_s - (1 + \alpha_s)^2. \quad (1.14)$$

where  $\alpha_d = \sqrt{1 - \frac{v^2}{c_d^2}}$ ,  $\alpha_s = \sqrt{1 - \frac{v^2}{c_s^2}}$  and  $D$  is the Rayleigh function the root of which is the Rayleigh wave speed.

### Infinite medium

For the case of crack propagation in an infinite medium, the SIF for a dynamic crack can be expressed in terms of a static crack under the same loading conditions and a factor that depends on crack speed and material parameters. In an infinite medium or in a finite medium before the waves reflected off the boundaries reach the crack tip, the SIF can be expressed to be (page 389 of (Freund, 1990))

$$K_I(t, l, v) = k(v)K_I(t, l, 0) \quad (1.15)$$

where  $k(v)$  is a function of crack speed and material properties. The energy release rate can be expressed similarly in terms of its value at equilibrium as

$$G(t, l, v) = A_I(v)k(v)^2 G(t, l, 0) \quad (1.16)$$

where  $A_I(v)$  is another function of crack speed. The function  $A_I(v)k(v)^2$  can be approximated by  $1 - \frac{v}{c_R}$ , where  $c_R$  is the Rayleigh wave speed.

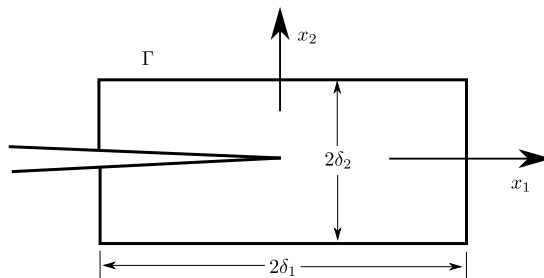


Figure 1.6: Rectangular contour  $\Gamma$  surrounding the tip. It is shrunk to the tip first by letting  $\delta_2 \rightarrow 0$  and then  $\delta_1 \rightarrow 0$ .

Hence, for the case of a mode-I crack moving in an infinite medium, a crack tip equation of motion can be written based on the expression developed for the energy release rate.

$$\frac{1 - v^2}{E} A_I(v) K_I(t, l, v)^2 = \gamma. \quad (1.17)$$

Since, in an infinite medium, the SIF can be expressed in terms of its value for a stationary crack under the same loading, the above expression can be simplified further to

$$\frac{E\gamma}{(1 - v^2)K_I(t, l, 0)^2} = A_I(v)k(v)^2 \approx 1 - v/c_R. \quad (1.18)$$

For the case where  $\gamma$  is a constant, it can be seen that since  $K_I(t, l, 0)$  is an increasing function of crack length, the left side of the above equation tends to zero as the crack becomes longer. Hence, the right side tends to zero as well in the limit  $v \rightarrow c_R$ . Hence, the theoretical upper bound on the crack speed in mode-I is the Rayleigh wave speed ( $c_R$ ).

### 1.2.2 Propagation direction

By expressing the external loading in terms of modes I, II and III, the condition for determining the crack path can be uncoupled from the condition for crack propagation in terms of surface energy. Then, the criteria for the selection of propagation direction can then be expressed in terms of the SIF in the corresponding modes (Cotterell & Rice, 1980). One of the first conditions to determine the direction of crack propagation was established by (Goldstein & Salganik, 1974) as 'Principle of local symmetry'. It suggests that *the path taken by a crack in brittle homogeneous isotropic material is the one where the local stress field is of a mode-I type. In other words, the crack chooses the direction along which the SIF in mode-II ( $K_{II}$ ) is zero.*

Other criteria such as the maximum hoop stress criterion (Erdogan & Sih, 1963), maximum energy release rate criterion (Hussain, Pu, & Underwood, 1974), stationary Sih energy density factor (Sih, 1973) also exist. These criteria are known to be consistent with each other (Cotterell & Rice, 1980) in that all these criteria state that if  $K_{II} \neq 0$ , the crack extends with an abrupt, non-zero, change in the tangent direction to the path.

In static conditions, these criteria are applied for the case of an inclined crack subjected to a mixed-mode loading. Experiments were performed accordingly and the results of the experiments were compared with the theoretical predictions in (Sih, 1973). As a special case, when the crack is subjected to a pure mode-II loading, the branch angle was found to be 70deg, which is consistent with the experimental findings.

Some other criteria were established to predict the crack turning in numerical simulations. For instance, (Belytschko, Chen, Xu, & Zi, 2003) uses the loss of ellipticity criterion to determine the direction of propagation of a crack. This criterion has been mentioned to be similar to the loss of material stability (Belytschko, Liu, & Moran, 2000). Other criteria based on configurational forces have been used in Finite Element simulations (Özenç, Kaliske, Lin, & Bhashyam, 2014). The configurational force vector is used to determine the propagation direction of the crack. The crack propagation takes place between the elements where a double node is introduced when the magnitude of the configurational forces satisfies some criterion (like that of the energy release rate criterion). The mesh is then adjusted so that the element edge lies along the direction of the configurational force.

Crack propagation can also be modeled by techniques such as the phase-field method (Bourdin, Francfort, & Marigo, 2000; C. Miehe, Welschinger, & Hofacker, 2010). In this method, the propagation of crack and the direction of propagation are taken care of by the evolution of the phase-field itself. Similarly, in other methods such as the gradient damage models (Marigo, Maurini, & Pham, 2016), integral type non-local damage models (Peerlings, De Borst, Brekelmans, & Geers, 2002), Thick Level Set method (Moës, Stolz, Bernard, & Chevaugeon, 2011), a separate criterion for crack propagation direction is not required.

### 1.3 WEAKLY NONLINEAR THEORY OF FRACTURE

The asymptotic crack-tip fields and the other quantities like SIF reported in the previous sections are based on the linearity of the material and small deformations. To understand the fracture of polymer gels where the strains are no longer small and the material is no longer linear at those strain levels, Weakly Nonlinear Theory of fracture (WNLT) has been introduced in (Bouchbinder, Livne, & Fineberg, 2008).

Fracture experiments were performed on brittle polyacrylamide gels in (Livne, Bouchbinder, & Fineberg, 2008). LEFM was used to predict the crack opening profile and strains ahead of the tip. It was, however, observed that the results from the experiments did not match the predictions by LEFM in regions close to the tip. The discrepancy was attributed to the non-linear behavior of the material at the tip since the material undergoes large deformations in that region. To address this discrepancy, higher-order displacement gradient contributions were included to develop the asymptotic crack tip fields while also considering the material non-linearity at the observed strain levels. A neo-Hookean model was used for this purpose. It was observed that the inclusion of the higher-order terms resulted in more singular strain terms ( $r^{-1}$ ) than the traditional square root singularity observed in LEFM. The inclusion of nonlinear corrections was seen to result in

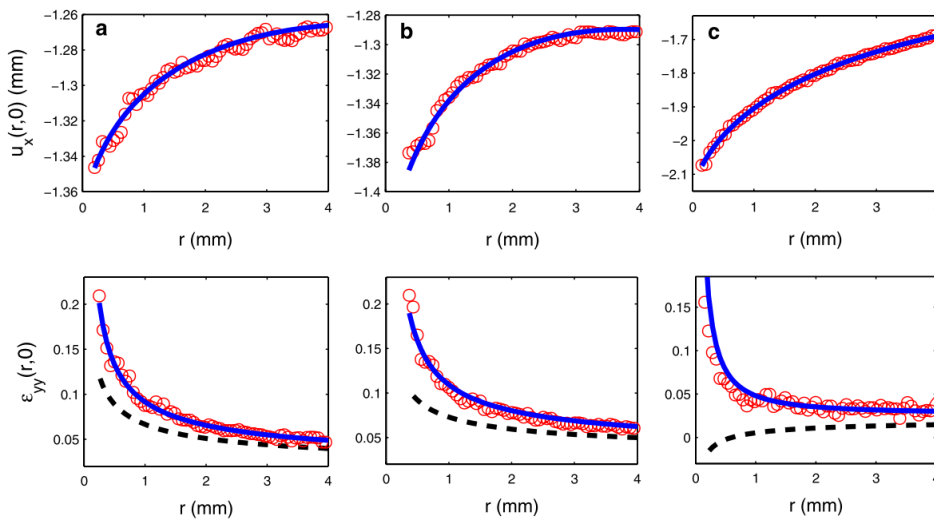


Figure 1.7: Comparison of experimental results with that of LEFM and WNLT at different crack speeds. The red circles indicate the experimentally measured values, black dotted line the predictions of LEFM, blue line the predictions of WNLT. The crack speeds are  $0.20c_s$  in (a),  $0.53c_s$  in (b), and  $0.78c_s$  in (c). (Bouchbinder, Livne, & Fineberg, 2008)

strain fields that match the observations from the experiments (see figure 1.7). Figure 6 of (Bouchbinder, Goldman, & Fineberg, 2014), a comparison has been made between the LEFM, WNLT and fully non-linear theory (Tarantino, 1999) has been made. It was observed that the fully nonlinear asymptotic fields match the crack profile closely even near the tip.

### 1.4 CRACK TIP FIELDS IN ELASTOMERS

Elastomers can undergo large deformations before a crack can propagate through. Also, the behavior of elastomers at such large strains cannot be described by the linear elastic material model and through small strain measures. Hence, the singularity at the crack tip may be different from what has been described in the earlier sections. Some studies establish the form of stresses at the crack tip under large strains using non-linear strain measures. Under quasi-static conditions, assuming the strain energy density to depend just on the first invariant of Green strain and the material to be incompressible, (Knowles, 1977) establishes the asymptotic crack tip fields under mode-III loading conditions. (Geubelle & Knauss, 1994; Krishnan, Hui, & Long, 2008) obtained the asymptotic crack tip stress for a crack in a Generalized Neo-Hookean model for a crack in mixed mode loading. The model condenses to a Neo-Hookean model for  $n = 1$ . For that case, the singular crack tip Piola stresses are seen to vary as

$$P_{21} \sim R^{-\frac{1}{2}} \sin(\Theta/2) \quad (1.19)$$

$$P_{22} \sim R^{-\frac{1}{2}} \cos(\Theta/2) \quad (1.20)$$

where  $R$  and  $\Theta$  are measured from the crack tip to the particle in the undeformed configuration. Similarly, singular Cauchy stresses are seen to vary as

$$\sigma_{21} \sim r^{-\frac{1}{2}} \frac{-\text{sign}(\theta)(2^{-3/2})}{\sqrt{2r \sin^2 \theta + \cos \theta}} \left( 1 - \frac{\cos \theta}{2r \sin^2 \theta + \cos \theta} \right)^{1/2} \quad (1.21)$$

$$\sigma_{22} \sim r^{-1} \frac{1}{2r \sin^2 \theta + \cos \theta} \quad (1.22)$$

where  $r$  and  $\theta$  are measured from the crack tip to the particle in the deformed configuration (see figure 1.8). The difference in the singularity of the stresses can be noticed. Also, the singularity of the Cauchy stresses varies with the angle. For instance,  $\sigma_{22}$  is singular as  $1/r$  along  $\theta = 0$  while it is singular as  $1/r^2$  along  $\theta = \pi/2$ .

This is different from LEFM where there is no difference between the deformed and the undeformed configurations and as a result all the stress measures coincide. The singularity is hence same in both the configurations.

The asymptotic crack tip fields in dynamic case was obtained by (Tarantino, 1999). Using a similar variable separable representation to that in (Geubelle & Knauss, 1994; Knowles, 1977), the leading singular terms were obtained. The deformation maps were observed to vary as

$$\varphi_1 \sim B_1(t; \tilde{v}) w(\Theta) R + o(R) \quad (1.23)$$

$$\varphi_2 \sim A_2(t; \tilde{v}) \hat{v}(\Theta; \tilde{v}) R^{1/2} + o(R) \quad (1.24)$$

where  $\tilde{v}$  is a function of crack speed  $v$  and material parameters ( $\mu$ ).  $w$  determines the angular variation of  $\varphi_1$ . The function  $\hat{v}$  can be seen below.

$$\hat{v}(\Theta; \tilde{v}) = \text{sgn}(\Theta) \left[ \frac{(1 - \tilde{v}^2 \sin^2 \Theta)^{1/2} - \cos \Theta}{2} \right]^{1/2}.$$

The PK1 stress components were seen to vary as

$$P_{21} = 2\mu R^{-1/2} A_2 \left( \frac{1}{2} \hat{v} \cos \Theta - \hat{v}_{,\Theta} \sin \Theta \right) + o(1) \quad (1.25)$$

$$P_{22} = 2\mu R^{-1/2} A_2 \left( \frac{1}{2} \hat{v} \sin \Theta + \hat{v}_{,\Theta} \cos \Theta \right) + o(1) \quad (1.26)$$

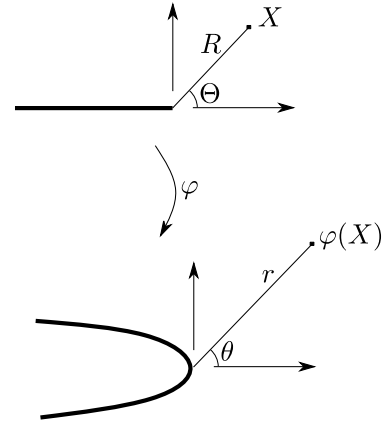


Figure 1.8: Polar coordinates centered at the crack tip in undeformed and deformed configurations.

It shall be noted that the order of singularity is similar to that of statics ( $R^{1/2}$ ). The stress components that are singular are same as that in the static case.

### 1.5 TRANSONIC CRACKS

As mentioned earlier, in LEFM, the crack speeds are restricted to  $c_R$  from below in mode-I and  $c_S$  in mode-III. The *Energy release rate* can be observed to change its sign to negative once the crack speed exceeds  $c_R$  and  $c_S$  in mode-I and mode-III, respectively. Since a positive energy supply is needed for the crack to propagate, the crack speeds are restricted to below the corresponding limiting speeds.

The sign of energy release rate is positive even in mode-II when the crack speeds are smaller than  $c_R$ . This translates to the condition that the stresses near the tip are singular as  $1/\sqrt{r}$ . For crack speeds between  $c_R$  and  $c_S$ , the sign of  $G$  becomes negative as earlier, and hence speeds in this regime are forbidden. However, for crack speeds that exceed  $c_S$ , it was observed that stresses at the tip are singular as  $1/r^m$ , where  $m \leq 0.5$  with the equality holding at a crack speed of  $\sqrt{2}c_S$ . The shear stress and horizontal velocity component for such a case can be seen to be (Freund, 1979)

$$\sigma_{xy} = \frac{K_2^*(t)}{(2\pi)^{1/2}} \left[ \frac{\cos(m\theta_l)}{r_l^m} + \frac{H(-\xi - \beta_s|\eta|) \sin(\pi m)}{(-\xi - \beta_s|\eta|)^m \tan m} \right], \quad (1.27)$$

$$\dot{u}_x = \frac{vK_2^*(t)}{2\mu\alpha_l(2\pi)^{1/2}} \left[ \frac{\sin(m\theta_l)}{r_l^m} - 2\alpha_l\beta_s \frac{H(-\xi - \beta_s|\eta|) \sin(\pi m)}{(-\xi - \beta_s|\eta|)^m \tan m} \right], \quad (1.28)$$

where  $H$  denotes the Heaviside function,  $\xi, \eta, \beta, m$  are functions of crack speed and material parameters.  $\pi m = \arctan[4\alpha_l\beta_s/(1 + \alpha_s^2)^2]$ . As mentioned earlier,  $m = 1/2$  when  $v = \sqrt{2}c_S$ . It can be seen that the stresses and particle speeds exhibit jumps along the surfaces  $-\xi - \beta_s|\eta| = 0$  and are singular along the surface as well. Since the singularity of the stress is  $m(\leq 1/2)$ , the energy release rate is 0 for all crack speeds above  $c_S$  except at  $\sqrt{2}c_S$ . This was seen to be the consequence of the sharp crack assumption and assuming that the failure happens over a finite region instead of just at the tip was seen to overcome this limitation. Overall, mode-II cracks are permitted to travel at speeds that exceed  $c_S$ . Such cracks have been observed experimentally, for instance, in (Rosakis et al., 2000; Gori, Rubino, Rosakis, & Lapusta, 2018).

In such experiments, shock waves that travel along with the crack were observed (see figure 1.9) in the photoelastic fringes. A sharp rise in particle velocities after the shock passes through were observed (Mello, Bhat, Rosakis, & Kanamori, 2010). These cracks were modeled using Finite Elements in (Miller, Freund, & Needleman, 1999). Simulations performed using molecular dynamics such as in (Abraham et al., 2002) also confirm the existence of such cracks.

Transonic cracks have been observed in opening mode in fracture experiments on rubber. Such cracks have been first reported to be observed by (Petersan, Deegan, Marder, & Swinney, 2004). More experiments performed by (Chen, Zhang, Niemczura, Ravi-Chandar, & Marder, 2011; Mai, Okuno, Tsunoda, & Urayama, 2020; Corre, Coret, Verron, Leblé, & Le Lay, 2020) confirm this. More details on this will be discussed later in this thesis.

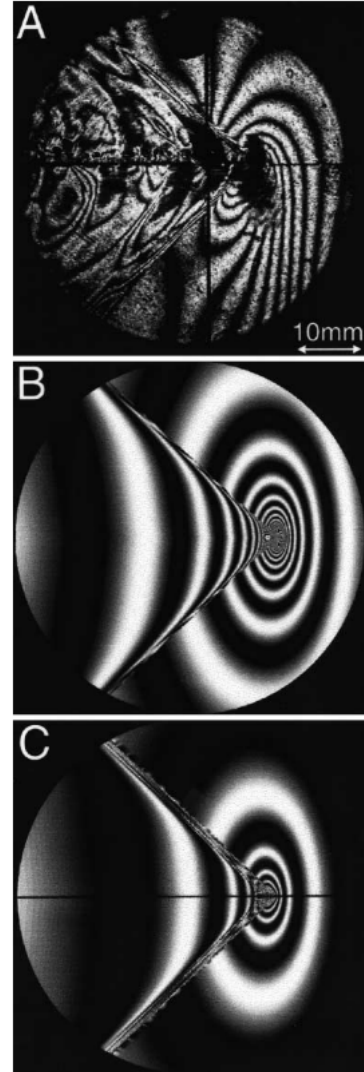


Figure 1.9: Comparison of experimental results (A) with the theory from (Freund, 1979) with a sharp crack assumption (B) and the theory with a finite failure zone (C). Reproduced from (Rosakis et al., 2000).

## **SUMMARY**

In this chapter, the theory of LEFM was briefly described. The asymptotic crack tip fields were presented for static and dynamic cases. Different propagation conditions for crack were briefly presented. The crack tip fields for the case of large deformations and Neo-Hookean model have been presented in static and dynamic cases. A brief discussion about Transonic cracks has been given.

# EXPERIMENTAL AND THEORETICAL STUDIES

# 2

---

This chapter introduces the available studies on the dynamic fracture. Different experimental specimen geometries used for elastomer fracture will be presented. Some available experimental and theoretical studies regarding the *quasi-static* and *high speed* fracture of elastomers will be presented. A brief summary of the notion of energy release rate and the energy flux integral will be presented.

---

## CONTENTS

2.1	Early studies . . . . .	16
2.2	'Instabilities' in dynamic fracture . . . . .	17
2.3	Fracture of elastomers . . . . .	18
2.3.1	Tearing . . . . .	18
2.3.2	SENT . . . . .	18
2.3.3	Pure Shear . . . . .	18
2.4	Experimental and theoretical studies on polymer fracture . . . . .	19
2.5	Energy release rate through integrals . . . . .	22
2.5.1	Energy flux integral . . . . .	22
2.5.2	Eshelby's integral . . . . .	24
2.5.3	Small strains . . . . .	26
2.5.4	Comparison between the two integrals . . . . .	26

## 2.1 EARLY STUDIES

The early investigations into the dynamic fracture can be traced back to the works of Dally, 1979; Ravi-Chandar and Knauss, 1984a and the references cited therein. The fracture of Homalite-100 was studied in Ravi-Chandar and Knauss, 1984a. The propagation of crack was studied under applied loading and the dimensions of the specimen were chosen so that considerable crack propagation occurred before the stress waves reflected from the boundaries interacted with the crack. The loading was applied on the crack faces through an electromagnetic device. The crack propagation was studied under different applied loads and loading rates.

One of the observations of that study is the change in the appearance of the fracture surfaces at different SIFs. It was observed that the crack speed remained almost the same during propagation but the size of the damage zone varied as the SIF varied. A change in the appearance of the fracture surfaces was noted in accordance with the change in the SIF (from photo-elastic measurements). The surface pattern was reported to change from 'mirror' to 'mist' to 'hackle', where the roughness progressively increased. Crack branching was observed to occur at crack speeds of about 50% of  $c_R$ . It was observed that the interaction with reflected waves is not necessary for the crack to undergo branching. A mechanism for branching has been proposed in Ravi-Chandar and Knauss, 1984a by taking into account the interaction of micro branches and voids in the crack path. Branching was thought to occur when the small cracks deviate from the main crack plane.

The results of the study were compared with that of Dally, 1979 (see figure 2.1). It can be seen that while Dally, 1979 reported a unique relationship between the SIF and crack speed, in the studies of Ravi-Chandar and Knauss, 1984b, the crack speed remained constant in the experiment while the SIF was seen to vary (with a corresponding change in crack surface appearance).

Further experiments were performed on PMMA by Fineberg, Gross, Marder, and Swinney, 1992. Some differences can be noted between the experimental setups in Fineberg et al., 1992 and Ravi-Chandar and Knauss, 1984a. In Ravi-Chandar and Knauss, 1984a, a gap was machined into the material and the loading was directly applied onto the crack faces using an electromagnetic device. In Fineberg et al., 1992, the specimen was first stretched quasi-statically to a certain strain level and a crack is then introduced in the specimen. Also, in Ravi-Chandar and Knauss, 1984a, the crack tip SIF is measured by using the method of caustics and the crack speed by a high speed camera. In Fineberg et al., 1992, the crack speed is measured by a change in the electrical resistance of the thin layer of Aluminum deposited onto the specimen faces. Starting from about  $0.34c_R$ , the crack speeds were observed to oscillate and this was seen to coincide with the development of roughness on the crack surfaces. The authors term this as 'microbranching instability'.

Many other fracture experiments were performed in the context of dynamic fracture, for instance, to investigate the effect of the fracture process zone on the terminal crack speed. In the references mentioned above, the crack was observed to undergo branching at a speed of about 40% to 60% of  $c_R$ . This was attributed to the development and propagation of micro branches from the main crack tip. To investigate if the cracks can propagate at higher speeds if the micro branches are suppressed, experiments were conducted in Washabaugh and Knauss, 1994. Micro branching is suppressed using two methods. In the first, the specimen is cut in half and the cut halves are machined to make the surfaces smooth. They are then molded in a vacuum at high temperature till the interface is strong enough, but not as strong as the base material. In the other method, an array of holes were

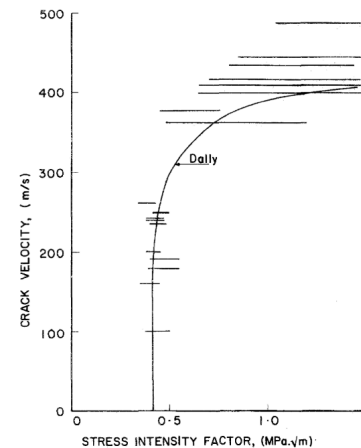


Figure 2.1: SIF vs crack speed. Comparison of results from Dally, 1979 and Ravi-Chandar and Knauss, 1984b. Adapted from Ravi-Chandar and Knauss, 1984b.

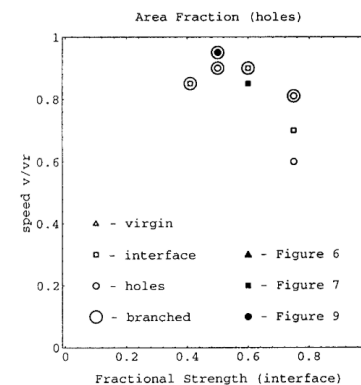


Figure 2.2: Crack speeds obtained when using a weak interface and holes (Washabaugh & Knauss, 1994).

drilled into the material along the prospective crack path at various spacing. It was reported that using the above techniques, the crack speed was able to approach  $c_R$  in the cases when the interface is ‘weak enough’ (see figure 2.2). A detailed review of the dynamic fracture of nominally brittle materials can be found in Ravi-Chandar and Yang, 1997. The results of various models to describe the evolution of defects and propagation of crack have been discussed.

## 2.2 ‘INSTABILITIES’ IN DYNAMIC FRACTURE

Even though the upper bound on the crack speed is  $c_R$ , in reality, cracks hardly reach that speed unless special measures are taken as discussed earlier. At crack speeds of about 40% to 60% of  $c_R$  (Ravi-Chandar & Knauss, 1984b), the tip is known to undergo branching where the main crack branches into multiple branches which later propagate. It was reported that the crack speeds remained at about 45% of  $c_R$  even when the loads applied were higher and the crack did not branch as well. The authors attribute the lower terminal speed observed and the events of branching to the growth and interaction of microcracks along with the main crack.

### Microbranching instability

In the experiments performed on PMMA by Sharon, Gross, and Fineberg, 1996; Sharon and Fineberg, 1996, it was observed that starting from a certain crack speed (called  $v_c$ ), the crack surfaces became rougher. Oscillations were also observed in the crack speed once it exceeded  $v_c$  ( $\approx 0.4c_R$ ). The authors termed the phenomenon as ‘Microbranching instability’ (Fineberg & Marder, 1991; Fineberg et al., 1992).

It was shown in those works that there was a corresponding increase in the area of the fracture surface created once the crack speed exceeded  $v_c$ . The increase in fracture energy during fracture was regarded as a consequence of an increase in the mean surface area of the crack. The same behavior was reported for glass and polyacrylamide gels as well in (Bouchbinder et al., 2014). It shall be noted that the cited references do not make any special comments about ‘macro-branching’ observed during the experiments as opposed to Ravi-Chandar and Knauss, 1984b.

### Oscillatory instability

It was also reported that the  $v_c$  mentioned earlier depended on the crack acceleration as well (page 17 of Bouchbinder et al., 2014).  $v_c$  was seen to be an increasing function of crack acceleration, increasing from its value ( $\approx 0.4c_R$ ) at lowest accelerations. It was also seen that  $v_c$  can be increased by suppressing the ‘instabilities’, for instance, by decreasing the specimen thickness. To this effect, fracture tests were performed on polyacrylamide gels in Livne, Ben-David, and Fineberg, 2006. Specimen were stretched to ‘very large strains’ and a crack was introduced. Also, a thin specimen was used to suppress any instabilities. Using both these techniques, it was reported that the cracks traveling as fast as  $0.9c_s$  were achieved. It was observed, however, that instead of the ‘micro-branching’ instability mentioned above, an oscillatory the crack path was observed. Similar oscillatory cracks were also observed in the works of Deegan, Petersan, Marder, and Swinney, 2002, although in a different context.

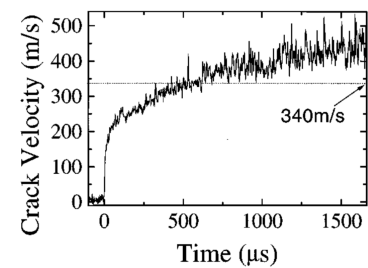


Figure 2.3: Microbranching instability in PMMA (Sharon et al., 1996). Oscillations in crack speed after a certain limit can be seen.

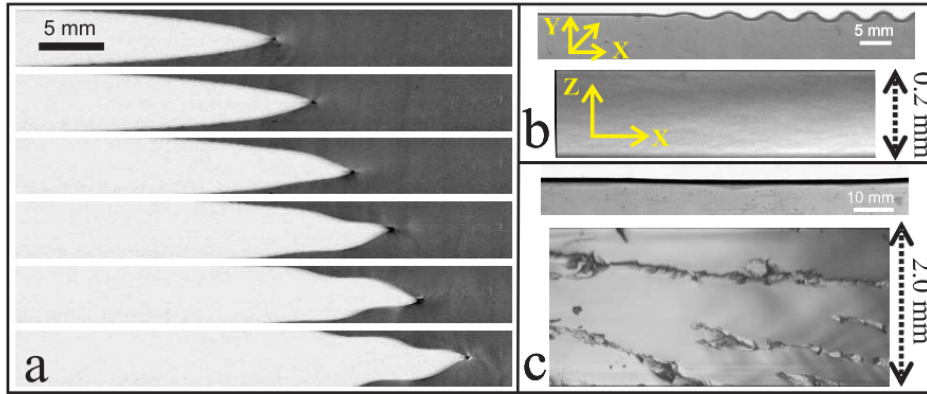


Figure 2.4: Oscillatory instability observed in Livne, Ben-David, and Fineberg, 2006. A sequence of photographs, shown at 0.69 ms intervals, of a propagating crack undergoing a transition from linear (top 2 pictures) to oscillatory motion. Photographs of XY profile (top) and (XZ) fracture surface (bottom) of (b) a 0.2 mm thick gel sample where oscillations developed and (c) a 2.0 mm thick gel where the crack retained its straight line trajectory.

## 2.3 FRACTURE OF ELASTOMERS

The investigation of fracture of elastomers can be traced back to Greensmith and Thomas, 1956. In that study, the fracture behavior and properties of elastomers were studied by using rubber specimen in ‘tearing’ and ‘pure shear’ configurations. A brief description of the specimen configurations and the fracture energy in those configurations can be seen below.

### 2.3.1 Tearing

A ‘trouser’ specimen is used for testing in this configuration. The specimen contains two ‘legs’ which are held on to a tensile machine that are pulled apart. The fracture energy in this configuration is computed using the stretch level in each arm and the expression 2.1. The force measurement can be obtained from the tensile machine and the stretch level can be obtained by measuring the final lengths of arms. The strain energy density can then be calculated.

$$G = wh_0 - \frac{2}{e_0} \lambda F. \quad (2.1)$$

The values of  $h_0$  and  $e_0$  can be obtained from the geometry as shown in the figure 2.5.  $w$  is the strain energy density corresponding to the strain state at the loading condition.

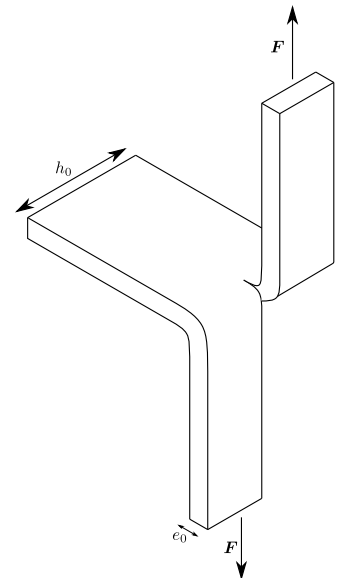


Figure 2.5: Tearing configuration.

### 2.3.2 SENT

Other specimen configuration that can be used is the ‘Single Edge Notched Tension’. The geometry can be seen in the figure 2.6. In this case, the energy release rate can be computed as

$$G = 2\beta w l, \quad (2.2)$$

where  $l$  denotes the crack length and  $\beta$  depends on the stretch level and can be approximated as  $3\lambda^{-1/2}$ .

### 2.3.3 Pure Shear

In this case, a specimen that is wide enough (about 5 times as tall as the specimen height) is clamped along its longer edges onto a tensile machine. The specimen is stretched to the target level and a crack is introduced. Once the crack reaches the

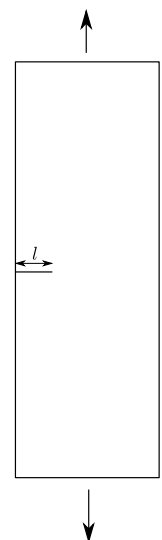


Figure 2.6: Single Edge Notched Tension specimen configuration.

center of the specimen, the energy release rate can be calculated by

$$G = wh_0, \quad (2.3)$$

where  $h_0$  is the initial specimen height (see figure 2.14).

## 2.4 EXPERIMENTAL AND THEORETICAL STUDIES ON POLYMER FRACTURE

Early experimental studies on the fracture of elastomers can be traced back to the works of R. S. Rivlin and Thomas, 1953. In that study, specimens of natural rubber were torn in the configurations described earlier to obtain a relation between the fracture energy vs speed. Further experiments were carried out by Greensmith and Thomas, 1956; Greensmith, 1957 and the references cited therein. Most of the works were carried out in the tearing configuration. Based on the nature of the traction separation curves observed and the fracture surfaces, the overall fracture behavior was classified into 'slip-stick' and 'steady' tearing. In 'slip-stick' tearing, large oscillations were observed in the crack speeds as well as the traction curves. It shall be observed that in all the studies mentioned above, a Griffith-like criterion has been used to interpret the experimental data in terms of fracture energy vs the crack speed.

On the other hand, the fracture of polymers was studied by Knauss and co-workers in W. Knauss and Mueller, 1971. In those studies, the pure shear configuration was used. The material tested is Solithane 113. The results of the experiments were presented in terms of the macroscopic strain imposed vs the crack speed observed (see figure 2.7).

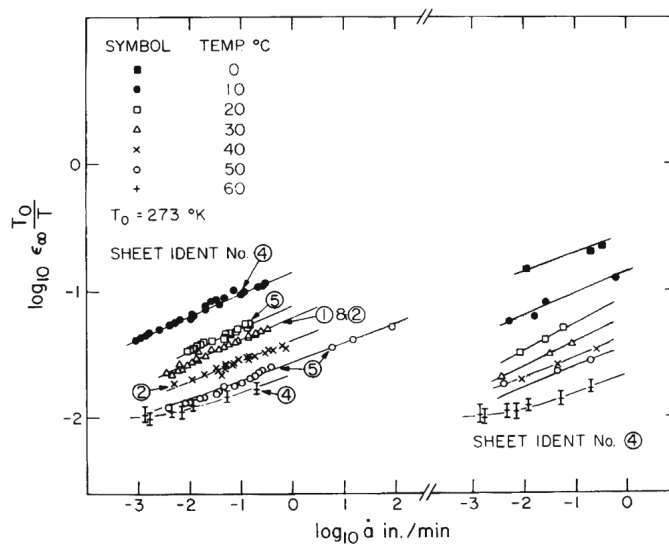


Figure 2.7: Crack propagation data for multiple production runs, prior to applying the time-temperature superposition process (W. Knauss, 2015).

To interpret the data, an analytical investigation was carried out. Using a cohesive zone type model to describe the behavior of the material failing at the tip, a relation between the crack speed, the applied load, and the viscoelastic properties of the bulk material was obtained in W. Knauss, 1970; W. Knauss and Mueller, 1971; W. Knauss, 2015. Two failure criteria were considered for crack propagation - failure strain criterion and an energy criterion.

In failure strain criterion, the cohesive zone was assumed to fail completely when the strain value reaches a certain limit. The tractions in the cohesive zone were taken to completely drop to zero at this value. This criterion can be written as

$$u_y(0, 0, \dot{a}) = u_0. \quad (2.4)$$

In the above equation, the coordinates  $(0, 0)$  denote the physical crack tip, and  $\dot{a}$  denotes the crack speed.  $u_0$  is the strain value at which the failure occurs.

In the energy criterion, a cohesive element was assumed to fail when the energy expended on the element by the surrounding material reached a certain value. This can be written as

$$- \int_{A_c} T_n(X) \cdot \frac{\partial u_y}{\partial X}(X, 0, \dot{a}) dX = \gamma, \quad (2.5)$$

where  $A_c$  denotes the area spanned by the failing material,  $T_n$  are the tractions,  $u_y$  is the y-component of the displacement of the crack surface.  $\gamma$  denotes the fracture energy.

The opening displacement of the crack faces under external loading for viscoelastic material was obtained by using the elastic solution under the same loading and correspondence principal. The constitutive behavior of the failing material is specified as a relation between the traction and separation. In W. Knauss, 2015, a constant traction value has been assumed over a span of  $\alpha$ . Using both the traction and separation, equations 2.4 and 2.5 can be evaluated. The displacement criterion hence becomes

$$\frac{3K\sqrt{\alpha}}{\sqrt{2\pi}E_\infty} \vartheta \left( \frac{\alpha}{\dot{a}} \right) = u_0, \quad (2.6)$$

where  $K$  is the SIF corresponding to the applied load,  $E_\infty$  is the long term elastic modulus and  $\vartheta$  is a parameter that depends on the viscoelastic properties of the material. The energy criterion becomes

$$\frac{3}{4}K^2\Theta_R \left( \frac{\alpha}{\dot{a}} \right) = E_\infty\gamma, \quad (2.7)$$

where  $\Theta_R$  is a function that depends on the viscoelastic properties of the material. The predictions of the above criterion were compared with the experiments whereby the values of parameters like  $\gamma$  and  $\alpha$  were obtained. It shall be noted that a similar development was carried out by Schapery, 1975b, 1975a, 1975c.

The above-mentioned studies use a failure zone at the tip to describe the fracture processes. Some other studies exist that follow Griffith's failure criterion that the energy to failure comes from the reduction of the energy in the bulk Christensen, 1979. In such a case, the global conservation of energy gives

$$\dot{a}\gamma + \int_V \Lambda dv + \dot{U} = 0. \quad (2.8)$$

In the above equation,  $V$  is the volume of the material,  $\Lambda$  is the energy dissipation rate in the material, and  $\dot{U}$  is the rate of change in strain energy. Inertial effects have been neglected. An earlier study in this direction was done by Kostrov and Nikitin, 1970. However, that study leads to a conclusion that the sharp crack modeling approach or Griffith's failure criterion leads to a conclusion that the viscoelastic properties do not affect the crack propagation (James R. Rice, 1979). This can be seen by examining equations 2.6 or 2.7 in the limit of  $\alpha \rightarrow 0$ . In that case, the equation 2.7, for instance, reduces to

$$\frac{3}{4}K^2\Theta_R(0) = E_\infty\gamma. \quad (2.9)$$

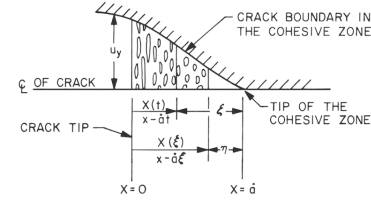


Figure 2.8: Description of cohesive zone from W. Knauss, 2015.

It can be seen that only the initial (glassy) viscoelastic properties enter the equation as opposed to the case when  $\alpha$  is not zero. However, Christensen, 1979 attributes this conclusion to *the omission of heat source term which indirectly leads to elimination of dissipation* in the formulation of Kostrov and Nikitin, 1970. The comparison between the theory and experiments has only been done for a limited range in Christensen, 1979.

Other studies where the sharp crack modeling technique has been used are that of B. N. Persson and Brener, 2005; B. N. J. Persson, Albohr, Heinrich, and Ueba, 2005. In this approach, the point of departure is the conservation of energy as earlier. In this case, however, the singularity at the crack tip has been considered explicitly as opposed to Christensen, 1979, where multiple terms of a power series were considered to approximate the crack tip singularity. The point of departure of B. N. Persson and Brener, 2005 is

$$G\dot{a} = G_0\dot{a} + P, \quad (2.10)$$

where the first term on the left indicates the global energy expenditure, the first term on the right indicates the energy consumed by the crack tip during the fracture process and  $P$  denotes the energy dissipation in the bulk material. The dissipation in the bulk material was calculated explicitly by using a power-law model for the relaxation function. The formulation was compared with the experimental results from Gent, 1996b. The slope of the energy release rate vs the crack speed curve was found to be 0.27, which was found to be in good agreement with the theory.

More experiments were conducted by Lake, Thomas, and Lawrence, 1992; Lake, Lawrence, and Thomas, 2000; Tsunoda, Busfield, Davies, and Thomas, 2000 on the fracture of elastomers. In Lake et al., 1992, the phenomenon of cavitation of elastomers has been investigated. More discussions on this will follow in later chapters. Other works such as that of Lake et al., 2000; Tsunoda et al., 2000 investigate the effect of various parameters such as the specimen geometry (thickness in particular), the chemical composition, the effect of fillers, etc. on the fracture properties of the specimen. The crack speeds in Tsunoda et al., 2000 are considerably smaller than that in Lake et al., 2000. Hence, inertial effects were not considered in that study.

### High speed fracture of elastomers

Studies in which the crack speeds are much smaller than the wave speed in the material do not need the consideration of inertial effects. When the crack speed is higher, typically more than about 30% of the shear wave speed, inertial effects become important. Such studies were performed by Stevenson and Thomas, 1979; Kadir and Thomas, 1981; Gent and Marteny, 1982a. Since the crack speeds in the studies are higher, a comparison to wave speeds was made. In Stevenson and Thomas, 1979, fracture tests were performed by using balloons made of natural rubber. A needle was used to initiate the crack once a target strain level was reached. The wave speeds were also measured by performing retraction experiments on rubber sheets. However, the crack speeds and wave speeds reported in that study are on the *deformed* configuration. It was observed and remarked that the crack speeds obtained in that study are considerably higher than the wave speeds measured and even the 'strain dependence of the wave speed' does not account for the observed higher crack speeds. The high rate of extensions at the crack tip was thought to modify the material stiffness and hence the wave speeds. This was regarded as a cause of the observed higher crack speeds. No specific mention of 'Transonic cracks' was made. The crack surface was found to have

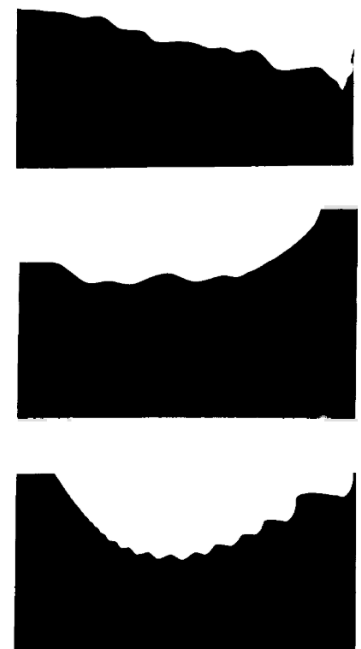


Figure 2.9: Undulations on fracture surfaces reported in Stevenson and Thomas, 1979.  $\lambda = 2.3, 3.7, 5.0$  in top, middle and bottom figures.

wavelike series of undulations, 5-8  $\mu\text{m}$  apart and 3-5  $\mu\text{m}$  deep over most of the fracture surface. Bi-axial strain state was stated to be the probable reason for the undulations. Livne et al., 2006 report such oscillatory crack path, but does not mention the study of Stevenson and Thomas, 1979.

In Gent and Marteny, 1982a, more experiments were made on unfilled and carbon-black-filled natural rubber specimens in pure shear geometry. Wave speeds were measured by performing retraction tests in a different study (Gent & Marteny, 1982b). The crack speeds are compared to  $0.3v_s$  (Mott, 1948), where  $v_s$  is the velocity of stress pulse in the material. The crack speeds and stress pulse speeds were reported in the *deformed* configuration as well. Also, specimens of different geometry (specifically heights) were subjected to the same stretch level and the crack speeds were measured. It was observed that the crack speeds become independent of the specimen height starting from a certain height. No mention was made about Transonic cracks as well.

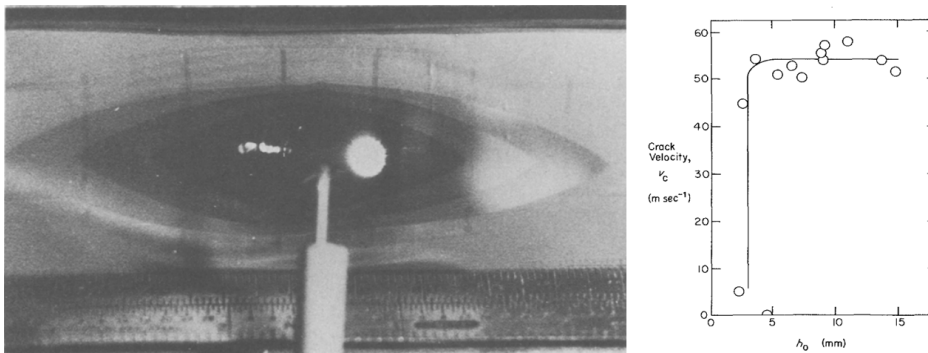


Figure 2.10: Crack propagation studied in pure shear configuration in Gent and Marteny, 1982a. Also can be seen is the result of the crack speed vs the specimen height for the same stretch level.

More experiments on dynamic fracture of elastomers were made by Petersan et al., 2004; Chen et al., 2011. These experiments were perhaps the first to report the existence of ‘Transonic cracks’ in the opening mode in elastomers. It was reported that in natural rubbers, starting from a certain stretch level, the crack speeds exceeded the Shear wave speed. It was also observed that the crack speeds became independent of the specimen height in this regime. More on this will be discussed later in this thesis.

## 2.5 ENERGY RELEASE RATE THROUGH INTEGRALS

The Energy release rate is related to the crack speeds observed in the experiments throughout the literature. It is measured by using the strain energy density in the material far ahead of the tip and far behind it - that the energy lost by the body as the crack propagates through it is consumed by the fracture processes. The expression for the energy release rate can also be obtained through contour integrals established in the literature. This section briefly reviews two of such integrals to bring out their similarities and differences.

### 2.5.1 Energy flux integral

In Freund, 1990, an expression was obtained to compute the instantaneous energy flux through a contour that moves along with the crack with a speed  $v$  along x-axis. The expression can be seen to be

$$F(\Gamma) = \int_{\Gamma} \left[ \sigma_{ji} n_j \frac{\partial u_i}{\partial t} + (U + T) v n_1 \right] dS, \quad (2.11)$$

where  $U$  is the stress work density and  $T$  is the kinetic energy density.  $\sigma_{ij}$  denotes the  $ij$ -th component of Cauchy stress in the Cartesian basis and  $n_j$  is the  $j$ -th component of the outward normal to the contour  $\Gamma$ . The expressions for  $U$  and  $T$  are given by

$$U = \int_{-\infty}^t \sigma_{ji} \frac{\partial^2 u_i}{\partial t' \partial x_j} dt' \quad \text{and} \quad T = \frac{1}{2} \rho \frac{\partial u_i}{\partial t} \frac{\partial u_i}{\partial t}, \quad (2.12)$$

where the summation on repeated indices is implied.

### **Path (in)dependence**

The path dependence of the above contour integral was examined by considering the difference in the value of flux integral evaluated along two different contours  $\Gamma_1$  and  $\Gamma_2$ . the difference can be seen to be

$$F(\Gamma_2) - F(\Gamma_1) = \int_{A_{12}} \left[ \left( \frac{\partial U}{\partial t} + v \frac{\partial U}{\partial x_1} \right) + \rho \frac{\partial u_i}{\partial t} \left( \frac{\partial^2 u_i}{\partial t^2} + v \frac{\partial^2 u_i}{\partial t \partial x_1} \right) \right] dA, \quad (2.13)$$

where  $\Gamma_2$  is outside  $\Gamma_1$  and  $A_{12}$  is the area enclosed between the two contours.

In the special case of a steady crack growth, the fields remain invariant in a frame traveling with the crack tip. In such a case, the fields depends on  $x_1$  and  $t$  only through the combination,  $\zeta = x_1 - vt$ . Thus, the terms in the parenthesis of the equation 2.13 go to zero and the contour integral is hence independent of  $\Gamma$  chosen. Also, in that case, using  $\frac{\partial}{\partial t} = -v \frac{\partial}{\partial x_1}$ , the contour integral reduces to

$$F(\Gamma) = v \int_{\Gamma} \left[ (U + T)n_1 - \sigma_{ji} n_j \frac{\partial u_i}{\partial x_1} \right] dS. \quad (2.14)$$

$U$  and  $T$  reduce to

$$U = \int_{x_1-vt}^{\infty} \sigma_{ji} \frac{\partial^2 u_i}{\partial x_j \partial \zeta} d\zeta \quad \text{and} \quad T = \frac{1}{2} \rho v^2 \frac{\partial u_i}{\partial x_1} \frac{\partial u_i}{\partial x_1}. \quad (2.15)$$

It shall be noted that the path independence for a steady state crack propagation has been established *without* using a constitutive model and hence is valid even for plastic, viscoplastic and viscoelastic materials.

### **Energy release rate**

The energy release rate has been defined using the expression in equation 2.11 as (Freund, 1990)

$$G = \lim_{\Gamma \rightarrow \text{tip}} \left\{ \frac{F(\Gamma)}{v} \right\} \quad (2.16)$$

$$= \lim_{\Gamma \rightarrow \text{tip}} \left\{ \frac{1}{v} \int_{\Gamma} \left[ \sigma_{ji} n_j \frac{\partial u_i}{\partial t} + (U + T)v n_1 \right] dS \right\} \quad (2.17)$$

Under steady state, the above equation reduces to

$$G = \oint_{\text{tip}} \left[ (U + T)n_1 - \sigma_{ji} n_j \frac{\partial u_i}{\partial x_1} \right] dS. \quad (2.18)$$

### 2.5.2 Eshelby's integral

In addition to the energy flux integral described above, other contour integrals exist in fracture mechanics that have been developed from the perspective of the mechanics in material manifold (Gurtin, 2000; Steinmann, 2000). The development in this direction relies on the change in the energy of the system as a result of the change in the material configuration (denoted  $\mathcal{B}_X(t)$ ) of the system (Runesson, Larsson, & Steinmann, 2009). The notions of a time invariant reference configuration (denoted  $\mathcal{B}_\xi$ ) and a time varying spatial configuration (denoted  $\mathcal{B}_x(t)$ ) have been defined for this purpose. The three configurations are related by maps as defined.

The maps  $\tilde{\varphi} : (\mathcal{B}_\xi, \mathbb{R}^+) \rightarrow \mathcal{B}_X(t)$  such that  $(\xi, t) \xrightarrow{\tilde{\varphi}} X := \tilde{\varphi}(\xi, t)$  between the reference configuration and the material configuration,  $\hat{\varphi} : (\mathcal{B}_\xi, \mathbb{R}^+) \rightarrow \mathcal{B}_x(t)$  such that  $(\xi, t) \xrightarrow{\hat{\varphi}} \mathbf{x} := \hat{\varphi}(\xi, t)$  between the reference configuration and the spatial configuration and  $\varphi : (\mathcal{B}_X(t), \mathbb{R}^+) \rightarrow \mathcal{B}_x(t)$  such that  $(X, t) \xrightarrow{\varphi} \mathbf{x} := \varphi(X, t)$  between the material configuration and the spatial configuration are defined. The three maps can be seen to be related by the composition  $\hat{\varphi}(\xi, t) = (\varphi \circ \tilde{\varphi})(\xi, t)$ .

As mentioned earlier, the intention is to study the dissipation in the system as a consequence of the change in material configuration, that is a variation of the map  $\tilde{\varphi}$ . Assuming the material to be homogeneous, free of body forces and elastic, the dissipation can be seen, under isothermal conditions to be

$$\mathcal{D}(\mathbf{w}_0) = \int_{\partial\Omega_X} C_k \mathbf{n}_0 \cdot \mathbf{w}_0 \, dS, \quad (2.19)$$

where  $\mathbf{w}_0 := \frac{\partial \mathbf{X}_{\text{tip}}}{\partial t}$  is, in this case, the crack speed in the material configuration,  $\mathbf{n}_0$  is the outward normal to the contour  $\partial\Omega_X$  and  $C_k$  is the Eshelby stress tensor in dynamics, defined as

$$C_k := (\psi + k)\mathbf{I} - \mathbf{F}^T \mathbf{P}. \quad (2.20)$$

Here,  $\psi$  is the strain energy density per unit volume in material configuration,  $k$  is the kinetic energy density per unit volume in material configuration,  $\mathbf{F} := \frac{\partial \mathbf{x}}{\partial \mathbf{X}}$  is the deformation gradient and  $\mathbf{P}$  is the first Piola Kirchhoff stress tensor. The contour  $\partial\Omega_X$  is taken as shown in the figure 2.12. From the figure, it can be seen that  $\partial\Omega_X = \partial\Omega_{X,\text{ext}} \cup \Gamma_c^+ \cup \Gamma_{\text{tip}} \cup \Gamma_c^-$ .  $\Gamma_c^\pm$  are the top and bottom of the portion of crack face that are not enclosed within  $\Gamma_{\text{tip}}$ .  $\Gamma_{\text{tip}}$  is a contour that goes around the tip from the bottom face of the crack to the top face. Realizing that  $\mathbf{w}_0 = \mathbf{o}$  on  $\partial\Omega_{X,\text{ext}}$  and  $\Gamma_c^\pm$ , the expression for dissipation reduces to just over the contour enclosing the tip, shrunk to the tip.

$$\mathcal{D}(\mathbf{w}_0) = \oint_{\text{tip}} C_k \mathbf{n}_0 \cdot \mathbf{w}_0 \, dS. \quad (2.21)$$

This allows to define the 'configurational forces' acting at the tip that is conjugate to the crack speed. The dissipation in the above equation can hence be expressed as

$$\mathcal{D}(\mathbf{w}_0) = \mathbf{w}_0 \cdot \mathbf{f}_{\text{tip}}, \quad (2.22)$$

where

$$\mathbf{f}_{\text{tip}} := \oint_{\text{tip}} C_k \mathbf{n}_0 \, dS, \quad (2.23)$$

is the configurational force acting at the tip.

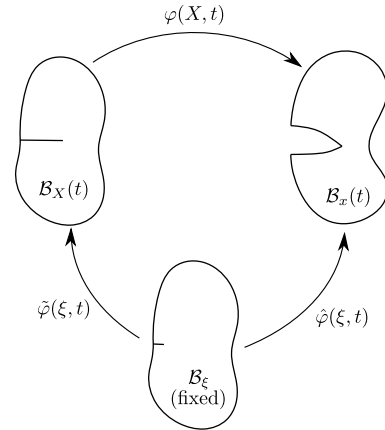


Figure 2.11: Reference configuration,  $\mathcal{B}_\xi$  (fixed), Material configuration,  $\mathcal{B}_X(t)$  and Spatial configuration,  $\mathcal{B}_x(t)$

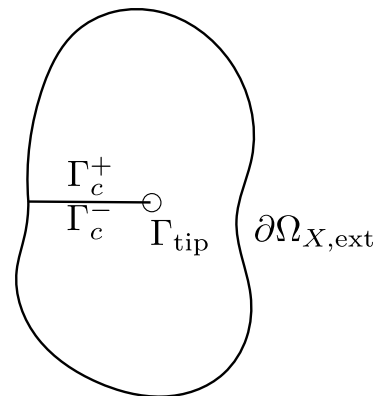


Figure 2.12: Contour on which the integration is performed in the material configuration.

If the material is inelastic, the dissipation in the bulk also contributes along with the dissipation at the tip. In that case, the dissipation expression becomes

$$\mathcal{D}(\mathbf{w}_0) = \oint_{\Gamma_{\text{tip}}} \mathbf{C}_k \mathbf{n}_0 \cdot \mathbf{w}_0 \, dS + \mathcal{D}_{\text{bulk}} = \mathbf{w}_0 \cdot \mathbf{f}_{\text{tip}} + \mathcal{D}_{\text{bulk}}, \quad (2.24)$$

where  $\mathcal{D}_{\text{bulk}} = \int_{\Omega_X \setminus \Omega_{\text{tip}}} \frac{\partial \psi}{\partial \mathbf{k}} \star \dot{\mathbf{k}} \, dV$ .  $\mathbf{k}$  indicates the array of internal variables and  $\star$ , a suitable contraction operation.  $\Omega_{\text{tip}}$  is the volume of material enclosed within  $\Gamma_{\text{tip}}$ .

### Steady state

For the case of a straight crack propagating in the  $X_1$ -direction under steady state conditions, as stated previously, the fields depend on  $X_1$  and  $t$  through the combination  $\zeta = X_1 - w_0 t$ . Hence, the spatial and temporal derivatives are related as  $\frac{\partial}{\partial t} = -w_0 \frac{\partial}{\partial X_1}$ . Hence, the bulk dissipation in the equation 2.24 can be written as

$$\mathcal{D}_{\text{bulk}} = -w_0 \int_{\Omega_X \setminus \Omega_{\text{tip}}} \frac{\partial \psi}{\partial \mathbf{k}} \star \frac{\partial \mathbf{k}}{\partial X_1} \, dV \quad (2.25)$$

The total dissipation becomes

$$\mathcal{D}(\mathbf{w}_0) = w_0 \left[ \mathbf{e}_1 \cdot \oint_{\Gamma_{\text{tip}}} \mathbf{C}_k \mathbf{n}_0 \, dS - \int_{\Omega_X \setminus \Omega_{\text{tip}}} \frac{\partial \psi}{\partial \mathbf{k}} \star \frac{\partial \mathbf{k}}{\partial X_1} \, dV \right] = w_0 \left[ \mathbf{e}_1 \cdot \int_{\partial \Omega_X} \mathbf{C}_k \mathbf{n}_0 \, dS \right] \quad (2.26)$$

A similar expression can be found in Simha, Fischer, Kolednik, and Chen, 2003; Simha, Fischer, Shan, Chen, and Kolednik, 2008 in the context of plasticity.

### Path (in)dependence

Considering another contour  $\Gamma_2$  that encloses  $\Gamma_{\text{tip}}$ , a relation can be found between the integrals on the two contours during the steady state.

$$\begin{aligned} w_0 \mathbf{e}_1 \cdot \left[ \int_{\Gamma_2} \mathbf{C}_k \mathbf{n}_0 \, dS - \oint_{\Gamma_{\text{tip}}} \mathbf{C}_k \mathbf{n}_0 \, dS \right] &= w_0 \mathbf{e}_1 \cdot \int_{\Gamma_{\text{tip}} \cup \Gamma_2 \cup \Gamma_c^{\pm}} \mathbf{C}_k \mathbf{n}_0 \, dS \\ &= w_0 \mathbf{e}_1 \cdot \int_{\Omega_2 \setminus \Omega_{\text{tip}}} \text{div}_0 \mathbf{C}_k \, dV, \end{aligned} \quad (2.27)$$

since on crack faces  $\mathbf{e}_1 \cdot \mathbf{n}_0 = 0$ . The divergence can be evaluated as below.

$$(\mathbf{C}_k)_{ij,j} = ((\psi + k)\delta_{ij} - \mathbf{F}_{ki} \mathbf{P}_{kj})_{,j} = \frac{\partial \psi}{\partial \mathbf{k}} \star \frac{\partial \mathbf{k}}{\partial X_i}. \quad (2.28)$$

Steady state has been assumed. Hence,  $\mathbf{e}_1 \cdot \text{div}_0 \mathbf{C}_k = \frac{\partial \psi}{\partial \mathbf{k}} \star \frac{\partial \mathbf{k}}{\partial X_1}$ .

Hence, the difference in contour integrals can be seen to be

$$w_0 \mathbf{e}_1 \cdot \left[ \oint_{\Gamma_{\text{tip}}} \mathbf{C}_k \mathbf{n}_0 \, dS - \int_{\Gamma_2} \mathbf{C}_k \mathbf{n}_0 \, dS \right] = -w_0 \mathbf{e}_1 \cdot \int_{\Omega_2 \setminus \Omega_{\text{tip}}} \frac{\partial \psi}{\partial \mathbf{k}} \star \frac{\partial \mathbf{k}}{\partial X_1} \, dV. \quad (2.29)$$

The RHS term can be identified as the dissipation in the volume between the two contours (see equation 2.25). Hence

$$w_0 \mathbf{e}_1 \cdot \left[ \oint_{\Gamma_{\text{tip}}} \mathbf{C}_k \mathbf{n}_0 \, dS - \int_{\Gamma_2} \mathbf{C}_k \mathbf{n}_0 \, dS \right] = \mathcal{D}_{\text{bulk}}^{\Omega_2 \setminus \Omega_{\text{tip}}}. \quad (2.30)$$

Hence, unless the material is elastic, which would mean zero bulk dissipation, the contour integral is **not** path independent.

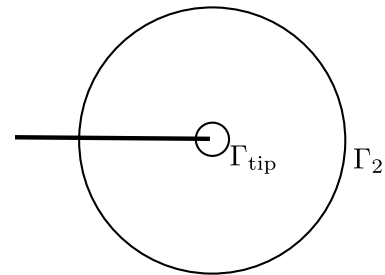


Figure 2.13: Contour enclosing the contour at the tip.

### 2.5.3 Small strains

Under small strain conditions, the integral in 2.23 can be simplified. Under small strain conditions,  $\mathbf{F} \approx \mathbf{I} + \nabla \mathbf{u}$ ,  $\mathbf{P} \approx \boldsymbol{\sigma}$ .

$$\oint_{\text{tip}} C_k \mathbf{n}_0 \, dS \approx \oint_{\text{tip}} \left( (\psi + k) \mathbf{I} - (\nabla \mathbf{u})^T \boldsymbol{\sigma} \right) \mathbf{n}_0 \, dS - \oint_{\text{tip}} \boldsymbol{\sigma} \mathbf{n}_0 \, dS. \quad (2.31)$$

If, at the tip, the stress components are singular as  $r^p$  where  $p < 1$ , the second term on the right side goes to  $\mathbf{o}$  (Gurtin, 2000). Hence, the contour integral can be expressed as

$$\oint_{\text{tip}} C_k \mathbf{n}_0 \, dS = \oint_{\text{tip}} \left( (\psi + k) \mathbf{I} - (\nabla \mathbf{u})^T \boldsymbol{\sigma} \right) \mathbf{n}_0 \, dS, \quad (2.32)$$

and the component along  $\mathbf{e}_1$  can be found to be

$$\mathbf{e}_1 \cdot \oint_{\text{tip}} C_k \mathbf{n}_0 \, dS = \oint_{\text{tip}} \left( (\psi + k) n_1 - \sigma_{ij} n_j \frac{\partial u_i}{\partial X_1} \right) dS. \quad (2.33)$$

### 2.5.4 Comparison between the two integrals

At this point, a comparison can be made between the two integrals in equations 2.18 and 2.33. The former integral contains  $U = \int_{-\infty}^t \sigma_{ji} \frac{\partial^2 u_i}{\partial t' \partial x_j} dt'$ , which is the stress work density, while the latter integral contains  $\psi$ , which is the strain energy density. In the elastic case, the two integrals, hence, coincide. Hence, the integral in 2.33 can be seen as the energy flux to the tip and the configurational force at the tip as well.

Also, the integral in 2.33 can be seen to be path dependent except in the case of an elastic material in steady state. The integral in 2.18, however, can be seen to be path independent in the steady state scenario regardless of the constitutive behavior of the material. The latter also has the significance of representing the energy flux through the contour  $\Gamma$ , while the former doesn't, even in the steady state (except if the material is elastic). For instance, in the case of crack propagation under steady state conditions in a strip (see figure 2.14), the first integral (in equation 2.33) when evaluated on a contour far from the tip results in

$$\mathbf{e}_1 \cdot \int_{\Gamma_\infty} C_k \mathbf{n}_0 \, dS = [\psi(+)-\psi(-)] h, \quad (2.34)$$

which is often stated as the energy release rate in literature (Greensmith & Thomas, 1956). The integral in 2.18 on the same contour gives a different value since it involves evaluation of  $U$  along the part of the curve labeled (-). Along this curve,  $U(-) \neq \psi(-)$ , since the evaluation of  $U$  requires integration over the entire history

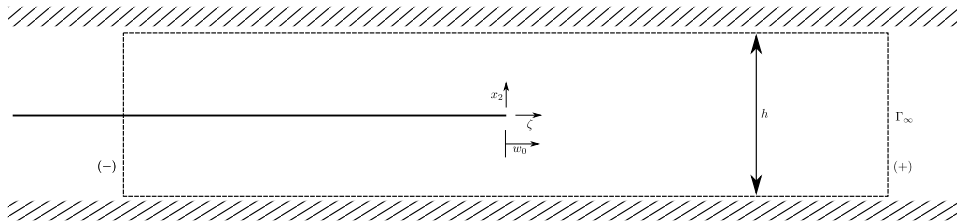


Figure 2.14: Crack propagation in an infinite strip.

of the strain states. But along the part of the curve (+),  $U(+) = \psi(+)$ . Hence, as stated earlier, unless the material is elastic,

$$\int_{\Gamma_\infty} (C_k)_{1j} (n_0)_j dS \neq \int_{\Gamma_\infty} \left[ (U + T)n_1 - \sigma_{ji} n_j \frac{\partial u_i}{\partial x_1} \right] dS \quad (2.35)$$

An illustration of the scenario where the inelastic effects can affect the evaluation of the contour integral can be seen in Freund and Hutchinson, 1985. In that study, the propagation of a crack in rate-dependent plastic solid was studied. The plastic deformation was assumed to remain within the region dominated by the SIF. Assuming a steady state, the relation between the near field and far field *Energy release rates* defined according to the equation 2.18 was obtained to be

$$G_{\text{tip}} = G - \int_{-h}^h U^* dx_2, \quad (2.36)$$

where  $h$  is the height of the plastic wake left behind by the propagating crack. In the above equation,  $G_{\text{tip}}$  has been defined as

$$G_{\text{tip}} = f(m) \frac{1 - \nu^2}{E} K_{\text{tip}}^2. \quad (2.37)$$

$K_{\text{tip}}$  denotes the amplitude of the near-tip stress singularities. Because of the constitutive assumption of the material behavior, the elastic strain rates dominate the plastic strain rates and hence, the solution near the tip is similar to that in an elastic material.  $G$  is defined as the far field energy release rate defined as  $f(m) \frac{1 - \nu^2}{E} K^2$ . Note the difference in the SIF used ( $K$  for far field vs  $K_{\text{tip}}$  for near field).  $U^*(x_2) = \lim_{x_1 \rightarrow -\infty} U(x_1, x_2)$  is the stress work density locked in the wake behind the tip.

## SUMMARY

This chapter presents an overview of the experiments of dynamic fracture performed on materials like Homalite-100, PMMA, and glass. This is followed by a description of the experimental setups used to study polymer fracture. Some theories on polymer fracture in the literature were presented. It was followed by an overview of the experimental studies available on high speed fracture of elastomers. It ends with a discussion about the integral formulations of energy release rate in the context of viscoelastic fracture.

# POLYMERS

# 3

---

This chapter provides a brief introduction to the polymer materials, dependence of their behavior on the strain rate. A brief description of the hyperelastic and viscoelastic models has been given as well.

---

## CONTENTS

3.1	Elastomers . . . . .	29
3.2	Nonlinear elasticity . . . . .	29
3.3	viscoelasticity . . . . .	32

### 3.1 ELASTOMERS

Elastomers are polymers that are generally amorphous comprised of long chains of macro-molecules (A. G. Holzappel, 2000; Verron, 2018). The chains are linked to each other through cross-linking. Elastomers are often reinforced by fillers such as Carbon black or Silica. This increases the stiffness of elastomers. Elastomers are characterized by their ability to undergo large deformations elastically.

When an elastomer is subjected to uniaxial tension the response typically looks like in the figure 3.1. The slope of the stress strain response can be seen to initially decrease from its value at zero strain level. After a certain strain level, however, the slope of the curve starts to raise again to higher values. As a result of sliding

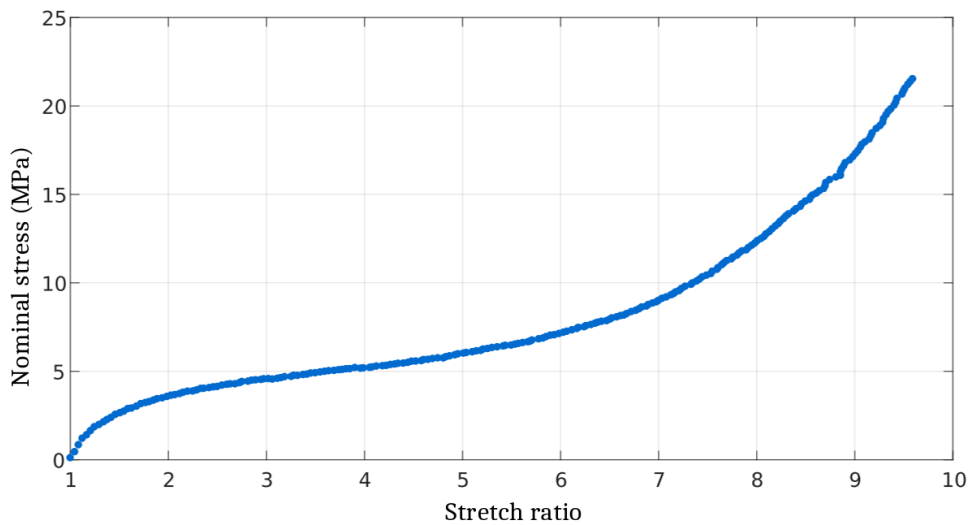


Figure 3.1: Typical stress-strain response of an elastomer, Polyurethane in particular. Extracted from Corre, 2018.

between the molecular chains, the behavior of the elastomers are a function of temperature and the loading rate. Based on the temperature and loading rate, the behavior of the elastomers can be classified into three categories.

- Brittle and rigid, which is called a glassy state.
- Soft and highly deformable, which is called the rubbery state.
- Transition behavior, where the polymer chains are highly mobile which makes the behavior rate dependent.

When subjected to high loading rates and/or smaller temperatures, the material has a modulus  $E_0$ , which is called *glassy modulus*. The modulus at small loading rates and higher temperatures is called *rubbery modulus*,  $E_\infty$ .

### 3.2 NONLINEAR ELASTICITY

A nondefective material body is a simply connected region  $\mathcal{B}$  of a three-dimensional Euclidean manifold  $\mathcal{M}$ , called the material manifold. The elements of this manifold are so-called material points  $\mathbf{X}$  (Marsden & Hughes, 1994; Gérard A Maugin, 2016). A configuration of  $\mathcal{B}$  is a mapping  $\phi : \mathcal{B} \rightarrow \mathcal{S} \subset \mathbb{R}^3$ . The set of all configurations of  $\mathcal{B}$  is denoted  $\mathcal{C}$ . A motion of a body is a curve in  $\mathcal{C}$ , that is, a mapping  $t \rightarrow \phi_t \in \mathcal{C}$ .

Letting  $\phi : \mathcal{B} \rightarrow \mathcal{S}$  to be smooth, the *deformation gradient* is defined as the tangent map of  $\phi$  and is denoted  $F = T\phi$  (Yavari, 2010). At each point  $\mathbf{X} \in \mathcal{B}$ , it is a linear map,  $F(\mathbf{X}) : \mathcal{T}_{\mathbf{X}}\mathcal{B} \rightarrow \mathcal{T}_{\phi(\mathbf{X})}\mathcal{S}$ , where  $\mathcal{T}_{\mathbf{X}}\mathcal{B}$  and  $\mathcal{T}_{\phi(\mathbf{X})}\mathcal{S}$  denote the tangent spaces to  $\mathcal{B}$  and  $\mathcal{S}$  at  $\mathbf{X}$  and  $\phi(\mathbf{X})$ , respectively.

Assuming  $\{X^A\}$  and  $\{x^a\}$  to be the local charts on  $\mathcal{B}$  and  $\mathcal{S}$ , respectively, the components of  $F$  are

$$F_A^a(X) = \frac{\partial \phi^a(X)}{\partial X^A}. \quad (3.1)$$

The transpose of  $F$  is defined by

$$F^T : \mathcal{T}_x \mathcal{S} \rightarrow \mathcal{T}_X \mathcal{B}, \quad \langle F \mathbf{v}_0, \mathbf{v} \rangle_{\mathbf{g}} = \langle \mathbf{v}_0, F^T \mathbf{v} \rangle_{\mathbf{G}} \quad \forall \mathbf{v}_0 \in \mathcal{T}_X \mathcal{B}, \mathbf{v} \in \mathcal{T}_x \mathcal{S}, \quad (3.2)$$

for  $X \in \mathcal{B}$ ,  $x \in \mathcal{S}$ . It has been assumed that  $\mathcal{B}$  and  $\mathcal{S}$  are Riemannian manifolds with inner products  $\langle \cdot, \cdot \rangle_{\mathbf{G}}$  and  $\langle \cdot, \cdot \rangle_{\mathbf{g}}$ , respectively.

The right Cauchy-Green deformation tensor is defined by

$$C(X) : \mathcal{T}_X \mathcal{B} \rightarrow \mathcal{T}_X \mathcal{B}, \quad C(X) = F(X)^T F. \quad (3.3)$$

In component form,  $C_B^A = (F^T)_a^A F_B^a$ .

### Isotropic hyperelasticity

The theory of hyperelasticity assumes the existence of a strain energy density functional,  $\psi$ , that depends on the deformation gradient  $\psi(F)$ . The nominal stress,

$$\begin{aligned} P &: \mathcal{T}_X^* \mathcal{B} \rightarrow \mathcal{T}_x \mathcal{S}, \\ \mathbf{N} &\mapsto \mathbf{T} = \mathbf{P} \mathbf{N}. \end{aligned} \quad (3.4)$$

is related to the strain energy density function as

$$\mathbf{P} = \frac{\partial \psi(F)}{\partial F}. \quad (3.5)$$

Requirements of objectivity require the strain energy density to depend on  $F$  through the combination  $F^T F = C$ . The Piola-Kirchhoff 2 stress tensor ( $\mathbf{S}$ ) is defined as

$$\begin{aligned} \mathbf{S} &: \mathcal{T}_X^* \mathcal{B} \rightarrow \mathcal{T}_X \mathcal{B}, \\ \mathbf{N} &\mapsto \tilde{\mathbf{T}} = \mathbf{S} \mathbf{N}. \end{aligned} \quad (3.6)$$

such that  $\mathbf{P} = \mathbf{F} \mathbf{S}$ . It is related to the strain energy density function as

$$\mathbf{S} = 2 \frac{\partial \psi(C)}{\partial C}. \quad (3.7)$$

Requirements of isotropy further dictate the strain energy functional to depend on  $C$  through its invariants. The three invariants of  $C$  are defined as

$$I_1 = \text{tr}(C), \quad (3.8)$$

$$I_2 = \frac{1}{2} \left( (\text{tr}(C))^2 - \text{tr}(C^2) \right), \quad (3.9)$$

$$I_3 = \det C. \quad (3.10)$$

Hence

$$\mathbf{S} = 2 \sum_{i=1}^3 \frac{\partial \psi}{\partial I_i} \frac{\partial I_i}{\partial C}. \quad (3.11)$$

Elastomers are treated to be incompressible materials and hence,  $\det \mathbf{F} = 1$ . As a consequence of incompressibility constraint, the PK2 stress can now be expressed as

$$\mathbf{S} = 2 \frac{\partial \psi(\mathbf{C})}{\partial \mathbf{C}} + \gamma J \mathbf{C}^{-1}, \quad (3.12)$$

where  $\gamma$  is a Lagrange multiplier that enforces incompressibility. It coincides with the pressure,  $p$ , if the strain energy functional is homogeneous of order 0,  $\frac{\partial \psi}{\partial C} : \mathbf{C} = 0$  (Bonet, 2001). This can be achieved by making it a function of the deviatoric part of  $\mathbf{C}$ ,  $\bar{\mathbf{C}} := J^{-\frac{2}{3}} \mathbf{C}$ . Defining  $\bar{\psi}(\mathbf{C}) = \psi(\bar{\mathbf{C}})$ ,

$$\mathbf{S} = 2 \frac{\partial \bar{\psi}(\mathbf{C})}{\partial \mathbf{C}} + p J \mathbf{C}^{-1}. \quad (3.13)$$

This can be further simplified as

$$\mathbf{S} = 2 J^{-\frac{2}{3}} \text{DEV} \left\{ \frac{\partial \psi(\bar{\mathbf{C}})}{\partial \bar{\mathbf{C}}} \right\} + p J \mathbf{C}^{-1}, \quad (3.14)$$

where  $\text{DEV} \left\{ \bullet \right\} = \bullet - \left( \frac{\bullet : \mathbf{C}}{3} \right) \mathbf{C}^{-1}$ . For isotropic materials,  $\psi$  is now a function of the first two invariants of  $\bar{\mathbf{C}}$ .

### Hyperelastic models

An overview on the available hyperelastic models and the physics behind them can be found in the review articles of Marckmann and Verron, 2006; Verron, 2018. A brief summary will be presented below.

In the Neo-Hookean hyperelastic model, the strain energy is a function of the first invariant,  $I_1$ , only (Treloar, 1943). This can be seen as an extension of Hooke's law to large deformations.

$$\psi^{NH} = \mu(I_1 - 3). \quad (3.15)$$

This model has been developed by using statistical mechanics for polymer networks.

A model that involves both the invariants has been developed by Mooney (Mooney, 1940). For this model, the strain energy functional is written as

$$\psi^{MR} = C_{10}(I_1 - 3) + C_{01}(I_2 - 3) \quad (3.16)$$

where  $C_{10} > 0$  and  $C_{01} \geq 0$ .

The polynomial model has been developed by Rivlin (R S Rivlin, 1948), where the strain energy functional is expressed as a polynomial function of the invariants.

$$\psi^{Poly} = \sum_{i=0, j=0}^{\infty, \infty} C_{ij} (I_1 - 3)^i (I_2 - 3)^j, \quad (3.17)$$

where  $C_{00} = 0$ .

In Ogden model (Ogden, 1972), the strain energy density is expressed directly in terms of the eigen values of  $\mathbf{C}$  instead of its invariants.

$$\psi^{Og} = \sum_{i=1}^n \frac{\mu_i}{\alpha_i} (\lambda_1^{\alpha_i} + \lambda_2^{\alpha_i} + \lambda_3^{\alpha_i} - 3) \quad (3.18)$$

where  $\mu_i \alpha_i > 0$  for all  $i$ .

More recent models include the 8-chain model by Arruda and Boyce, 1993, limiting chain extensibility model by Gent, 1996a, the extended tube-model (Kaliske & Heinrich, 1999) and many others.

### 3.3 VISCOELASTICITY

The theory of viscoelasticity can be easily described under small strain setting. Under small strains, all the stress measures described in the previous section coincide. The strain measures are replaced by the small strain tensor,  $\epsilon$ , which is defined as the symmetric part of the gradient of the displacement.

$$\epsilon = \frac{\nabla \mathbf{u} + (\nabla \mathbf{u})^T}{2}. \quad (3.19)$$

In the case of a linearly elastic material under small strains, the stress becomes a unique function of the strain. Roughly, in a viscoelastic material, the stress is seen to depend on the strain as well the strain rate,  $\sigma(\epsilon, \dot{\epsilon})$ .

A viscoelastic material is typically represented by a spring-dash pot mechanical system in various configurations such as by Kelvin or a Maxwell branch or a combination of both. Their behavior is characterized by time dependent material functions. More generally, the stress is made to depend on the current strain and its history. In differential representation of linear viscoelasticity, the general equation relating the stress and strain can be written as

$$\sum_{n=0}^{\infty} u_n \frac{\partial^n \sigma(t)}{\partial t^n} = \sum_{m=0}^{\infty} q_m \frac{\partial^m \epsilon(t)}{\partial t^m}, \quad (3.20)$$

where  $u_n$  and  $q_m$  are constant coefficients. The above equation, written in an operator form, can be seen to be

$$\mathcal{U}[\sigma(t)] = \mathcal{Q}[\epsilon(t)], \quad (3.21)$$

where  $\mathcal{U}$  and  $\mathcal{Q}$  are differential operators.

The difference between the elastic and viscoelastic behaviors of the materials can be seen through Dynamic Mechanical Analysis (DMA) tests, where the stresses (reaction forces) are monitored on a test sample on which a cyclic strain is imposed. In the case of the elastic material, the stress is seen to vary in phase with the strain cycles. In a viscoelastic material, however, as a consequence of the time dependence of the material, the stress cycles are seen to lag the strain cycles, the lag depending on the frequency. This can be seen by taking the Laplace transform of equation 3.21. The transformed equation can be seen to be

$$\bar{u}(s)\bar{\sigma}(s) = \bar{q}(s)\bar{\epsilon}(s). \quad (3.22)$$

For suddenly imposed strain,  $\epsilon(t) = \epsilon_0 H(t)$ , where  $H$  denotes the Heaviside function, the relation between the transformed stress and strain can be seen to be

$$\bar{\sigma}(s) = \frac{\bar{Q}(s)}{s} \epsilon_0, \quad (3.23)$$

where  $\bar{Q}(s) = \frac{\bar{q}(s)}{\bar{u}(s)}$ . The quantity  $\frac{\bar{Q}(s)}{s}$  can be defined to be  $\bar{G}(s)$ , the Laplace transformed *relaxation function*. This function can be defined in the time domain to be

$$G(t) = \mathcal{L}^{-1} \frac{\bar{Q}(s)}{s}. \quad (3.24)$$

Now, for a harmonic excitation,  $\epsilon(t) = \epsilon_0 \exp(i\omega t)$ , the transformed stress can be seen to be

$$\bar{\sigma} = \frac{\epsilon_0 \bar{Q}(s)}{s - i\omega}. \quad (3.25)$$

Steady state response can be obtained by setting  $s = i\omega$  and inverting the transform.

$$\sigma_{ss}(\omega) = \bar{Q}(i\omega)\epsilon(\omega). \quad (3.26)$$

The complex modulus can be defined as  $G^*(\omega) = \bar{Q}(i\omega)$ . The real part of the complex modulus is termed as the *storage modulus* and the imaginary part as *loss modulus*.

For a *standard linear solid*, after some algebraic manipulations, the storage and loss modulus can be seen to be

$$G_s(\omega) = G_0 \left[ 1 - \sum_{i=1}^N \gamma_i \right] + G_0 \sum_{i=1}^N \frac{\gamma_i \tau_i^2 \omega^2}{1 + \tau_i^2 \omega^2}, \quad (3.27)$$

$$G_l(\omega) = G_0 \sum_{i=1}^N \frac{\gamma_i \tau_i \omega}{1 + \tau_i^2 \omega^2}. \quad (3.28)$$

An elastic material is characterized by  $\tau_i \rightarrow \infty$  in which case, the storage and loss modulus can be seen to be  $G_0$  and 0 respectively. They can be observed to be frequency independent.

The *dynamic modulus* is then defined as  $G_d(\omega) := \sqrt{G_s^2 + G_l^2}$ . The *loss tangent*,  $\delta$ , is defined as  $\delta := \arctan(G_l/G_s)$ . The typical variation of dynamic modulus and loss tangent for an elastomer can be seen in the figure 3.2.

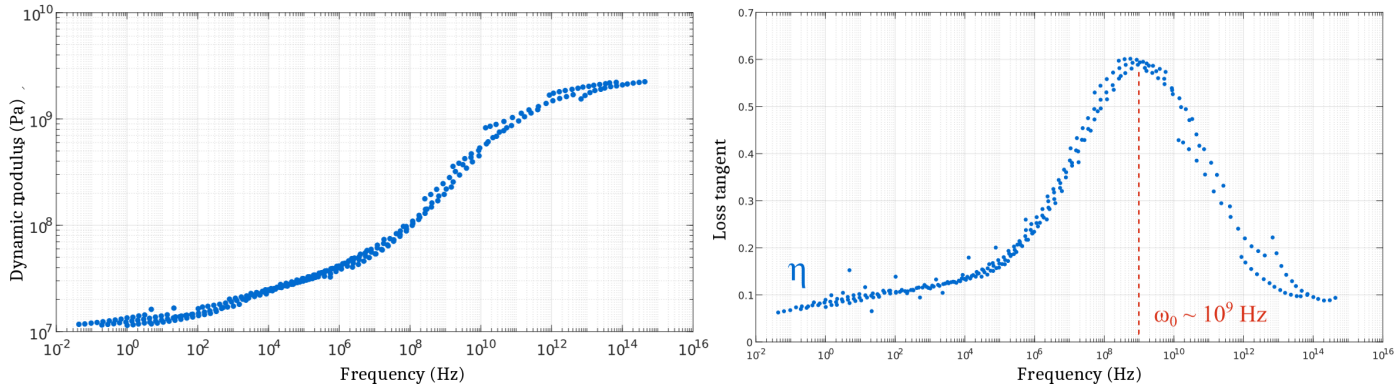


Figure 3.2: Evolution of dynamic modulus and loss tangent with frequency for polyurethane elastomer. Extracted from Corre, 2018.

The DMA experiments are thus used to characterize the viscoelastic behavior of the elastomer and calibrate the relaxation times and stiffness ratios. The dynamic modulus at small frequencies is called *rubbery modulus* to indicate the material behaves in a rubbery fashion at these frequencies. At larger frequencies, the modulus is called *glassy modulus* to indicate that the material behaves in a glassy fashion. The loss tangent can be seen to increase from a small value at small frequencies to a maximum at the intermediate frequencies and decrease to a smaller value again at large frequencies. In the figure 3.2, it can be seen that the loss tangent attains a maximum at about  $\omega = 10^9$  Hz.

When in large strains, the effects of viscoelasticity can be considered by either introducing an internal variable (Coleman & Gurtin, 1967) or by considering the current state of stress to be a function of current deformation state and the deformation history (Green & Rivlin, 1997; Coleman & Noll, 1961). A detailed discussion on the different approaches can be found in Gerard A Maugin and Muschik, 1994; Germain, Nguyen, and Suquet, 1983 and the references therein. In the framework of *Standard Generalized Materials*, the internal variables are evolved using a convex dissipation functional and its (Legendre-Fenchel) dual (Halphen & Nguyen, 1975).

### Convolution integral formulation

A multiple integral constitutive equation has been proposed in Green and Rivlin, 1997 to consider the effect of deformation history on the current state of stress. The state of stress at any time has been expressed as

$$\boldsymbol{\sigma}(t) = \mathcal{G} [E(t-s)|_{s=0}^{\infty}] F(t)^T \quad (3.29)$$

Assuming that the functional  $\mathcal{G}$  is continuous in the sense of Drapaca, Sivaloganathan, and Tenti, 2007, a form of stress has been obtained in the form of multiple integral series (Wineman, 2009).

$$\begin{aligned} \mathcal{G} [E(t-s)|_{s=0}^{\infty}] &= \int_{-\infty}^t \mathbf{K}_1(t-s_1) dE(s_1) \\ &+ \int_{-\infty}^t \int_{-\infty}^t \mathbf{K}_2(t-s_1, t-s_2) dE(s_1) dE(s_2) \\ &+ \int_{-\infty}^t \int_{-\infty}^t \int_{-\infty}^t \mathbf{K}_3(t-s_1, t-s_2, t-s_3) dE(s_1) dE(s_2) dE(s_3) + \dots \end{aligned} \quad (3.30)$$

### Finite Linear Viscoelasticity

Using the hypothesis of fading memory in Coleman and Noll, 1961, the stress was made to depend on recent deformations. To account for history effects, the relative deformation gradient,  $F_t(\tau)$ , has been introduced.  $F_t(\tau)$  can be seen to describe the configuration of system at a time  $\tau < t$  with respect to the current configuration at time  $t$  (Coleman & Noll, 1961). The stress at the current time is then expressed as a functional of the current strain and of the history.

$$\boldsymbol{\sigma}(t) = F(t) \left\{ \mathbf{k}_2[C(t)] + \int_{-\infty}^t \mathbf{K}_2[C(t), t-s] [F(t)^T (C_t(s) - I) F(t)] ds \right\} F(t)^T \quad (3.31)$$

The first term in the above expression can be taken to represent the ‘long term’ behaviour of the material. The second term characterizes the history dependence. It shall be noted that the use of the above form of stress is restricted to infinitesimal deformations if applied for a ‘fast’ process. Using it for large deformations restricts its application to ‘slow’ process. The notions of ‘fast’ and ‘slow’ can be found in (Coleman & Noll, 1961). Many other formulations of linear and non-linear viscoelastic models exist. A review together with the notions of ‘weak’ and ‘strong’ fading memory can be found in Wineman, 2009 and Drapaca et al., 2007.

### Internal variable formulation

In the internal variable formulation of viscoelasticity, the history dependence accounted for by an internal variable. The usual approach in these models is to decompose the deformation gradient into an elastic and a viscoelastic part ( $F = F_e F_v$ ). The internal variable is taken as the strain in the dash pot ( $F_v$ ) in a Maxwell element. The evolution of the internal variable is represented by a differential equation (Halphen & Nguyen, 1975). Many viscoelastic models have been formulated using this approach as in (Reese & Govindjee, 1998; Bergström & Boyce, 1998).

**SUMMARY**

In this chapter, a brief introduction to the polymer materials was provided. Some hyperelastic and viscoelastic models have been presented briefly. Different approaches to model the inelastic behavior of polymers have been presented briefly as well.

**THE CURRENT THESIS**

In the current thesis, the fracture experiments performed in Polyurethane elastomers in Corre, 2018 will be analyzed first. It will be determined if any shock-front-like features are present in the material. The velocity and strain fields obtained from the experiments will be examined.

More experiments performed on the elastomer samples of different geometries will be presented next. These experiments have been conducted to confirm the observations of Chen et al., 2011 for polyurethane elastomers. The importance of including viscous effects while performing the analysis of dynamic fracture of elastomers will be discussed next. In that part of the thesis, the crack speeds will be imposed implicitly on the model using the displacement fields extracted from the experiments.

A rate dependent cohesive zone will be presented next and will be used to predict the crack speeds. The crack speeds will be obtained and compared for various stretch levels and geometries.

The non linear viscoelastic model by Reese and Govindjee, 1998 will be implemented next under plane stress conditions and used to compute the viscoelastic dissipation during the crack growth. The strain energy loss in the body will be compared with the viscous dissipation and the energy expended in the cohesive zone.

PART II  
**EXPERIMENTS**

# FRACTURE OF POLYURETHANE

# 4

---

Since the majority of the work in this thesis is the continuation of the works of Corre, 2018; Corre et al., 2020, this chapter reviews the experimental setup, the experiments performed and some results from that study. Additional observations from that study will be presented in a later chapter.

---

## CONTENTS

4.1	Experimental setup . . . . .	38
4.2	Procedure . . . . .	38
4.3	Results . . . . .	39
4.4	Complex geometry and crack path . . . . .	41
4.5	Comparison with literature . . . . .	42

The fracture experiments have been conducted on Polyurethane elastomer in pure shear configuration in Corre, 2018. This chapter presents an overview of the experimental protocol followed and the results obtained in that thesis. The same setup will be used later on to conduct more tests on different geometries.

#### 4.1 EXPERIMENTAL SETUP

The setup can be found in Corre, 2018, but is repeated here for convenience. The specimen has dimensions such that its length ( $l_0$ ) is greater than its height ( $h_0$ ) which, in turn, is greater than the thickness ( $e_0$ ). It is held on its longest side in the jaws of a tensile machine and stretched to the target level using the supports molded onto it. See figures 4.1 and 4.2. The strain state is homogeneous at the center, but the homogeneity is lost towards the right and left edges. The deformation gradient at the center of the specimen after being stretched (with respect to the coordinate system in figure 4.1) is

$$\mathbf{F} = \begin{pmatrix} 1 & 0 & 0 \\ 0 & \lambda_y & 0 \\ 0 & 0 & \frac{1}{\lambda_y} \end{pmatrix} \mathbf{e}_x, \mathbf{e}_y, \mathbf{e}_z \quad (4.1)$$

where  $\lambda_y = \frac{h_f}{h_0}$ ,  $h_f$  is the final height of the specimen after being stretched. The specimens tested in Corre, 2018 were 200 mm long, 40 mm tall and 3 mm thick.

A razor blade is used to initiate a seed crack once the specimen is stretched. A stand is used to mount the razor blade, the height of which is adjusted to the required level depending on the specimen stretch.

#### 4.2 PROCEDURE

The specimen is initially painted in speckles that allow tracking the displacement fields of speckle particles using a DIC software. Once painted, the specimen is mounted on the tensile machine using the supports on its ends. Once secured, the top end is pulled at a speed of 20 mm/min. Once, the target stretch level is reached, a seed crack is initiated using a razor blade. It shall be noted that the tensile machine continues to pull the specimen when the crack is propagating through it. However, as will be seen later, as the crack propagation process typically lasts for about 10 ms, the displacement of the top end during this time is negligible.

The entire process is monitored by using two cameras - a High Resolution (HR) and a High Speed (HS) camera. The HR camera monitors the initial stretching part of the process, while the HS camera monitors the fracture part. The HR camera

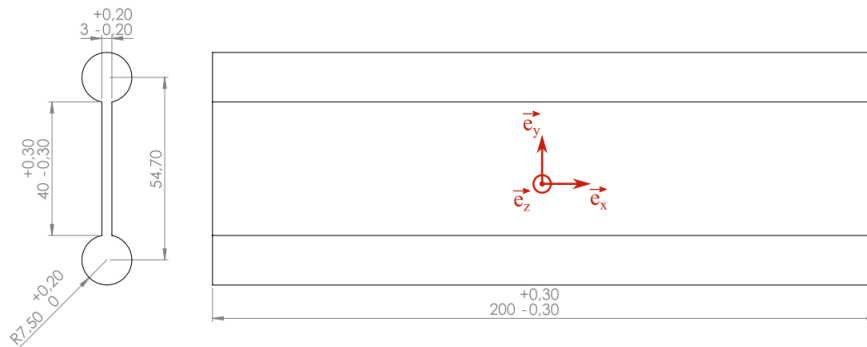


Figure 4.1: Specimen geometry used in the experiments. Adopted from Corre, 2018.

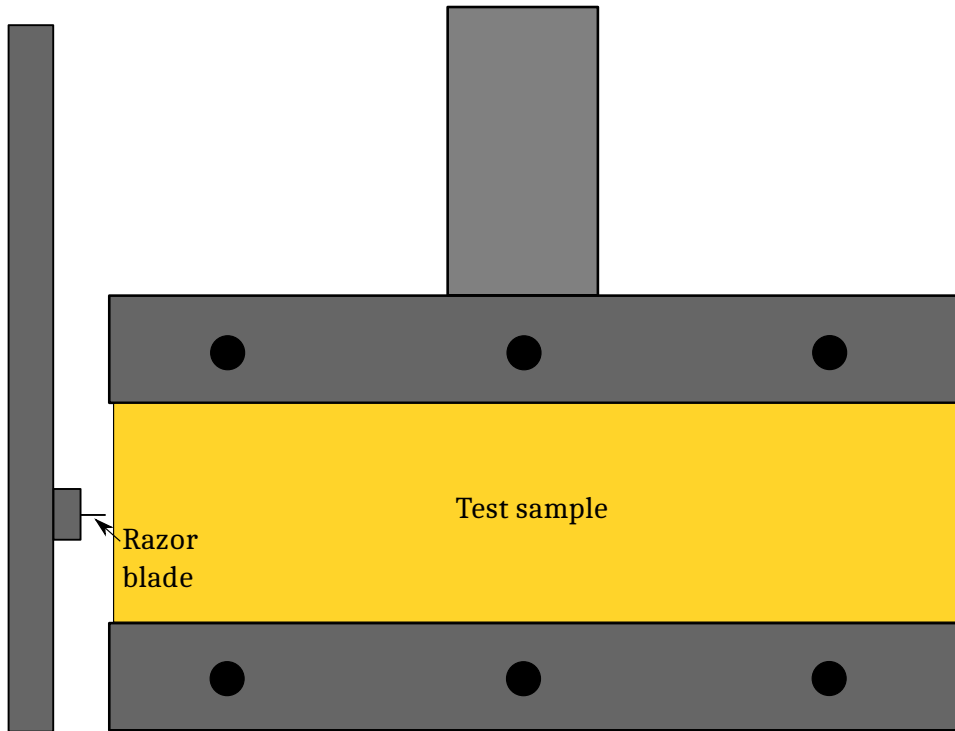


Figure 4.2: Specimen held in tensile machine and razor blade mounted.

captures the images at about 2 frames/s and the HS camera at 10000 to 30000 frames/s. A trigger device is used to stop the HS camera once the crack completely passes through the specimen. The images from the two cameras are then used to obtain the displacement fields all through the crack propagation phase using the Digital Image Correlation (DIC) technique using VIC-2D software (“VIC-2D, Correlated Solutions”, 2019). This procedure can be found in Corre, 2018.

### 4.3 RESULTS

The primary outputs of the experiments are the crack speeds. The use of the DIC technique enables to access the displacement fields all through the duration of the experiment. Other quantities such as velocities and strains can be derived from the displacement fields through their differentiation in space and time.

The crack speeds obtained from the experiments in Corre, 2018 can be found below. Distinguishing the cracks into either subsonic or transonic requires the definition of the shear wave speed. For linear elastic material subjected to small strains, this can be computed trivially as  $\sqrt{\frac{G}{\rho}}$ ,  $G$  and  $\rho$  are the shear modulus and density, respectively. However, elastomers are soft materials that can be subjected to large deformations and a non-linear model is necessary to describe their behavior at these strain levels. Hence, the expression for shear wave speed in a linear elastic material cannot be used for the current scenario.

Mooney-Rivlin model (Ronald S Rivlin & Saunders, 1951) can be used to describe the behavior of elastomers until a strain level of about 250%. The expression for shear wave speed for this material model has been obtained by Boulanger and Hayes, 2001. The cited reference obtains the speed of a finite perturbation that travels in a material described by the Mooney-Rivlin model. No assumption has been made in regards to the amplitude of perturbation. Hence, it can be used to obtain the speed of even large perturbations that are superposed on a base strain

state. The strain energy density of the material in Mooney-Rivlin model is

$$\psi = C_{10}(I_1 - 3) + C_{01}(I_2 - 3), \quad (4.2)$$

where  $I_1$  and  $I_2$  are the invariants of the right Cauchy green tensor,  $C = F^T F$ .  $C_{10}$  and  $C_{01}$  are the material parameters. The shear wave speed in this case can be obtained to be

$$c_s^2 = \frac{1}{2\rho_0} \left( C_{10} \mathbf{n} \cdot \mathbf{b} \mathbf{n} + C_{01} \mathbf{a} \cdot \mathbf{b}^{-1} \mathbf{a} \right), \quad (4.3)$$

where  $\mathbf{b} = F F^T$  is the left Cauchy green tensor corresponding to the background deformation on which the perturbation is superposed,  $\rho_0$  is the density of the material.  $\mathbf{n}$  and  $\mathbf{a}$  are the propagation and polarization directions respectively. For a shear wave, hence,  $\mathbf{n} \cdot \mathbf{a} = 0$ . It shall be noted that the wave speed in the above expression is on the *deformed* state. The speed in the *undeformed* state can be obtained by using the expression  $\mathbf{w} - \mathbf{v} = F \mathbf{w}_0$ , where  $\mathbf{w}$  and  $\mathbf{w}_0$  are the speeds in the deformed and undeformed configuration respectively.  $\mathbf{v}$  is the particle velocity.

Attention should be drawn towards a couple of assumptions made during the development of the expression for shear wave speed in equation 4.3. First, the background deformation state on which the perturbation has been imposed is assumed to be homogeneous. The spatial derivatives of quantities like  $\mathbf{b}$  have hence been ignored (see equations 49-51 of Boulanger and Hayes, 2001). Another assumption is that of the existence of a perturbation of the form  $f = h(\mathbf{x} \cdot \mathbf{n} - c_s t) + k(\mathbf{x} \cdot \mathbf{n} + c_s t)$ . Physically, this means that the form of perturbation should remain unchanged with respect to an observer traveling with the wave. It has not been discussed whether such a waveform can indeed exist. Saccomandi, 2007 mentions that in non-linear materials, solutions that retain their form may not exist. Perhaps a perturbation of the form  $f = h(\mathbf{x} \cdot \mathbf{n} - c_s t) + k(\mathbf{x} \cdot \mathbf{n} + c_s t)$  can exist as long as it is infinitesimal.

The shear wave speed can be computed using the equation 4.3. It can then be used to distinguish the crack speeds to belong to either subsonic or transonic regime. Transonic cracks have been observed in elastomers, first reported in Petersan et al., 2004 and later in Chen et al., 2011; Mai et al., 2020; Corre et al., 2020. The results of crack speeds from Corre et al., 2020 together with the shear wave speed can be seen in figure 4.3. As will be discussed later, the shear wave speed seen in the figure 4.3 is slightly different from what has been obtained in Corre et al., 2020. As can be seen, the general trend is for the crack speed to increase with the applied strain. At larger strains, the increase in crack speed is not as big as that at smaller strains for the same strain increment. The crack speeds remain smaller than  $c_s$  for stretches smaller than 2.5. Starting from a stretch value of about 2.5, the crack speeds exceeded the shear wave speed. The former cracks are said to be Subsonic, while the latter is Transonic. The crack opening profiles for crack propagating in different regimes can be found in figures 4.13 and 4.14 of Corre, 2018. It is generally known (Chen et al., 2011; Petersan et al., 2004) that the crack opening changes from parabolic to a wedge shape once the crack speed exceeds  $c_s$ .

Some more data that can be obtained from that study is the variation of crack speed along the length of the specimen during the fracture process. The speeds in the deformed and undeformed configurations can be seen in the figure 4.4. The speeds in the two configurations are related by  $w e_x = w_0 F e_x$ . It can be seen that the speeds in both the configurations are almost the same at the center of the

specimen where  $F$  takes the form  $\begin{pmatrix} \lambda_x & 0 & 0 \\ 0 & \lambda_y & 0 \\ 0 & 0 & \frac{1}{\lambda_x \lambda_y} \end{pmatrix}$ , where  $\lambda_x \approx 1$ . At the edges,

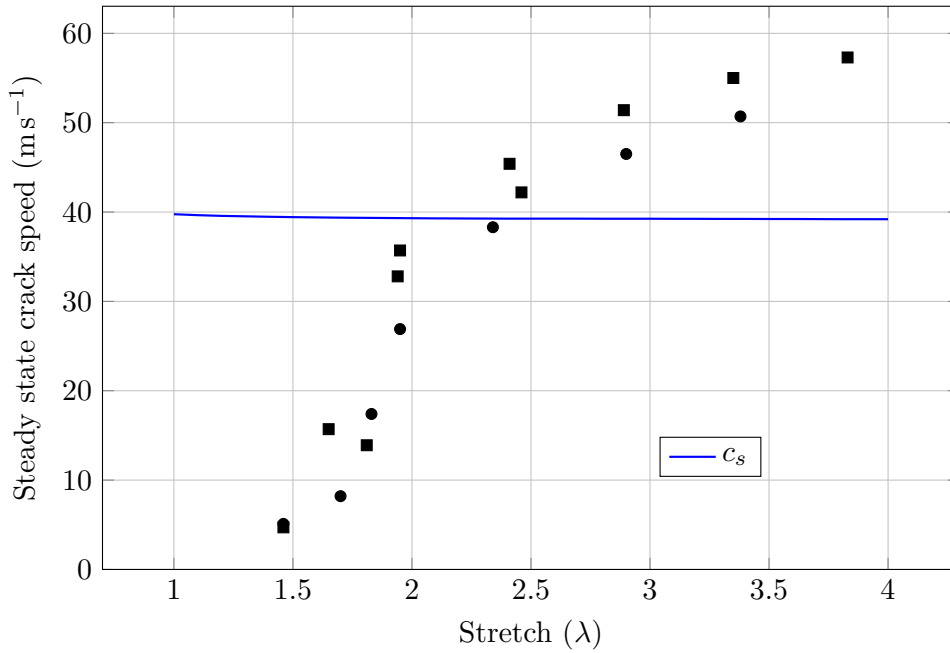


Figure 4.3: Crack speed vs stretch results obtained in Corre, 2018. Shear wave speed can also be seen as a blue line.

$\lambda_x < 1$  and so,  $c_0$  can be seen to be greater than  $c$ .

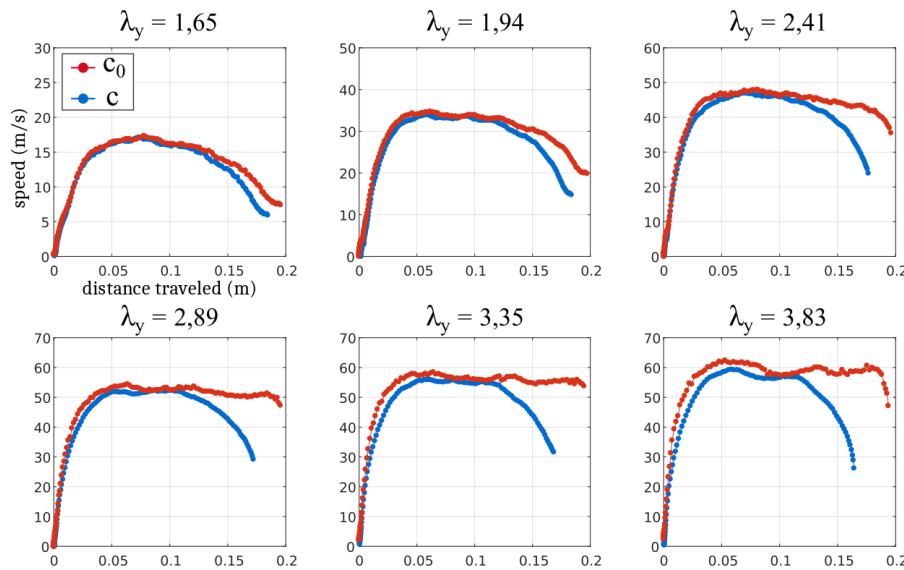


Figure 4.4: Crack speeds in deformed ( $c$ ) and undeformed configurations ( $c_0$ ). Figure adopted from Corre, 2018 with axes relabeled.

#### 4.4 COMPLEX GEOMETRY AND CRACK PATH

Some more experiments were performed where the specimen was made non-homogeneous by introducing a profile into the specimen (see figure 4.5). The crack, initiated at the left end of the specimen, propagates at a higher speed till it reaches the geometric non-homogeneity. It slows down, propagates at a smaller speed in the region where the stretch level is smaller because of the inserted profile and accelerates back to a different speed towards the right end.

In another case, the crack was initiated closer to the top of the specimen instead of at the middle between the two supports to study the path it takes (see figure 4.7). The crack, after a brief instance of traveling straight, turned towards the center of the specimen. The vertical speed of the crack gradually goes to zero once the

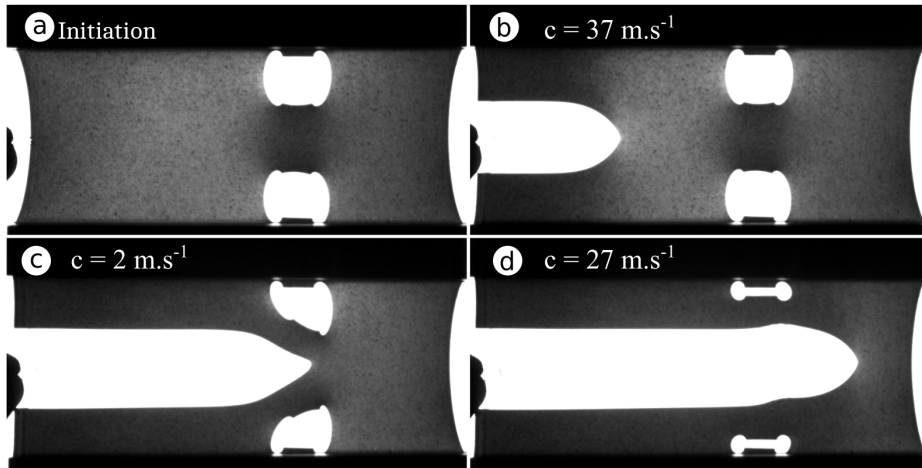


Figure 4.5: Specimen with a profile drilled-in. Figure adopted from Corre, 2018 with labels in English.

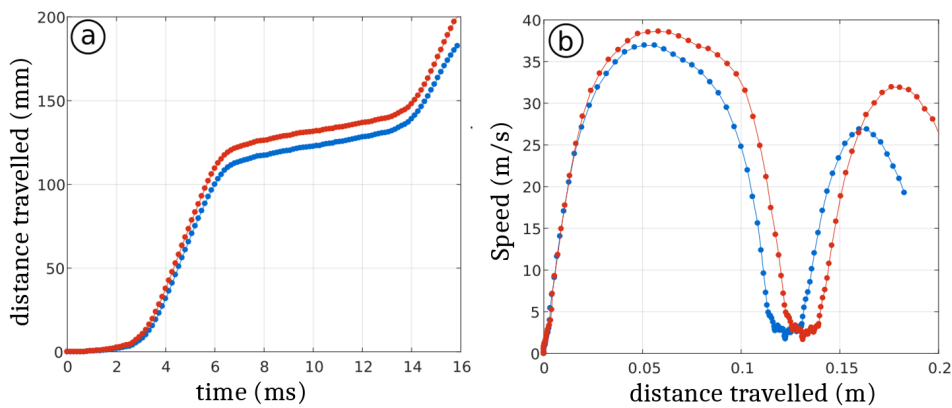


Figure 4.6: Results of the experiment with non-homogeneous geometry. (a) Evolution of distance travelled by the crack with time elapsed. (b) Crack speed vs the distance travelled by the crack. Figure adapted from Corre, 2018 with axes relabeled in English.

crack reaches the center of the specimen. Some snapshots from the experiment can be found in figure 4.7 and the variation of horizontal and vertical components of crack speed with time can be seen in figure 4.8.

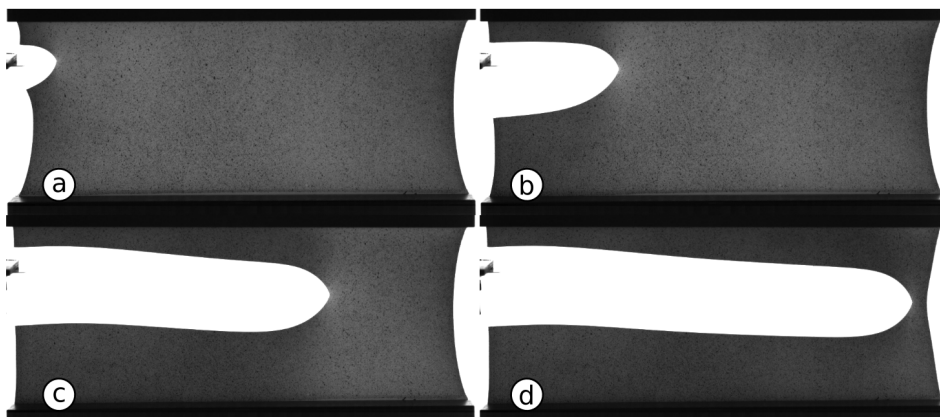


Figure 4.7: Propagation of an oblique crack. Figure adopted from Corre, 2018. (a) crack initiated at the left near the top end. (b) crack propagates straight before turning. (c) crack turns and (d) propagates straight.

#### 4.5 COMPARISON WITH LITERATURE

It shall be noted that Trasonic cracks were first reported in literature in the works of Petersan et al., 2004. In that article, the shear modulus was measured through the experiments and was then used to compute the shear wave speed. It was reported that the cracks traveled about 10-20% faster than the shear wave speeds

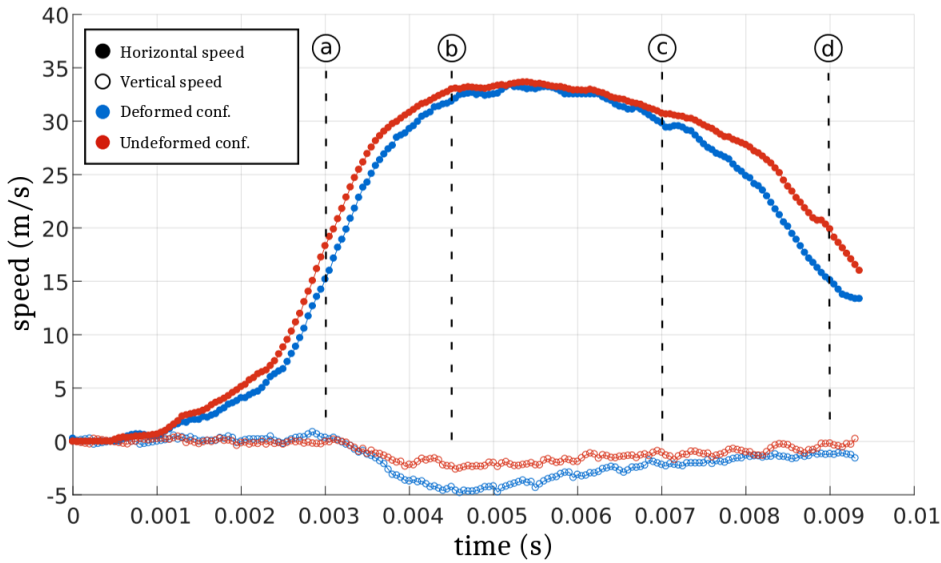


Figure 4.8: Horizontal and vertical crack speeds for the turning crack. Figure adapted from Corre, 2018 with labels renamed in English.

thus computed. However, no shock was reported to have been observed. Usually, in the case of a mode-II crack propagating in a brittle solid along a weak plane, mach cones were observed along which the particle speeds exhibit jumps (Rosakis et al., 2000; Rosakis, 2002). Petersan et al., 2004 does not report such jumps in their study. Instead, the crack opening was reported to be *wedge-like and is strikingly similar to the Mach cone*. The problem was studied analytically and numerically in Marder, 2006 by treating the material as a triangular lattice. It was mentioned in that work that the inclusion of Kelvin dissipation in the model increases the *imaginary* modulus of the rubber and also the high frequency sound speed (page 26 of the article). The next instance where Transonic cracks were reported is in Chen et al., 2011 (see figure 4.10). The experiments were performed on natural rubber specimen. The specimens were stretched to the target level and the crack propagation was studied. An additional observation was reported in that study that the crack speeds become independent of the specimen height in the Transonic regime. Meaning, the crack speeds were seen to be a function of specimen height for a given stretch level when the crack speeds are smaller than the shear wave speed. Once the crack enters the Transonic regime, its speed was seen to not depend on the specimen height. Meaning, in this regime, crack speeds in specimens of different geometry subjected to the same stretch level will remain same. Some similarity can be noted between this observation and that in Gent and Marteny, 1982b (see figure 4.9). In Gent and Marteny, 1982b, specimens of different heights are all subjected to the same stretch level and crack speeds were measured. It was observed that after a certain specimen height, the crack speeds did not increase.

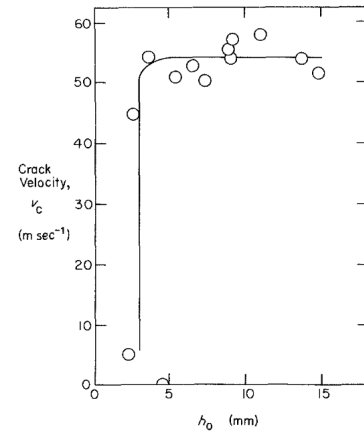


Figure 4.9: Crack speeds vs specimen height in Gent and Marteny, 1982b. Material is subjected to  $\lambda_x = 2$  and  $\lambda_y = 4$ .

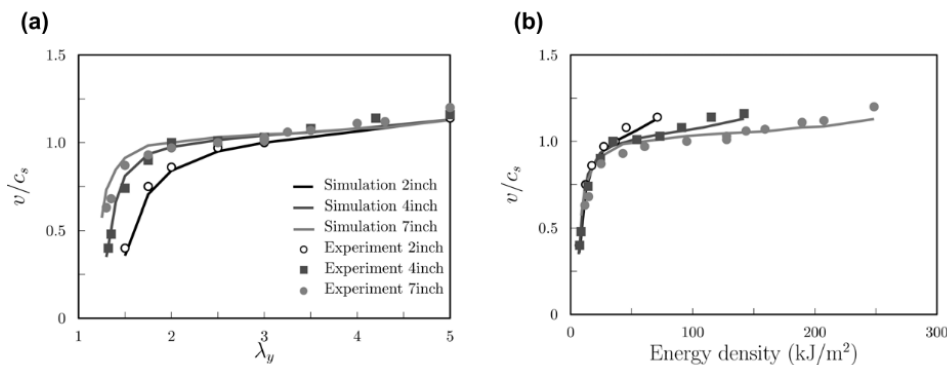


Figure 4.10: Results from Chen, Zhang, Niemczura, Ravi-Chandar, and Marder, 2011. In the figure (a), crack speeds were plotted against applied stretch while in the figure (b), crack speeds were plotted against the *Energy density*, measured as  $wh_0$ .

Whether the two observations are similar is unclear and will be discussed in the later chapters.

Further experiments in this direction were also carried out by Corre et al., 2020; Mai et al., 2020. Transonic cracks were reported in these studies as well. However, experiments on different geometries have only been conducted in Chen et al., 2011. Hence, more experiments have been performed on the specimens of Polyurethane elastomer to see if the phenomenon of height independence is observed here as well. These will be reported in the next chapter.

#### **SUMMARY**

In this chapter, the experiments performed in Corre et al., 2020 have been presented. Samples that are 40 mm tall were tested and Transonic cracks were observed starting from a stretch level of about 2.5. More experiments were performed where the sample geometry was made non-homogeneous and where the crack initiation was made nearer to top edge of the sample. The height independence of crack speed in Transonic regime wasn't investigated and it will be the point of departure of the next chapter.

## ADDITIONAL EXPERIMENTS

---

To test the effect of specimen geometry on the crack speeds, we tested Polyurethane samples of different geometries to obtain the crack speeds at different loads. This chapter will present the additional experiments performed on different geometries of the polyurethane elastomers. It also describes the tests performed using different test protocols. Temperature measurements performed on some test specimens will be presented as well.

---

### CONTENTS

5.1	Results of 20 mm and 60 mm samples . . . . .	46
5.2	Other experiments on the 40 mm specimen . . . . .	48
5.3	Samples of another batch (Batch 2) . . . . .	49
5.4	Temperature measurements . . . . .	50
5.5	Discussion . . . . .	52

As already mentioned, in Chen et al., 2011, it was reported that the crack speeds remained independent of the specimen height in the Transonic regime. No other studies exist that report a similar observation. Hence, experiments have been conducted on the Polyurethane elastomers of different geometries in addition to what has been done in Corre, 2018. Those will be reported below.

## 5.1 RESULTS OF 20 mm AND 60 mm SAMPLES

### Batch 1

The other specimens tested were 20 mm and 60 mm tall and belonged to a different batch (to be called batch 1). The length (200 mm) and the thickness (3 mm) were the same as that of the 40 mm samples. The test protocol followed was the same as that followed for the 40 mm samples. The specimens had bulges molded into them which have been used to hold them in a tensile machine. They were then stretched to different stretch levels and a crack is introduced. The initial stretching and the crack propagation phases were monitored with an HR and an HS camera as was done for the 40 mm specimen tests. The specimens were pulled with the same speed while testing the 20 and 60 mm tall samples as the 40 mm tall sample, that is 20 mm/min.

As opposed to the tests in Corre, 2018, in the tests performed on the new test samples, the test setup has been changed to include strain gauges at the left and the right ends of the support. See figure 5.1. This enables to obtain the evolution of reaction forces (from the strains from the strain gauges) at the left and right ends separately as the crack propagates through the specimen.

The crack speeds obtained for these two specimen sizes can be seen in figure 5.2 along with the 40 mm tall specimen results from Corre, 2018. It can be seen that the overall trend is an increase in crack speed with an increase in the stretch level.

However, the trend is not monotonic. In some experiments, it was observed that the crack did not accelerate to a higher speed after initiation. Instead, it continued to propagate at a speed that is smaller than that at smaller stretches. In some experiments, the crack speed varied drastically as it progressed along the specimen. It was also observed that the crack surfaces were considerably rougher in the places where the crack slowed down. The variation of crack speed along the length of the specimen in such cases can be seen in the figure 5.3. The cases where the crack speed varied all through the propagation phase are indicated by black dots and circles in figure 5.2. The crack speeds reported for such cases are for when the crack is at the center of the specimen, ie at about 100 mm from the left end. It shall be noted that these experiments were performed only on the 20 and 60 mm specimens and the fluctuations in the crack speeds were observed in both the geometries.

The variation of reaction forces measured from the strains in the strain gauges as the crack propagated through can be seen in the figure 5.4. The results reported correspond that presented in figure 5.3 (60 mm tall specimen and  $\lambda_y = 3.0$ ). As the crack begins to propagate and breaks a part of the specimen, the reaction force computed from the left strain gauge begins to drop. After a little delay, the force from the right strain gauge begins to drop as well. Corresponding to the large variations observed in the crack speed, oscillations can be seen in the force evolution as well.

The intent in performing the above experiments is to obtain the crack speeds in

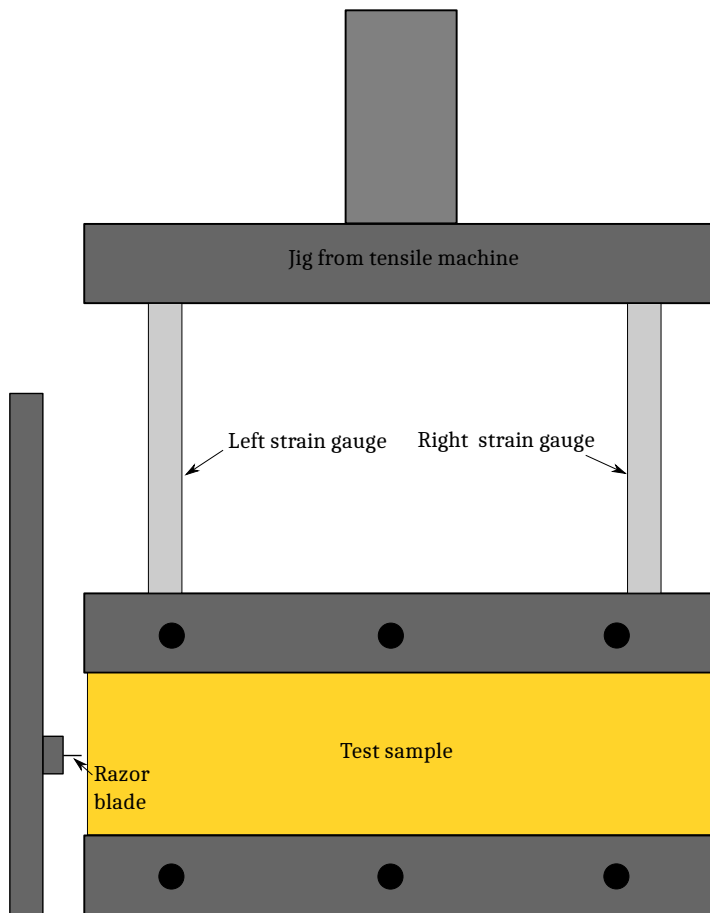


Figure 5.1: Experimental setup including strain gauges.

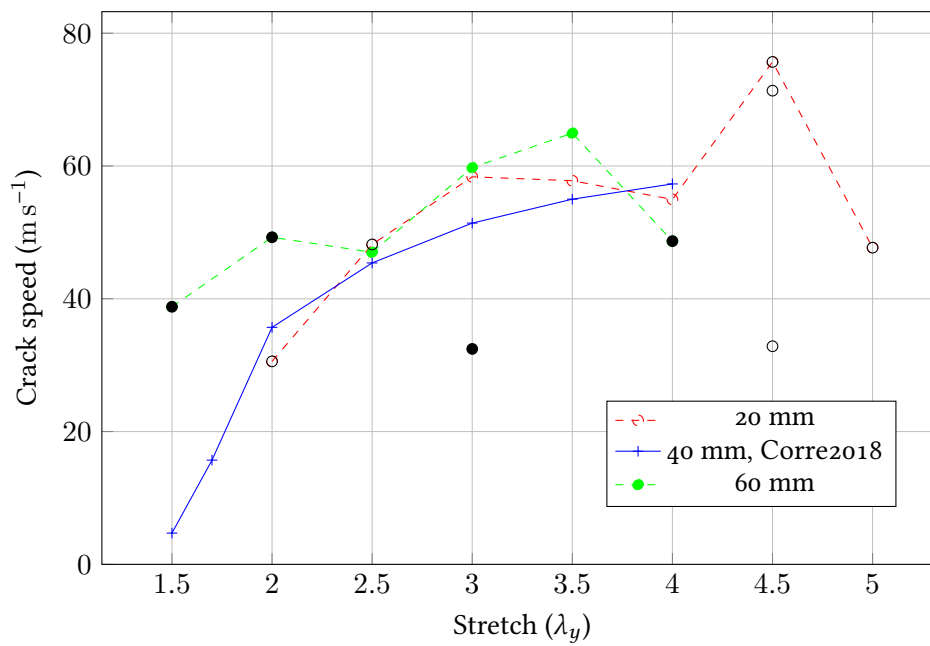


Figure 5.2: Results of the experiments performed on the 20 mm and 60 mm samples. The 40 mm specimen results from Corre, 2018 can also be seen.

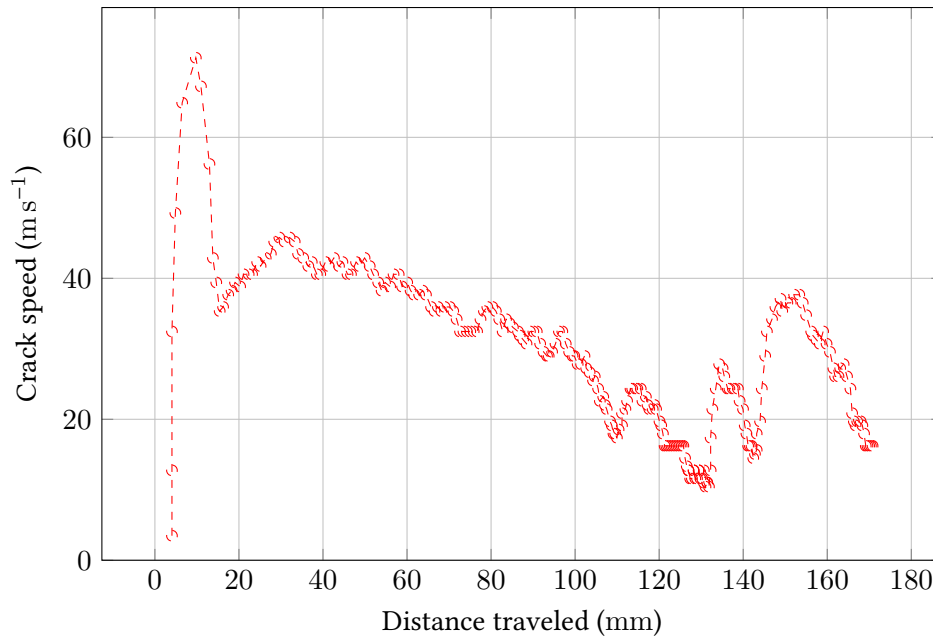


Figure 5.3: Crack speed (in the deformed configuration) vs distance traveled for 60 mm tall specimen under  $\lambda_y = 3.0$ . A significant variation of the crack speed can be seen.

different geometries and compare them to verify the findings of Chen et al., 2011. However, it can be seen that because of the significant variations of crack speeds observed in 20 and 60 mm geometries, the speeds in those geometries could not be compared with the 40 mm geometry as well as with each other. Hence, it was decided to procure another batch of samples, this time to test all the sizes.

## 5.2 OTHER EXPERIMENTS ON THE 40 mm SPECIMEN

Since the 40 mm tall specimens were already tested in Corre, 2018, other kinds of experiments were performed on that geometry (still belonging to batch 1). The test protocol is different from the previous section and is as follows. An initial seed crack of about 5 mm is introduced in the specimen before it is stretched. The specimen is then held in the jaws of the tensile machine and is pulled at different speeds from the previous section. Tests were conducted at cross-head speeds of  $10 \text{ mm s}^{-1}$ ,  $30 \text{ mm s}^{-1}$ ,  $60 \text{ mm s}^{-1}$ ,  $120 \text{ mm s}^{-1}$  and  $240 \text{ mm s}^{-1}$ . It was intended to see if the crack initiation and speeds obtained depend on the initial stretching rate of the specimen.

It was observed that the crack did not propagate in a straight line like the other tests and instead, branching occurred at different locations. In some cases, one of the branches stopped propagating and the other propagated alone while in the other cases, both the branches propagated. Result for one such instance where the specimen is pulled at  $30 \text{ mm s}^{-1}$  and the crack is near the right end of the specimen can be seen in figure 5.5. Similar observations have been made in the other tests as well, when the crack was at different locations. The locations where the crack attempted to branch in different experiments can be seen in figure 5.6. However, the results could not be reproduced when the experiments were repeated multiple times. The experiments which resulted in crack branching earlier did not do so the second time under similar loading conditions.

Some 40 mm geometry samples were then tested under the same protocol as the rest of the other geometries (20 and 60 mm) to check if the properties of the specimen in batch-1 are same as that in Corre, 2018. The specimen was stretched to a stretch level of 3.0 and a seed crack was introduced. An attempted branching was observed when the crack was at the center of the specimen! See figure 5.7.

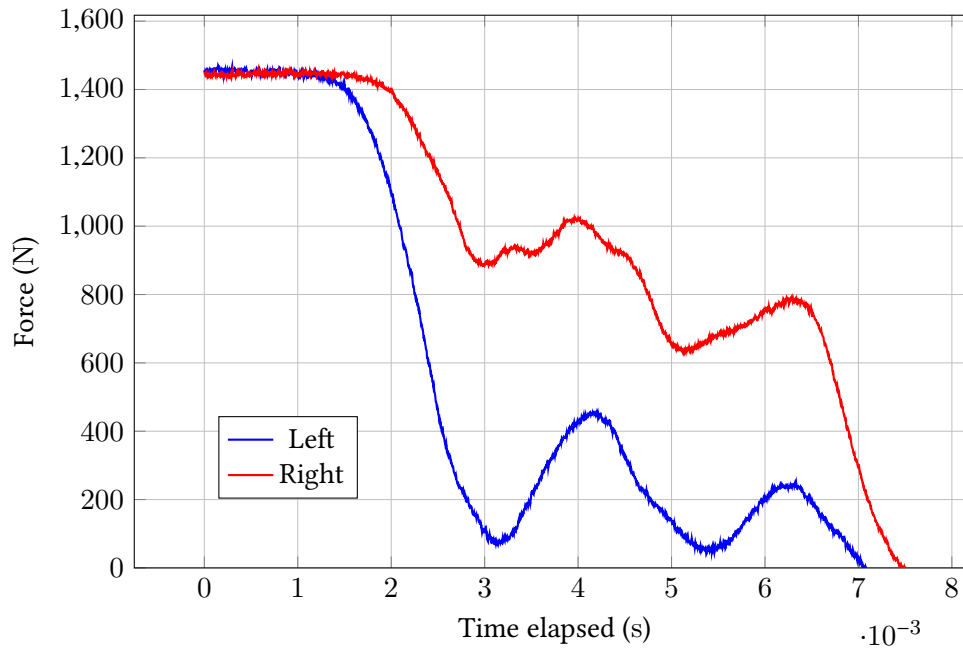


Figure 5.4: Evolution of reaction forces vs time in the left and the right LVDT. This corresponds to the 60 mm tall specimen and  $\lambda_y = 3.0$ .

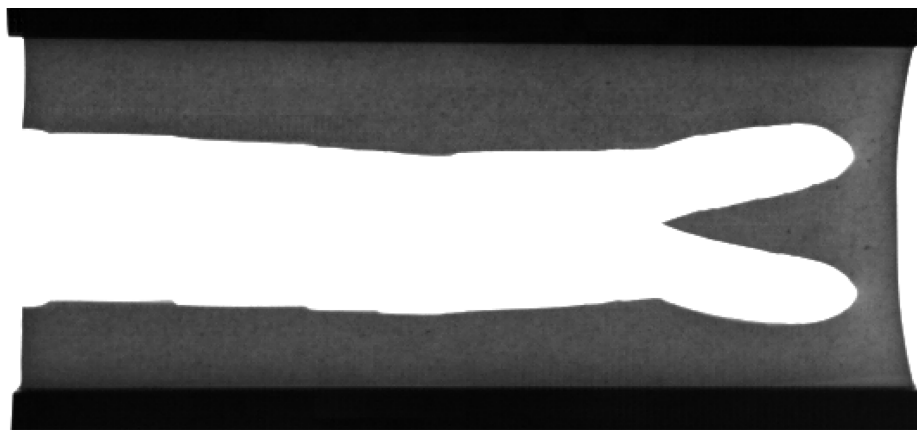


Figure 5.5: Crack branching event in 40 mm specimen (batch-1) with an initial seed crack when pulled at  $30 \text{ mm s}^{-1}$ . Both the branches propagate further and the specimen is finally broken into three pieces.

It shall be noted that no such observations were made prior to this except for the studies of Moulinet and Adda-Bedia, 2015. However, in Moulinet and Adda-Bedia, 2015, experiments were conducted on balloons where the stress state is bi-axial and hence, there is a considerable stress along the crack path in addition to perpendicular to it.

### 5.3 SAMPLES OF ANOTHER BATCH (BATCH 2)

Since the results from batch-1 were not as expected, experiments were conducted on specimen of a different batch (to be noted as batch-2). The test protocol followed is exactly the same as that in section the previous sections (as in Corre, 2018), where the specimens were stretched and a crack is introduced. The crack propagation was again monitored by an HR and an HS camera. The crack speeds obtained from this batch of specimen can be seen in figure 5.8.

It can be seen that the crack speeds in this new batch are entirely different from those obtained from the batch-1 as well as in Corre, 2018. For instance, at a stretch level of 3.5, the crack surface was considerably rougher and the crack speeds were considerably lower for all the geometries than in the previous batch. It might be possible that the specimen properties varied considerably between

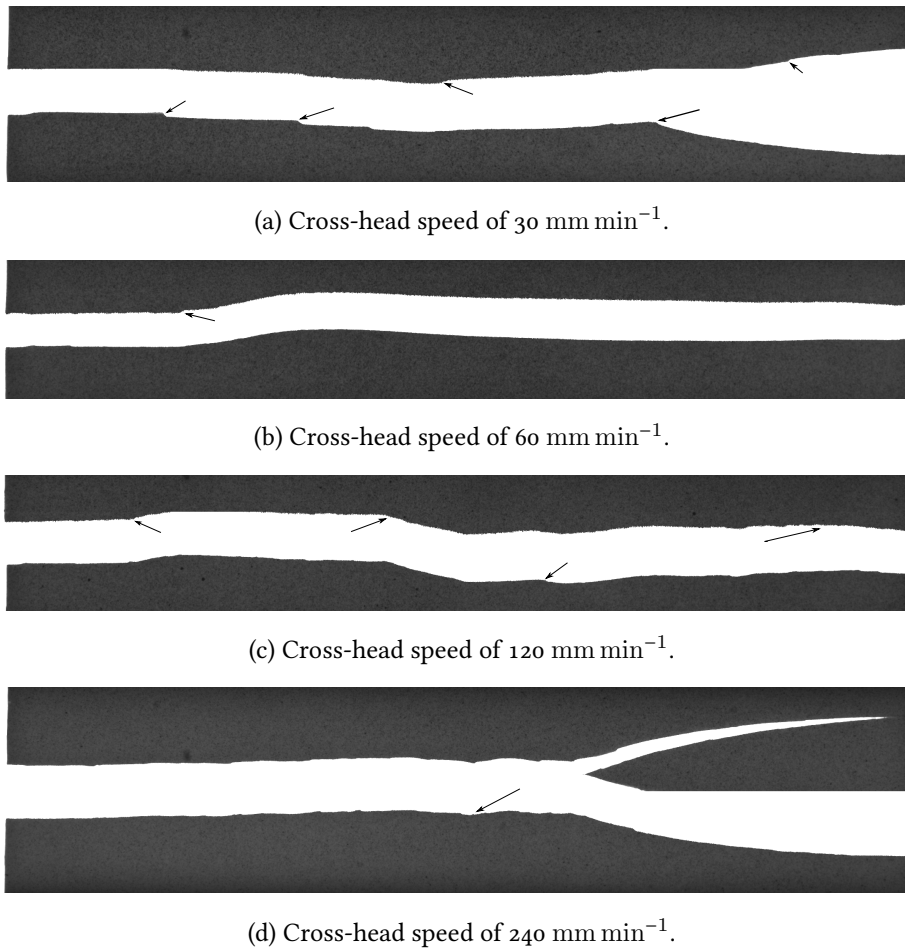


Figure 5.6: Branching attempts made by crack in the 40 mm specimens (indicated on the broken samples). The arrow points to the location where the branching was attempted. Some branching events were successful while the others were not. An initial seed crack was present in all the cases. The cross-head of the tensile machine was pulled at different rates as indicated in the captions.

different batches. No visible defects were present in the specimen.

The uniaxial response of the material from the new batch is determined by extracting the test sample from the 60mm tall specimen. The response can be seen in the figure 5.9. The response of the sample in pure shear configuration can also be seen. It can be observed that starting from a stretch level of about 3.0, the behavior of the material from the new batch considerably differs from that of the previous batch in the uniaxial case. Similarly, in pure shear case, the behaviors of the two batches can be seen to be similar until about a stretch of 3.0, beyond which they were observed to diverge. This observed difference in the material behavior may be one of the reasons for the observed differences in the crack speeds between the two batches.

#### 5.4 TEMPERATURE MEASUREMENTS

In addition to obtaining the displacement fields in the specimen all throughout the experiment, attempts were made to measure the temperature change in the specimen (of batch 2) as the crack propagated. Some other instances of measurements of temperature raise during the crack propagation can be seen in Fuller, Fox, and Field, 1975; D'Amico, Carbone, Foglia, and Galietti, 2013. Two techniques were used in Fuller et al., 1975 for this. The first method is called *Liquid crystal film technique*, where a thin, even film of the liquid crystal is spread on the surface of the specimen. The color of the liquid crystal is sensitive to temperature and hence, a change in the color of the layer was used to determine the temperature raise. This technique was used to measure the temperature raise of the PMMA specimen

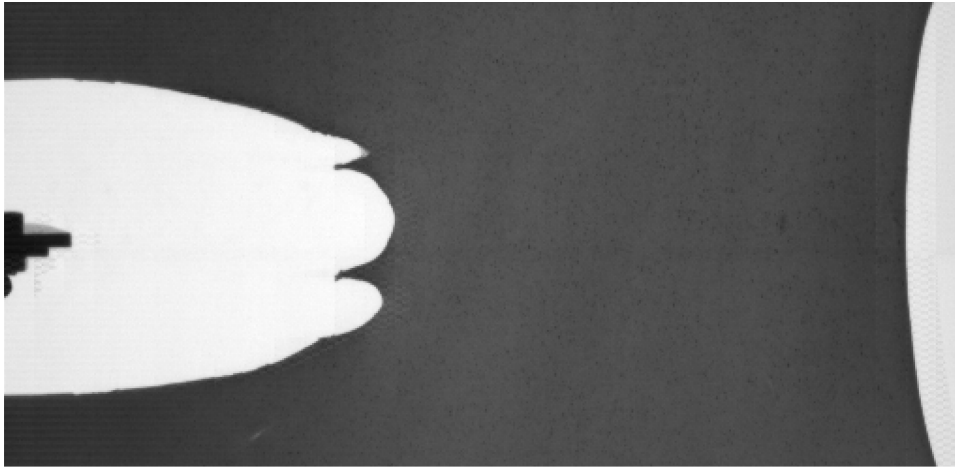


Figure 5.7: Crack branching attempt in 40 mm specimen (batch-1) following the normal test protocol. The two side branches were arrested and the center branch propagated further.

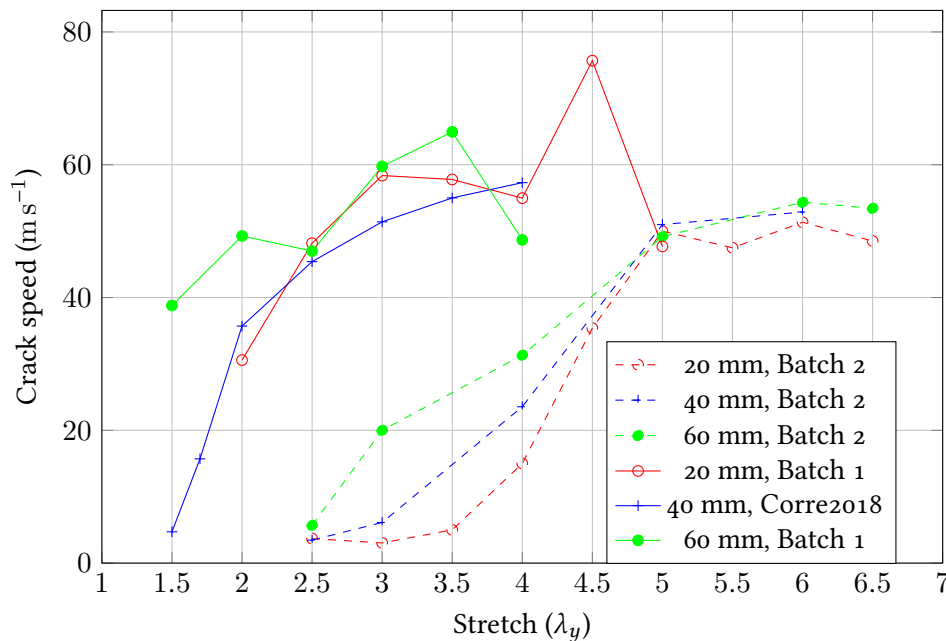


Figure 5.8: Results of the experiments from batches 1 and 2. Results from Corre, 2018 can also be seen.

as a crack passed through it. The second method is using thermocouple junctions, where one junction was placed about 0.5 mm above the crack path while the other junction is placed remotely. This setup is used to measure the temperature raise during crack propagation. An Infrared detector was used in the same study as well. In D'Amico et al., 2013, the temperature raise due to the crack propagation in a viscoelastic solid has been measured. The material used is SBR. An IR camera was used. A temperature raise of about  $1^\circ\text{C}$  was reported. However, the crack speeds in that study are of the order of  $50 \text{ mm s}^{-1}$ .

The temperature measurements were made on the samples in batch-2. It was not possible to measure the temperature for many experiments because of limited number of samples. The measurement was done for the 40 mm sample for an applied stretch level of 3. For this batch, the crack speed for this stretch is about  $5 \text{ m s}^{-1}$ , which is much smaller than observed in Corre, 2018. Hence, these temperature measurements should only be considered qualitatively. Due to the low acquisition rate of the IR camera, only one frame was obtained when the crack was propagating through the specimen. The results for that case can be in figures 5.10 and 5.11.

It can be seen from the figures that there is a large increase in temperature in the material at the vicinity of the crack tip. The temperature of the specimen during

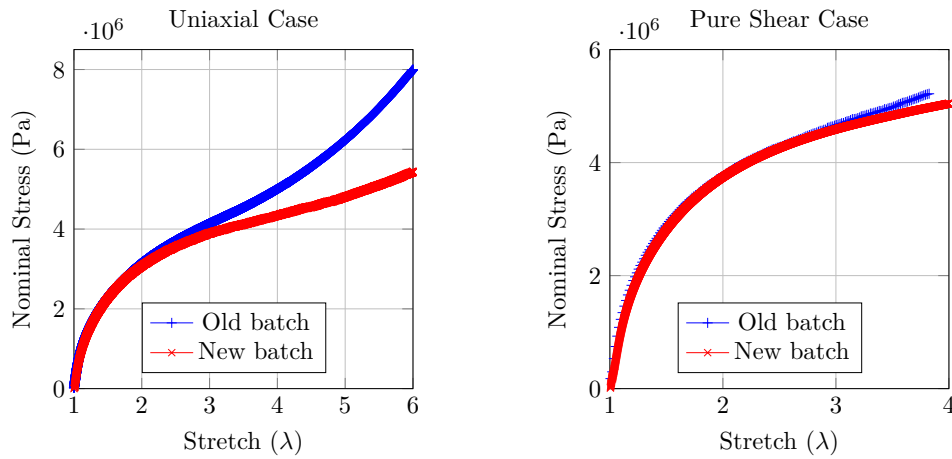


Figure 5.9: Uniaxial and pure shear response of the material from batch-2. Corresponding results from the material from Corre, Coret, Verron, Leblé, and Le Lay, 2020 can also be seen.

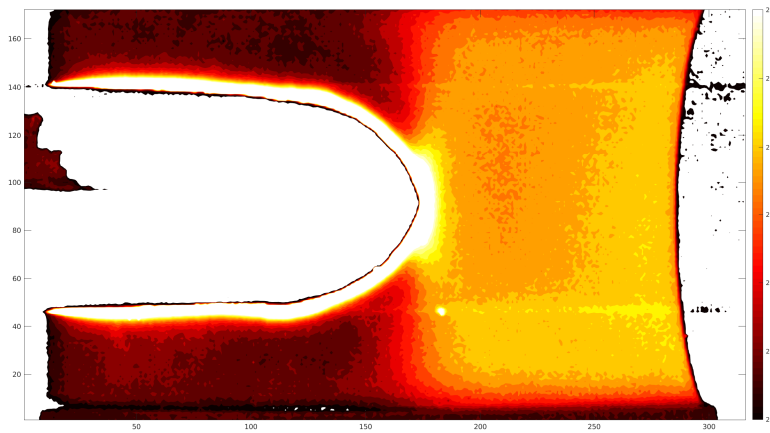


Figure 5.10: Temperature distribution (in °C) when the crack is about at the center of the specimen. The upper value of the scale is truncated to bring out the temperature far ahead of the tip and far behind the tip.

the stretching process changed from about 25 to 27 °C. This can be observed from the temperature difference in the material far away from the tip in front of and behind it. The temperature of the material in the vicinity of the tip (and hence the crack faces) can be seen to rise to about 70 °C. This can perhaps be attributed to the viscoelastic dissipation in the vicinity of the tip as a consequence of high strain rates in that region. In the later chapters, an attempt will be made to identify and compare the region in which the material dissipates to the results just presented.

## 5.5 DISCUSSION

The reason for performing additional experiments on samples of different sizes is to verify the phenomenon of the crack speed (in-)dependence on the specimen size in Transonic regime as reported in Chen et al., 2011. However, as was presented, the crack speeds for the 20 mm and 60 mm (batch-1) samples did not follow a monotonic trend as observed in Corre, 2018. A large variation of crack speed was observed in some experiments and there was a corresponding change in the appearance of the crack surface. The crack surface was observed to become rougher with a decrease in the crack speed. However, a quantitative relation between the two has not been obtained. Upon visual inspection, later on, it was observed that some specimens contained air bubbles throughout the specimen (and so, probably along the prospective crack path). Some specimens contained air bubbles that were initially invisible but became visible once they were stretched. This might be one of the reasons for the observed variation in the crack speeds.

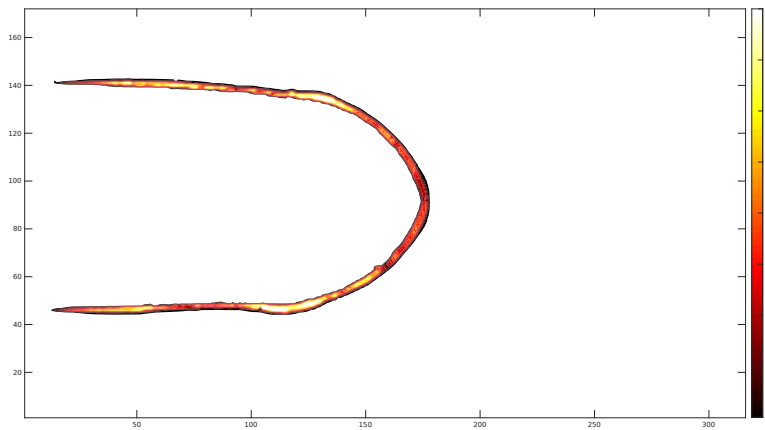


Figure 5.11: Temperature distribution in the vicinity of the tip (in  $^{\circ}\text{C}$ ). Temperatures as high as  $70^{\circ}\text{C}$  can be seen (ambient at about  $25^{\circ}\text{C}$ ).

Different type of experiments were conducted on the 40 mm specimen from batch-1 as data was already available for this geometry from Corre, 2018. A seed crack was introduced into the specimen and the specimen was then pulled at different speeds. It was observed that the crack underwent branching in multiple cases. Since this was unexpected, the 40 mm specimen was then subjected to the same protocol to check if similar results as that of Corre, 2018 can be obtained. However, a different behavior was observed. In Corre, 2018, the crack, once initiated travels straight through the specimen. The crack speed remained constant in the middle of the specimen in most cases. In the current study, an attempted branching was observed when the crack is at the center. Three branches can be seen to originate in figure 5.7. The top and bottom branches stopped propagating while the center crack moved on. As already mentioned, this is in contrast to the observations from Corre, 2018. More tests, however, could not be conducted as there were no more samples available from batch-1.

Another batch (batch-2) of samples of all the geometries, 20, 40, and 60 mm were procured to repeat the experiments, this time on the samples from the same batch. Experiments conducted on this new batch, however, resulted in crack speeds that are entirely different from the previous batches. At the same stretch levels, the crack speeds were considerably smaller than in the previous batches. The crack surface was considerably rougher as well. However, it can be seen from figure 5.8 that, in the experiments conducted on the new batch, the crack speeds in the three geometries settled down at a certain speed after certain stretch level. Beyond a stretch of 500 %, the crack speeds settled down at about  $50 \text{ m s}^{-1}$  in all the three geometries. Perhaps, this can be compared with the results obtained by Chen et al., 2011. The uniaxial and pure shear responses of the samples from batch 2 differed from that in Corre, 2018 (see figure 5.9). This may explain the observed differences in the crack speeds.

The images taken from the HR and the HS camera during the initial stretching and the crack propagation for samples from batch-1 and batch-2 can be found at Kamasamudram and Coret, 2019a, 2019b.

Temperature measurements have been taken on some of the samples from batch-2. It has been observed that the temperature of the material in the vicinity of the crack tip rises to about  $70^{\circ}\text{C}$ . The rest of the sample remains at about  $26^{\circ}\text{C}$ . A change in temperature of the sample has been observed during the initial stretching process as well, which corresponds to the entropic elasticity of polymers. This effect can also be observed when the crack is at the center of the specimen. In regions far from the tip, a change in temperature can be observed in front of and

behind the crack tip. This temperature difference is about 2°C.

As a consequence of different results from different batches, the results from these two batches will not be considered for the analyses that will be performed in this thesis.

#### **SUMMARY**

The additional experiments performed on different geometries and batches of polyurethane specimens have been described in this chapter. As a consequence of the variation of material properties between different batches and presence of defects in specimens, the results from the experiments could not be compared with those from Corre, 2018. Additionally, temperature measurements have been taken on the specimens from batch-2. A considerable increase in the temperature near and behind the crack top along the crack faces has been observed.

# REVISITING THE FRACTURE EXPERIMENTS

# 6

---

The experiments performed in Corre et al., 2020 will be revisited in this chapter. The intent is to examine the velocity and the strain fields to look for any shock waves in the transonic regime. The variation of surface roughness with the crack speed in different experiments will be presented as well.

---

## CONTENTS

6.1	Displacement, Velocity and Strain fields . . . . .	57
6.1.1	Horizontal displacement . . . . .	57
6.1.2	Velocity fields . . . . .	57
6.1.3	Strain fields . . . . .	58
6.2	Observations on the variation of surface roughness . . . . .	58
6.3	Discussion . . . . .	62

Crack propagation in Polyurethane sheets has been studied in **corre2018**. The specimens that are 40 mm tall were stretched and a crack was introduced in the specimen. Transonic cracks were observed in that study starting at a stretch value of 2.5. Transonic cracks were first reported in the studies of Petersan et al., 2004. In that study, natural latex rubber sheets were stretched and a crack is introduced. It was observed that at a stretch level of about 3.2, the crack speed was able to exceed the shear wave speed. The authors of Petersan et al., 2004 remark

*Last, we note that when a moving object travels in an elastic medium faster than the wave speed, it creates a shock wave in the form of a Mach cone. The wedgelike crack opening typical of cracks in rubber (shown in Fig. 2) is strikingly similar to the Mach cone, suggesting that rubber cracks are shocklike, exceeding some response speed of the medium.*

This has been further studied in Marder, 2006, where lattice models were used to simulate the crack propagation. A Neo-Hookean model was used to describe the hyperelastic part of the material behavior. Kelvin dissipation is added to describe the viscoelastic dissipation of the material. The author comments

*Buehler et al. (2003) have proposed that hyperelasticity plays a critical role in dynamic fracture, and that in particular an increase of sound speed near a crack tip can allow cracks to travel faster than the distant shear wave speed. In the analysis of this paper, there is an increase of elastic modulus near the tip of the rupture, but it is not in the form that Buehler et al. proposed. The theory here involves an increase in the imaginary modulus of rubber with frequency, rather than an increase in the real modulus of rubber with extension.*

This is somewhat similar to what will be discussed in this thesis. However, a FE analysis will be used along with a continuum based viscoelastic material model.

Other studies of this nature were made in Chen et al., 2011. Rubber sheets were used to perform fracture experiments in that study. However, as natural rubber tends to strain-crystallize at high strains, the crack could not propagate at those strains (Zhang, Niemczura, Dennis, Ravi-Chandar, & Marder, 2009). To circumvent this, the experiments in Chen et al., 2011 were conducted at 85°C. High temperatures prevent the crystals from forming at higher strains. Numerical studies were also performed in that study using lattice models. Kelvin dissipation was introduced as in Marder, 2006, but the model was calibrated based on retraction tests performed on rubber in Niemczura and Ravi-Chandar, 2011. However, it shall be noted that the experiments in Niemczura and Ravi-Chandar, 2011 were carried out at 24°C. It is not clear whether any adjustments were made to take the temperature difference into account.

Other notable studies are that of Corre et al., 2020; Mai et al., 2020. In both the studies, Transonic cracks were observed. Mai et al., 2020 considers the crack opening to be of a wedge shape and to resemble a shock front as in Petersan et al., 2004. The experiments of Corre et al., 2020 will be analyzed in this thesis to look for shock fronts in the Transonic regime.

It shall be noted that in mode-II cracks propagating along weak planes in the Transonic regime, a shock front was observed that travels along with the crack (Rosakis et al., 2000). The shock waves were clearly visible in the density of the photoelastic fringes observed. The crack speed was seen to exceed  $c_s$ , reach  $c_l$  and settle down at about  $\sqrt{2}c_s$ . Particle velocities were seen to rise sharply when the Mach front passes through in the material (see figure 23 of Mello et al., 2010). Photoelastic fringes confirm the passage of Mach front corresponding to the velocity jump observed.

In the studies performed on the fracture of elastomers, such shock fronts have

not been reported. Instead, as already mentioned, the crack faces behind the tip were noted to be of wedge shape and resemble a shock front. Since no reports of a Mach front were found in the literature and since the displacement, strain and velocity profiles are available for the experiments in Corre, 2018 from DIC technique, they can be used to determine the presence or absence of the Mach fronts. It shall be noted that a jump in particle speeds should be observed across any such mach fronts. Hence, examining the velocity profiles for the presence of such jumps will help determine the presence of mach fronts.

## 6.1 DISPLACEMENT, VELOCITY AND STRAIN FIELDS

The experiments in Corre, 2018 reveal that the crack speed at a stretch level of 1.7 is about  $17\text{m s}^{-1}$  which is subsonic, while the crack speed at a stretch level of 3.5 is about  $56\text{m s}^{-1}$ , which is transonic. Hence, examining the velocity profiles from these two experiments will help determine the presence, or absence thereof, shock fronts (Kamasamudram, Coret, & Moës, 2021).

### 6.1.1 Horizontal displacement

Presence of a *Mach front* in experiments will result in discontinuity of velocity and strain fields. The displacement fields however, do not exhibit any *jumps*. However, for the sake of comparison later on with the simulations, the horizontal displacement fields for the two experimental cases of  $\lambda_y = 1.7, 3.5$  will be presented. Only top half of the specimen is included.

The horizontal displacement fields can be seen for both the cases in figures 6.1 and 6.2 when the crack is about the center of the specimen. In both the cases, a distinct kidney-bean-shaped profile can be observed in the material just behind the tip. A similarity in both the distributions can be seen even though the former crack is subsonic and the latter is transonic.

### 6.1.2 Velocity fields

The velocity fields for stretches 1.7 and 3.5 when the crack is at about the center of the specimen can be seen in the figures 6.3a and 6.3b. It can be seen that the velocity fields do not show a significant difference in form between the two experiments. The peak value, however, is higher in the case of 3.5 as a consequence of a higher crack speed. However, the velocity is continuous.

To obtain a better comparison, the velocity magnitudes are extracted at about 5 mm above the crack path and plotted in figure 6.4.

The velocity fields are continuous. A jump was not observed as was the case in the experiments in mode-II (Mello et al., 2010). And as mentioned earlier, the maximum value of particle velocity is different between the two cases because of different stretch levels and crack speeds.

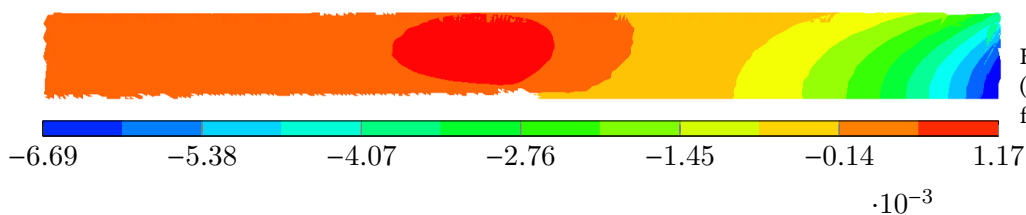


Figure 6.1: Horizontal displacement (in m) for  $\lambda = 1.7$  plotted on undeformed configuration.

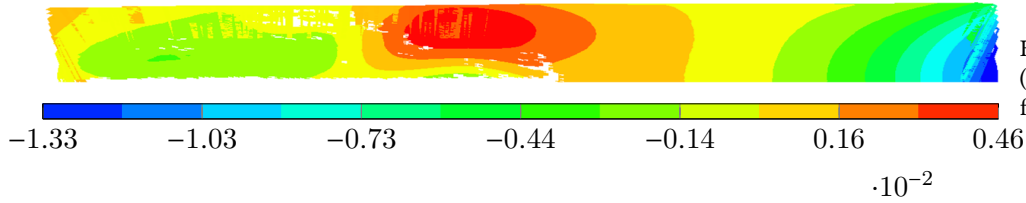
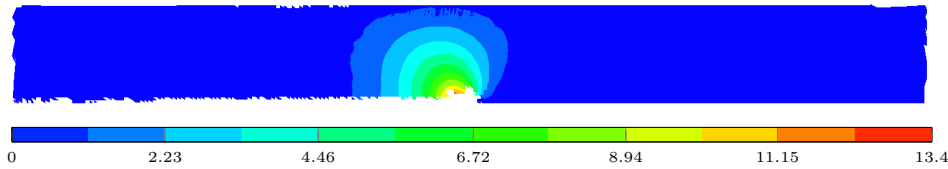
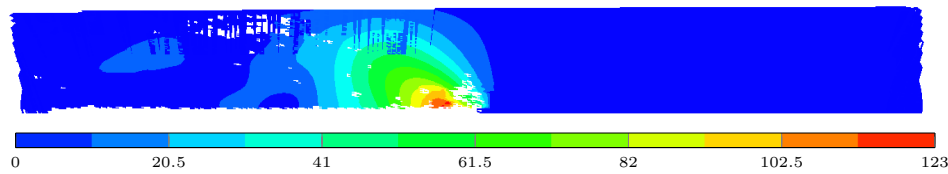


Figure 6.2: Horizontal displacement (in m) for  $\lambda = 3.5$  plotted on undeformed configuration.



(a) Particle velocity magnitude in  $\text{m s}^{-1}$  for a stretch of 1.7 and crack speed of  $17 \text{ m s}^{-1}$ .



(b) Particle velocity magnitude in  $\text{m s}^{-1}$  for a stretch of 3.5 and crack speed of  $56 \text{ m s}^{-1}$ .

Figure 6.3: Particle velocity magnitudes in sub- and transonic cases.

### 6.1.3 Strain fields

Since the deformations in the current study are large, non-linear strain measures are required for comparison. The vertical component of deformation gradient,  $F_{yy}$  has been chosen for this. The distribution of  $F_{yy}$  for stretches of 1.7 and 3.5 can be seen in the figures 6.5a and 6.5b, analogous to the velocity fields in 6.3a and 6.3b.

Like in the case of velocity, a sharp jump could not be seen even for the deformation gradient. Similar to what has been done for velocities, the variation of yy-component of deformation gradient at about 5 mm above the crack path in the undeformed configuration has been extracted and plotted in figure 6.6. It can be seen that  $F_{yy}$  varies continuously along the specimen length for both  $\lambda_y = 1.7$  and  $\lambda_y = 3.5$ .

An additional observation has been made from the fracture tests on the 40 mm tall specimen. As mentioned earlier, a Pure Shear specimen is stretched to a required value and a seed crack is initiated using a razor blade on the left edge. The crack then runs from the left to the right edge. When the crack is just near the right edge (for example at about 20 mm from the right edge), it has been observed that the specimen at the left does not go back to zero strain level - some residual strain is left behind (Figure 6.6), which eventually goes to zero after about a few minutes to few days after the experiment. The strain level at the left end at the instant described depends on the initial stretch and hence the crack speed. This indicates the presence of relaxation times that are larger than the duration of the experiment, which is typically about 10 ms. The yy-component of the deformation gradient near the left edge are seen to vary between 1.1 and 1.9 for prestretch levels between 1.7 and 3.5.

## 6.2 OBSERVATIONS ON THE VARIATION OF SURFACE ROUGHNESS

In the studies on the fracture of elastomers, another aspect of interest is the appearance of the fracture surface once the specimen is broken. Throughout the

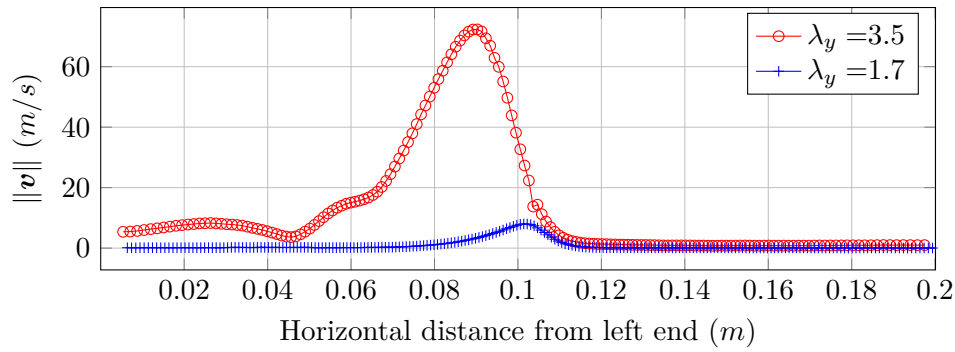


Figure 6.4: Comparison of particle velocity magnitude at about 5 mm above the crack path for stretches 1.7 and 3.5.

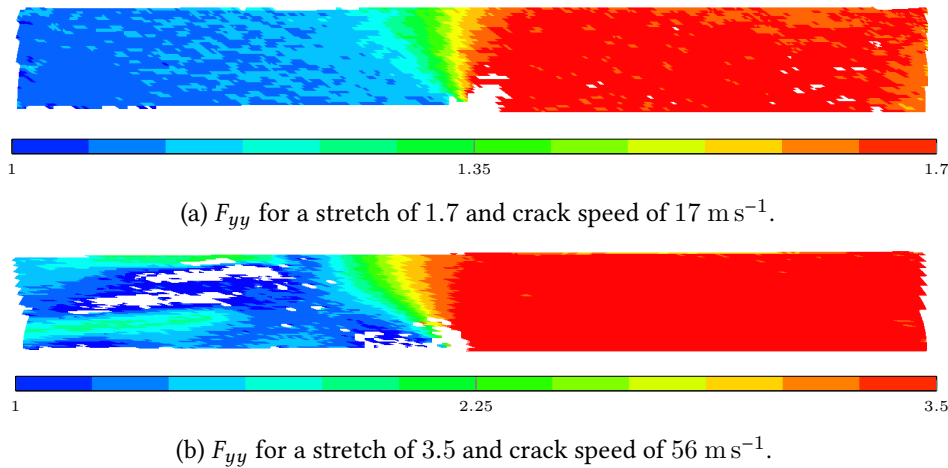


Figure 6.5: Particle velocity magnitudes in sub- and trans-sonic cases.

literature, there are reports of changes in the appearance of the crack surfaces with crack speed and in some cases, the thickness of the specimen used for the study. One of the earlier studies that discuss this aspect is Greensmith and Thomas, 1956. In that study, the propagation of a crack in an elastomer in ‘tearing’ configuration was studied and the process of crack propagation was classified into steady and stick-slip modes based on the reaction vs time behavior observed. A smooth surface was observed in the steady tearing mode, while a rougher surface was observed in the stick-slip mode. The stick-slip mode is attributed to the presence of a toughening structure as a result of high strains at the tip, typically crystallization.

Another such observation can be found in Stevenson and Thomas, 1979, where fracture of elastomers in balloon geometry was studied. The surfaces were reported to contain ‘undulations’ that are about 5-8  $\mu\text{m}$  apart and 3-5  $\mu\text{m}$  deep, but nothing more was discussed about them. Another such discussion can be found in Kadir and Thomas, 1981, 1984 where again the fracture surfaces of specimen tested in the pure-shear configuration were reported to appear smooth but with small ‘paraboloidal’ marks pointing in the direction of propagation at higher crack speeds and a rougher surface at smaller crack speeds. However, Gent and Marteny, 1982a reports smooth crack faces despite the smaller crack speeds observed in some load cases.

Cavitation was regarded as the reason for the change of surface roughness with the crack speed in Kadir and Thomas, 1981. The smoother surface observed at higher crack speeds was attributed to the absence of cavitation because of the ‘viscoelastic stiffening’ of the region in the vicinity of the tip as a consequence of high strain rates as the crack moves. This theory was further investigated in Lake et al., 1992, where an SBR sample was placed in a chamber filled with Ethylene Glycol which was used to apply external pressure to the sample. The crack propagation was studied under different applied pressures to study its influence

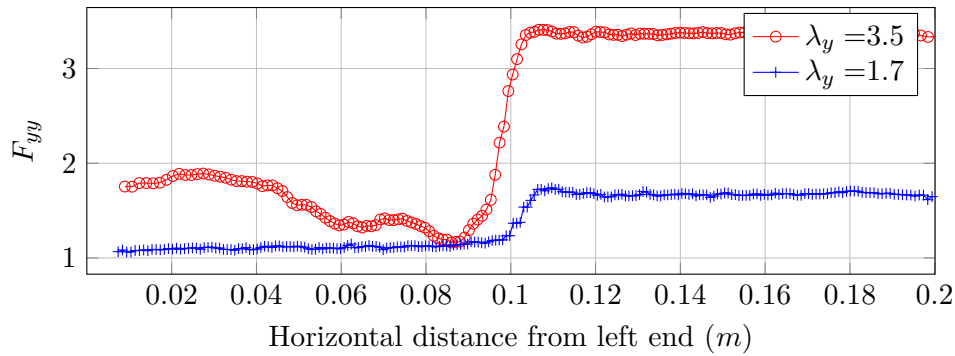


Figure 6.6: Comparison of  $F_{yy}$  at about 5 mm above the crack path for stretches 1.7 and 3.5.

on the occurrence or the suppression of cavitation. The results, however, were reported to be unclear in that study for the lack of extensive data.

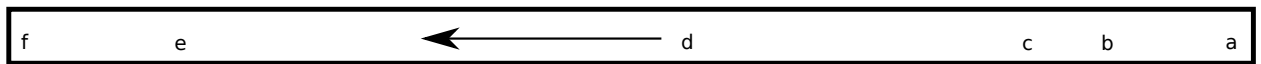
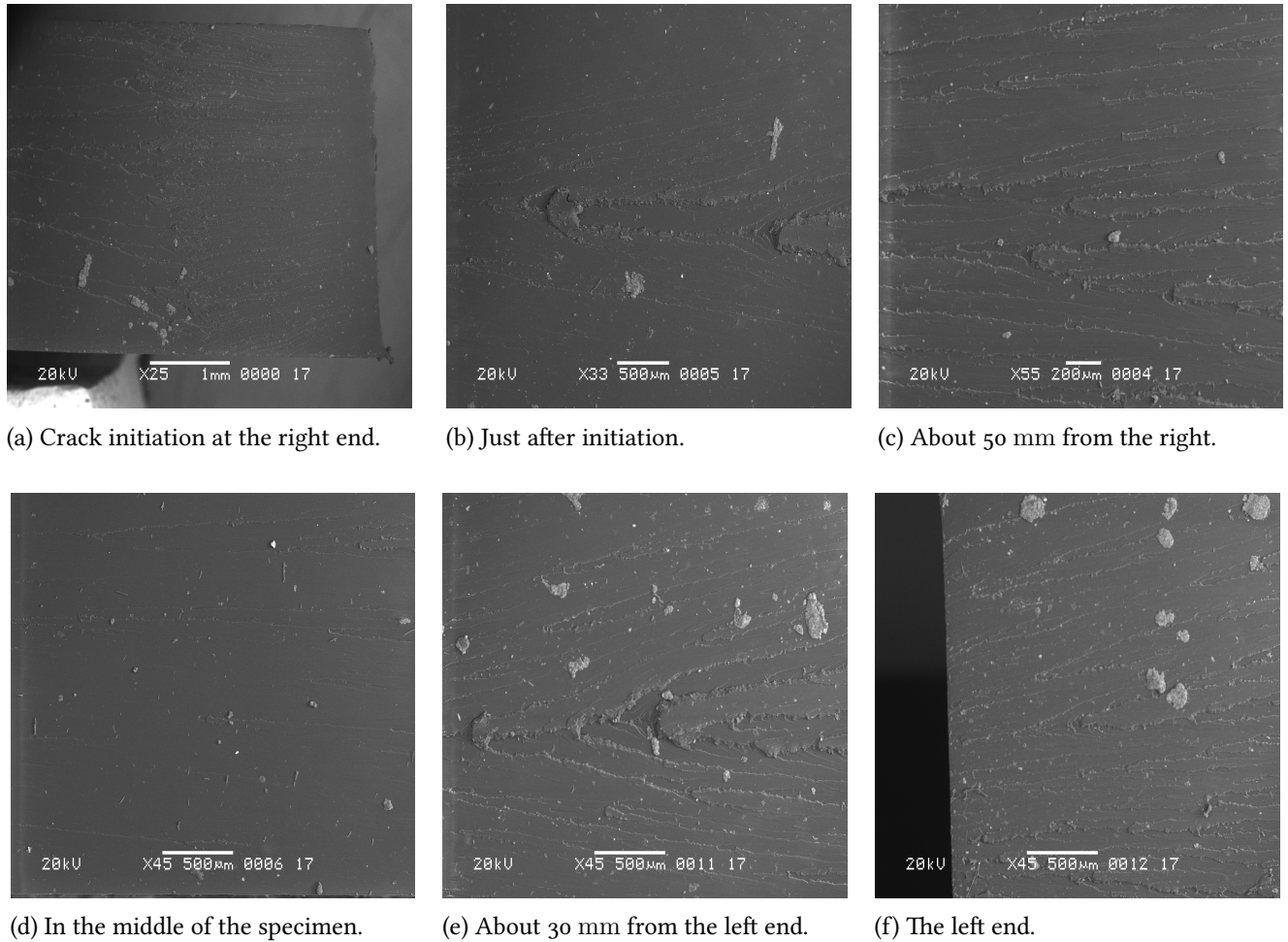
In Lake et al., 2000, the phenomenon of cavitation was examined by studying the effects of specimen thickness on the surface roughness. It was found that the specimen thickness affected the crack speeds and the surface roughness at smaller crack speeds and that they remain independent of the thickness in the high-speed regime. The observed behavior in the low-speed regime was attributed to the ‘transverse stresses’ that develop at the tip as a result of an increase in the specimen thickness which in turn promotes cavitation. Further studies in this direction were performed by Tsunoda et al., 2000, where the effects of specimen thickness and viscoelastic properties of SBR on the crack speed and surface roughness were examined. The SBR samples were swollen to various levels by Dibutyl Adipate to modify the viscoelastic properties of the material. In other cases, unswollen specimens with various thicknesses were used. In the case where the specimen is swollen, the surface was observed to become rougher at smaller crack speeds. In the case where specimens of different thicknesses were used, the crack speed was observed to change with thickness in the low-speed regime. High-speed regime was seen to be unaffected by thickness. Both these results were attributed to the presence (or absence) of cavitation.

When the fracture surfaces of the specimens broken in Corre, 2018 were examined using Scanning Electron Microscope, some variations in the surface roughness with crack speed were observed. The variations in the surface roughness observed can be seen in figures 6.7 and 6.8.

Before presenting the observations from these figures, it shall be noted that the thickness of the specimen that is used in this study is 3 mm. This value is higher than what has been used in the literature, like in Chen et al., 2011; Gent and Marteny, 1982a; Mai et al., 2020; Greensmith and Thomas, 1956. Also to be noted is the fact that the surface patterns presented in each figure are from the different regions of the *same* experiment as opposed to the cited literature where the roughness transition is observed between *different* experiments as the crack speed is varied. Other experiments that study the crack propagation in high speed regime do not report such an observation.

Now, regarding the surface patterns in the figures, the arrow in the figures 6.7g and 6.8g gives the direction in which the crack runs. Each subfigure is associated with a region in the specimen through an alphabet. In each of the subfigures, the direction of crack propagation is from right to left. The results presented here are for the stretches of 2 and 3 where the crack speeds are about  $33 \text{ m s}^{-1}$  and  $52 \text{ m s}^{-1}$  respectively. In each case, the crack starts from the right end of the specimen, accelerates to some speed, which it maintains for most of the experiment. For the case of stretch level of 2, it was observed that the crack slightly decelerates as it approaches the other end, while for the case of stretch level of 3, it was seen to

almost remain at the same speed (see figure 4.4 and Corre, 2018).



(g) Locations where the roughness were measured.

Figure 6.7: Variation in surface roughness for the case  $\lambda_y = 2.0$ .

The corresponding variation in the surface roughness can also be seen. In figure 6.7, at the right end near the initiation, a very rough surface can be seen, probably from the razor blade used for the initiation. Once initiated, it can be seen from figures 6.7b, 6.7c and 6.7d that the surface becomes smoother. During this phase, the crack speed can be seen to increase as well. However, as the crack approaches the left end, the surface can be seen to become rougher again (figures 6.7e and 6.7f). The crack speed towards the left end can be seen to decrease for this stretch level.

For the case of  $\lambda_y = 3.0$ , a similar trend in the surface roughness can be observed in the initiation and acceleration phases (figures 6.8a, 6.8b and 6.8c). When the crack is at the center of the specimen, the surface is smooth at the magnification level used. However, at the left end of the specimen, it can be seen that the surface remains almost smooth as opposed to the case when  $\lambda_y = 2.0$ . Correspondingly, the crack speed at the left edge for  $\lambda_y = 3.0$  can be seen to remain at the same value as it was at the center. Between the two cases, it can be seen that the surface is considerably smoother for the case of  $\lambda_y = 3.0$  than for  $\lambda_y = 2.0$ .

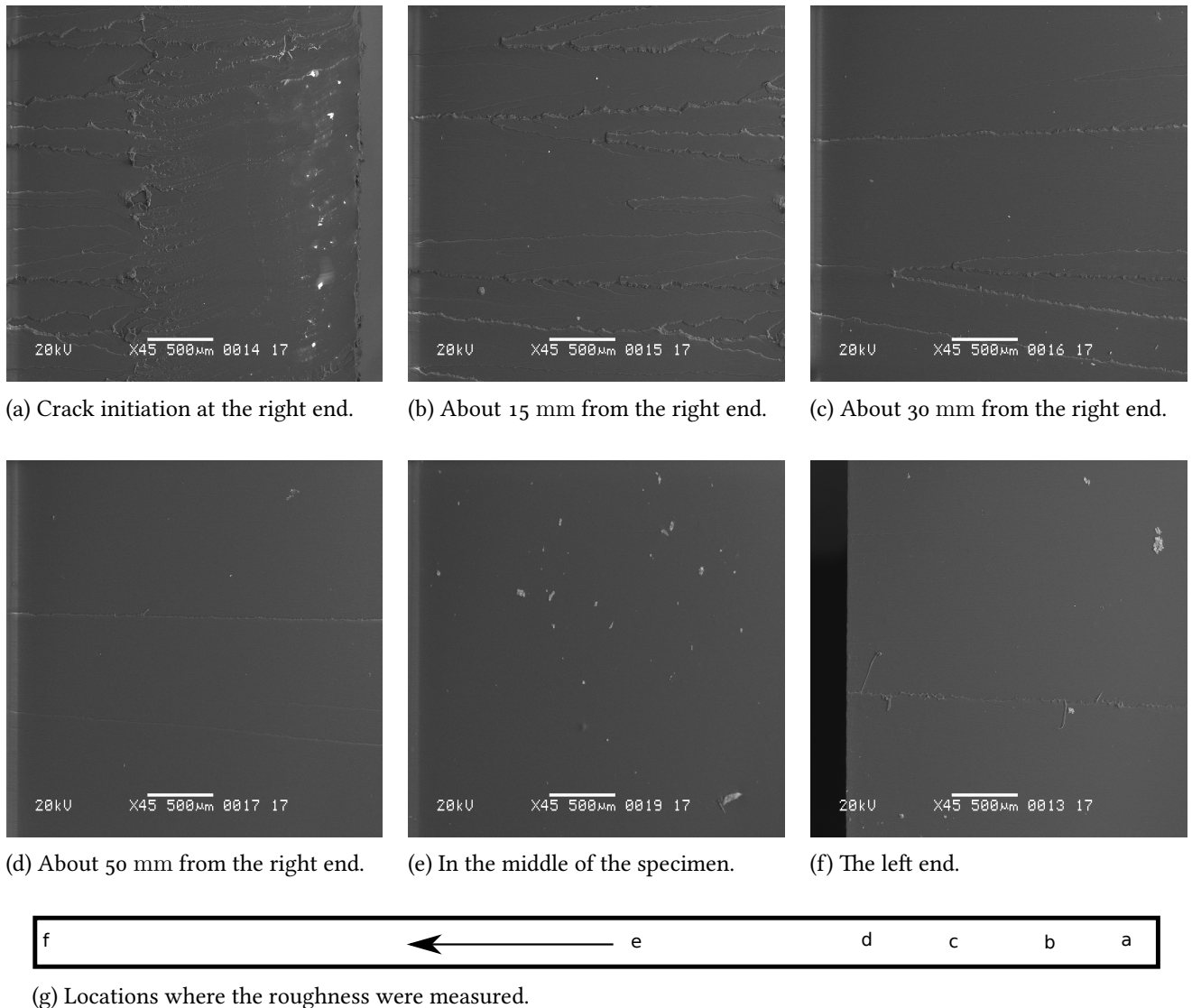


Figure 6.8: Variation in surface roughness for the case  $\lambda_y = 3.0$ .

A quantitative analysis has not been performed to link the roughness of the surface at a location (in terms of RMS roughness) with the crack speed at that location. One of the reasons for not having such observations from literature could be because of the smaller specimen thicknesses used in those studies. As stated at the beginning of this section, the specimen thickness is seen to influence the crack speeds and the surface pattern in the low-speed regime which would be the case when the crack starts from the rest at the right end of the specimen. Thus, an interesting question would be if the same pattern will be obtained if a specimen of different (smaller) thickness is used for the current study or if the surface would be completely smooth in such a case.

### 6.3 DISCUSSION

It can be seen from figures 6.4 and 6.6 that the velocity and strain vary continuously across the specimen even in the Transonic regime. A jump cannot be seen in either of these quantities. A difference in the crack opening has been noted between the two regimes. In Petersan et al., 2004; Corre et al., 2020, it has been noted that the crack opening changed from a parabolic to a wedge shape as the crack propagation

regime changes from subsonic to transonic. It has been remarked in Petersan et al., 2004 that the crack opening resembles a shock wave that propagates with the crack tip. This is, however, different from the shock front in the traditional sense where jumps in particle velocities and strains can be observed along a moving front within the material.

This is different from the Transonic cracks propagating in mode-II along weak planes. In studies where this crack propagation is studied (Rosakis et al., 2000; Rosakis, 2002), a *mach cone* can be clearly observed from the photoelastic fringes. In Mello et al., 2010, the particle velocities are monitored just above the crack path, and a sharp rise in particle speeds was observed in the Transonic regime. The experiments on elastomers do not report any such observations. Hence, the following questions might be asked (Kamasamudram et al., 2021) - *Why don't we observe shocks in the bulk material even when a crack propagating in an elastomer travels faster than the shear wave (in the transonic regime)? Which material model more appropriately captures the behavior of the bulk material?*

## **SUMMARY**

This chapter presents additional observations made regarding the velocity and strain fields together with the variation of crack surface roughness in the studies of Corre, 2018. A variation of surface roughness has been observed with the crack speed. Jumps have not been observed in either the velocities or strains. This will be explored further in the following chapter.

PART III  
**SIMULATIONS**

# THE ROLE OF VISCOELASTICITY IN THE BULK



---

This chapter examines the phenomena of hyperelastic and viscoelastic stiffening to determine the phenomenon responsible for observing transonic cracks in polyurethane elastomers. Crack speeds are implicitly imposed on the model using the data from the experiments as described in this chapter. The predictions of the hyperelastic and the viscoelastic model will be compared with the experimental observations. The methodology presented in this chapter can also be viewed as a method of calibrating the viscoelastic model.

---

## CONTENTS

7.1	Using momentum balance . . . . .	67
7.1.1	Calibration of hyperelastic model . . . . .	68
7.1.2	Checking momentum balance . . . . .	69
7.2	Using the cracks speed as an input . . . . .	71
7.2.1	Methodology . . . . .	71
7.2.2	Simulations . . . . .	72
7.3	Discussions . . . . .	78

In the previous chapter, it has been observed that the particle velocity and strain fields did not exhibit jumps in the Transonic regime. Traditionally, two main hypotheses are proposed for crack speeds in elastomers to enter the Transonic regime. The first of these rely on the dependence of the wave speed on the strain state because of the material non-linearity (Gent & Marteny, 1982a; Stevenson & Thomas, 1979). The stress-strain response of elastomers first exhibits a drop in the slope at moderate strains followed by an increase at larger strains. The upturn in the stress-strain response then increases wave speed. Presence of a crack in the material results in a strain concentration near the tip. This implies that the material near the tip is subject to larger strains than the bulk material. Since the stress-strain response of the material exhibits an upturn at higher strains, this would in turn mean that the wave speeds in the vicinity of the crack tip are higher than that in the bulk material far from the tip. This hypothesis has been investigated in M. Buehler, Abraham, and Gao, 2003, where the propagation of a crack in a material whose modulus increases beyond a certain strain level (called the offset strain) is studied. Crack speeds that exceeded the Rayleigh wave speed (and also the shear wave speed) of the bulk material were observed depending on the values of the onset strain used. However, it was reported in that study that the crack tip is followed by mach cones corresponding to the shear waves.

In M. J. Buehler, 2008, the problem of crack propagation along the interface of two solids with a large difference (a factor of 10) in stiffness was studied. It was observed that the crack propagated at speeds greater than the shear wave speed of the softer material. It was observed that the crack was able to propagate in the supersonic regime (with respect to the softer material) while remaining sub-Rayleigh with respect to the harder material. A mother-daughter propagation mechanism was observed similar to in mode-II. Shock fronts can be observed in the softer material (figures 6.80, 6.81, and 6.82 of the reference). However, it was remarked that this hasn't been observed in the experiments conducted on the crack propagation through the interface in a bi-material system.

In Guo, Yang, and Huang, 2003, the propagation of a mode-III crack in a solid that exhibits an upturn in the stress-strain response was investigated. In the vicinity of the crack tip, the material is stiffer than the bulk. The distribution of shear stress in the bulk was presented in that study. The equations of motion lose their ellipticity in the region where the crack speed is higher than the shear wave speed. As a result, discontinuities in the stresses can be observed along with the characteristics.

The other hypothesis proposed for observing transonic cracks comes from Stevenson and Thomas, 1979. In that reference, the author suggests that the *higher* crack speeds observed in that study are a consequence of the viscoelastic stiffening of the material as a result of the high strain rates present in the vicinity of the crack tip. A suggestion of this kind was also made in Marder, 2005, where a lattice based method is used to simulate the propagation of crack in rubber. However, to the knowledge of the author, no continuum based numerical studies exist that examine this hypothesis.

The velocity and strain fields analyzed in the previous chapter did not show the presence of any jumps. The maximum value of velocity varied between the experiments but it varied continuously along the length of the specimen. Hence, in this section, an analysis will be performed to determine the appropriate material behavior responsible for transonic cracks. A part of this chapter is an extract from the article Kamasamudram et al., 2021.

### 7.1 USING MOMENTUM BALANCE

In this section, the hypothesis of hyperelastic stiffening leading to transonic cracks will be examined. Since the displacement and velocity fields in the bulk material are obtained from the experiments, a hyperelastic model that exhibits an upturn in stress-strain response can be used to compute stresses and in turn momentum balance. A weak form of the momentum balance equation will be used for this purpose. It is intended to see if a hyperelastic model with an upturn in stress strain response, when applied for the crack propagation in transonic regime, will result in zero residual forces. The region where a non-zero residual is observed can be regarded as where the constitutive assumption is inappropriate. Thus, the hypothesis of hyperelastic stiffening can be examined. A weak form of the equilibrium will be developed below (Belytschko et al., 2000).

Beginning with the strong form of the momentum balance equation

$$\operatorname{div}_0 \mathbf{P} = \rho_0 \mathbf{a}, \quad (7.1)$$

where  $\mathbf{P}$  is the first Piola Kirchhoff stress,  $\rho_0$  is the density in the undeformed configuration and  $\mathbf{a}$  is the acceleration. Defining the space of admissible functions that are sufficiently smooth to be  $\mathcal{V}$ ,

$$\mathcal{V} = \{ \mathbf{w} \text{ that is sufficiently smooth} | \mathbf{w} = \mathbf{o} \text{ on } \partial\Omega_0^D \}, \quad (7.2)$$

$\Omega_0^D$  is the part of the boundary on which the Dirichlet boundary conditions are described. The weak form of momentum balance equation can be written as

$$\int_{\Omega_0} \mathbf{v} (\operatorname{div}_0 \mathbf{P} - \rho_0 \mathbf{a}) dV = 0 \quad \forall \quad \mathbf{v} \in \mathcal{V}. \quad (7.3)$$

Using the divergence theorem and that on  $\Omega_0^N$ ,  $\mathbf{P}\mathbf{n}_0 = \mathbf{t}$ , the above equation can be written as

$$\int_{\partial\Omega_0^N} \mathbf{v} \cdot \mathbf{t} dS - \int_{\Omega_0} \mathbf{P} : \nabla_0 \mathbf{v} dV = \rho_0 \int_{\Omega_0} \mathbf{v} \cdot \mathbf{a} dV. \quad (7.4)$$

To discretize the above equation using finite elements,  $\mathbf{v}$  is expressed in terms of its nodal values and shape functions. Hence

$$v_i = v_{iI} N_I(\mathbf{X}), \quad (7.5)$$

where  $i = 1, 2, 3$  indicates the spatial direction and  $I$  indicates the node number. Summation over repeated index is implied. Using this and also expressing the displacement field in a similar way, the internal, external and inertial nodal forces can be written as

$$f_{iI}^{\text{int}} = \int_{\Omega_0} \frac{\partial N_I}{\partial X_j} P_{ji} d\Omega_0, \quad (7.6)$$

$$f_{iI}^{\text{ext}} = \int_{\Omega_0^N} N_I t_i dS, \quad (7.7)$$

$$f_{iI}^{\text{kin}} = \int_{\Omega_0} \rho_0 N_I a_i d\Omega_0, \quad (7.8)$$

and the momentum equation becomes

$$f_{iI}^{\text{ext}} - f_{iI}^{\text{int}} = f_{iI}^{\text{kin}}. \quad (7.9)$$

For the sake of discussion that follows, the residual is defined as follows:

$$r_{iI} = f_{iI}^{\text{ext}} - f_{iI}^{\text{int}} - f_{iI}^{\text{kin}}. \quad (7.10)$$

The computation of  $f_{iI}^{\text{ext}}$  and  $f_{iI}^{\text{kin}}$  require the external force applied and the time derivatives of displacement respectively which are readily available from the experiments and so, no constitutive assumption is needed regarding the material behavior. The computation of  $f_{iI}^{\text{int}}$ , however, requires the computation of  $\mathbf{P}$  which depends on the constitutive behavior of the material. Hence, if an incorrect constitutive behavior of the material is assumed, non-zero residual forces will be observed.

### Computation of stresses

The material is assumed to be perfectly incompressible. Hence, the strain energy depends only on the first two invariants of the deviatoric part of the Cauchy-Green tensor. Defining  $\bar{\mathbf{C}} = J^{-2/3}\mathbf{C}$ , strain energy can be expressed as  $\hat{\psi} = \psi(\bar{I}_1, \bar{I}_2)$ . The PK2 stresses can be computed as (G. A. Holzapfel, 2000; Bonet & Wood, 2008)

$$\mathbf{S} = -Jp\mathbf{C}^{-1} + 2J^{-2/3}\text{DEV}\left\{\frac{\partial\psi}{\partial\bar{\mathbf{C}}}\right\}, \quad (7.11)$$

$$\text{DEV}\left\{\bullet\right\} := \bullet - \frac{1}{3}[\bullet : \mathbf{C}]\mathbf{C}^{-1}, \quad (7.12)$$

where  $p$  is the lagrange multiplier that enforces incompressibility condition. In plane stress conditions,  $p$  can be found by enforcing  $S_{33} = 0$ . As a consequence of incompressibility and plane stress conditions, the third component of  $\mathbf{C}$  can be defined to be  $C_{33} = 1/\det(\mathbf{C}_{2d})$ , where  $\mathbf{C}_{2d}$  is the in-plane part of  $\mathbf{C}$ .

$$\mathbf{C} = \begin{bmatrix} \mathbf{C}_{2d} & \mathbf{o} \\ \mathbf{o}^T & C_{33} \end{bmatrix} \quad (7.13)$$

Instead of this, the strain energy function can be made to depend on the three invariants of  $\mathbf{C}_{2d}$  where in the incompressibility condition is strictly imposed by taking  $C_{33} = 1/\det(\mathbf{C}_{2d})$  (Bonet & Wood, 2008). This can be done by realizing that  $\bar{I}_1 = \text{tr}(\bar{\mathbf{C}}) = \text{tr}(\mathbf{C}_{2d}) + 1/\det(\mathbf{C}_{2d})$ . Likewise,  $\bar{I}_2 = \frac{1}{2}(\bar{I}_1^2 - \bar{\mathbf{C}} : \bar{\mathbf{C}}) = \frac{1}{2}(\text{tr}(\mathbf{C}_{2d})^2 + 2\text{tr}(\mathbf{C}_{2d})C_{33} - \mathbf{C}_{2d} : \mathbf{C}_{2d})$ . In such a case, PK2 stress can be simply written as

$$\mathbf{S}_{2d} = 2\frac{\partial\psi}{\partial\mathbf{C}_{2d}}. \quad (7.14)$$

It shall be noted that finding  $p$  by enforcing  $S_{33} = 0$  and substituting back into the equation 7.11 will lead to the same result as in the equation 7.14.

#### 7.1.1 Calibration of hyperelastic model

A hyperelastic model that exhibits the upturn in stress-strain response is first calibrated using the data from uniaxial tensile and pure shear tests. A polynomial model of third degree has been picked for this. The resulting model prediction vs the experimental data can be seen in the figure 7.1. It can be seen that there is a slight deviation between the model prediction and the experimental data.

In the studies performed in Corre, 2018, the hyperelastic model, Ogden model for instance, has been calibrated to match the uniaxial test data without any deviations (figure 4.8 of Corre, 2018). Simulations have been performed using that model and parameters where a rectangular specimen of dimensions 40 mm

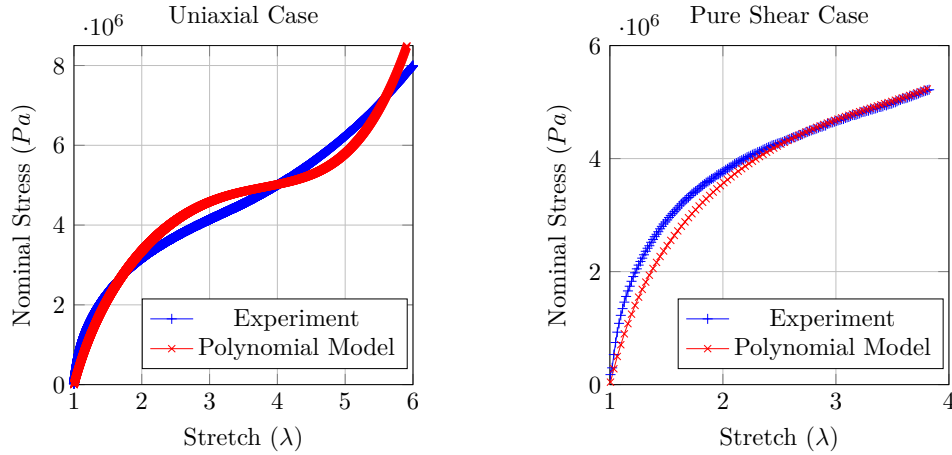


Figure 7.1: Experimental results vs Model prediction, Uniaxial and Pure Shear case.

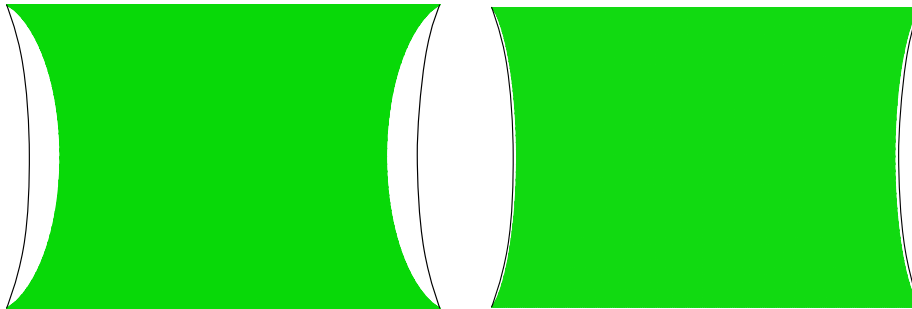
times 200 mm is stretched to a level of 3.5. The deformed shape of the specimen along with the deformed shape from the experiments can be seen in figure 7.3a. A significant difference can be seen. It was found to be necessary that the model coefficients be modified to bring the deformed shape closer to the experiments. The deformed shape predicted by the polynomial model with current coefficients can be seen in figure 7.3b. They can be seen to be quite close. Hence, these coefficients (in table 7.1) will be used in the current study.

Table 7.1: Model Co-efficients

Parameter	$C_{10}$	$C_{20}$	$C_{30}$	$C_{21}$
Value (Pa)	1.044E6	-0.02273E6	336.0	124.0

### 7.1.2 Checking momentum balance

Using the hyperelastic model, the residuals in equation 7.10 can be computed for different experiments. As a recollection, if the hyperelastic model is correct and appropriate, the momentum balance equation should be satisfied exactly. This is first carried out for the case of  $\lambda = 3.5$ . The residual forces are first computed just before the crack is introduced into the specimen. Since the strain rates during this time are quite small, it is expected that the residual computed will be small throughout the sample. The residual forces thus computed can be seen in figure 7.4a. Non zero and large forces can be seen on the boundaries of the specimen. The forces on the top and the bottom are the consequence of the applied loading and hence can be considered the reaction forces, acting along these boundaries,  $f_{iI}^{\text{ext}} = f_{iI}^{\text{int}}$ . Some forces can also be observed on the left and right edges of the specimen. This is because of the lack of data along the boundary from DIC technique. These



(a) Model fitted to Uniaxial test only.

(b) Current model parameters.

Figure 7.2: Deformed shape comparison,  $\lambda = 3.5$ . The black lines indicate the deformed shape from experiment.

forces can be seen to be the reaction forces applied by the missing material on the analyzed part of the material. Inside the material, small residual forces of about 0.02N (compared to that of about 17N along the top and bottom boundaries) can be observed. These can be considered to be the consequence of the errors induced by the DIC technique and the constitutive model.

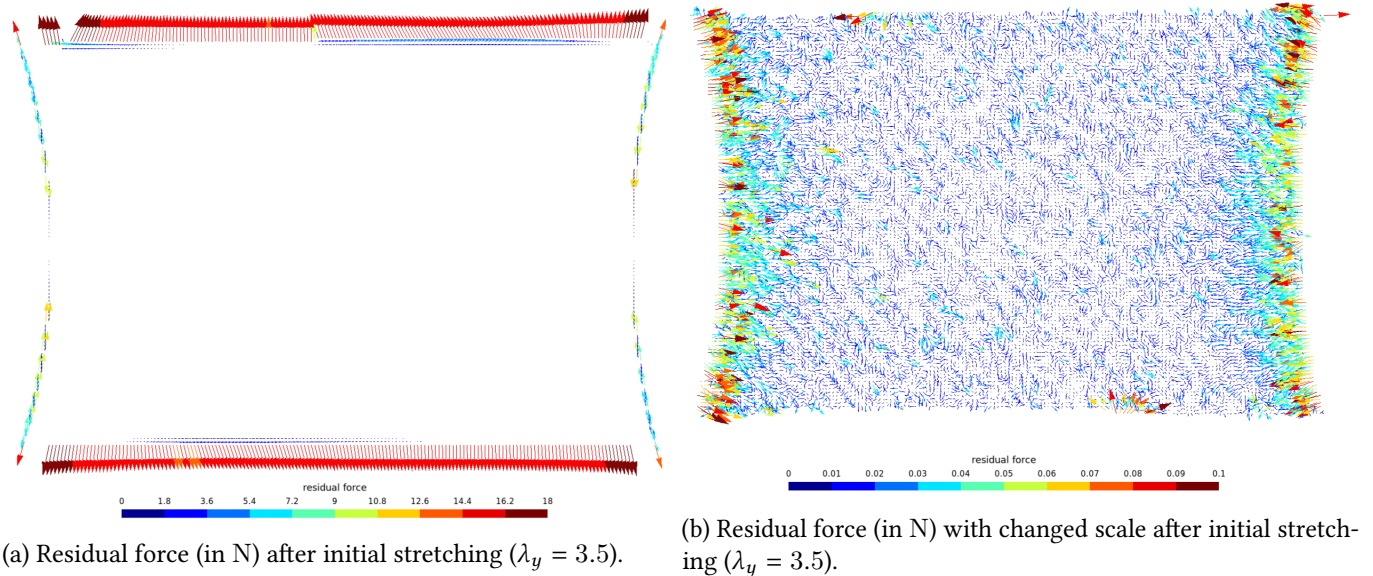


Figure 7.4: Residual nodal forces plotted on deformed configuration after initial stretching for  $\lambda_y = 3.5$ .

The residual forces when the crack is at the center of the specimen can be seen in figure 7.5. The scale has been truncated in figure 7.5b. It can be seen that towards the right of the crack where the material is relatively stationary, the residual forces are comparatively smaller than in the material to the left of the crack. Similar observations can be seen in figure 7.6, where the residual forces are computed similarly for the case of  $\lambda_y = 2.5$ . It shall be noted that higher residuals may also be observed in the material behind the tip even in the case of  $\lambda_y = 1.7$ , where the crack speed is subsonic. This is a consequence of the residual strains in the material after the crack passed through (see figure 6.6).

It can be seen from figure 6.6, where the vertical component of deformation gradient is presented for two experiments, that the material behind the crack tip does not completely relax to zero strain level even after the crack tip has passed and the material is broken. This, along with a hyperelastic model, will result in non-zero stresses in this region since in a hyperelastic model, a nonzero strain will imply a non zero stress. This contributes to the observed residual forces in the region behind the tip. Also, the presence of crack tip in the material will result in strain concentration in the vicinity of the tip. Hence, the material stiffness and hence the wave speeds are higher in this region when compared to the bulk. This implies that the equations of motion remain their ellipticity in the region near the tip, but the ellipticity is lost in the far field region (Guo et al., 2003). Hence, a shock-front-like feature along which the field variables like velocity and strain exhibit discontinuities is expected. But since the fields observed in the experiments are continuous, this contributes to the residual forces as well. In short, the residual forces presented are a combination of contributions from non-zero residual strains in the region behind the tip and loss of ellipticity in the bulk away from the tip.

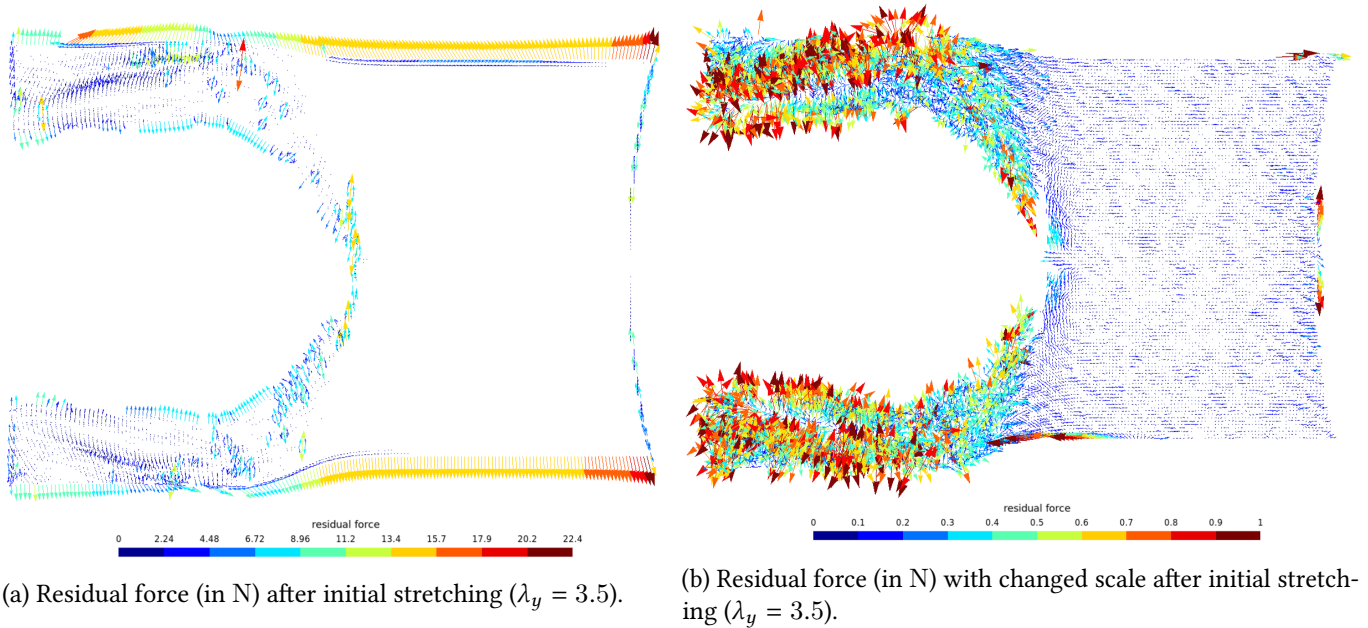


Figure 7.5: Residual nodal forces plotted on deformed configuration after initial stretching for  $\lambda_y = 3.5$ .

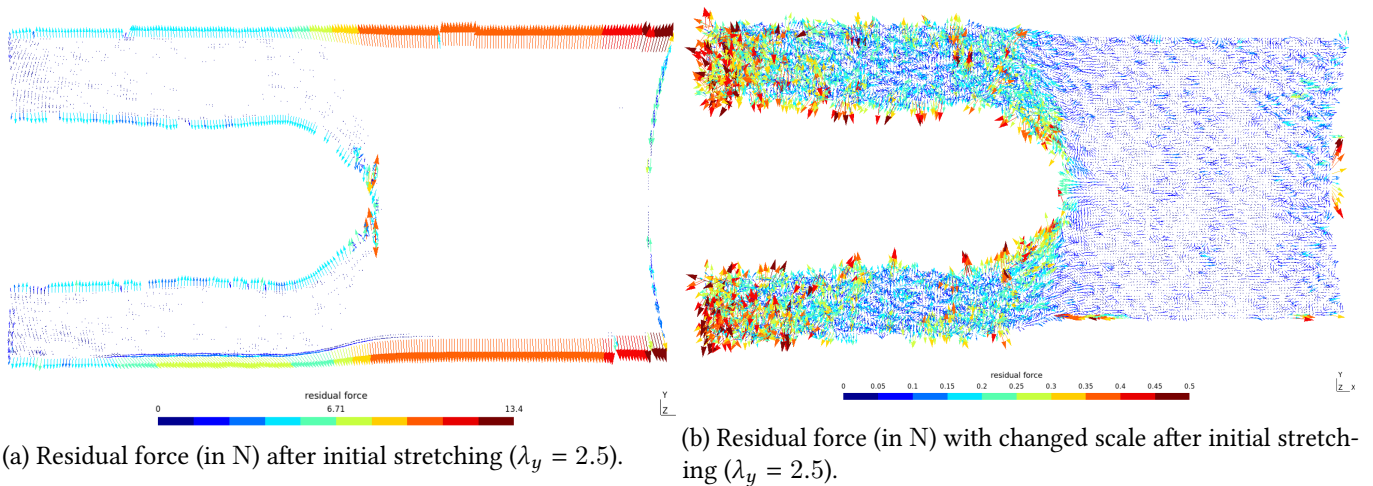


Figure 7.6: Residual nodal forces plotted on deformed configuration after initial stretching for  $\lambda_y = 2.5$ .

## 7.2 USING THE CRACKS SPEED AS AN INPUT

In the analysis performed so far, the bulk material is assumed to be hyperelastic with an upturn in the stress strain response. The residual forces computed in this case contains a combined contribution of the residuals due to the strains behind the tip and due to the loss of ellipticity. To gain a better understanding on the two hypotheses, another approach will be presented in this section. The effect of including viscoelastic effects in the bulk will be examined as well (Kamasudram et al., 2021).

### 7.2.1 Methodology

The analysis methodology is as follows. Displacement fields are available from the experiments throughout the duration of the experiment. The intent is to use these fields to implicitly impose the crack speeds on the geometry and study the response of the bulk material by assuming different constitutive behaviors. The geometry of

the specimen and the FE model used for this purpose can be seen in the figure 7.7. The crack propagation path in the experiments is indicated by a dashed red line in the figure (in the undeformed configuration). Extracting the displacement fields from the experiments along this line and using them as (time varying) displacement boundary conditions in the FE model is equivalent to imposing the crack speed in the FE model. However, the DIC technique does not provide the displacement fields along the boundary. Hence, the extraction line is moved to just (about 1.5 mm) above the crack path. The new data extraction region can be seen as a green line in figure 7.7. The top part of the specimen is constrained from moving horizontally but pulled vertically till the target stretch level is reached. Once the target stretch level is reached, the displacement is held constant on the top face.

At this point of time, it shall be noted that the crack propagation has not been explicitly modeled. The boundary conditions imposed on the model are similar to when the crack passes through the material (Kamasamudram et al., 2021). The same analysis can be made by using a cohesive zone model where the damage profile is moved through the material. This approach, however, requires an additional assumption to be made regarding the behavior of the failing material. The approach discussed above bypasses the need to make a constitutive assumption regarding the behavior of the failing material.

The integration of the momentum equation in time has been performed using HHT- $\alpha$  time integration scheme (Hilber, Hughes, & Taylor, 1977). The simulations performed using value of 0 for  $\alpha$  did not result in convergence. Hence, a value of  $-0.33$  has been used. This value of  $\alpha$  results in maximum numerical dissipation.

### 7.2.2 Simulations

Simulations have been performed using Finite Elements by the methodology prescribed above. Two cases have been examined. One for  $\lambda_y = 1.7$ , where the crack speed is about  $17\text{m s}^{-1}$  and other for  $\lambda_y = 3.5$  where the crack speed is about  $56\text{m s}^{-1}$ . In the former case, the crack speed lies in subsonic regime while in the latter case, it is Transonic.

#### *With hyperelastic bulk*

The polynomial hyperelastic model described and calibrated earlier has been used. As already mentioned, hyperelastic stiffening was deemed to be one of the reasons for observing Transonic cracks (M. Buehler et al., 2003). The velocity profile obtained from the simulation for the case of  $\lambda_y = 1.7$  can be seen in figure 7.8 (to be compared with figure 6.3a). A good agreement can be seen between both the cases.

The velocity profile obtained from the simulation for the case of  $\lambda_y = 3.5$  can be seen in figure 7.9 (to be compared with figure 6.3b). A sharp rise in the particle speeds can be seen along a front, which corresponds to the existence of a Mach front.

To obtain a better comparison with the experiments for the case of  $\lambda_y = 3.5$ ,

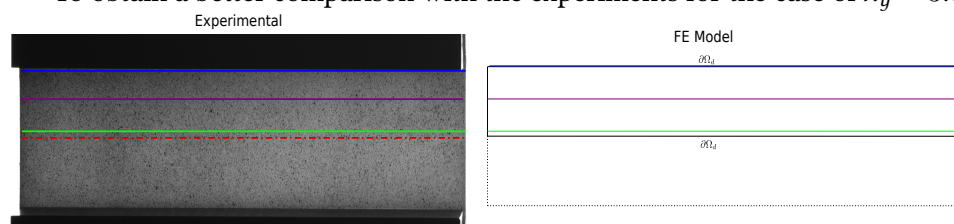


Figure 7.7: Data extraction from experiments as input to FE model.

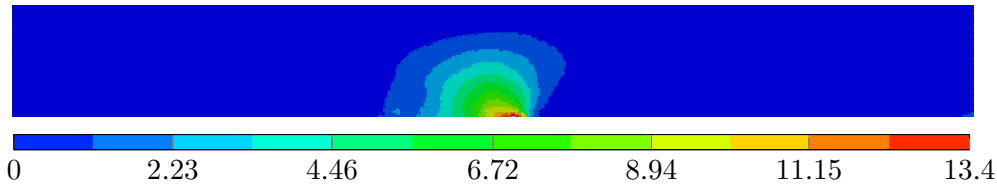


Figure 7.8: Particle velocity magnitude in  $\text{m s}^{-1}$  for  $\lambda = 1.7$  plotted on undeformed configuration.

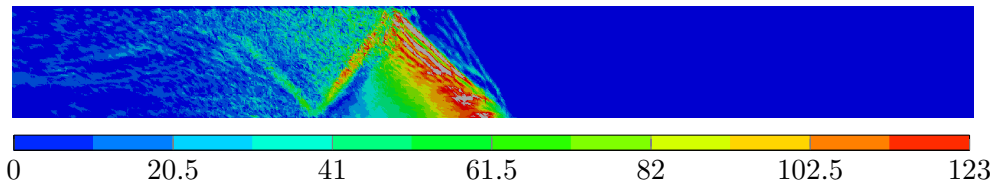


Figure 7.9: Particle velocity magnitude in  $\text{m s}^{-1}$  for  $\lambda = 3.5$  plotted on undeformed configuration.

the variation of velocity magnitude along a line about 5 mm above the crack path has been plotted in figure 7.10. Corresponding to what has been observed in figure 7.9, a sharp rise in particle speeds can be seen just behind the tip corresponding to the Mach front. The variation of particle speeds from the experiment can also be seen. There is a significant difference between both the observations. Also, oscillations in particle speeds can be seen behind the mach front which is typical of the FE simulations containing a jump.

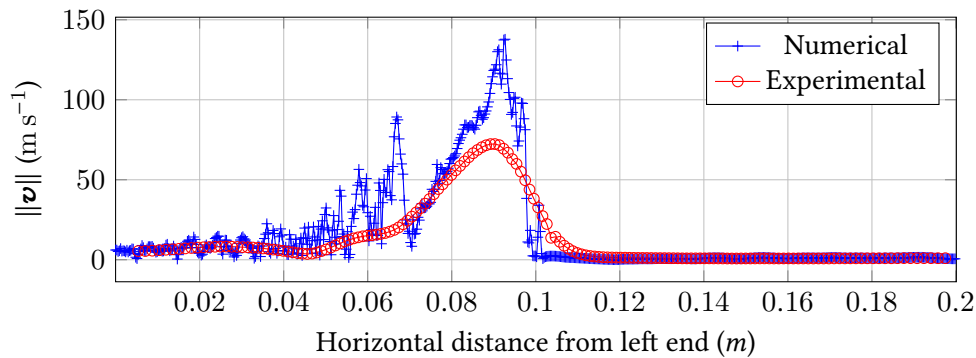


Figure 7.10: particle velocity magnitude in  $\text{m s}^{-1}$  for  $\lambda = 3.5$  plotted on undeformed configuration.

The horizontal displacements in both the cases can be seen in figures 7.11 and 7.12 (to be compared with figures 6.1 and 6.2 respectively). Similar to what has been seen for velocity profiles, a difference can be seen in the horizontal displacements between simulation and experiment for the case of  $\lambda_y = 3.5$ .

The results obtained are coherent with what has already been observed in the literature (Guo et al., 2003; M. Buehler et al., 2003). In both the cited studies, where the propagation of a transonic crack in a material with an upturn in stress strain response is studied, the crack was observed to be accompanied by *Mach fronts* along which the velocity and strain fields exhibit jumps. However, as already shown earlier, the fields obtained from the experiments do not exhibit such jumps. Hence, it can be concluded that at least for the current material, hyperelastic stiffening is not sufficient for the cracks to enter the transonic regime.

### With viscoelastic bulk

Since it has been shown that the upturn in the stress strain response is insufficient to reproduce the displacement and velocity fields in the bulk material, the simulations above will be rerun with viscoelastic bulk. A Finite Linear Viscoelastic (FLV)

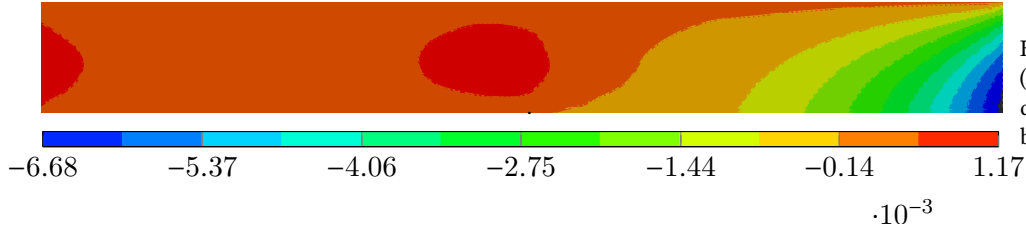


Figure 7.11: Horizontal displacement (in m) for  $\lambda = 1.7$  plotted on undeformed configuration (hyperelastic bulk).

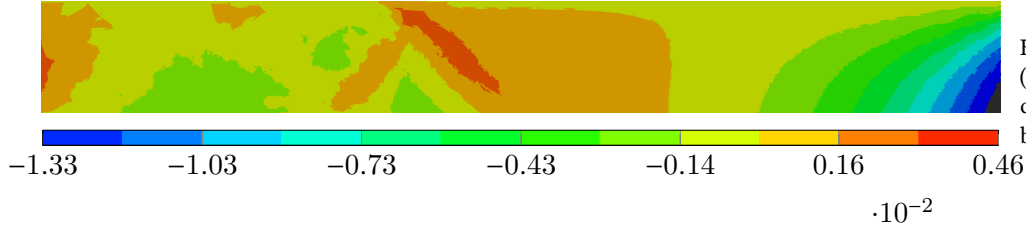


Figure 7.12: Horizontal displacement (in m) for  $\lambda = 3.5$  plotted on undeformed configuration (hyperelastic bulk).

model (Simo, 1987) will be used for this purpose. Later on, the simulations will be performed again by using a Finite Viscoelastic (FV) model (Reese & Govindjee, 1998; Bergström & Boyce, 1998; Dal & Kaliske, 2009) in the bulk.

In FLV model, the stresses can be expressed as a sum of a long term hyperelastic part and a viscous over-stress. The total stress in this case is

$$\mathbf{S} = -Jp\mathbf{C}^{-1} + J^{-2/3}\text{DEV}_t\left\{\mathbf{H}\right\}, \quad (7.15)$$

$$\mathbf{H} := \int_0^t g(t-s)\frac{\partial}{\partial s}\left[\text{DEV}_s\left\{2\frac{\partial\psi^0}{\partial\mathbf{C}}(s)\right\}\right] ds, \quad (7.16)$$

$$\text{DEV}_\alpha\left\{\bullet\right\} := \bullet - \frac{1}{3}[\bullet : \mathbf{C}_\alpha]\mathbf{C}_\alpha^{-1}, \quad (7.17)$$

$$g(s) = g_\infty + \sum_{i=1}^N g_i \exp(-s/\tau_i). \quad (7.18)$$

It shall be noted that the  $\text{DEV}_t$  in equation 7.15 shall be evaluated using the quantities at the current time, while the  $\text{DEV}_s$  in equation 7.16 shall be evaluated using the quantities at time  $s$ . In the equation 7.18,  $g_\infty$  and  $g_i$ s are the ratio of the modulus of the hyperelastic and viscous arms to the glassy modulus respectively.  $\psi^0$  is the strain energy corresponding to the instantaneous behavior of the material. Under small strain loading, the above constitutive model reduces to the linear viscoelastic model. In such a scenario, the model can be seen to represent the material by a spring that is in parallel to the Maxwell elements. An extension of such an interpretation of this model to finite strains is not possible.  $p$  in the equation is Lagrange multiplier that enforces incompressibility. In plane stress scenario,  $p$  can be found by enforcing that the third component of stress,  $S_{33}$  is zero. See Appendix A.

The model is initially calibrated by using the DMA tests performed on the material in Corre, 2018. When the simulations in the previous section are performed with that model parameters, the *Mach fronts* appearing in figure 7.9 disappear. However, the displacement and velocity fields were observed to be over-predicted. Hence, the model parameters were further *adjusted* to bring the results closer to the experiments. The adjusted model parameters can be seen in table 7.2.

The velocity field predicted by the FLV model for the case of  $\lambda_y = 3.5$ , where the crack speed is transonic can be seen in figure 7.13 (to be compared with figures

Table 7.2: Viscoelastic model parameters

Branch(i)	1	2	3	4	5	6	7	8	9	10
$g_i$	0.7312	0.02	0.02	0.2	0.01	0.005	0.0014	0.0011	0.0012	0.0005
$\tau_i$ (s)	1E-10	1E-9	1E-8	1E-7	1E-6	1E-5	1E-4	1E-3	1E-2	1E-1

7.9 and 6.3b).

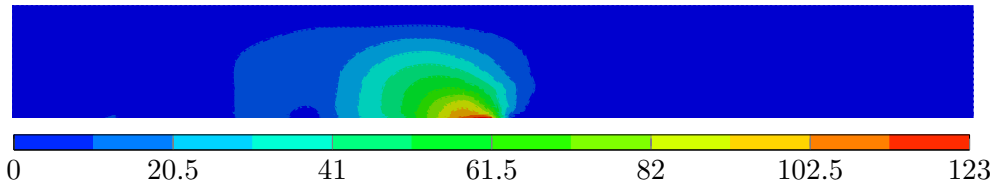


Figure 7.13: Particle velocity magnitude in  $\text{m s}^{-1}$  for  $\lambda = 3.5$  plotted on undeformed configuration (viscoelastic bulk).

The variation of particle speeds at about 5 mm above the crack path can be seen in figure 7.14. It can be seen that the velocity distribution obtained with a viscoelastic bulk more closely matches the experimental results than with a hyperelastic bulk. The displacement fields obtained from the FE simulations can be

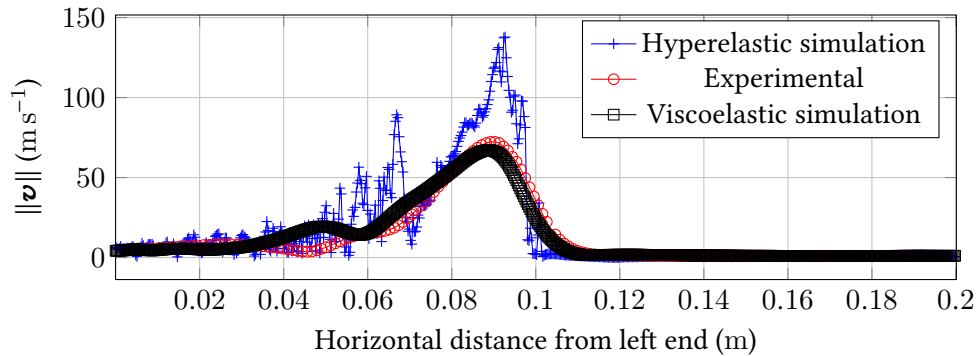


Figure 7.14: Velocity magnitude in  $\text{m s}^{-1}$  for  $\lambda = 3.5$  plotted on undeformed configuration.

seen in figure 7.15 (to be compared with figures 7.12 and 6.2). The results from FE simulations with a viscoelastic bulk can be seen to be similar to the experiments. The particle velocity profiles plotted on the deformed configuration can be seen

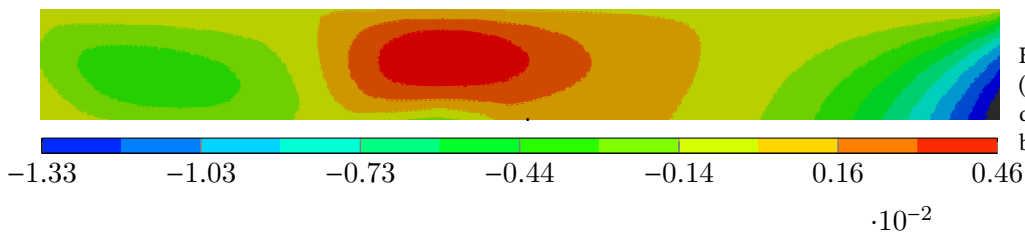


Figure 7.15: Horizontal displacement (in m) for  $\lambda = 3.5$  plotted on undeformed configuration (viscoelastic bulk).

in the figure 7.16. The closeness between the experiments and the FE simulations with viscoelastic model can be noticed.

Once the crack passes through the material, the faces behind the crack tip are (ideally) traction free. Since the displacements from the experiments are used as an input in the FE analysis, it is expected that the tractions predicted by the model along the crack faces will remain close to zero as well. The tractions resulting from hyperelastic and viscoelastic bulk can be seen in the figure 7.17.

It can be seen that in the hyperelastic case, the stresses remain far from zero for a significant region behind the tip whereas in the viscoelastic case, the stresses

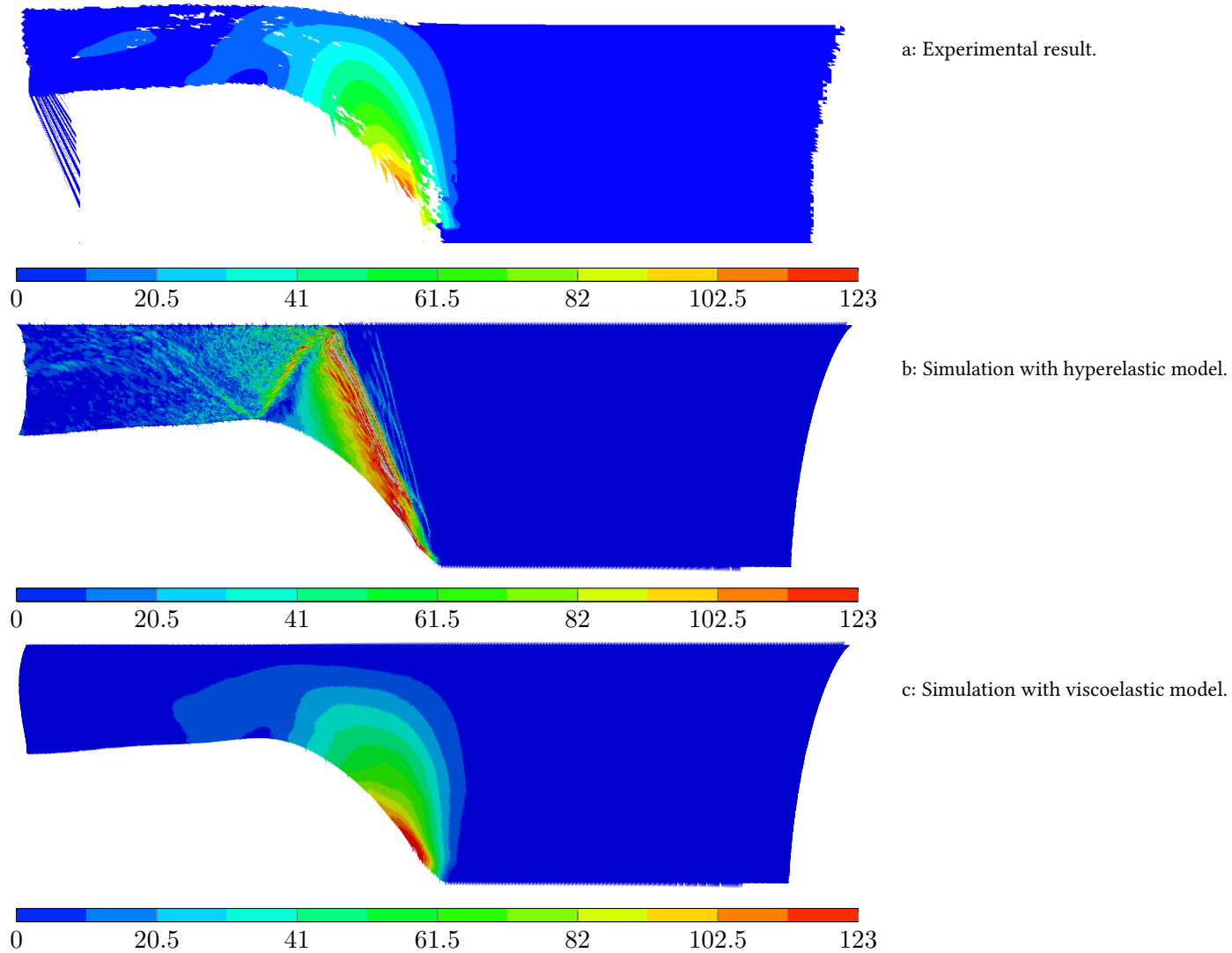


Figure 7.16: Particle velocity magnitude ( $\text{m s}^{-1}$ ) for  $\lambda_y = 3.5$  plotted on deformed configuration.

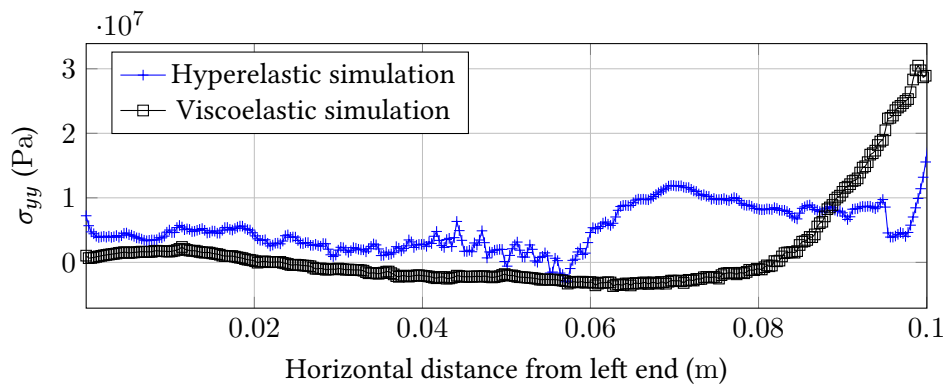


Figure 7.17: Cauchy stress ( $\sigma_{yy}$ ) in Pa for  $\lambda = 3.5$  plotted on undeformed configuration.

drop to values close to zero and remain so all along behind the crack face.

Since the viscoelastic model is ‘calibrated’ using the experimental data for the case of  $\lambda_y = 3.5$ , it has been applied to the other experimental case ( $\lambda_y = 2.5$ ) to verify its validity. The variation of particle speeds about 5 mm above the crack path can be seen in figure 7.18. When compared with figure 7.14, a sharp rise in the particle speeds cannot be seen for the hyperelastic case. A smooth variation to the maximum value can be seen. However, the velocity variation observed in the

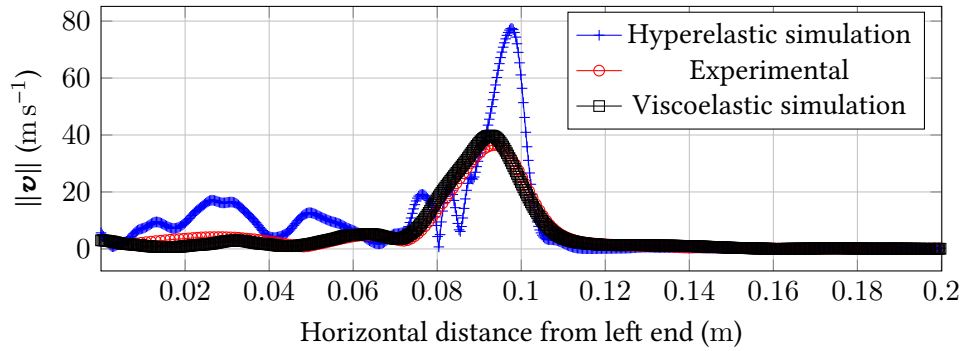


Figure 7.18: Velocity magnitude in  $\text{m s}^{-1}$  for  $\lambda = 2.5$  plotted on undeformed configuration.

experiments is closer to the viscoelastic case than the hyperelastic case. Similarly, the variation of stress behind the tip can be seen figure 7.19.

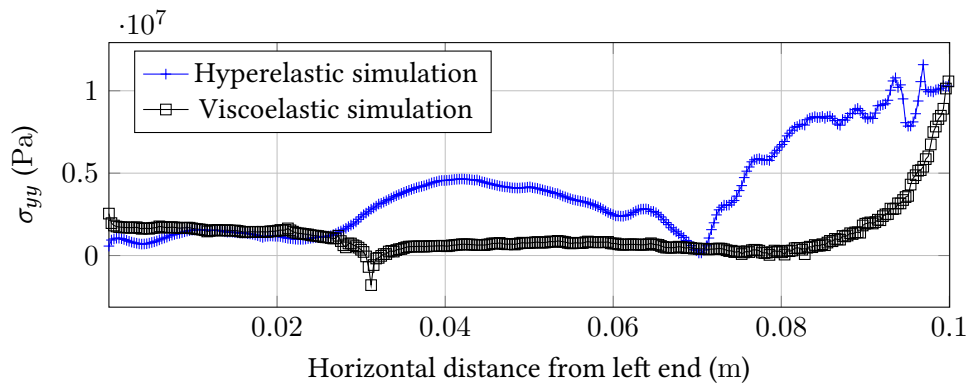


Figure 7.19: Cauchy stress ( $\sigma_{yy}$ ) in Pa for  $\lambda = 2.5$  plotted on undeformed configuration.

It can be clearly seen that as in the case of  $\lambda_y = 3.5$ , the viscoelastic model predicts smaller stresses than the hyperelastic case. Hence, it can be concluded that the viscoelastic model ‘calibrated’ using the experiments of  $\lambda_y = 3.5$  is able to predict the results of the  $\lambda_y = 2.5$  with a good accuracy.

### ***Sensitivity of results with respect to the data extraction line***

In the analyses performed thus far, data are extracted from the experiments at about 1.5 mm above the crack path. Here, it will be determined if the results of the FE analysis obtained is sensitive to the position of the location along which the data are extracted from the experiments. For this purpose, another set of analyses have been performed where the data extraction from the experiments is done at about the midway (about 10 mm above the crack path) of the half of the specimen. This has been done for  $\lambda_y = 3.5$ . The results can be seen in figures 7.20 and 7.21.

In the results for horizontal displacements, a distinct kidney bean shaped profile can be observed in the experimental results which can also be seen in the results from simulation with a viscoelastic bulk. Simulation with hyperelastic bulk does not exhibit this feature. Similarly, the velocity profile obtained with a viscoelastic bulk can be seen to be closer to the experiments than with a hyperelastic bulk. This demonstrates the robustness of the viscoelastic model as well as the simulation methodology presented.

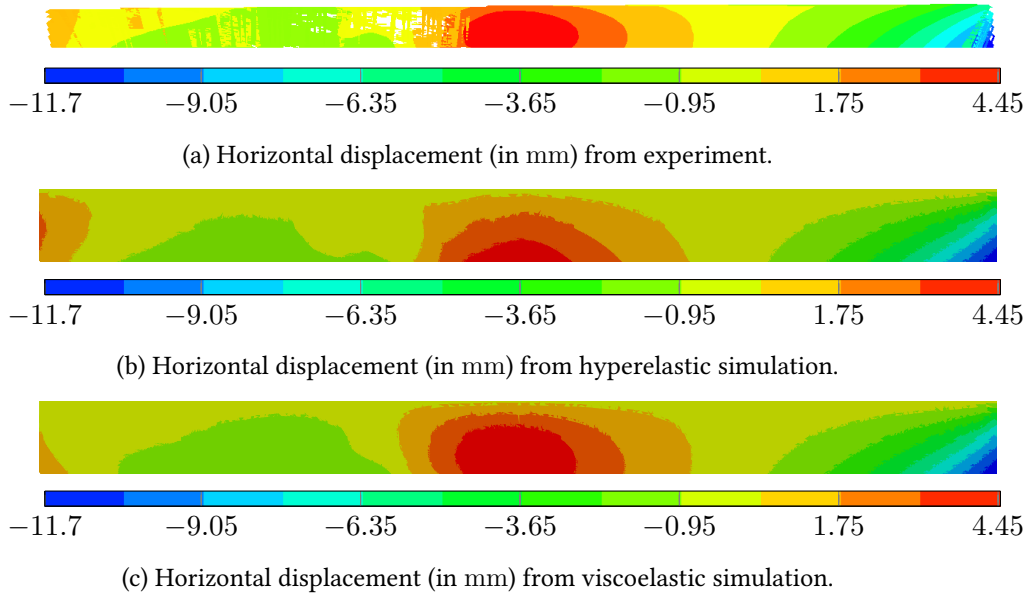


Figure 7.20: Horizontal displacement fields for a different data extraction location,  $\lambda_y = 3.5$ .

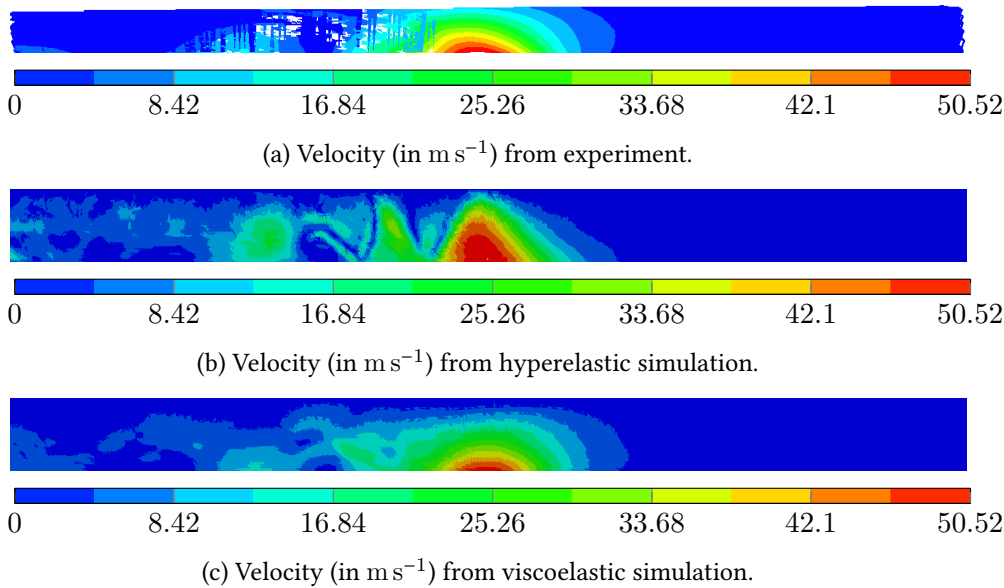


Figure 7.21: Velocity magnitude fields for a different data extraction location,  $\lambda_y = 3.5$ .

### 7.3 DISCUSSIONS

The previous sections contain the results from the experiments together with the results from FE simulations with hyperelastic and viscoelastic models. Experiments indicate that a ‘shock front’ was not observed even after the crack speeds exceed the elastic shear wave speed - a jump has not been observed either in velocity or strain fields which would have been the case if a shock front was present.

The crack speeds have been observed to exceed the shear wave speed in other studies in the literature like Petersan et al., 2004; Chen et al., 2011 and Mai et al., 2020. The material tested in Chen et al., 2011 is Latex rubber and the tests were performed at 85 °C to prevent strain crystallization. SBR was tested in Mai et al., 2020. The current study is performed on Polyurethane. The strain fields reported in

Mai et al., 2020 do not exhibit any jumps as is the case in the current study even for crack speeds in Transonic regime. Chen et al., 2011 does not report any such shock fronts as well, but instead report that the crack faces in this regime are wedge shaped (which were noted to resemble a shock front in Petersan et al., 2004).

An interesting comparison can be made regarding the ratios of crack speed to the shear wave speed at a prestretch level of 3.5 in different studies. In Mai et al., 2020, the speed ratio can be seen to be 1.84, while in Chen et al., 2011, the ratio is smaller than 1.25. In the current study, the ratio is about 1.38. This indicates perhaps an obvious conclusion that the material properties (mainly viscoelasticity) determine the extent to which the crack speed can exceed the shear wave speed.

The hyperelastic model calibrated using the uniaxial and pure shear cases is used to perform FE simulations with the displacements extracted from the experiments in Corre et al., 2020. It shall be noted that the hyperelastic model does not exactly follow the Uniaxial stress-strain curve. The calibrated model, however, is seen to exhibit an upturn in the stress-strain curve which is usually deemed to be one of the reasons for crack speeds to go into Transonic regime (Gent & Marteny, 1982a; Stevenson & Thomas, 1979; M. Buehler et al., 2003). The FE result using this model, however, is seen to produce ‘jumps’ in both the velocity and strain fields for the cases when the crack speeds are Transonic - a result not seen in the experiments.

Including viscoelasticity is seen to bring the results closer to the experiments. The strain and velocity fields no longer exhibit the discontinuities that were observed in the hyperelastic case. The maximum horizontal displacements and the velocity magnitudes have been observed to be within 10 % of the experiment results.

The crack faces behind the tip, being a free edge, are ideally traction-free. As presented in figure 6.6, the residual strains behind the tip are non-zero. The computation of tractions from strains involves making a constitutive assumption about the material. Using a hyperelastic model in the simulations results in non-zero stresses along the edge as a consequence of the non-zero strain (despite it being a free edge in the experiments). See figure 7.17, where the  $yy$  component of Cauchy stress is plotted along the data extraction location (1.5 mm above the crack path). However, using a viscoelastic model with relaxation times that are comparable to the duration of the experiment, the stresses along the edge behind the tip quickly drop to small values within 15 % of the far-field stresses (and smaller than in the hyperelastic case). Refining the model further can perhaps bring even those stresses to zero.

Hence, at least for the material in the current study, the cracks can go Transonic as a result of the viscoelastic ‘stiffening’ of the material. A suggestion of this kind can be found in Stevenson and Thomas, 1979. However, no evidence has been presented in that study as to whether the Transonic cracks are a result of Viscoelastic stiffening or hyperelastic stiffening. A similar comment has been made in Marder, 2006. However, in that work, a Kelvin type model has been assumed for the elastomer where the wave speeds increase unboundedly with the frequency. Hyperelastic stiffening has been deemed to be not necessary, but its sufficiency has not been discussed. In studies where this sufficiency has been studied M. Buehler et al., 2003, ‘Mach cones’ corresponding to shear waves were reported that trail the crack tip (Figure 4 of the reference).

The notion of limiting speed for a crack comes from the inclusion of inertial effects in the study of the problem (Freund, 1990). The LEFM establishes the limiting speed as the Rayleigh wave speed in mode-I, while in mode-III, it is the Shear

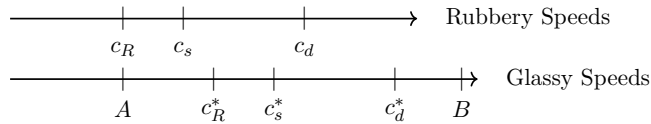


Figure 7.22: Rubbery and glassy wave speeds in linear viscoelasticity. R stands for Rayleigh, s for shear, d for dilatational. A and B indicate the possible range of the wave speeds that depend on the glassy to rubbery modulus ratio.

wave speed based on the elastic properties of the material. In studies where the inertial effects are included together with Viscous effects (Graham & Walton, 1995; Atkinson & Popelar, 1979; Willis, 1967), the limiting speed is seen to depend on the *glassy* modulus of the material rather than on the *rubbery* modulus (Figure 7.22). Hence, the crack is allowed to exceed the rubbery shear wave speed. Such a result can also be observed in Geubelle, Danyluk, and Hilton, 1998, where spectral methods are used to investigate the problem of viscoelastodynamic mode-III crack. Using a rate independent cohesive zone type model, an analysis has been made on the effect of relaxation times on crack speeds. From the Figure 11 of the reference, it can clearly be seen that the crack speed exceeds the *rubbery* shear wave speed ( $c_s$ ), but remains smaller than the *glassy* shear wave speed ( $c_s^*$ ). However, no specific comments have been made in regards to the presence or absence of shock fronts in those references.

In Fisher and Gurtin, 1965, the propagation of waves of order  $N$  in viscoelastic media has been studied. Waves of order  $N$  have the solution,  $\mathbf{u}$ , which is  $N - 1$  times continuously differentiable and exhibit discontinuities in the  $N^{th}$  derivative along a hypersurface. It has been determined in that study that such waves, should they exist, travel with a speed that is derived based on the glassy modulus of the material rather than the rubbery modulus. Shock fronts, by definition, are waves of order 1 and hence travel with that speed as well. Hence, it might be possible that shock fronts can be observed in viscoelastic material only when the crack speed exceeds even the glassy shear wave speed of the material. In short, a weak discontinuity, should it exist, would be made of high frequency waves at the sharp front. As a consequence of viscoelasticity, this region behaves with a high modulus which in turn roughly raises the shear wave speeds to a value that is (equal to or) greater than the crack speed. This, in turn, prevents a shock wave from developing.

Perhaps, the cracks whose speeds exceed  $c_s$  while still remaining below  $c_s^*$  should be called *r-Transonic* (*r* stands for *rubbery*) to distinguish them from cracks that travel faster than  $c_s^*$ . One such instance may be found in Gori et al., 2018, where a mode-II crack propagating in a PMMA specimen along a weak plane has been studied experimentally. It was observed that because of the viscoelastic behavior of the material, the crack speed exceeds  $c_s^*$  (hence  $c_s$ ) and  $c_d$  as well. Based on the inclination of the ‘mach fronts’ observed, the shear wave speed was computed and was seen to be in good agreement with the shear wave speed computed based on the modulus corresponding to the strain rates in that region.

As already mentioned, in the current chapter, the crack speeds are implicitly imposed on the material by using the displacement evolution from the experiments. In the next chapter, a cohesive zone model will be used to predict the crack speeds using the viscoelastic model calibrated in this chapter to represent the bulk material. The crack speeds thus obtained will be compared with those from the experiments.

**SUMMARY**

In this chapter, the hypotheses of hyperelastic vs viscoelastic stiffening for the crack speeds to enter the transonic regime were tested. The momentum balance check performed by using a hyperelastic stiffening showed the presence of large residual forces in the region behind the tip. This is expected since the material behind the tip was observed to not completely relax. The residual strains together with a hyperelastic model results in residual stresses as can be observed. However, the residual obtained from the analysis can be regarded as the combined effect of the residual strains behind the tip and the 'loss of ellipticity' in the regions far from the tip. Hence, some more analysis were performed where the crack speed is used as an input in the model. The displacement field data from the experiments obtained using DIC technique were used as boundary conditions in the FE model. This way, the crack speed and hence the crack propagation are implicitly modeled. Results from the FE analysis indicate that the hyperelastic model with an upturn in the stress-strain response resulted in a *Mach front* across which the particle speeds and strains exhibited 'jumps'. Results with a viscoelastic bulk closely match the experimental observations. The viscoelastic model was refined further to match the results for one experimental case. The same model parameters when used to simulate another load case predicted displacement and velocity fields close to the experiment demonstrating the robustness of the model and the 'calibration technique'.

# COHESIVE ZONE MODEL

# 8

---

In this chapter, a rate dependent cohesive zone model will be used to predict the crack speeds at different applied stretches. The Finite Linear Viscoelastic model will be used for the bulk material. The simulations will be performed at different geometries and different stretches to determine their effect on the crack speed.

---

## CONTENTS

8.1	Bulk material . . . . .	85
8.2	Rate independent cohesive zone model . . . . .	85
8.2.1	Specimen geometry and loading . . . . .	86
8.2.2	Observed crack speeds with different cohesive zone parameters . . . . .	86
8.3	Viscous Cohesive zone model . . . . .	88
8.4	Finite Element Implementation . . . . .	90
8.4.1	Computation of residual . . . . .	92
8.4.2	Computation of tangent . . . . .	92
8.4.3	Implementation into user subroutine . . . . .	93
8.5	Crack speeds prediction and traction - separation relations . . . . .	94
8.6	Discussions . . . . .	98

In Finite Element simulations, Cohesive Zone Models (CZM) are used extensively to predict the crack growth in scenarios where the crack path is known in advance. This might be in the case of a crack growth in mode-II along a weak interface Needleman, 1999 or delamination Corigliano and Ricci, 2001 or for peel testing Rahulkumar, Jagota, Bennison, and Saigal, 2000; Geißler, Kaliske, Nase, and Grellmann, 2007. In other scenarios, the cohesive elements are inserted between all the elements of the FE model Miller et al., 1999; X. P. Xu and Needleman, 1994 to predict the crack path as well. In the latter scenario, some mesh dependency of the crack path was observed. The CZM technique involves specifying the behavior of the material undergoing failure. The output of the simulation is the crack speed or in some cases, the time to failure Schapery, 1975c. CZM have been successfully used in the simulation of brittle fracture in the references cited earlier, in the case of plastic materials in Hutchinson and Tvergaard, 1992 and in the case of viscoelastic fracture in W. Knauss and Mueller, 1971; Schapery, 1975b; Elmukashfi and Kroon, 2014.

Failure process in brittle elastic solids are usually rate independent - the fracture energy per unit area created remains constant. The fracture energy increases with crack speed as a consequence of an increase in the area of crack surface created due to micro branches (Sharon et al., 1996). A correlation was found between the area of the crack surface and the crack speed once the crack speed exceeds about 30 % of  $c_R$ . It was attributed to the development of micro branches that attempt to propagate along with the main branch, but are arrested. When the fracture surfaces of elastomers are examined, the opposite pattern is observed. The crack surfaces tend to be rougher at smaller crack speeds and get smoother with an increase in crack speed. Crack surfaces of Polyurethane elastomer analyzed using SEM can be found in the earlier chapter confirm this observation. The variation in the surface roughness is usually attributed to cavitation. At higher cracks speeds, the material in the vicinity of the crack tip stiffens as a consequence of viscoelastic effects and hence the cavitation is suppressed. To the author's knowledge, no conclusive study however exists that confirms this effect.

During the fracture of an elastomer, the total amount of energy dissipated is usually divided into dissipation in bulk (as a consequence of viscoelastic effects) and in the fracture processes (in the creation of new surfaces). The fracture processes involve formation and coalescence of micro voids and chain scission. It is possible that the fracture processes themselves are rate dependent as a consequence of rate dependent effects during fracture. Analyzing the peel tests of polymers, it was determined in Rahulkumar et al., 2000; Jagota, Bennison, and Smith, 2000 that the fracture processes are indeed rate dependent. A rate dependent cohesive model based on that of W. G. Knauss and Losi, 1993 has been used in those studies. Hereditary integral type model together with damage parameter has been used. Other studies that perform this type of analysis are Elmukashfi and Kroon, 2012, 2014. In those studies, it was found that the cohesive zone parameters are to be modified between different experiments to match the observed crack speeds with the experiment. The rate dependent traction separation relation used in those works are based on a dash pot in parallel with a spring as opposed to the earlier mentioned hereditary integral type.

Theoretical and experimental analysis of crack growth in viscoelastic materials have been performed by several researchers. A exhaustive review of such studies can be found in W. Knauss, 2015. Knauss broadly classifies the studies into the ones that involve global energy balance in the structure (R. S. Rivlin & Thomas, 1997) and the ones that involve examining the crack tip fields and establishing criterion

based on a cohesive zone like model (W. Knauss & Mueller, 1971; W. Knauss, 1970; Schapery, 1975b, 1975a, 1975c) at the tip. In fact, there have been some discussions, such as in Kostrov and Nikitin, 1970; James R. Rice, 1979, regarding the need to eliminate the singularity at the crack tip in viscoelastic fracture. The discussion goes as follows - a sharp crack model predicts singular stresses, strains and strain rates at the crack tip regardless of the speed of the crack. This would imply that the material near the tip behaves in a glassy fashion (as a result of the singular strain rates at the tip) even at low crack speeds. Also, using the failure criterion of Knauss and Schapery (Equation 48 of W. Knauss, 2015), if the length of failure zone is taken to tend to zero, it can be shown that only the glassy modulus of the material enters the equation (page 445 of Freund, 1990) and the overall viscoelastic properties do not seem to influence the crack speed. There have, of course, been some works that disagree with this analysis, for example Christensen, 1979, that suggests that the discrepancy that arose is a consequence of the assumption that material behaves in a glassy fashion even far away from the tip. With a sharp crack model, even though the material near the tip behaves in a glassy fashion, a viscoelastic zone surrounds and follows the crack tip which controls the energy input and hence the speed of the crack. Other such instances of sharp crack model are B. N. Persson and Brener, 2005; B. N. J. Persson et al., 2005, where the dissipation of the material has been explicitly taken into account. Hence, the whole spectrum of viscoelastic properties are seen to affect the crack propagation behaviour. A point to be noted is that the cited references so far do not take the inertial effects into consideration.

In dynamic fracture, LEFM bounds the speeds of the crack from below by Rayleigh Wave speed ( $c_R$ ) for modes I and II, shear wave speed  $c_S$  for mode-III (Freund, 1990). The theory is then extended to include the Transonic cracks observed during the laboratory experiments of mode-II cracks and during earthquakes (Rosakis, 2002). Some experiments performed on literature (Petersan et al., 2004; Chen et al., 2011; Corre et al., 2020) revealed the presence of Transonic cracks in mode-I as well in elastomers. By revisiting the experiments performed on Polyurethane elastomer in Corre et al., 2020, the current authors show that the Transonic cracks are a consequence of the viscoelastic stiffening of the material in Kamasamudram et al., 2021.

Presently, using Finite Element Method together with the Cohesive Zone type model (Barenblatt, Salganik, & Cherepanov, 1962) to model the propagation of crack, an attempt will be made to reproduce the experimental results and understand the nature of fracture processes and dissipation mechanisms that accompany a moving crack. Similar studies have been performed by Kroon, 2014; Elmukashfi and Kroon, 2012, 2014; Yin and Kaliske, 2019; Loew, Peters, and Beex, 2019 on fracture of elastomers using a Cohesive Zone or a Phase field method. However, the emphasis of those studies are not to examine the transonic cracks or to investigate the effect of geometry on crack dynamics in that regime. Infact, except for the analysis in Elmukashfi and Kroon, 2012, 2014, the crack speeds in the other studies are significantly smaller when compared to the elastic shear wave speed and hence, the inertial effects do not play a significant role. The studies of Elmukashfi and Kroon, 2012, 2014 use a rate dependent cohesive model to analyze the dynamic fracture of elastomers. But the parameters in the traction separation relations used in those studies are modified as the crack speed changes to match the experimentally observed crack speeds. In this work, an attempt will be made to reproduce the experimentally observed crack speeds using traction separation relation that relies on a set of parameters that do not change with crack speed. This will be done using the cohesive zone model proposed in W. G. Knauss and Losi, 1993.

### 8.1 BULK MATERIAL

The Finite Linear Viscoelastic model that was used in Kamasamudram et al., 2021 and in the earlier chapters has been used in this analysis as well. The hyperelastic part of the material is represented by a Polynomial model with  $N = 3$  as

$$W = \sum_{i+j=1}^N C_{ij}(\bar{I}_1 - 3)^i(\bar{I}_2 - 3)^j, \quad (8.1)$$

where  $\bar{I}_1$  and  $\bar{I}_2$  are the first and second invariants of the deviatoric part of Green strain tensor,  $\bar{C} = J^{-2/3}C$  and  $J$  is the determinant of the deformation gradient.  $C_{ij}$ s are the model parameters. The model calibration has been done in Kamasamudram et al., 2021 and the parameters can be found in the previous chapters. Plane stress conditions are assumed to prevail. As a consequence, the stresses can be completely written in terms of the in-plane components of  $C$ . More details on this can be found in the next chapter (see equation 9.31).

The finite linear viscoelastic model of Simo, 1987 has been used for the bulk. The expression for the stress can be written as

$$S = -JpC^{-1} + J^{-2/3}\text{DEV}_t\{H\}, \quad (7.15)$$

$$H := \int_0^t g(t-s)\frac{\partial}{\partial s}\left[\text{DEV}_s\left\{2\frac{\partial\psi^0}{\partial C}(s)\right\}\right] ds, \quad (7.16)$$

$$\text{DEV}_\alpha\{\bullet\} := \bullet - \frac{1}{3}[\bullet : C_\alpha]C_\alpha^{-1}, \quad (7.17)$$

$$g(s) = g_\infty + \sum_{i=1}^N g_i \exp(-s/\tau_i). \quad (7.18)$$

The plane stress version of the above model can be obtained by obtaining the expression of  $p$  using the condition  $S_{33} = 0$ . The expression of  $p$  when put back in the above equations gives the plane stress version of the constitutive model. This algebra has been performed in the appendix A. The final expression for the stress can be seen to be

$$S_{2d} = \int_{-\infty}^t g(t-s)\frac{\partial}{\partial s}\left[\text{DEV}_s^{2D}\left\{\hat{S}^s\right\}\right] + \frac{C_{33}^t}{3}(C_{2d}^t)^{-1} \int_{-\infty}^t g(t-s)\frac{\partial}{\partial s}\left[\text{tr}(\hat{S}^s C_{2d}^s)(C_{33}^s)^{-1}\right]. \quad (\text{A.27})$$

In the above,  $S_{2d}$  represents the restriction of the stresses to the in-plane components. The above equation can be integrated using the algorithm in Taylor, Pister, and Goudeau, 1970.

### 8.2 RATE INDEPENDENT COHESIVE ZONE MODEL

The experiments performed by Corre et al., 2020 have been analyzed in the previous chapter and in Kamasamudram et al., 2021 to study the importance of viscoelastic effects in the bulk material in transonic regime. The crack speed has been used as an input in the analysis. This chapter aims at predicting the crack speeds by using a viscoelastic model in the bulk and a Cohesive Zone Model to predict the crack growth. Similar attempts were made earlier in Elmukashfi and Kroon, 2012, 2014 where the simulations were performed to match the experiments performed in Gent and Marteny, 1982a. A rate dependent cohesive zone model based on a

Maxwell element was found to be necessary in those studies to be able to match the crack speeds in the experiment. The rate dependent Cohesive Zone was seen to be a consequence of the rate dependence of the failing material. However, in those studies, no particular emphasis was made on Transonic cracks or on their behavior in specimens of different geometries.

A rate independent cohesive model will be initially used here to confirm the observations from the earlier studies. It will be determined if the experimental results can be reproduced with this simple model using the same parameters for all the experiments. A model with initial stiffness and a linear unloading response will be used. The traction can be expressed in this model as

$$\mathbf{t} = (1 - d)\mathbf{K}\Delta, \quad (8.2)$$

where  $d$  is the damage variable,  $\mathbf{K}$  is the stiffness and  $\Delta$  is the separation vector.  $d$  is taken to depend on the current separation in the cohesive zone,  $\Delta := [\mathbf{u}]$ , and is represented in the case of a linear cohesive law as

$$d = \begin{cases} 0, & \text{if } \Delta_{\max} < \Delta_o \\ \frac{\Delta_f(\Delta_{\max} - \Delta_o)}{\Delta_{\max}(\Delta_f - \Delta_o)}, & \text{if } \Delta_{\max} \in [\Delta_o, \Delta_f] \\ 1, & \text{if } \Delta_{\max} > \Delta_f \end{cases} \quad (8.3)$$

where  $\Delta_{\max}(t) = \max_{\tau \in [0, t]} \Delta(\tau)$  is taken as the maximum value of separation over the entire time history to enforce the irreversibility constraint on the damage variable.  $\Delta_o$  and  $\Delta_f$  denote the value of separations at which the damage begins and the material completely fails, respectively. The energy dissipated in the cohesive zone can be found to be  $G = \frac{1}{2}K\Delta_o\Delta_f$ . This cohesive zone model can be seen as a special case of a rate-dependent model, the implementation of which has been described later. Hence, only the results of this model will be presented in this section.

### 8.2.1 Specimen geometry and loading

The specimen that is 40 mm tall and 200 mm long has been analyzed. Plane stress conditions have been assumed to prevail. Cohesive elements have been inserted in the middle all along the length of the specimen. An element size of 50  $\mu\text{m}$  has been used in the cohesive zone. Linear plane stress elements (CPS4) have been used to mesh the bulk region. The degrees of freedom of Cohesive elements are tied to be bulk elements.

The bottom part of the specimen is held fixed while the top is stretched at a speed of 0.3  $\text{mm s}^{-1}$  till the target stretch level is reached. After reaching the stretch level, a seed crack that is about 3 mm long is imposed at the left end of the specimen (by reducing the  $\Delta_o$  for those elements) which then propagates and breaks it into two pieces. The position of the crack tip is then extracted which is then used to compute the crack speed.

### 8.2.2 Observed crack speeds with different cohesive zone parameters

The parameters of the Cohesive model ( $\Delta_o$  and  $\Delta_f$ ) are calibrated to match the crack speed at a stretch level of 3.5. The initial stiffness of cohesive elements,  $\mathbf{K}$  is taken to be  $1 \times 10^7 \text{ MPa m}^{-1}$ . It shall be noted that the crack speed in viscoelastic fracture is affected by not just the cohesive energy but also either the strain at failure or the

fracture initiation stress (specifying one of them together with the fracture energy determines the other). For a given cohesive energy, different initiation stresses will result in different crack speeds. The effect of cohesive parameters such as the strength, cohesive energy and length on steady-state viscoelastic crack growth has been studied in T. D. Nguyen and Govindjee, 2006. A similar study, in the context of peeling has been studied by Rahulkumar et al., 2000. In both these studies the effect of non-dimensional parameters based on the cohesive zone and bulk model has been studied. An analytical investigation has been made by D. B. Xu, Hui, and Kramer, 1992.

A cohesive strength of 27 MPa (or  $\Delta_o = 2.7 \cdot 10^{-6}$ m) and the separation at failure of 2 mm was used for the analysis initially. This corresponds to an energy of 27 kJ/m<sup>2</sup>. This yielded a crack speed of about 58 m s<sup>-1</sup> at a stretch level of 3.5, which is approximately the experimental value (56 m s<sup>-1</sup>). However, the same cohesive parameters gives a crack speed of about  $5 \times 10^{-3}$  m s<sup>-1</sup> at a stretch level of 1.7 while a crack speed of about 17 m s<sup>-1</sup> was observed in the experiments.

Further attempts were made to decrease the cohesive strength and increase the separation at a stretch level of 3.5 to maintain the crack speeds close to the experiment. It was observed that the increase in the cohesive strength had a larger effect on reducing the crack speeds than increasing the failure separation for the same cohesive energy. Hence, when the cohesive strength was reduced to 20 MPa (or  $\Delta_o = 2 \cdot 10^{-6}$ m), it was found that the separation needed to obtain a crack speed comparable to the experiments was 3 mm. The crack speed was about 59 m s<sup>-1</sup>. This, however, did not result in an increase in crack speed at a stretch of 1.7, which was still observed to be about  $6 \times 10^{-3}$  m s<sup>-1</sup>. Hence, the cohesive zone parameters were further modified, this time the cohesive strength to 15 MPa (or  $\Delta_o = 1.5 \cdot 10^{-6}$ m) and critical separation to 5 mm resulting in crack speed at a stretch of 3.5 to be 59.5 m s<sup>-1</sup>. No improvement was observed at a stretch level of 1.7 even at this point. It shall be noted that the cohesive energies varied for different cases as 27 kJ/m<sup>2</sup>, 30 kJ/m<sup>2</sup> and 37.5 kJ/m<sup>2</sup> while the crack speed was maintained in the range  $58 \pm 2$  m s<sup>-1</sup>. The parameter combinations tried can be seen in the table 8.1.

Table 8.1: Crack speeds obtained for various cohesive zone parameter combinations.

$\Delta_0$ (m)	$\Delta_f$ (m)	$G_{\text{coh}}$ (kJ/m <sup>2</sup> )	$\lambda$	$w_0$ (m s <sup>-1</sup> )
$2.7 \times 10^{-7}$	$2 \times 10^{-3}$	27	3.5	58
			1.7	$5 \times 10^{-3}$
$2 \times 10^{-7}$	$3 \times 10^{-3}$	30	3.5	59
			1.7	$6 \times 10^{-3}$
$1.5 \times 10^{-7}$	$5 \times 10^{-3}$	37.5	3.5	59.5
			1.7	$6 \times 10^{-3}$

It can be observed that using the same cohesive parameters across different loading does not result in the desired crack speed variation as observed in the experiments. Hence, rate dependence will be introduced in the subsequent sections to see if the same cohesive zone parameters can be used across different loading to obtain crack speeds closer to the experiments. The need for rate dependence in cohesive model has been arrived at by a similar analysis in Rahulkumar et al., 2000; Elmukashfi and Kroon, 2014 as mentioned earlier.

### 8.3 VISCOUS COHESIVE ZONE MODEL

The rate dependence of the energy dissipated in polymer fracture is attributed to the dissipation in bulk or the failure zone or both. The form of energy dissipated is usually taken as a product of an intrinsic energy ( $G_0$ ) and a term that depends on crack speed,  $G = G_0(1 + f(v, T))$  (Gent, 1996b; B. N. Persson & Brener, 2005). Other forms for this dependence are available like in Schapery, 1975b; W. Knauss, 2015 where the rate dependence factor is obtained from the rheological properties of the material. The total energy in these studies is written as a product of intrinsic energy and a term that depends on the crack speed (instead of the sum mentioned earlier). However, the intrinsic fracture energy or the energy that is dissipated at the tip during the fracture process is taken as a constant.

In the case of failure of adhesively bonded joints, the rate dependence is solely attributed to the rate dependence arising due to the viscoelastic nature of the failing material alone. In such instances, the failure processes are taken into account by rate dependent cohesive zones (Musto & Alfano, 2011; Rahulkumar et al., 2000; Geißler & Kaliske, 2010). In some studies as in T. D. Nguyen and Govindjee, 2006; Rahulkumar et al., 2000, the rate dependence is included in both the bulk as well as in the failure zone. The studies are however, restricted to the crack propagation in thin strips where the interaction of the bulk dissipation with the boundaries of the specimen is studied. In the context of dynamic fracture of elastomers, rate dependence in the cohesive zone is deemed to be necessary in the studies made by Elmukashfi and Kroon, 2012, 2014. In a similar manner presented above, the authors of the cited reference note that using a rate independent cohesive zone is insufficient to predict the crack speeds under all the loading conditions. Rate dependence in the cohesive zone was introduced through a Kelvin-Voigt element. No specific link has been made between the rate dependence property of the cohesive zone and the bulk material. Also, no specific attention was paid to the transonic regime. In the context of phase field modeling of polymer fracture, rate dependence of fracture energy was included in Loew et al., 2019 by the inclusion of damage rate in the damage evolution equation. More studies on polymer fracture using phase field method have been made by Christian Miehe and Schänzel, 2014; Christian Miehe, Schänzel, and Ulmer, 2015. However, the crack speeds in these studies are not high enough for dynamic effects to become important.

The rate dependence in the cohesive zone can be introduced in a number of ways. The cohesive strength can be made rate dependent while keeping the separation constant or the latter can be made rate dependent while keeping the former the same or both of them can be varied with the crack speed. Different criteria are known to result in different crack speeds as a consequence of viscoelastic bulk (W. Knauss, 2015). Some models used to prevent localization problems like delay-damage model (Suffis, Lubrecht, & Combescure, 2003) can also be used to obtain rate dependent cohesive laws. In this study, a strain (crack opening in this case) based criterion will be used to predict damage initiation in the cohesive zone while keeping the failure to separation to be constant. This results in the maximum traction in the cohesive zone to change with the crack speed. As mentioned earlier, increasing the cohesive strength has been observed to result in a larger decrease in the crack speed while a larger variation in separation was found to be needed. The traction can be made a function of separations as well as their rates which is equivalent to introducing a dashpot in parallel with the spring that indicates a Kelvin type model (Geißler & Kaliske, 2010; Elmukashfi & Kroon, 2014). Or a convolution integral type law can be chosen where the traction can be

made to depend on the (entire) separation history like in materials with memory (Rahulkumar et al., 2000; Zreid, Fleischhauer, & Kaliske, 2013). In W. G. Knauss and Losi, 1993, the failure material is modeled by multiplying the stress strain law that is used in the bulk with a degradation function that depends on strain that results in the softening of the material. In the current study, the latter model has been chosen and the kernels in the integrals (resembling W. G. Knauss and Losi, 1993; Rahulkumar et al., 2000) have been chosen to be same as that for the bulk material thereby establishing a link between the cohesive and the bulk properties. As will be seen later, this type of cohesive model is able to predict the crack speeds for the entire range of applied stretches and also different geometries.

The traction separation relation for the cohesive law has been chosen to be

$$\mathbf{t} = (1 - d) \int_{-\infty}^t g(t-s) \mathbf{K} \frac{\partial \Delta}{\partial s} ds \quad (8.4)$$

Here, the memory kernel  $g(t) = g_{\infty} + \sum_{i=1}^N g_i e^{-\frac{t}{\tau_i}}$ .  $g_i$ s are the stiffness ratios while  $\tau_i$ s are the relaxation times. It is intended to see if the same stiffness ratios as that of the bulk material can be used in the cohesive zone as well. This way, cohesive zone can be regarded as the bulk material that is undergoing failure.

The evolution equation for damage is same as earlier as in equation 8.3. But it can be seen that the traction in equation 8.4 depends not just on the current separation but its entire history. Since, storing all the separation data until the current time step demands large storage space, the integration is performed by taking advantage of the exponential dependence of the memory kernel using the technique presented in Taylor et al., 1970 or Simo and Hughes, 1998. The integration technique is as follows.

From the equation 8.4, the traction can be written as

$$\mathbf{t} = (1 - d) \left\{ \mathbf{K} \Delta + \mathbf{K} \sum_{i=1}^N \left( \int_{-\infty}^t g_i e^{-\frac{t-s}{\tau_i}} \frac{\partial \Delta}{\partial s} ds \right) \right\} \quad (8.5)$$

It shall be noted that the  $g_i$ s in the above equation are to be scaled with respect to the rubbery modulus instead of the glassy modulus in the previous section. Each of the integrals in the parenthesis can be evaluated by using the Exponential mapping technique presented in Simo and Hughes, 1998. Denoting the  $i^{\text{th}}$  term to be  $\mathbf{h}_i(t)$ ,

$$\mathbf{h}_i(t) = \int_{-\infty}^t g_i e^{-\frac{t-s}{\tau_i}} \frac{\partial \Delta}{\partial s} ds \quad (8.6a)$$

$$= \int_{-\infty}^{t-\Delta t} g_i e^{-\frac{t-s}{\tau_i}} \frac{\partial \Delta}{\partial s} ds + \int_{t-\Delta t}^t g_i e^{-\frac{t-s}{\tau_i}} \frac{\partial \Delta}{\partial s} ds \quad (8.6b)$$

$$= e^{-\frac{\Delta t}{\tau_i}} \mathbf{h}_i(t - \Delta t) + \int_{t-\Delta t}^t g_i e^{-\frac{t-s}{\tau_i}} \frac{\partial \Delta}{\partial s} ds \quad (8.6c)$$

### Computation of the second term

The second term in the above expression can be computed in a number of ways. Simo and Hughes (Simo & Hughes, 1998) propose integrating the term using a midpoint rule.

$$\int_{t-\Delta t}^t e^{-\frac{t-s}{\tau_i}} \frac{\partial \Delta}{\partial s} ds \approx \left( e^{-\frac{t-s}{\tau_i}} \frac{\partial \Delta}{\partial s} \right) \Big|_{s=t-\frac{\Delta t}{2}} \Delta t = e^{-\frac{t}{2\tau_i}} [\Delta(t) - \Delta(t - \Delta t)] \quad (8.7)$$

Hence

$$\int_{t-\Delta t}^t e^{-\frac{t-s}{\tau_i}} \frac{\partial \Delta}{\partial s} ds \approx e^{-\frac{\Delta t}{2\tau_i}} [\Delta(t) - \Delta(t - \Delta t)] \quad (8.8)$$

In Taylor et al., 1970, the second term is integrated assuming that strain rate,  $\frac{\partial \Delta}{\partial s}$ , is constant during  $\Delta t$ .

$$\int_{t-\Delta t}^t e^{-\frac{t-s}{\tau_i}} \frac{\partial \Delta}{\partial s} ds \approx \frac{\Delta(t) - \Delta(t - \Delta t)}{\Delta t} e^{-\frac{t}{\tau_i}} \int_{t-\Delta t}^t e^{\frac{s}{\tau_i}} ds \quad (8.9)$$

Evaluating the integral in the above equation,

$$\int_{t-\Delta t}^t e^{-\frac{t-s}{\tau_i}} \frac{\partial \Delta}{\partial s} ds \approx \frac{1 - e^{-\Delta t/\tau_i}}{\Delta t/\tau_i} [\Delta(t) - \Delta(t - \Delta t)] \quad (8.10)$$

In the case when the ratio  $\Delta t/\tau_i$  in the equation 8.10 falls below  $10^{-7}$ , the expression  $\frac{1 - e^{-\Delta t/\tau_i}}{\Delta t/\tau_i}$  is approximated by  $1 - \frac{\Delta t}{2\tau_i}$ .

The coefficients of the displacement increment in the equations 8.8 and 8.10 can be noted. The coefficients will be generally denoted as  $m_i(t)$  for convenience from hereon. Hence

$$\int_{t-\Delta t}^t e^{-\frac{t-s}{\tau_i}} \frac{\partial \Delta}{\partial s} ds \approx m_i(t) [\Delta(t) - \Delta(t - \Delta t)] \quad (8.11)$$

Using the above integration techniques in 8.6c, the expression for  $\mathbf{h}_i(t)$  can be expressed as (no sum on  $i$ )

$$\mathbf{h}_i(t) \approx e^{-\frac{\Delta t}{\tau_i}} \mathbf{h}_i(t - \Delta t) + g_i m_i(t) [\Delta(t) - \Delta(t - \Delta t)] \quad (8.12)$$

The expression for traction can hence be found to be

$$\mathbf{t} = (1 - d) \left\{ \mathbf{K}\Delta + \mathbf{K} \sum_{i=1}^N \mathbf{h}_i(t) \right\} \quad (8.13)$$

#### 8.4 FINITE ELEMENT IMPLEMENTATION

In this section, the Finite Element implementation of Cohesive model will be discussed. Beginning with the strong form of momentum balance equation

$$\text{div}_0 \mathbf{P} = \rho_0 \mathbf{a} \quad (8.14)$$

Defining the space of admissible functions that are sufficiently smooth to be  $\mathcal{V}$ ,

$$\mathcal{V} = \{ \mathbf{w} \text{ that is sufficiently smooth} | \mathbf{w} = \mathbf{o} \text{ on } \partial\Omega_0^D \}, \quad (8.15)$$

Converting the momentum equation into weak form

$$\int_{\Omega_0} (\text{div}_0 \mathbf{P} - \rho_0 \mathbf{a}) \delta \mathbf{v} d\Omega_0 = 0 \quad \forall \delta \mathbf{v} \in \mathcal{V} \quad (8.16)$$

which after simplifications gives

$$\int_{\partial\Omega_0} \mathbf{t} \cdot \delta \mathbf{v} ds - \int_{\Omega_0} (\mathbf{P} : \nabla_0 \delta \mathbf{v} + \rho_0 \mathbf{a} \cdot \delta \mathbf{v}) d\Omega_0 = 0 \quad (8.17)$$

The boundary of the body can be divided into external boundary and the crack surfaces,  $\partial\Omega_0 = \partial\Omega_{ext} \cup \Gamma_0^\pm$ . Using this in the above equation

$$\int_{\partial\Omega_{ext}} \mathbf{t} \cdot \delta \mathbf{v} \, dS + \int_{\Gamma_0^\pm} \mathbf{t} \cdot \delta \mathbf{v} \, dS - \int_{\Omega_0} (\mathbf{P} : \nabla_0 \delta \mathbf{v} + \rho_0 \mathbf{a} \cdot \delta \mathbf{v}) \, d\Omega_0 = 0 \quad (8.18)$$

Since they are initially coincident, the integral on both the crack faces can be replaced by an integral on one crack face as

$$\int_{\Gamma_0^\pm} \mathbf{t} \cdot \delta \mathbf{v} \, dS = \int_{\Gamma_0} [\delta \mathbf{v}] \cdot \mathbf{t} \, dS \quad (8.19)$$

where  $[\bullet]$  denotes the jump of  $\bullet$ .

Using their values at nodes and the shape functions,  $\delta \mathbf{v}$  can be expressed to be

$$\delta \mathbf{v} = N_i \delta \mathbf{v}_i \quad (8.20)$$

In one element, the jump in displacement can be expressed similarly as

$$\Delta = [\mathbf{u}] = [\mathbf{B}]\{\mathbf{u}\} \quad (8.21)$$

$\{\mathbf{u}\}$  is a vector containing the nodal values of quantities, expressed as

$$\{\mathbf{u}\} = [u_{x1} \ u_{y1} \ u_{x2} \ u_{y2} \ u_{x3} \ u_{y3} \ u_{x4} \ u_{y4}]^T \quad (8.22)$$

and

$$[\mathbf{B}] = \begin{bmatrix} N_1 & 0 & N_2 & 0 & -N_2 & 0 & -N_1 & 0 \\ 0 & N_1 & 0 & N_2 & 0 & -N_2 & 0 & -N_1 \end{bmatrix}. \quad (8.23)$$

See figure 8.2.  $N_i$ s are the shape functions and  $N_1 = \frac{1-\xi}{2}$ ,  $N_2 = \frac{1+\xi}{2}$ . It has been

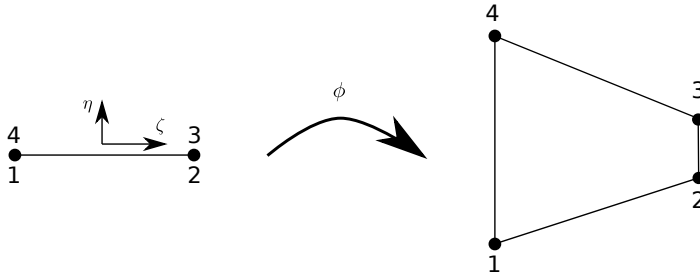


Figure 8.2: Cohesive element.

taken into consideration that the nodes 1 and 4, and the nodes 2 and 3 coincide with each other in the undeformed configuration. The term  $\int_{\Gamma_0} [\delta \mathbf{v}] \cdot \mathbf{t} \, dS$  can be expressed using the nodal values of actual and virtual displacements as

$$\int_{\Gamma_0} [\delta \mathbf{v}] \cdot \mathbf{t} \, dS = \{\delta \mathbf{v}\}^T \int_{\Gamma_0} [\mathbf{B}]^T \mathbf{t} \, dS = \{\delta \mathbf{v}\}^T \{\mathbf{f}_{coh}\} \quad (8.24)$$

The integration in 8.24 is performed numerically as

$$\{\mathbf{f}_{coh}\} = \sum_{i=1}^{n_p} w_i \left( [\mathbf{B}]^T \mathbf{t} \right) |_i \quad (8.25)$$

where  $w_i$ s are weights and  $([\mathbf{B}]^T \mathbf{t}) |_i$  indicates that the quantity  $[\mathbf{B}]^T \mathbf{t}$  is computed at the corresponding integration point.

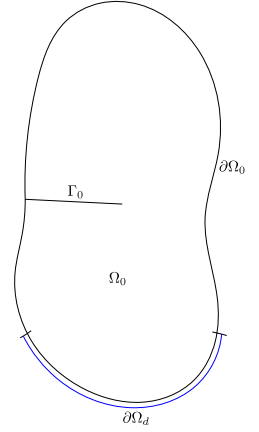


Figure 8.1: Body with a crack.

Using 8.21, the jump in displacement can be expressed in terms of nodal displacements. The above equations can hence be expressed as

$$\mathbf{t} = (1 - d) \left\{ [\mathbf{K}][\mathbf{B}]\{\mathbf{u}\} + [\mathbf{K}] \sum_{i=1}^N \mathbf{h}_i(t) \right\} \quad (8.26)$$

$\mathbf{h}_i(t)$  is computed recursively from the value at the previous time step as

$$\mathbf{h}_i(t) = e^{-\frac{\Delta t}{\tau_i}} \mathbf{h}_i(t - \Delta t) + g_i m_i(t) [\mathbf{B}] d\{\mathbf{u}\} \quad (8.27)$$

where  $d\{\mathbf{u}\} = \{\mathbf{u}(t)\} - \{\mathbf{u}(t - \Delta t)\}$ . The expression for traction can be further simplified as

$$\mathbf{t} = (1 - d) [\mathbf{K}] \left\{ [\mathbf{B}] \left( \{\mathbf{u}\} + \sum_{i=1}^N g_i m_i(t) d\{\mathbf{u}\} \right) + \sum_{i=1}^N e^{-\frac{\Delta t}{\tau_i}} \mathbf{h}_i(t - \Delta t) \right\} \quad (8.28)$$

Hence, tractions at the integration point can be evaluated by computing  $[\mathbf{B}]$  and  $\mathbf{h}_i$  at those points. The  $m_i(t)$  obtained from Simo and Hughes, 1998 is known to be sensitive to the time step size and hence the  $m_i(t)$  from Taylor et al., 1970 will be used for this study. The tangent computation will be presented next.

#### 8.4.1 Computation of residual

The weak form of momentum equation is integrated in time using the HHT- $\alpha$  (Hilber et al., 1977) time integration technique. Since a zero thickness cohesive zone has been considered for the analysis, there is no contribution to the mass matrix from the cohesive zone. The only computation from the cohesive comes from the term  $f_{coh}$ . The residual on the weak form of momentum equation can hence be written as

$$\mathbf{r}^{n+1} = -(1 + \alpha) \mathbf{f}_{coh}^{n+1} + \alpha \mathbf{f}_{coh}^n. \quad (8.29)$$

The above equation together with the contribution from the bulk is solved using Newton's method in Abaqus. The above equation is hence linearized about the current displacement.

$$\mathbf{r}_{k+1}^{n+1} = \mathbf{r}_k^{n+1} + \frac{\partial \mathbf{r}_{k+1}^{n+1}}{\partial \mathbf{u}} \Delta \mathbf{u} = 0. \quad (8.30)$$

The tangent matrix can hence be seen to be  $(1 + \alpha) \frac{\partial \mathbf{f}_{coh}}{\partial \mathbf{u}}$ .

#### 8.4.2 Computation of tangent

Tangent computation involves differentiating 8.25 with respect to displacement.

$$\frac{\partial \mathbf{f}_{coh}}{\partial \mathbf{u}} = \int_{\Gamma_0} [\mathbf{B}]^T \frac{\partial \mathbf{t}}{\partial \mathbf{u}} dS = \int_{\Gamma_0} [\mathbf{B}]^T \frac{\partial \mathbf{t}}{\partial \Delta} \frac{\partial \Delta}{\partial \mathbf{u}} dS = \int_{\Gamma_0} [\mathbf{B}]^T \frac{\partial \mathbf{t}}{\partial \Delta} [\mathbf{B}] dS \quad (8.31)$$

The traction derivative with respect to separation is computed as

$$\frac{\partial \mathbf{t}}{\partial \Delta} = (1 - d) \left\{ [\mathbf{K}] + [\mathbf{K}] \sum_{i=1}^N \frac{\partial \mathbf{h}_i}{\partial \Delta} \right\} - \mathbf{t} \left[ \frac{\partial d}{\partial \Delta} \right]^T \quad (8.32a)$$

$$= (1 - d) \left\{ \left( 1 + \sum_{i=1}^N g_i m_i(t) \right) [\mathbf{K}] \right\} - \mathbf{t} \left[ \frac{\partial d}{\partial \Delta} \right]^T \quad (8.32b)$$

From 8.3, the derivative of damage with respect to separation can be seen to be

$$\frac{\partial d}{\partial \Delta} = \frac{\Delta_0}{\Delta_f - \Delta_0} \frac{\Delta_f}{\Delta^3} \Delta \quad (8.33)$$

The final expression for the tangent can be seen to be

$$(1 + \alpha) \int_{\Gamma_0} [\mathbf{B}]^T \left[ (1 - d) \left\{ \left( 1 + \sum_{i=1}^N g_i m_i(t) \right) [\mathbf{K}] \right\} - \frac{\Delta_0}{\Delta_f - \Delta_0} \frac{\Delta_f}{\Delta^3} \mathbf{t} \Delta^T \right] [\mathbf{B}] \, dS \quad (8.34)$$

Since only mode-I fracture is considered in this study,  $\Delta$  can be approximated by  $\Delta_y$ , the vertical component of the displacement jump.

### 8.4.3 Implementation into user subroutine

The above formulation of the cohesive zone has been implemented in to the user subroutine UELMAT of Abaqus (Dassault, 2014). The implementation details can be seen below.

It can be seen from the equation 8.13 that the computation of traction vector requires the computation of the jump vector,  $\Delta$  and the history variables,  $\mathbf{h}_i$ . The computation of  $\mathbf{h}_i$  at the current time step requires its value at the previous time step as well as the displacement increment between the two time steps. Hence, the history variables  $\mathbf{h}_i$  (of size  $2 \times 1$ ) are stored in the state variable array (SVARS) that is supplied by Abaqus. The displacement increment between the two steps is supplied by Abaqus as the variable DU. In addition to this, the half step residual check from Abaqus at the end of each time step and the computation of residual for time integration require the force vector (of size  $8 \times 1$ ) computed at the previous iteration. This is hence stored in the SVARS array as well. The damage variable is also stored to take the irreversibility constraint into consideration. This computation is done at each integration point to get the right hand side of the force vector in the equation 8.26. Since the current formulation uses 10 viscous arms, the total size of the state variable array at each integration point is 29 (= 1 (damage) + 8 (force) + 10  $\times$  2 (internal variables)). Since two integration points are used for each element, the size of the state variable array is 58. The structure of the SVARS array can be seen in the figure 8.3.

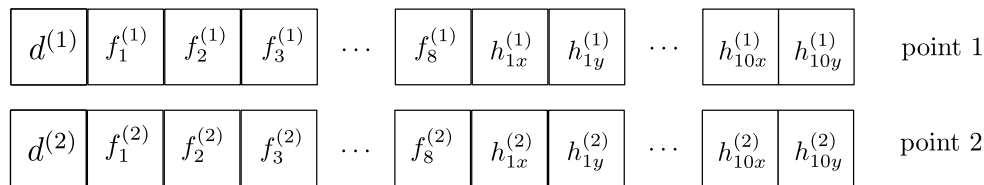


Figure 8.3: Structure of SVARS array of the UELMAT subroutine.

The quantities to be returned to Abaqus is determined from the LFLAGS array of the subroutine. Per the documentation, the internal variables are updated when  $LFLAGS(3) = 1$ . In that case, the stiffness matrix and the force vector are computed at each integration point and are combined with the weights from the integration rule to get the overall stiffness matrix and the force vector, which is then supplied to Abaqus through the arrays AMATRX and RHS, respectively. The internal variables are updated using the equation 8.27.

### 8.5 CRACK SPEEDS PREDICTION AND TRACTION - SEPARATION RELATIONS

The implementation of the CZM has been first checked by making it rate independent and comparing the results against the results from the COH2D4 element of Abaqus. In the rate independent case, the results from the two simulations are expected to match. This was tested for the case of  $\lambda = 2.5$  and with  $\Delta_0 = 1 \times 10^{-6}$  m and  $\Delta_f = 1.5 \times 10^{-3}$  m. Both the analyses resulted in the crack speed of about  $59 \text{ m s}^{-1}$  and similar displacement and velocity profiles.

#### 40 mm specimen

The cohesive model presented has been implemented into the UELMAT subroutine of ABAQUS. The model parameters that are to be calibrated are the separation at initiation ( $\Delta_0$ ) and the separation at failure ( $\Delta_f$ ). The material in the bulk has been taken to be the same as that in the previous section. As mentioned earlier, the  $g_{is}$  and  $\tau_{is}$  of the cohesive zone are taken to be the same as that of the bulk material.

The values of  $1 \times 10^{-6}$  m and  $1.5 \times 10^{-3}$  m for  $\Delta_0$  and  $\Delta_f$ , respectively, were seen to give a crack speed of  $56 \text{ m s}^{-1}$  at a stretch level of 3.5 and a crack speed of about  $6 \text{ m s}^{-1}$  at a stretch level of 1.7, which is much larger than what was observed with a rate independent cohesive zone. The crack speed observed in the experiments varied between 9 and  $16 \text{ m s}^{-1}$ . Hence, the rate dependent model with the aforementioned choice of parameters was used to obtain crack speeds for the whole range of loading conditions to compare them with the experiments. The results can be seen in the figure 8.4.

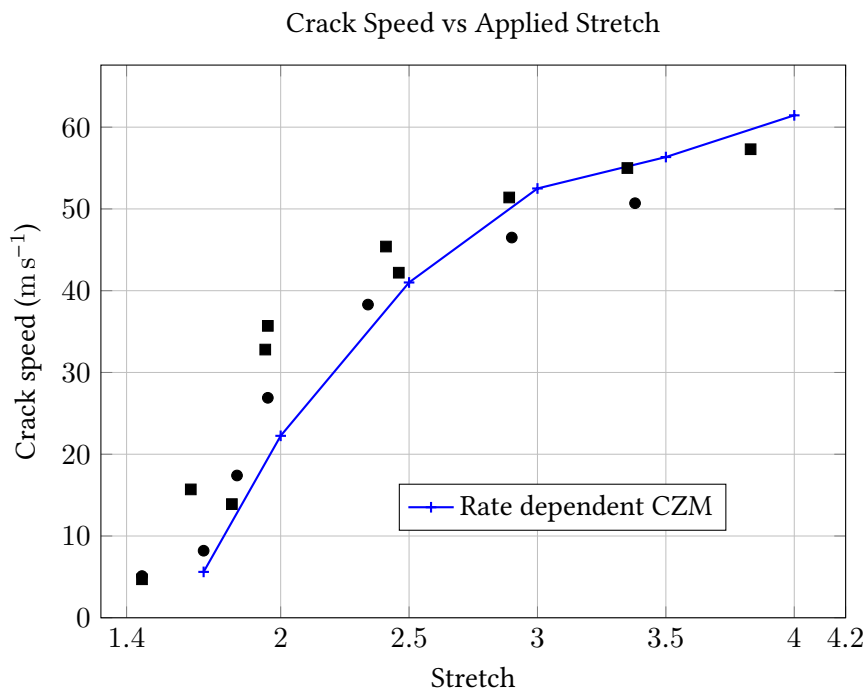


Figure 8.4: Crack speeds vs Stretch. The symbols indicate the experimental results obtained in Corre, Coret, Verron, Leblé, and Le Lay, 2020. The solid line indicates the crack speeds from the simulation obtained using a rate dependent CZM.

It can be seen that the crack speeds from the simulation follows the experimental trend at least up to a stretch level of 3.5. A slight upturn in the trend has been

observed in the simulations after the stretch level of 3.5. The data point available from the experiments does not seem to follow this trend after the stretch of 3.5.

### Specimen of other geometry

In crack propagation experiments performed by Chen et al., 2011, it was observed that the crack speed becomes independent of the specimen height in the transonic regime. Lattice model was used as well in that study to simulate the propagation of crack. In this section, it will be tested if the rate dependent cohesive model presented earlier will be able to predict the same result for polyurethane as well. For this purpose, the crack propagation in specimen of other heights such as 10 mm, 20 mm, 60 mm, 100 mm and 150 mm will be studied. The lengths of the 100 mm and 150 mm specimen have been increased to 500 mm to make sure that the steady state can be achieved when the crack is at the center. The results of the simulations can be seen in the figure 8.5.

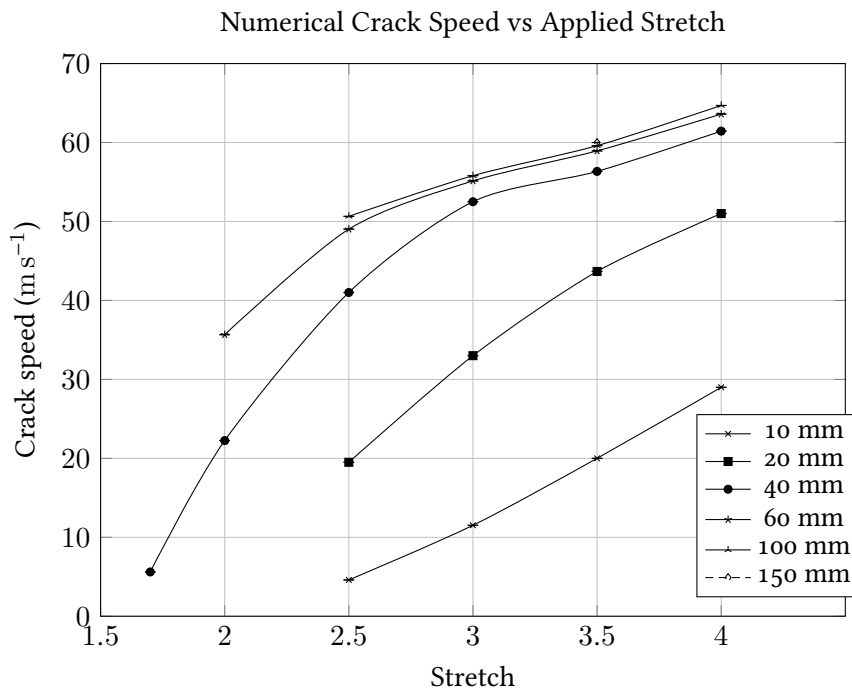


Figure 8.5: Crack speeds vs Stretch, all heights

It can be seen that at a given stretch level, the rate of increase in crack speed decreases as the specimen height is increased. In fact, it can be seen that the crack speeds saturate at some height and does not increase further with an increase in height. This can be observed if the crack speeds are plotted against the specimen height instead of the stretch level (see figure 8.6).

As mentioned earlier, the crack speeds seem to saturate at a particular height and does not increase any further. Figure 8.6 can be compared with Figure 3 of Gent and Marteny, 1982a. In that study experiments were conducted on specimen of different heights all stretched to the same level. The crack speeds were observed to not increase once a specific height level is reached as is the case in the simulations performed in the current study.

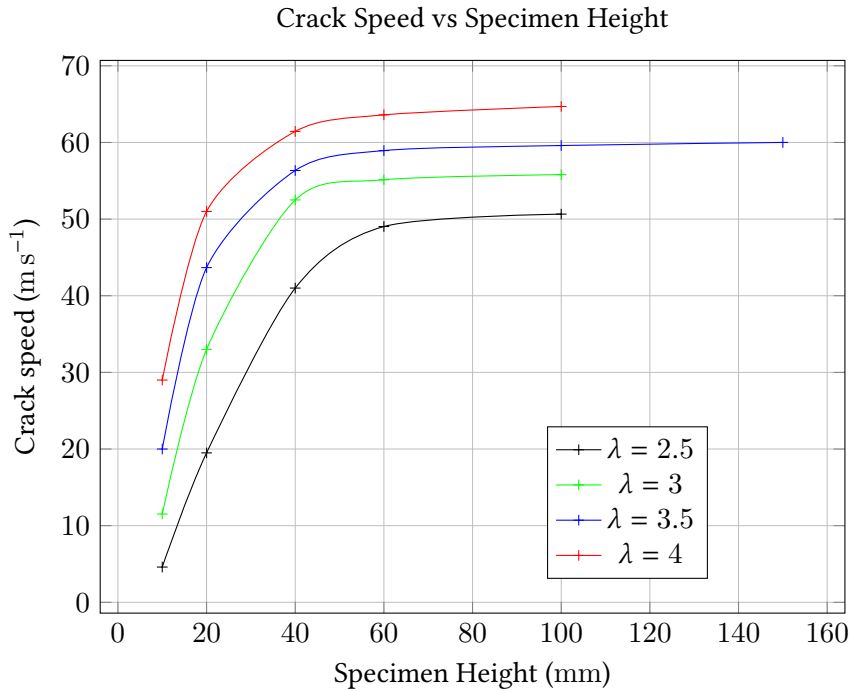


Figure 8.6: Crack speeds vs Stretch, all heights

### ***Traction separation curves***

Since the traction separation law was made rate dependent, a variation in crack speed results in a variation in the traction separation law. It is expected that the maximum stress in the cohesive zone is larger than the cohesive strength in the rate independent case.

The traction separation behavior of the cohesive zone is extracted from the simulations and plotted vs the crack speed in figure 8.7.

It can be seen that the maximum traction value increases rapidly to a value of about 21 MPa for a crack speed of  $5.6 \text{ m s}^{-1}$ . In the other cases where the crack speeds are about  $41 \text{ m s}^{-1}$  and  $56 \text{ m s}^{-1}$ , the critical stress can be similarly seen to increase to about 40 MPa and 46 MPa respectively. This, of course, leads to an increase in fracture energy as well. The fracture energies can be computed as the area under the traction separation curves. For the results presented in figure 8.7, they can be seen to be  $12.89 \text{ kJ/m}^2$ ,  $18.5 \text{ kJ/m}^2$ , and  $21 \text{ kJ/m}^2$ , for  $\lambda = 1.7$ , 2.5, and 3.5, respectively.

### ***Traction inside the cohesive zone***

The variation of cohesive traction and the damage variable inside the cohesive zone for the three cases presented in the figure 8.7 can be seen in figures 8.8 and 8.9.

As can be seen from the figure 8.8, the stress at the entry of the cohesive zone increases slightly with the crack speed. From its value at the entry, the cohesive traction increases to a maximum value and starts to decrease again. As the material in the cohesive zone starts to damage, the crack faces start to separate faster resulting in an increase in traction as a consequence of viscous effects. However, as the crack faces separate, the damage variable increases and reaches 1 at the end of cohesive zone. Hence, it can be seen that the traction increases at the beginning of the cohesive zone as a consequence of viscous effects and decreases once the damage variable increases. A similar trend can be observed for all the crack speeds

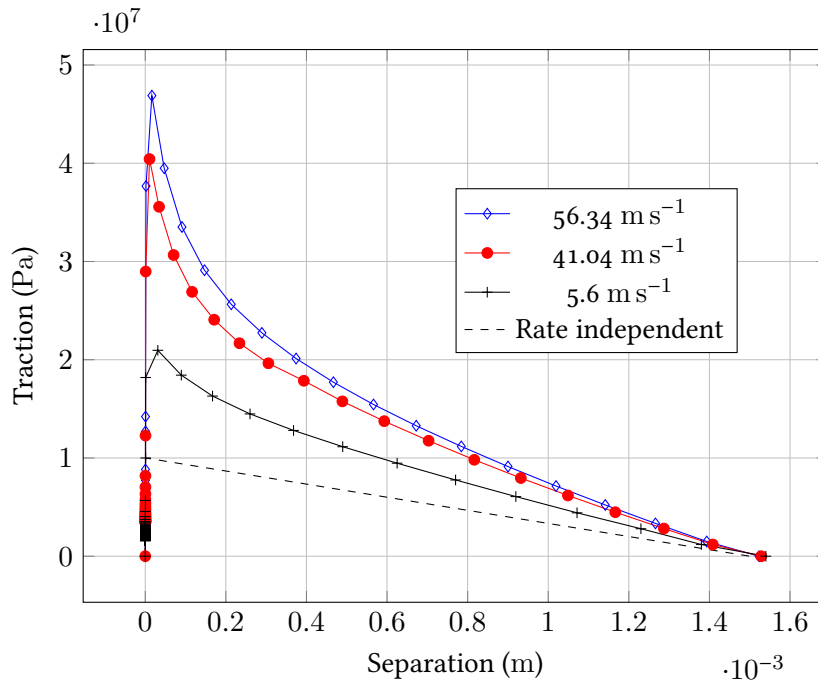


Figure 8.7: Traction separation curve for various crack speeds

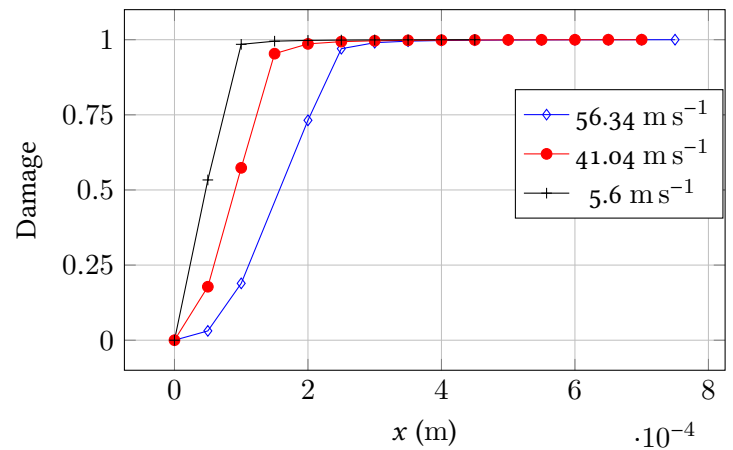
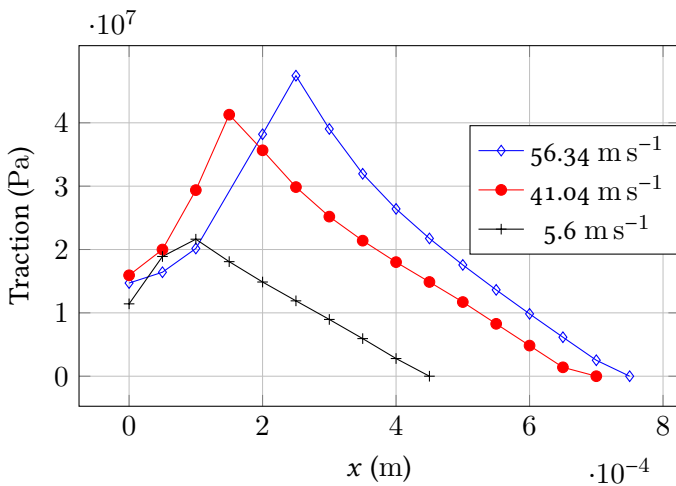


Figure 8.8: Traction separation curve for various crack speeds

presented.

In the figure 8.9, the cohesive tractions are presented with the distance along the zone normalized with the length of cohesive zone. The length of the cohesive zone is measured in the undeformed configuration from the location where the separation reaches  $\Delta_0$  till the location where it reaches  $\Delta_f$ . The length of the cohesive zone can be seen to be  $4.5 \times 10^{-4}$  m,  $7 \times 10^{-4}$  m, and  $7.5 \times 10^{-4}$  m for  $\lambda = 1.7$ , 2.5 and, 3.5, respectively. From the figure 8.9, it can be observed that the normalized distance at which the cohesive traction attains the maximum moves to the right with an increase in the crack speed. The damage profile can also be seen to move towards the right with an increase in the crack speed.

**Comparison of profile of crack faces, displacement and velocity fields**

The profile of crack faces behind the tip obtained from the experiments and the simulations for the 40 mm sample for the case of  $\lambda = 3.5$  can be seen in the figure

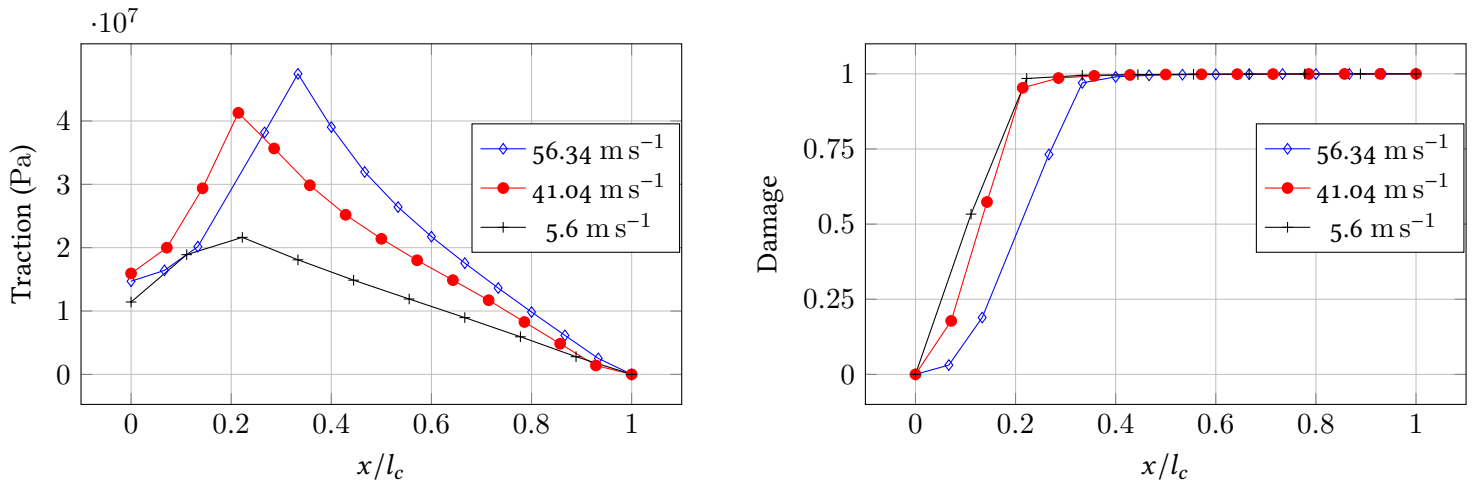


Figure 8.9: Traction separation curve for various crack speeds

8.10. The crack speed observed in the experiment is about  $56 \text{ m s}^{-1}$  and the speed obtained from the simulation is about  $57 \text{ m s}^{-1}$ . The profile obtained from the simulation is steeper than what was observed in the experiments. This could be a consequence of the viscoelastic model being 'less stiff' than expected at the strain rates experienced. However, as can be seen, the crack speed obtained from the simulation is about the same as in the experiments.

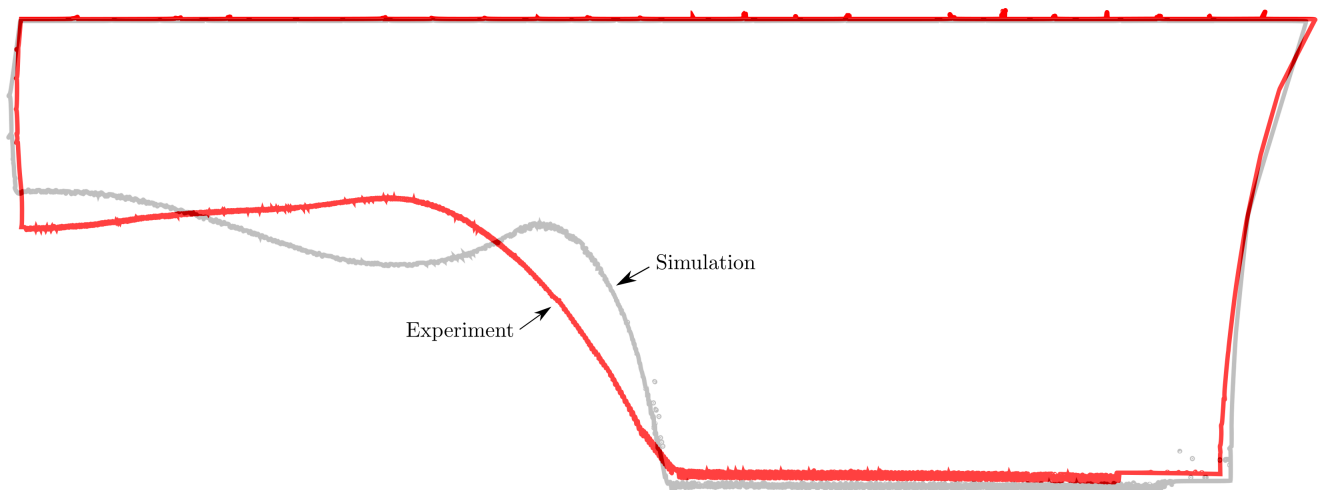


Figure 8.10: Comparison of the crack opening profile between the experiment and simulation for the case of  $\lambda = 3.5$  when the crack is at about the center of the specimen.

The displacement and velocity fields when the crack is at about the center of the specimen can be seen in the figures 8.11 and 8.12 (to be compared with figures 7.16a and 6.2), respectively. It can be seen that in the displacement and velocity fields over predicted in the simulations when compared with the experiments.

## 8.6 DISCUSSIONS

In this chapter, the crack propagation through the elastomer has been simulated using a cohesive zone model. Finite Linear Viscoelastic model has been assumed for the bulk material. Initial attempts were made to model the crack propagation using a rate independent cohesive zone. It was found that the cohesive zone parameters which result in crack speeds that match the experiment at  $\lambda = 3.5$  either does not result in the crack propagation at  $\lambda = 1.7$  or result in a very low crack speed

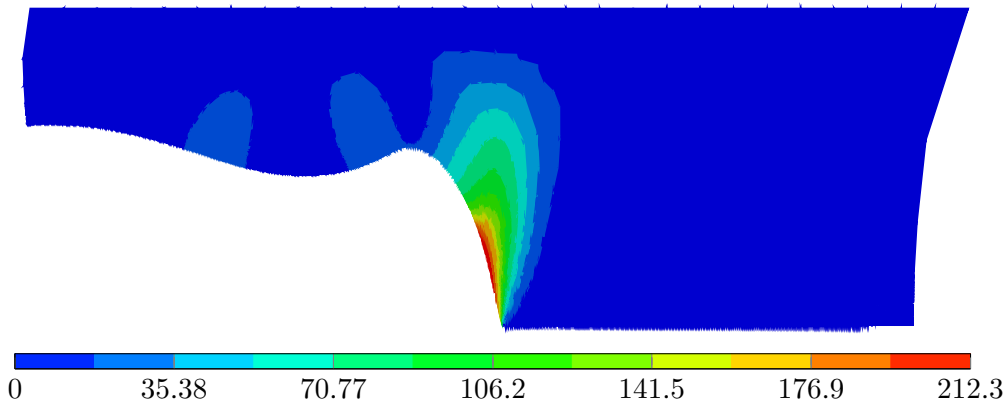


Figure 8.11: Particle velocity magnitude in  $\text{m s}^{-1}$  for  $\lambda = 3.5$  plotted on deformed configuration.

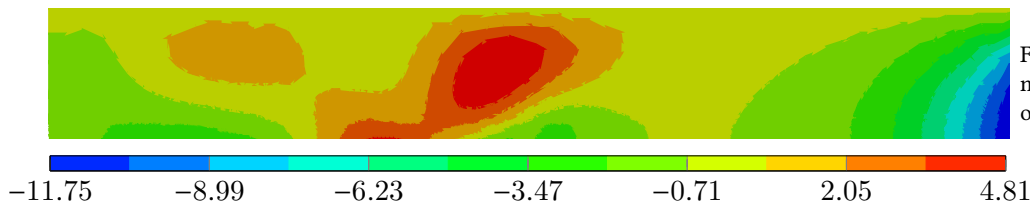


Figure 8.12: Horizontal displacement magnitude in mm for  $\lambda = 3.5$  plotted on undeformed configuration.

(orders of magnitude smaller than the experiments) at that stretch level. Hence, the entire range of crack speeds could not be predicted using the same cohesive zone parameters with a rate independent cohesive zone.

Studies performed in the literature using a cohesive zone model to predict the crack growth in polymers or adhesives (Rahulkumar et al., 2000; Geißler and Kaliske, 2010; Elmukashfi and Kroon, 2014 and the references cited therein) underline the need for a rate-dependent cohesive zone. The rate dependence in the cohesive zone can be attributed to the rate dependence in the fracture processes as a consequence of viscoelastic effects. A rate dependent cohesive zone has hence been employed in the current study as well. The rate dependence has been introduced by using convolution integrals as in the bulk. The relaxation times and the stiffness ratios of the viscous arms have been picked to be the same as that of the bulk. This just leaves two parameters in the cohesive zone to be calibrated,  $\Delta_0$  and  $\Delta_f$ . The parameters were chosen to reproduce the experimental crack speed at a stretch level of 3.5. Then, using the same parameters, the cohesive zone model was able to predict the entire range of the crack speeds observed in the experiments. See figure 8.4. When used to predict the crack speeds for different geometries, it was observed that the crack speeds became independent of the specimen height at a given stretch level as was reported in Chen et al., 2011. The height independence was, however, observed for specimen heights starting from about 60 mm. For specimens of smaller heights, the crack speeds still changed with a change in the specimen height for the same stretch. See figure 8.6. The specimen heights tested in Chen et al., 2011 were 2 inch (50.8 mm), 4 inch (101.6 mm), and 7 inch (177.8 mm). Hence, it is possible that the phenomenon of height independence observed in that study was the consequence of the geometries used for the experiments. For instance, in this thesis, the geometries that are 20 mm, 40 mm, and 60 mm were tested by the authors. From the figure 8.6, it can be seen that for this height range, the crack speeds have yet not become independent of the specimen height in the transonic regime.

The traction-separation curves in the rate dependent cohesive zone for different crack speeds can be seen in the figure 8.7 along with the rate independent case.

It can be seen that the maximum traction in the cohesive zone is a function of crack speed and it increases to about 47 MPa for the case of  $\lambda = 3.5$ , where the crack speed is about  $57 \text{ m s}^{-1}$ . The variation of traction in the cohesive zone for different crack speeds can be seen in the figures 8.8 and 8.9. In all the cases, the traction at the entry into cohesive zone can be seen to slightly increase with the crack speed. It reaches a value of 16 MPa for a crack speed of about  $57 \text{ m s}^{-1}$ . The location of maximum traction can be seen to be behind the mathematical crack tip (where  $\Delta = \Delta_0$ ). It can also be observed that the location moves away from the mathematical tip with an increase in the crack speed. The maximum occurs at about  $x/l_c < 0.2$ ,  $\approx 0.2$ , and  $0.37$  for three crack speeds presented. The results from the current study in figure 8.8 can be compared with the results from W. G. Knauss and Losi, 1993 in figure 8.13. Only one case from W. G. Knauss and Losi, 1993 is presented here. All the cases can be found in the figure 8 of that publication. In that study, the stresses at the entry of cohesive zone was found to vary non-monotonically with the crack speed. However, for range of crack speeds in the figure 8.13, it can be seen that the stress at the entry of the cohesive zone is a weakly increasing function of crack speed as is the case in the current study. The maximum traction can also seen to increase with the crack speed till a certain crack speed. In the current study, the maximum traction increases with crack speed as well, and may also probably settle down for higher crack speeds (at higher stretches).

The cohesive model chosen in this study is intrinsic (Kubair & Geubelle, 2003) since it has a finite initial stiffness. The damage initiation criterion in this case has been described in terms of a critical opening displacement ( $d = 0$  and  $\dot{d} > 0$  when  $\Delta = \Delta_0$  and  $\dot{\Delta} > 0$ ). As the crack approaches a material point, the strain levels (and hence the separation) increases as a result of the strain concentration near the tip. This results in the stress at the entry of the cohesive zone being a function of crack speed as a consequence of the rate dependence. The cohesive element is taken to fail completely when  $d = 1$ , which happens at  $\Delta = \Delta_f$ . However, if an extrinsic cohesive zone is used for the analysis, the separation remains at 0 till a certain critical stress is reached. In such a case, the damage initiation criterion used in this study may not be applicable. One alternative is to make the initiation stress as a (unknown) function of crack speed. However, as can be seen from the results of this study, even with a critical opening criterion, the stresses at the entry of the cohesive zone do not vary drastically with the crack speed (as compared to the maximum traction). Hence, the damage initiation stress in the case of an

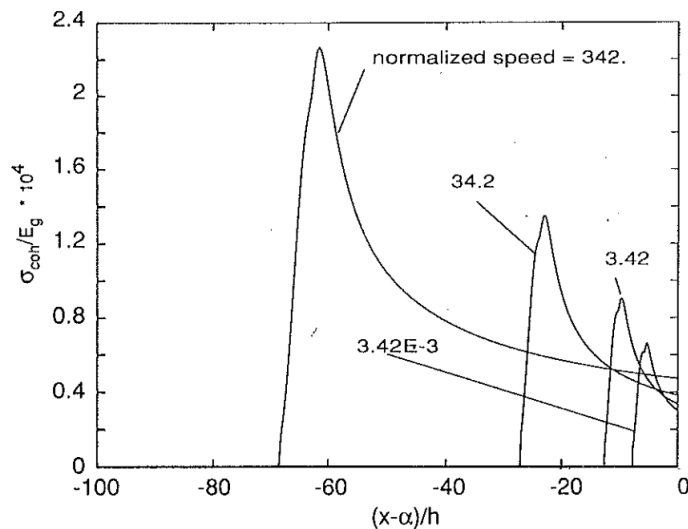


Figure 8.13: Evolution of traction within the cohesive zone. Extracted from W. G. Knauss and Losi, 1993.  $h$  denotes the thickness of the layer used in that study.  $\alpha$  denotes the position of the mathematical tip .

extrinsic cohesive model can be taken to be a constant while still retaining the rate dependent behavior from this study.

Another feature of interest is the length of the cohesive zone. The lengths are  $4.5 \times 10^{-4}$  m,  $7 \times 10^{-4}$  m, and  $7.5 \times 10^{-4}$  m for  $\lambda = 1.7$ , 2.5 and, 3.5, respectively. In W. G. Knauss and Losi, 1993, the cohesive zone length was reported to be a non-monotonic function of crack speed. However, at large crack speeds, the length was observed to increase with the crack speed (see figure 8.13). As mentioned already, in the current study, for the crack speeds considered, the cohesive zone length increases with the crack speed. If the failure of the material is taken to occur within the process zone, the roughness of the crack surface presented in the earlier chapter in the figures 6.7 and 6.8 can be taken to represent the variation of cohesive zone with the crack speed. Hence, this observation is in contrast with the result from the simulations.

The opening profile of the cracked surface behind the tip from the experiments and simulation can be seen in the figure 8.10. It can be seen that the profile obtained numerically is steeper than the experimentally observed profile. Also, the magnitude of velocity and the horizontal displacement can be seen in the figures 8.11 and 8.12, respectively. The FE simulations can be seen to over predict these quantities when compared with the experiments. The reason for this can be described as follows. From the figures 7.17 and 7.19, the reaction forces behind the tip do not go to 0 directly behind the tip. Instead, they go to 0 gradually over some length behind the tip. The magnitude of these stresses are positive as well, indicating that they are 'holding back' the crack faces from moving upward. In the simulations, however, since these faces are traction free, they are free to move until the material in front resists their motion. This can be seen to be the reason behind obtaining a steeper profile in the simulations. As mentioned in the earlier chapter, if the viscoelastic model is further refined to make the reaction in the figures 7.17 and 7.19 go to 0 over a smaller span, the profile from the simulations may match closely with the ones from the experiments.

The total energy expenditure in the bulk and the cohesive zone during the dynamic fracture, however, cannot be computed with the Finite Linear Viscoelastic model. Hence, the Finite Viscoelastic model has been implemented and this will be the focus of the next chapter. The energy expenditure during the viscoelastodynamic fracture will be examined. The portion of energy lost due to viscoelastic effects of the bulk and the fracture processes will be examined.

## SUMMARY

A rate dependent cohesive model has been used to predict the crack speeds in Polyurethane elastomer. A convolution integral type model has been used for the cohesive zone, the coefficients of which are taken to be the same as that of the bulk material. The results from the simulations match the experimental results from Corre et al., 2020 for the 40 mm geometry. When applied for the case of other geometries, it was observed that for a given stretch level, the crack speeds did not depend on the specimen geometry starting from the specimen size of 60 mm. This coincides with the observations from Chen et al., 2011 where the specimens of the natural rubber were tested. The evolution of traction within the cohesive zone, the maximum traction, the traction at the entry of the cohesive zone are similar to the observations from W. G. Knauss and Losi, 1993. The area under the traction separation curves was observed to increase with the crack speed which is analogous to an increase in fracture energy with crack speed. To conclude, the

hyperelastic model along with viscous contributions modeled in terms of Finite Linear Viscoelasticity and a convolution type cohesive zone was observed to predict crack speeds similar to the experimentally observed speeds.

# FINITE VISCOELASTIC MODEL

# 9

---

In this chapter, the Finite Viscoelastic model (Reese & Govindjee, 1998; Bergström & Boyce, 1998) will be presented and its implementation will be described in a plane stress setting. At first, the model will be presented in a 3D setting and the differences arising in the implementation in plane stress will be discussed. After this, some comparisons will be made between the current model and the Finite Linear Viscoelastic model. Finally, energetic analysis will be performed on the experiments and the simulations using the current model.

---

## CONTENTS

9.1	Thermodynamics . . . . .	104
9.2	Integration of the evolution equation . . . . .	105
9.3	Plane stress formulation . . . . .	106
9.3.1	Stress and tangent computation . . . . .	106
9.3.2	Tangent computation . . . . .	109
9.3.3	Implementation details . . . . .	112
9.4	Model checks . . . . .	112
9.4.1	Hyperelastic case . . . . .	112
9.4.2	Viscoelastic case - small strains and small perturbations . . . . .	113
9.4.3	Viscoelastic case - large strains and small perturbations . . . . .	115
9.5	Application of FV model to the experiments . . . . .	116
9.5.1	Model with adjusted parameters . . . . .	119
9.6	Energy budget in viscoelastodynamic fracture . . . . .	123
9.6.1	From the experiments . . . . .	123
9.6.2	From the simulations with cohesive model . . . . .	125
9.7	Discussions . . . . .	128

The Finite Linear Viscoelastic (FLV) model has been used in the previous chapters to describe the viscoelastic behavior of the bulk material. However, the energy dissipated in the bulk material during the propagation of a crack cannot be computed with that model as it does not involve an explicit expression for energy or dissipation. To the author's knowledge, a plane stress implementation of the model by Reese and Govindjee, 1998 does not exist. Hence, the current chapter discusses its plane stress implementation and its use to compute the energy dissipated in the material during the propagation of a dynamic crack.

### 9.1 THERMODYNAMICS

In order to describe the processes that are far from equilibrium, a viscoelastic model has been proposed in Bergström and Boyce, 1998; Reese and Govindjee, 1998 in a thermodynamically consistent way. In this model, the strain energy density is taken to be a function of the deformation as well as some internal variables that characterize the rate dependence of the material. The strain energy density can be written as

$$\psi = \hat{\psi}(C, Q_1, Q_2, \dots, Q_n), \quad (9.1)$$

where  $C$  is the right Cauchy Green deformation tensor and  $Q_i$  are the internal variables. The evolution of internal variables are described by  $n$  equations of the form

$$\dot{Q}_k = \hat{f}_k(C, Q_1, Q_2, \dots, Q_n). \quad (9.2)$$

The evolution equations and the expression for the internal energy shall satisfy the dissipation inequality

$$\mathcal{D} := \frac{1}{2} \mathbf{S} : \dot{\mathbf{C}} - \dot{\psi} \geq 0. \quad (9.3)$$

Using a Maxwell type spring-dash pot model to represent the material, the strain energy function can be split into equilibrium and non-equilibrium parts as

$$\psi := \psi_{EQ}(\bar{C}) + \psi_{NEQ}(C_e) = \psi_{EQ}(\bar{C}) + \psi_{NEQ}(F_i^{-T} \bar{C} F_i^{-1}), \quad (9.4)$$

where  $C_e$  is the elastic part of the deviatoric Cauchy Green tensor,  $\bar{C} := \bar{F}^T \bar{F}$ . It has been assumed that  $\bar{F} = J^{-\frac{1}{3}} F$  admits a decomposition into an elastic and an inelastic part,  $\bar{F} = F_e F_i$  (Dal & Kaliske, 2009). Using the above expressions in the internal dissipation inequality gives the expressions for stress as

$$\mathbf{S} = -pJ\mathbf{C}^{-1} + J^{-2/3} \text{DEV} \left\{ \mathbf{S}_{EQ} + \mathbf{S}_{NEQ} \right\}. \quad (9.5)$$

$\mathbf{S}_{EQ}$  and  $\mathbf{S}_{NEQ}$  denote the elastic and viscous contributions to the total stress.  $\text{DEV} \left\{ \bullet \right\}$  represents the deviatoric projection and the first term is a consequence of the incompressibility constraint. These stresses are given by

$$\mathbf{S}_{EQ} := 2 \frac{\partial \psi_{EQ}}{\partial \bar{C}}, \quad (9.6)$$

$$\mathbf{S}_{NEQ} := 2 F_i^{-1} \frac{\partial \psi_{NEQ}}{\partial C_e} F_i^{-T}, \quad (9.7)$$

and the deviatoric projector by

$$\text{DEV} \left\{ \bullet \right\} := \bullet - \frac{\bullet : \mathbf{C}}{3} \mathbf{C}^{-1}. \quad (9.8)$$

The Kirchhoff stress is then obtained as

$$\boldsymbol{\tau} = \mathbf{F}\mathbf{S}\mathbf{F}^T = -p\mathbf{J}\mathbf{I} + \boldsymbol{\tau}^{iso} = -p\mathbf{J}\mathbf{I} + \mathbb{P} : \bar{\boldsymbol{\tau}}, \quad (9.9)$$

where  $\bar{\boldsymbol{\tau}} = \bar{\boldsymbol{\tau}}_{EQ} + \bar{\boldsymbol{\tau}}_{NEQ}$  are defined as

$$\bar{\boldsymbol{\tau}}_{EQ} := 2 \frac{\partial \psi_{EQ}(\bar{\mathbf{b}})}{\partial \bar{\mathbf{b}}} \bar{\mathbf{b}}, \quad (9.10)$$

$$\boldsymbol{\tau}_{NEQ} := 2 \frac{\partial \psi_{NEQ}(\mathbf{b}_e)}{\partial \mathbf{b}_e} \mathbf{b}_e. \quad (9.11)$$

$\mathbb{P}$  is the deviatoric projector in the deformed configuration defined as

$$\mathbb{P} := \mathbb{I} - \frac{\mathbf{I} \otimes \mathbf{I}}{3}. \quad (9.12)$$

The dissipation inequality becomes

$$\mathcal{D} = -\boldsymbol{\tau}_{NEQ} : \frac{1}{2} \mathcal{L}_v \mathbf{b}_e \cdot \mathbf{b}_e^{-1} \geq 0, \quad (9.13)$$

where  $\mathcal{L}_v \mathbf{b}_e$  denotes the Lie derivative of  $\mathbf{b}_e$  defined as

$$\mathcal{L}_v \mathbf{b}_e = \dot{\bar{\mathbf{F}}} \bar{\mathbf{C}}_i^{-1} \bar{\mathbf{F}}^T. \quad (9.14)$$

The expression 9.13 can be satisfied by specifying the evolution equation as

$$-\frac{1}{2} \mathcal{L}_v \mathbf{b}_e \cdot \mathbf{b}_e^{-1} = \gamma_0 \mathbb{V}^{-1} : \boldsymbol{\tau}_{NEQ}. \quad (9.15)$$

where  $\mathbb{V}$  is a fourth order isotropic positive definite tensor possibly a function of  $\mathbf{b}_e$  and  $\gamma_0 > 0$ . A slightly different equation has been proposed by Bergström and Boyce, 1998. In fact, the model of Reese and Govindjee, 1998 can be seen to be a special case of the model of Bergström and Boyce, 1998.

## 9.2 INTEGRATION OF THE EVOLUTION EQUATION

The integration of equation 9.13 is carried out by a predictor-corrector type algorithm. In the elastic predictor step, the inelastic strains are taken to be fixed and so,

$$(\mathbf{C}_i^{-1})_{tr} = (\mathbf{C}_i^{-1})_{t_{n-1}} \implies \mathbf{b}_e^{tr} = \bar{\mathbf{F}}(\mathbf{C}_i^{-1})_{t_{n-1}} \bar{\mathbf{F}}^T. \quad (9.16)$$

In the inelastic corrector step, the total deformation is assumed to be held fixed and so,  $\mathcal{L}_v \mathbf{b}_e = \dot{\mathbf{b}}_e$ . Using this in equation 9.15 gives

$$\dot{\mathbf{b}}_e \mathbf{b}_e^{-1} = -2\gamma_0 [\mathbb{V}^{-1} : \boldsymbol{\tau}_{NEQ}]. \quad (9.17)$$

The above equation can be integrated using the exponential mapping technique (Weber & Anand, 1990). The resulting expression is

$$\mathbf{b}_e = \exp \left[ -2\gamma_0 \int_{t_{n-1}}^{t_n} \mathbb{V}^{-1} : \boldsymbol{\tau}_{NEQ} dt \right] \mathbf{b}_e^{tr}, \quad (9.18)$$

$$(\mathbf{b}_e)_{t_n} \approx \exp \left[ -2\gamma_0 \Delta t (\mathbb{V}^{-1} : \boldsymbol{\tau}_{NEQ})_{t=t_n} \right] \mathbf{b}_e^{tr}. \quad (9.19)$$

The above equation is first order accurate.

Since the material is assumed to be isotropic,  $\mathbf{b}_e, \mathbf{b}_e^{tr}$  and hence  $\boldsymbol{\tau}_{NEQ}$  share the Eigen space. Since  $\mathbb{V}^{-1} := \frac{1}{2\eta_D} \left[ \mathbb{I} - \frac{\mathbf{I} \otimes \mathbf{I}}{3} \right]$  is isotropic, equation 9.19 can be written in Eigen basis as

$$\lambda_{Ae}^2 = \exp \left[ -\frac{\gamma_0 \Delta t}{\eta_D} \text{dev}(\boldsymbol{\tau}_A) \right] (\lambda_{Ae}^2)_{tr}. \quad (9.20)$$

Taking logarithm of both sides,

$$\epsilon_{Ae} = -\frac{\gamma_0 \Delta t}{2\eta_D} \text{dev}(\boldsymbol{\tau}_A) + (\epsilon_{Ae})_{tr}, \quad (9.21)$$

where  $\epsilon_{Ae} = \ln \lambda_{Ae}$ ,  $(\epsilon_{Ae})_{tr} = \ln(\lambda_{Ae})_{tr}$ . The above equation is non-linear if  $\boldsymbol{\tau}_A$  is a non-linear function of  $\epsilon_e$ . Hence, Newton iterations are used to solve it as below.

Defining

$$r_A := \epsilon_{Ae} + \frac{\gamma_0 \Delta t}{2\eta_D} \text{dev}(\boldsymbol{\tau}_A) - (\epsilon_{Ae})_{tr} = 0, \quad (9.22)$$

it can be solved by linearizing around  $\epsilon_{Ae} = (\epsilon_{Ae})_k$  as

$$r_A + \frac{\partial r_A}{\partial \epsilon_{Be}} \Delta \epsilon_{Be} = 0 \implies K_{AB} \Delta \epsilon_{Be} = -r_A. \quad (9.23)$$

where  $K_{AB} = \frac{\partial r_A}{\partial \epsilon_{Be}}$ . The above equation is solved to obtain  $\Delta \epsilon_e$ , which is then used to update the elastic strain as  $(\epsilon_e)_{k+1} = (\epsilon_e)_k + \Delta \epsilon_e$ .

### 9.3 PLANE STRESS FORMULATION

As already mentioned, to the author's knowledge, a plane stress implementation of the FV model does not exist. This and the further sections discuss this implementation. *It shall be noted that no changes to the model will be made. Rather, all the expressions for the stresses and the tangents will be rewritten so that they can be computed only using the in-plane components of the deformation gradient ( $\mathbf{F}$ ) and its elastic part ( $\mathbf{F}_e$ ).*

#### 9.3.1 Stress and tangent computation

##### **Stress computation**

In plane stress scenario and for an incompressible material, the computation of stress can be simplified. The value of  $p$  in the equation 9.9 can be found by using the condition that  $\tau_{33} = 0$ . This condition can be imposed separately for the elastic and the viscous branches and the results can be combined. Beginning with the elastic branch, the term  $\frac{\partial \psi}{\partial \bar{\mathbf{b}}} \bar{\mathbf{b}}$  can be computed as

$$\frac{\partial \psi}{\partial \bar{\mathbf{b}}} \bar{\mathbf{b}} = \left[ \frac{\partial \psi}{\partial I_1} \mathbf{I} + \frac{\partial \psi}{\partial I_2} (I_1 \mathbf{I} - \mathbf{b}) \right] \bar{\mathbf{b}}, \quad (9.24)$$

where the incompressibility of the material has been taken into account. The deviatoric projection of the above term is

$$\mathbb{P} : \left( \frac{\partial \psi}{\partial \bar{\mathbf{b}}} \bar{\mathbf{b}} \right) = \left[ \frac{\partial \psi}{\partial I_1} \mathbf{I} + \frac{\partial \psi}{\partial I_2} (I_1 \mathbf{I} - \mathbf{b}) \right] \bar{\mathbf{b}} - \frac{1}{3} \left[ \frac{\partial \psi}{\partial I_1} I_1 + 2 \frac{\partial \psi}{\partial I_2} I_2 \right] \mathbf{I}. \quad (9.25)$$

The contribution of the elastic branch to  $\mathbf{p}$ , denoted  $p_e$ , can be written as (using  $\tau_{33} = 0$ )

$$p_e = 2 \left[ \frac{\partial \psi}{\partial I_1} b_{33} + \frac{\partial \psi}{\partial I_2} (I_1 b_{33} - b_{33}^2) \right] - \frac{2}{3} \left[ \frac{\partial \psi}{\partial I_1} I_1 + 2 \frac{\partial \psi}{\partial I_2} I_2 \right]. \quad (9.26)$$

The total elastic part of the stress can then be found as

$$-p_e \mathbf{I} + 2\mathbb{P} : \left( \frac{\partial \psi}{\partial \bar{\mathbf{b}}} \right) = 2 \frac{\partial \psi}{\partial I_1} (\mathbf{b} - b_{33} \mathbf{I}) + 2 \frac{\partial \psi}{\partial I_2} \left( I_1 (\mathbf{b} - b_{33} \mathbf{I}) - (\mathbf{b}^2 - b_{33}^2 \mathbf{I}) \right). \quad (9.27)$$

The above equation, written with its components restricted to within the plane, can be seen to be

$$\boldsymbol{\tau}^e = 2 \frac{\partial \psi}{\partial I_1} (\mathbf{b}^{2d} - b_{33} \mathbf{I}^{2d}) + 2 \frac{\partial \psi}{\partial I_2} \left( I_1 (\mathbf{b}^{2d} - b_{33} \mathbf{I}^{2d}) - ((\mathbf{b}^{2d})^2 - b_{33}^2 \mathbf{I}^{2d}) \right). \quad (9.28)$$

$\mathbf{b}^{2d}$  is the restriction of  $\mathbf{b}$  to within the plane. As a consequence of plane stress assumption,  $\mathbf{b}$  has been assumed to be of the form  $\mathbf{b} = \begin{bmatrix} \mathbf{b}^{2d} & \mathbf{o} \\ \mathbf{o}^T & b_{33} \end{bmatrix}$ . Expressing the first and the second invariants in terms of in-plane components as (realizing that  $b_{33} = 1/\det \mathbf{b}^{2d}$ )

$$I_1 = \text{tr}(\mathbf{b}^{2d}) + 1/\det(\mathbf{b}^{2d}), \quad (9.29)$$

$$I_2 = \frac{1}{2} \left[ (I_1(\mathbf{b}^{2d}))^2 - (\mathbf{b}^{2d} : \mathbf{b}^{2d} + 1/\det(\mathbf{b}^{2d})^2) \right], \quad (9.30)$$

the term  $\mathbf{b}^{2d} - b_{33} \mathbf{I}^{2d}$  in the equation 9.28 can now be simply written as  $\frac{\partial I_1}{\partial \mathbf{b}^{2d}} \mathbf{b}^{2d}$  and the term  $I_1(\mathbf{b}^{2d} - b_{33} \mathbf{I}^{2d}) - ((\mathbf{b}^{2d})^2 - b_{33}^2 \mathbf{I}^{2d})$  as  $\frac{\partial I_2}{\partial \mathbf{b}^{2d}} \mathbf{b}^{2d}$ . The total stress in the equation 9.28 then simply becomes

$$\boldsymbol{\tau}^e = 2 \left[ \frac{\partial \psi}{\partial I_1} \frac{\partial I_1}{\partial \mathbf{b}^{2d}} + \frac{\partial \psi}{\partial I_2} \frac{\partial I_2}{\partial \mathbf{b}^{2d}} \right] \mathbf{b}^{2d} = 2 \frac{\partial \psi}{\partial \mathbf{b}^{2d}} \mathbf{b}^{2d}. \quad (9.31)$$

By a similar exercise for the viscous branches, the viscous contribution to the total stress becomes

$$\boldsymbol{\tau}^v = 2 \frac{\partial \psi}{\partial \mathbf{b}_e^{2d}} \mathbf{b}_e^{2d}. \quad (9.32)$$

Hence the equations 9.5 and 9.9 become

$$\boldsymbol{\tau} = \boldsymbol{\tau}^e + \boldsymbol{\tau}^v, \quad \text{and} \quad (9.33)$$

$$\mathbf{S} = \mathbf{F}^{-1} \boldsymbol{\tau} \mathbf{F}^{-T}. \quad (9.34)$$

The above equations are restricted to in-plane components and the superscript  $2d$  has been eliminated for convenience. The total stress in the equation 9.33 can be written for the case of multiple (say,  $N$ ) viscous branches simply as  $\boldsymbol{\tau} = \boldsymbol{\tau}^e + \sum_{i=1}^N (\boldsymbol{\tau}^v)^{(i)}$ , where each of the  $(\boldsymbol{\tau}^v)^{(i)}$  s now denote the viscous stress in the corresponding viscous arm, defined as  $(\boldsymbol{\tau}^v)^{(i)} := 2 \frac{\partial \psi^{(i)}}{\partial (\mathbf{b}_e^{2d})^{(i)}} (\mathbf{b}_e^{2d})^{(i)}$ .  $(\mathbf{b}_e^{2d})^{(i)}$  is the left cauchy green tensor in the  $i^{\text{th}}$  viscous arm.

The two invariants written in terms of principal stretches become

$$I_1 = \lambda_A^2 + \lambda_B^2 + \lambda_C^2 = \lambda_A^2 + \lambda_B^2 + 1/\lambda_A^2 \lambda_B^2, \quad (9.35)$$

$$I_2 = \lambda_A^2 \lambda_B^2 + \lambda_B^2 \lambda_C^2 + \lambda_C^2 \lambda_A^2 = \lambda_A^2 \lambda_B^2 + 1/\lambda_A^2 + 1/\lambda_B^2, \quad (9.36)$$

where  $\lambda_C^2 = 1/\lambda_A^2\lambda_B^2$  has been used.

Using the above, the Kirchhoff stress can be written in principal basis to be

$$\tau_A = 2\lambda_A^2 \frac{\partial\psi}{\partial\lambda_A^2} = 2\lambda_A^2 \left[ \frac{\partial\psi}{\partial I_1} \frac{\partial I_1}{\partial\lambda_A^2} + \frac{\partial\psi}{\partial I_2} \frac{\partial I_2}{\partial\lambda_A^2} \right], \quad (9.37)$$

$$\tau_B = 2\lambda_B^2 \frac{\partial\psi}{\partial\lambda_B^2} = 2\lambda_B^2 \left[ \frac{\partial\psi}{\partial I_1} \frac{\partial I_1}{\partial\lambda_B^2} + \frac{\partial\psi}{\partial I_2} \frac{\partial I_2}{\partial\lambda_B^2} \right], \quad (9.38)$$

and  $\tau_C = 0$  as a consequence of the plane stress assumption. The partial derivatives of the invariants can be evaluated as

$$\frac{\partial I_1}{\partial\lambda_A^2} = 1 - 1/\lambda_A^4\lambda_B^2, \quad \frac{\partial I_1}{\partial\lambda_B^2} = 1 - 1/\lambda_A^2\lambda_B^4, \quad (9.39)$$

$$\frac{\partial I_2}{\partial\lambda_A^2} = \lambda_B^2 - 1/\lambda_A^4, \quad \frac{\partial I_2}{\partial\lambda_B^2} = \lambda_A^2 - 1/\lambda_B^4. \quad (9.40)$$

The stresses can be expressed in global Cartesian basis by using

$$\boldsymbol{\tau} = \tau_1 \mathbf{n}_1 \otimes \mathbf{n}_1 + \tau_2 \mathbf{n}_2 \otimes \mathbf{n}_2, \quad (9.41)$$

where  $\mathbf{n}_1$  and  $\mathbf{n}_2$  are the eigen vectors of  $\mathbf{b} = \mathbf{F}\mathbf{F}^T$ . As a recollection, the stresses obtained this way are the total stresses,  $\boldsymbol{\tau} = -p\mathbf{J}\mathbf{I} + \boldsymbol{\tau}^{iso} = -p\mathbf{J}\mathbf{I} + \mathbb{P} : \bar{\boldsymbol{\tau}}$ .

Stresses can be similarly computed in viscous branches where  $\lambda$  is replaced by  $\lambda_e$ , which are the eigen values of  $\mathbf{b}_e = \mathbf{F}_e\mathbf{F}_e^T$  and the  $\psi$  replaced by the strain energy of the corresponding viscous arm.

### Integration of evolution equation

For viscous branches, the evolution equation remains same even in the plane stress scenario. The residual can be written, similar to the equation 9.22 as

$$r_A = \epsilon_{Ae} + \frac{\gamma_0\Delta t}{2\eta_D} \text{dev}(\tau_A) - (\epsilon_{Ae})_{tr} = 0, \quad (9.42)$$

Since plane stress condition is assumed to prevail, only the in-plane components of the above equation are considered. Also, the deviatoric part of the Kirchhoff stress can be expressed as  $\text{dev}(\boldsymbol{\tau}) = \boldsymbol{\tau} + p\mathbf{I}$ , where  $p$  is the Lagrange multiplier that enforces incompressibility, which is found by using the condition that  $\tau_3 = 0$ .  $\boldsymbol{\tau}$  can be evaluated by using the procedure in the previous section. The expression for  $p$  can be seen to be

$$p = -\frac{\tau_1 + \tau_2}{3}. \quad (9.43)$$

The above equation can be obtained by taking the trace of the equation 9.9 and realizing that  $\tau_3 = 0$  as a consequence of plane stress assumption and that trace of the deviatoric projector is 0. The in-plane evolution equations then become

$$r_1 = \epsilon_{1e} + \frac{\gamma_0\Delta t}{2\eta_D} (\tau_1 + p) - (\epsilon_{1e})_{tr} = 0, \quad (9.44)$$

$$r_2 = \epsilon_{2e} + \frac{\gamma_0\Delta t}{2\eta_D} (\tau_2 + p) - (\epsilon_{2e})_{tr} = 0. \quad (9.45)$$

In the third direction, the evolution equation becomes  $\epsilon_{3e} + \frac{\gamma_0\Delta t}{2\eta_D} p - (\epsilon_{3e})_{tr} = 0$ . It can be shown that solving the first two equations exactly will result in the third

equation being satisfied automatically. Adding the equations 9.44 and 9.45 will result in  $\epsilon_{1e} + \epsilon_{2e} + \frac{\gamma_0 \Delta t}{2\eta_D} (\tau_1 + \tau_2 + 2p) - [(\epsilon_{1e})_{tr} + (\epsilon_{2e})_{tr}] = 0$ . This, in conjunction with the assumption of incompressibility and plane stress condition, results in  $\epsilon_{3e} + \frac{\gamma_0 \Delta t}{2\eta_D} p - (\epsilon_{3e})_{tr} = 0$ , which is the third equation.

The equations 9.44 and 9.45 are solved iteratively using Newton method.

$$\mathbf{r}_A^{(k+1)} = \mathbf{r}_A^{(k)} + \frac{\partial \mathbf{r}_A}{\partial \epsilon_{Be}} \Delta \epsilon_{Be} = 0. \quad (9.46)$$

This in turn requires the evaluation of  $K_{AB} = \frac{\partial \mathbf{r}_A}{\partial \epsilon_{Be}}$ . This can be evaluated as

$$K_{AB} = \frac{\partial \mathbf{r}_A}{\partial \epsilon_{Be}} = \delta_{AB} + \frac{\gamma_0 \Delta t}{2\eta_D} \left( \frac{\partial \tau_A}{\partial \epsilon_{Be}} + \frac{\partial p}{\partial \epsilon_{Be}} \right). \quad (9.47)$$

The pressure derivative can be computed from equation 9.43 as

$$\frac{\partial p}{\partial \epsilon_{Ae}} = -\frac{1}{3} \left( \frac{\partial \tau_1}{\partial \epsilon_{Ae}} + \frac{\partial \tau_2}{\partial \epsilon_{Ae}} \right). \quad (9.48)$$

The computation of derivative  $\frac{\partial \tau_A}{\partial \epsilon_{Be}}$  can be carried out as shown in the following sections.

### 9.3.2 Tangent computation

#### For elastic branch

The computation of tangent first involves the computation of  $\mathfrak{C} = 2 \frac{\partial \mathbf{S}}{\partial \mathbf{C}}$ . The derivative can be computed by noting that (Bonet, 2001)

$$\dot{\mathbf{S}} = \frac{\partial \mathbf{S}}{\partial \mathbf{C}} : \dot{\mathbf{C}}. \quad (9.49)$$

Since  $\mathbf{C} = \sum_{i=1}^2 \lambda_i^2 \mathbf{N}_i \otimes \mathbf{N}_i$ ,  $\dot{\mathbf{C}} = \sum_{i=1}^2 \left[ \frac{\partial \lambda_i^2}{\partial t} \mathbf{N}_i \otimes \mathbf{N}_i + \lambda_i^2 \dot{\mathbf{N}}_i \otimes \mathbf{N}_i + \lambda_i^2 \mathbf{N}_i \otimes \dot{\mathbf{N}}_i \right]$ .  $\dot{\mathbf{N}}_i = \sum_{j=1}^2 W_{ij} \mathbf{N}_j$ , where  $W_{ij} = -W_{ji}$  are the components of a skew symmetric tensor. Hence

$$\dot{\mathbf{C}} = \sum_{i=1}^2 \frac{\partial \lambda_i^2}{\partial t} \mathbf{N}_i \otimes \mathbf{N}_i + \sum_{i,j=1, i \neq j}^2 W_{ij} (\lambda_i^2 - \lambda_j^2) \mathbf{N}_i \otimes \mathbf{N}_j. \quad (9.50)$$

As a consequence of isotropy,  $\mathbf{S}$  and  $\mathbf{C}$  share the eigen vectors. Hence, following the same procedure,

$$\dot{\mathbf{S}} = \sum_{i,j=1}^2 2 \frac{\partial^2 \psi}{\partial \lambda_i^2 \partial \lambda_j^2} \frac{\partial \lambda_j^2}{\partial t} \mathbf{N}_i \otimes \mathbf{N}_i + \sum_{i,j=1, i \neq j}^2 W_{ij} (S_i - S_j) \mathbf{N}_i \otimes \mathbf{N}_j. \quad (9.51)$$

The tangent can hence be written as

$$\mathfrak{C} = \sum_{i,j=1}^2 4 \frac{\partial^2 \psi}{\partial \lambda_i^2 \partial \lambda_j^2} \mathbf{N}_i \otimes \mathbf{N}_i \otimes \mathbf{N}_j \otimes \mathbf{N}_j + \sum_{i,j=1, i \neq j}^2 \frac{S_i - S_j}{\lambda_i^2 - \lambda_j^2} (\mathbf{N}_i \otimes \mathbf{N}_j \otimes \mathbf{N}_i \otimes \mathbf{N}_j + \mathbf{N}_i \otimes \mathbf{N}_j \otimes \mathbf{N}_j \otimes \mathbf{N}_i). \quad (9.52)$$

Its push forward to the spatial configuration can be seen to be

$$\begin{aligned} \mathbf{c} = & \sum_{i,j=1}^2 (C_{ij} - 2\sigma_i\delta_{ij})\mathbf{n}_i \otimes \mathbf{n}_i \otimes \mathbf{n}_j \otimes \mathbf{n}_j \\ & + \sum_{i,j=1, i \neq j}^2 \frac{\sigma_i\lambda_j^2 - \sigma_j\lambda_i^2}{\lambda_i^2 - \lambda_j^2} (\mathbf{n}_i \otimes \mathbf{n}_j \otimes \mathbf{n}_i \otimes \mathbf{n}_j + \mathbf{n}_i \otimes \mathbf{n}_j \otimes \mathbf{n}_j \otimes \mathbf{n}_i), \end{aligned} \quad (9.53)$$

where  $C_{ij} = \frac{\partial^2\psi}{\partial \ln \lambda_i \partial \ln \lambda_j} = \frac{\partial \tau_i}{\partial \epsilon_j}$  and  $\sigma_i = \tau_i$ , since the material is incompressible.

The components of the above fourth order tensor can be stored in a matrix as

$$[\mathbf{c}] = \begin{bmatrix} 1111 & 1122 & 1112 \\ 2211 & 2222 & 2212 \\ 1211 & 1222 & 1212 \end{bmatrix}_{\mathbf{n}_1, \mathbf{n}_2}. \quad (9.54)$$

The components of the tangent can be converted to Cartesian basis by using the transformation (Reese & Wriggers, 1995)

$$[\mathbf{c}]_{(\mathbf{e}_1, \mathbf{e}_2)} = [\mathbf{P}][\mathbf{c}]_{(\mathbf{n}_1, \mathbf{n}_2)}[\mathbf{P}]^T, \quad (9.55)$$

where

$$[\mathbf{P}] = \begin{bmatrix} Q_{11}^2 & Q_{12}^2 & 2Q_{11}Q_{12} \\ Q_{21}^2 & Q_{22}^2 & 2Q_{21}Q_{22} \\ Q_{11}Q_{21} & Q_{12}Q_{22} & Q_{11}Q_{22} + Q_{12}Q_{21} \end{bmatrix}. \quad (9.56)$$

Here,  $Q_{ij}$ s are the elements of  $[\mathbf{Q}]$  matrix which is the transpose of  $[\tilde{\mathbf{Q}}]$ ,  $[\mathbf{Q}] = [\tilde{\mathbf{Q}}]^T$ . The columns of  $[\tilde{\mathbf{Q}}]$  matrix are the components of eigen vectors of  $\mathbf{b}$  in cartesian basis.

The tangent to be supplied to abaqus ( $\mathcal{C}^{(JK)}$ ) corresponds to the Jaumann rate of the Kirchhoff stress (N. Nguyen & Waas, 2016) written as

$$\overset{\nabla}{\boldsymbol{\tau}}^{(JK)} = \dot{\boldsymbol{\tau}} + \boldsymbol{\tau}\mathbf{W} - \mathbf{W}\boldsymbol{\tau} = \mathcal{C}^{(JK)} : \mathbf{d}. \quad (9.57)$$

$\mathcal{C}^{(JK)}$  is related to  $\mathbf{c}$  as

$$C_{ijkl}^{(JK)} = c_{ijkl} + \frac{1}{2}(\sigma_{ij}\delta_{kl} + \sigma_{kl}\delta_{ij} + \sigma_{il}\delta_{jk} + \sigma_{jk}\delta_{il}). \quad (9.58)$$

The computation of  $\mathbf{c}$  requires the computation of  $\frac{\partial \tau_i}{\partial \epsilon_j}$ , which can be carried out as follows

$$\frac{\partial \tau_i}{\partial \epsilon_j} = 2\lambda_j^2 \frac{\partial \tau_i}{\partial \lambda_j^2}, \quad i,j=1,2. \quad (9.59)$$

$$\frac{\partial \tau_i}{\partial \lambda_j^2} = 2 \left[ \frac{\partial^2 \psi}{\partial \lambda_j^2 \partial I_1} \lambda_i^2 \frac{\partial I_1}{\partial \lambda_i^2} + \frac{\partial \psi}{\partial I_1} \frac{\partial}{\partial \lambda_j^2} \left( \lambda_i^2 \frac{\partial I_1}{\partial \lambda_i^2} \right) + \frac{\partial^2 \psi}{\partial \lambda_j^2 \partial I_2} \lambda_i^2 \frac{\partial I_2}{\partial \lambda_i^2} + \frac{\partial \psi}{\partial I_2} \frac{\partial}{\partial \lambda_j^2} \left( \lambda_i^2 \frac{\partial I_2}{\partial \lambda_i^2} \right) \right]. \quad (9.60)$$

The partial derivatives can be further evaluated as

$$\frac{\partial^2 \psi}{\partial \lambda_i^2 \partial I_j} = \frac{\partial^2 \psi}{\partial I_1 \partial I_j} \frac{\partial I_1}{\partial \lambda_i^2} + \frac{\partial^2 \psi}{\partial I_2 \partial I_j} \frac{\partial I_2}{\partial \lambda_i^2} \quad (9.61)$$

$$\frac{\partial}{\partial \lambda_A^2} \left( \lambda_A^2 \frac{\partial I_1}{\partial \lambda_A^2} \right) = 1 + 1/\lambda_A^4 \lambda_B^2, \quad \frac{\partial}{\partial \lambda_B^2} \left( \lambda_A^2 \frac{\partial I_1}{\partial \lambda_A^2} \right) = 1/\lambda_A^2 \lambda_B^4, \quad (9.62)$$

$$\frac{\partial}{\partial \lambda_A^2} \left( \lambda_A^2 \frac{\partial I_2}{\partial \lambda_A^2} \right) = \lambda_B^2 + 1/\lambda_A^4, \quad \frac{\partial}{\partial \lambda_B^2} \left( \lambda_A^2 \frac{\partial I_2}{\partial \lambda_A^2} \right) = \lambda_A^2. \quad (9.63)$$

**Remark.** The total stress and tangent computation in the case of plane stress condition for incompressible materials involves the computation of derivatives **after** enforcing all the material (incompressibility) and geometric (plane stress) constraints.

In case of equal eigen values  $\lambda_1 = \lambda_2$ , the second term of equation 9.53 takes a  $\frac{0}{0}$  form and so, L'Hospital's rule is used to compute it.

$$\lim_{\lambda_2 \rightarrow \lambda_1} \frac{\sigma_1 \lambda_2^2 - \sigma_2 \lambda_1^2}{\lambda_1^2 - \lambda_2^2} = \frac{1}{2} \left[ \frac{\partial^2 \psi}{\partial \epsilon_2 \partial \epsilon_2} - \frac{\partial^2 \psi}{\partial \epsilon_1 \partial \epsilon_2} \right] - \sigma_2 = \frac{1}{2} \left[ \frac{\partial \tau_2}{\partial \epsilon_2} - \frac{\partial \tau_2}{\partial \epsilon_1} \right] - \sigma_2. \quad (9.64)$$

### For viscous branches

For the viscous branches, the following procedure will be used to compute the tangent similar to as in Reese and Govindjee, 1998. All the stress and strain components are now restricted to within the plane.

In the elastic trial state, since the inelastic strain is held fixed,  $\mathbf{F}^n = \mathbf{F}_e^{tr} \mathbf{F}_i^{n-1} \implies \mathbf{C}^n = (\mathbf{F}_i^{n-1})^T \mathbf{C}_e^{tr} \mathbf{F}_i^{n-1}$ . Hence,

$$\frac{\partial S_{IJ}}{\partial C_{KL}} = \frac{\partial S_{IJ}}{\partial (C_e^{tr})_{\alpha\beta}} \frac{\partial (C_e^{tr})_{\alpha\beta}}{\partial C_{KL}} = \left( (\mathbf{F}_i^{n-1})^{-1} \right)_{K\alpha} \left( (\mathbf{F}_i^{n-1})^{-1} \right)_{L\beta} \frac{\partial S_{IJ}}{\partial (C_e^{tr})_{\alpha\beta}}. \quad (9.65)$$

where the symmetry of  $C_e^{tr}$  has been used. Since in viscous branches,

$$\mathbf{S} = \mathbf{F}^{-1} \boldsymbol{\tau} \mathbf{F}^{-T} = (\mathbf{F}_i^{n-1})^{-1} \cdot \underbrace{(\mathbf{F}_e^{tr})^{-1} \boldsymbol{\tau} (\mathbf{F}_e^{tr})^{-T}}_{\tilde{\mathbf{S}}} \cdot (\mathbf{F}_i^{n-1})^{-T}, \quad (9.66)$$

the stress derivative can be further refined as

$$\frac{\partial S_{IJ}}{\partial (C_e^{tr})_{\alpha\beta}} = \left( (\mathbf{F}_i^{n-1})^{-1} \right)_{I\gamma} \left( (\mathbf{F}_i^{n-1})^{-1} \right)_{J\delta} \frac{\partial \tilde{S}_{\gamma\delta}}{\partial (C_e^{tr})_{\alpha\beta}}. \quad (9.67)$$

Hence,

$$2 \frac{\partial S_{IJ}}{\partial C_{KL}} = 2 \left( (\mathbf{F}_i^{n-1})^{-1} \right)_{I\gamma} \left( (\mathbf{F}_i^{n-1})^{-1} \right)_{J\delta} \left( (\mathbf{F}_i^{n-1})^{-1} \right)_{K\alpha} \left( (\mathbf{F}_i^{n-1})^{-1} \right)_{L\beta} \frac{\partial \tilde{S}_{\gamma\delta}}{\partial (C_e^{tr})_{\alpha\beta}}. \quad (9.68)$$

The push-forward of above by  $\mathbf{F}$  results in

$$\begin{aligned} c_{ijkl} &= 2 F_{iI} F_{jJ} F_{kK} F_{lL} \frac{\partial S_{IJ}}{\partial C_{KL}} \\ &= 2 (\mathbf{F}_e^{tr})_{i\gamma} (\mathbf{F}_e^{tr})_{j\delta} (\mathbf{F}_e^{tr})_{k\alpha} (\mathbf{F}_e^{tr})_{l\beta} \frac{\partial \tilde{S}_{\gamma\delta}}{\partial (C_e^{tr})_{\alpha\beta}}. \end{aligned} \quad (9.69)$$

$\tilde{\mathbf{S}}$ , written in Eigen basis is

$$\tilde{\mathbf{S}} = \sum_{A=1}^2 \frac{\tau_A}{(\lambda_{Ae})_{tr}^2} \tilde{\mathbf{N}}_A \otimes \tilde{\mathbf{N}}_A. \quad (9.70)$$

It is to be noted that the  $\tau_A$  in the above equation is a function of  $\epsilon_e$ . The development from here is similar to that used to arrive at the equation 9.53 except that  $C_{ij}$

in that equation will be replaced by  $C_{ij}^{alg}$ , which will be defined below. A crucial factor is that  $\mathbf{b}_e$  and  $(\mathbf{b}_e)_{tr}$  share the same eigen space as a consequence of isotropy.

$$\begin{aligned} \mathbf{c} = & \sum_{i,j=1}^2 (C_{ij}^{alg} - 2\sigma_i \delta_{ij}) \mathbf{n}_i \otimes \mathbf{n}_i \otimes \mathbf{n}_j \otimes \mathbf{n}_j \\ & + \sum_{i,j=1, i \neq j}^2 \frac{\sigma_i (\lambda_j)_{tr}^2 - \sigma_j (\lambda_i)_{tr}^2}{(\lambda_i)_{tr}^2 - (\lambda_j)_{tr}^2} (\mathbf{n}_i \otimes \mathbf{n}_j \otimes \mathbf{n}_i \otimes \mathbf{n}_j + \mathbf{n}_i \otimes \mathbf{n}_j \otimes \mathbf{n}_j \otimes \mathbf{n}_i). \end{aligned} \quad (9.71)$$

In the above,  $C_{AC}^{alg} = \frac{\partial \tau_A}{\partial (\epsilon_{Ce})_{tr}}$ . Since  $\tau_{AS}$  are a function of  $\epsilon_e$ s, the derivative is computed using chain rule.

$$\frac{\partial \tau_A}{\partial (\epsilon_{Ce})_{tr}} = \frac{\partial \tau_A}{\partial \epsilon_{Be}} \frac{\partial \epsilon_{Be}}{\partial (\epsilon_{Ce})_{tr}}. \quad (9.72)$$

The derivative  $\frac{\partial \epsilon_{Be}}{\partial (\epsilon_{Ce})_{tr}}$  can be computed by realizing that the equations  $r_B = 0$  are satisfied at the end of local Newton iterations and hence are valid at all the times during the global Newton iterations. Hence, during the global Newton iterations,  $\frac{\partial r_B}{\partial (\epsilon_{Ce})_{tr}} = 0$  as well. Hence,

$$\frac{\partial \epsilon_{Be}}{\partial (\epsilon_{Ce})_{tr}} = K_{BC}^{-1}, \quad (9.73)$$

where  $K_{BC}$  is defined in equation 9.47.

The expression for dissipation becomes

$$\mathcal{D} = \frac{1}{\eta_D} \text{dev}\{\boldsymbol{\tau}_{NEQ}\} : \text{dev}\{\boldsymbol{\tau}_{NEQ}\} = (\boldsymbol{\tau} + p\mathbf{I}) : (\boldsymbol{\tau} + p\mathbf{I}) + p^2, \quad (9.74)$$

which can be seen to be positive since  $\eta_D > 0$ . In the above equation,  $\boldsymbol{\tau}$  is as evaluated in the equation 9.41.

### 9.3.3 Implementation details

The above has been implemented into a UMAT subroutine of Abaqus. The subroutine computes the updated stress and tangent for a given time step and also updates the internal variables. The implementation details will be discussed in this section.

The deformation gradient is obtained as an input to the subroutine from Abaqus. The internal variables ( $C_i$ ) at the beginning of the step are stored in an array. The working of the subroutine can be seen below.

As can be seen, the internal variables are updated and the strain energy density and dissipation are computed with the updated values of  $\mathbf{b}_e$  and  $\boldsymbol{\tau}$ . The value of  $TOL$  has been chosen to be  $10^{-5}$ .

The C++ implementation of the model can be found at Kamasamudram, 2021 and in the appendix C.

## 9.4 MODEL CHECKS

### 9.4.1 Hyperelastic case

The correctness of the implementation of the material model in the UMAT subroutine will be checked first. The polynomial strain energy functional calibrated in the

**Data:**  $F^n, C_i^{n-1}, \Delta t$   
**Result:**  $\tau^n, C_i^n, C(\mathcal{JK}), \psi^n, \mathcal{D}^n$   
 $(\mathbf{b}_e)_{tr} = F^n (C_i^{n-1})^{-1} (F^n)^T$ ;  
 Compute  $(\lambda_e)_{tr}$ s and  $\mathbf{n}_{AS}$  so that  $(\mathbf{b}_e)_{tr} = \sum_{A=1}^2 (\lambda_{Ae})_{tr}^2 \mathbf{n}_A \otimes \mathbf{n}_A$ ;  
 Define  $(\epsilon_{Ae})_{tr} = \ln((\lambda_{Ae})_{tr})$ ;  
 $k = 0, \epsilon_{Ae} \leftarrow (\epsilon_{Ae})_{tr}$ ;  
**do**  
   Compute  $\tau$  and  $p$  from  $\epsilon_{Ae}$ ;  
    $r_A := \epsilon_{Ae} + \frac{\Delta t}{2\eta}(\tau_A + p) - (\epsilon_{Ae})_{tr} = 0$ ;  
   Compute  $\frac{\partial \tau_A}{\partial \epsilon_{Be}}, \frac{\partial p}{\partial \epsilon_{Be}}$ ;  
    $K_{AB} = \delta_{AB} + \frac{\Delta t}{2\eta} \left( \frac{\partial \tau_A}{\partial \epsilon_{Be}} + \frac{\partial p}{\partial \epsilon_{Be}} \right)$ ;  
    $\Delta \epsilon_{Ae}^k = -K_{AB}^{-1} r_A$ ;  
    $\epsilon_{Ae}^{k+1} \leftarrow \epsilon_{Ae}^k + \Delta \epsilon_{Ae}^k$ ;  
    $k \leftarrow k + 1$   
**while**  $\|r_A\| > TOL$ ;  
 Update  $\tau^n, p, \lambda_{Ae} = \exp(\epsilon_{Ae})$ , and  $K_{AB}$ ;  
 $\mathbf{b}_e = \sum_{A=1}^2 \lambda_{Ae}^2 \mathbf{n}_A \otimes \mathbf{n}_A, \mathbf{b}_e^{-1} = \sum_{A=1}^2 \lambda_{Ae}^{-2} \mathbf{n}_A \otimes \mathbf{n}_A$ ;  
 $C_i^n = (F^n)^T \mathbf{b}_e^{-1} F^n$ ;  
 Compute  $C(\mathcal{JK})$  using  $C^{alg}, \tau_A$ , and  $\lambda_{Ae}$ ;  
 Compute  $\psi^n$  and  $\mathcal{D}^n$ ;  
**Algorithm 1:** Steps followed in UMAT for Finite Viscoelastic model

chapter 7 will be used. The results of the predictions from UMAT will be compared with that from Abaqus to check the sanity of the implementation.

The geometry along with the mesh can be seen in the figure 9.1. The top end of the sample is subjected to displacement  $u_x = 40$  mm, and  $u_y = 50$  mm, while the bottom end is held fixed. The 22 component of Cauchy stress,  $\sigma$  predicted by the UMAT and the internal Abaqus implementation can be seen in figure 9.2. It can be seen that they are identical. The other components of the Cauchy stress have been found identical as well and will be presented in the appendix B.

#### 9.4.2 Viscoelastic case - small strains and small perturbations

Under small strain conditions, the deformation gradient can be approximated by  $F \approx I + \epsilon$  and  $C \approx I + 2\epsilon$ . The principal stretches can be approximated as  $\lambda_1^2 \approx 1 + 2\epsilon_1$  and  $\lambda_2^2 \approx 1 + 2\epsilon_2$ , where the  $\epsilon_i$ s are the eigen values of  $\epsilon$ , the small strain tensor. The small perturbation assumption allows similar approximations for the viscous branches as well.  $F_e \approx I + \epsilon_e$  and  $C_e \approx I + 2\epsilon_e$ . Similarly,  $\lambda_{1e}^2 \approx 1 + 2\epsilon_{1e}$  and  $\lambda_{2e}^2 \approx 1 + 2\epsilon_{2e}$ . Plane stress conditions are assumed to prevail. Material is taken to be incompressible. In that case, the stresses in the principal directions in the equations 9.37 and 9.38 become

$$\tau_A \approx 2C_{10} (4\epsilon_A + 2\epsilon_B), \quad (9.75)$$

$$\tau_B \approx 2C_{10} (2\epsilon_A + 4\epsilon_B). \quad (9.76)$$

$\frac{\partial \psi}{\partial I_1}$  has been approximated by  $C_{10}$  for polynomial model. The equation 9.43 becomes

$$p \approx -4C_{10} (\epsilon_A + \epsilon_B). \quad (9.77)$$

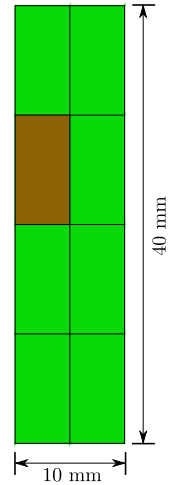


Figure 9.1: Geometry and mesh to test the implementation of UMAT.

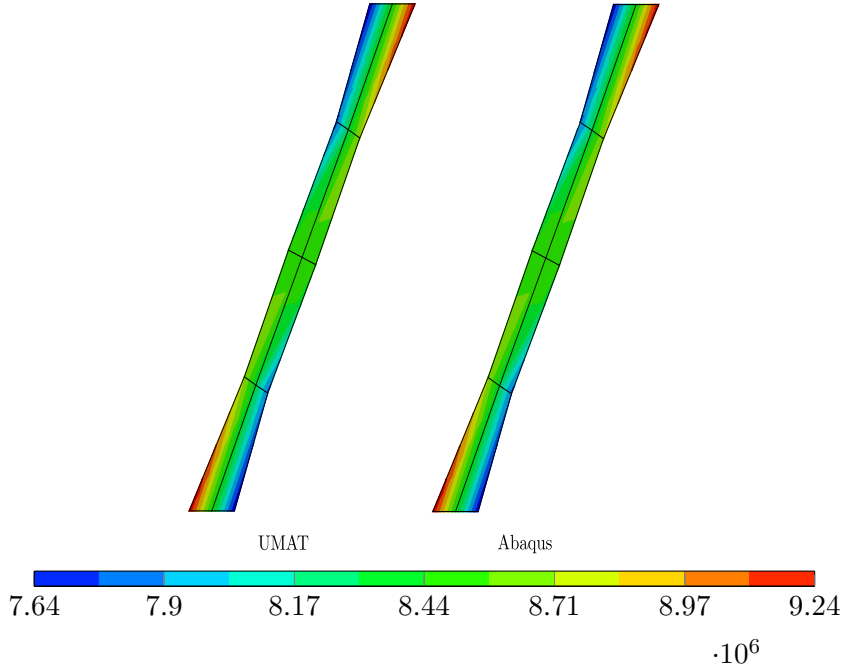


Figure 9.2:  $\sigma_{22}$  (in Pa) predicted by UMAT and the polynomial model from Abaqus.

Then  $\tau_A + p = 4C_{10}\epsilon_A$  and  $\tau_B + p = 4C_{10}\epsilon_B$ . The evolution equations 9.44 and 9.45 become, with  $\gamma_0 = 1$ ,

$$r_1 = \epsilon_{1e} + \frac{\Delta t}{2\eta_D} 4C_{10}\epsilon_{1e} - (\epsilon_{1e})_{tr} = 0 \implies \epsilon_{1e} = \frac{(\epsilon_{1e})_{tr}}{1 + \frac{\Delta t}{\tau}}, \quad (9.78)$$

$$r_2 = \epsilon_{2e} + \frac{\Delta t}{2\eta_D} 4C_{10}\epsilon_{2e} - (\epsilon_{2e})_{tr} = 0 \implies \epsilon_{2e} = \frac{(\epsilon_{2e})_{tr}}{1 + \frac{\Delta t}{\tau}}, \quad (9.79)$$

where  $\eta_D := 2C_{10}\tau$  has been used. The above equations can be seen to be the backward Euler discretization in time of the PDE

$$\dot{\epsilon}_{Ae} + \frac{\epsilon_{Ae}}{\tau} = \dot{\epsilon}_A. \quad (9.80)$$

This can be proved by using  $\dot{\epsilon}_{Ae} = \frac{\epsilon_{Ae}^n - \epsilon_{Ae}^{n-1}}{\Delta t}$  and  $\dot{\epsilon}_A = \frac{\epsilon_A^n - \epsilon_A^{n-1}}{\Delta t}$ . The equation 9.80 then becomes

$$\frac{\epsilon_{Ae}^n - \epsilon_{Ae}^{n-1}}{\Delta t} + \frac{\epsilon_{Ae}^n}{\tau} = \frac{\epsilon_A^n - \epsilon_A^{n-1}}{\Delta t} \implies \epsilon_{Ae}^n = \frac{(\epsilon_{Ae})_{tr}}{1 + \frac{\Delta t}{\tau}}, \quad (9.81)$$

which is the equation 9.79. In the above equation,  $(\epsilon_{Ae})_{tr} = \epsilon_A^n - \epsilon_{Av}^{n-1} = \epsilon_A^n - (\epsilon_A^{n-1} - \epsilon_{Ae}^{n-1})$ .

The FLV model in equation A.27 can be written in the case of small strains and small perturbations by realizing that

$$C_{33}^s = \frac{1}{\det C_{2d}^s} \approx 1, \quad \forall \quad 0 \leq s \leq t, \quad (9.82)$$

$$(C_{2d}^s)^{-1} \approx \mathbf{I} - 2\epsilon^s, \quad \forall \quad 0 \leq s \leq t, \quad (9.83)$$

$$\text{tr}(\hat{\mathbf{S}}^s C_{2d}^s) = \text{tr}(\tau^s), \quad \forall \quad 0 \leq s \leq t, \quad (9.84)$$

$$\hat{\mathbf{S}}^s \approx \tau^s \quad \forall \quad 0 \leq s \leq t. \quad (9.85)$$

Using all the above, equation A.27 can be written as

$$\tau_A = \int_{-\infty}^t g(t-s) \frac{\partial \tau_A^s}{\partial s} ds = \tau_A^\infty + \tau_{Ae}, \quad (9.86)$$

where  $\tau_A^\infty$  is the stress in the elastic branch and  $\tau_{Ae} = 2C_{10}(4\epsilon_{Ae} + 2\epsilon_{Be})$  is the stress in the viscous branch,  $\epsilon_{Ae} = \int_{-\infty}^t \exp(-\frac{t-s}{\tau}) \frac{\partial \epsilon_A}{\partial s} ds$ . This, in turn, can be seen to be the analytical solution of equation 9.80. Hence, both FLV and FV models can be seen to give the exactly same result in the limit  $\frac{\Delta t}{\tau} \rightarrow 0$ . However, when  $\frac{\Delta t}{\tau}$  does not tend to 0, the two models can result in slightly different result as the FLV model uses the semi-group property of the exponent to integrate the equations while FV model uses backward Euler.

The predictions of FLV and FV models are examined for the geometry in figure 9.1. The top portion of the model is fixed in the x-direction,  $u_x = 0$  and is displaced in y-direction as follows. It is subjected to a displacement of 5 mm in  $5 \times 10^6$  sec to make sure that the viscoelastic effects do not come into the picture. It is then subjected to a cyclic displacement  $A + B \sin(2\pi\omega t)$ , where  $A = 5$  mm,  $B = 2$  mm, and  $\omega = 1000 \text{ s}^{-1}$ . The constants  $g_1$  and  $g_2$  for FLV have been taken to be 0.3 and 0.4, respectively, while  $\tau_1$  and  $\tau_2$  to be  $1 \times 10^3$  s and  $1 \times 10^4$  s, respectively. The stiffness ratios of FV model are adjusted accordingly using the equation 9.88 and the  $\eta_{Ds}$  are computed as  $2C_{10}\tau$ . Time step size has been set to  $1 \times 10^{-4}$  s. Hence,  $\frac{\Delta t}{\tau}$  is about  $10^{-7}$ . The evolution of  $\sigma_{22}$  and  $\epsilon_{22}$  with time for the two models along with the difference between them at the centroid of the element shaded in brown in the figure 9.1 can be seen in the figure 9.3.

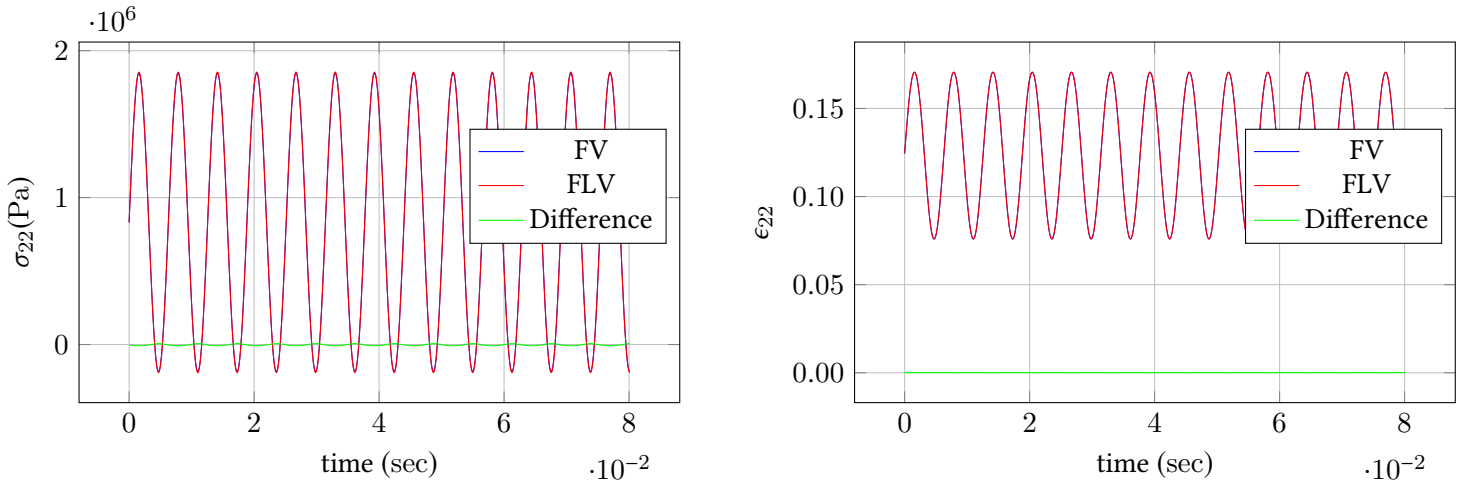


Figure 9.3:  $\sigma_{22}$  and  $\epsilon_{22}$  vs time for FLV and FV models. The FLV model has already been implemented within Abaqus while the FV model in the UMAT.

As can be seen, the two models predict the same result within plotting accuracy. The difference between the stresses predicted by them lies within 3% of the maximum value and the difference between the strains lies within 0.2% of the maximum value. This demonstrates the accuracy of implementation of the FV model into the UMAT subroutine.

### 9.4.3 Viscoelastic case - large strains and small perturbations

In this case, the approximations of  $F_e$  and  $C_e$  in the previous section still hold. However, the background strains are taken to be finite and so, they cannot be

approximated using small strain measures. In this case, the evolution equations for FV model for viscous branches remain similar to the equation 9.79, except that the total strains,  $\epsilon_A$ , are now logarithmic,  $\epsilon = \frac{1}{2} \ln C$ . The evolution equations in this case can be shown to be exactly that of Lubliner, 1985.

The model in the figure 9.1 is again used to test this scenario. The top edge of the model is fixed in the x-direction,  $u_x = 0$  and is displaced first vertically by 40 mm in a span of  $5 \times 10^7$  sec. It is then subjected to a cyclic displacement  $A + B \sin(2\pi\omega t)$ , where  $A = 40$  mm,  $B = 2$  mm, and  $\omega = 1000 \text{ s}^{-1}$ . The model coefficients are as in the previous section and the time step has been set to  $1 \times 10^{-4}$  s as well.

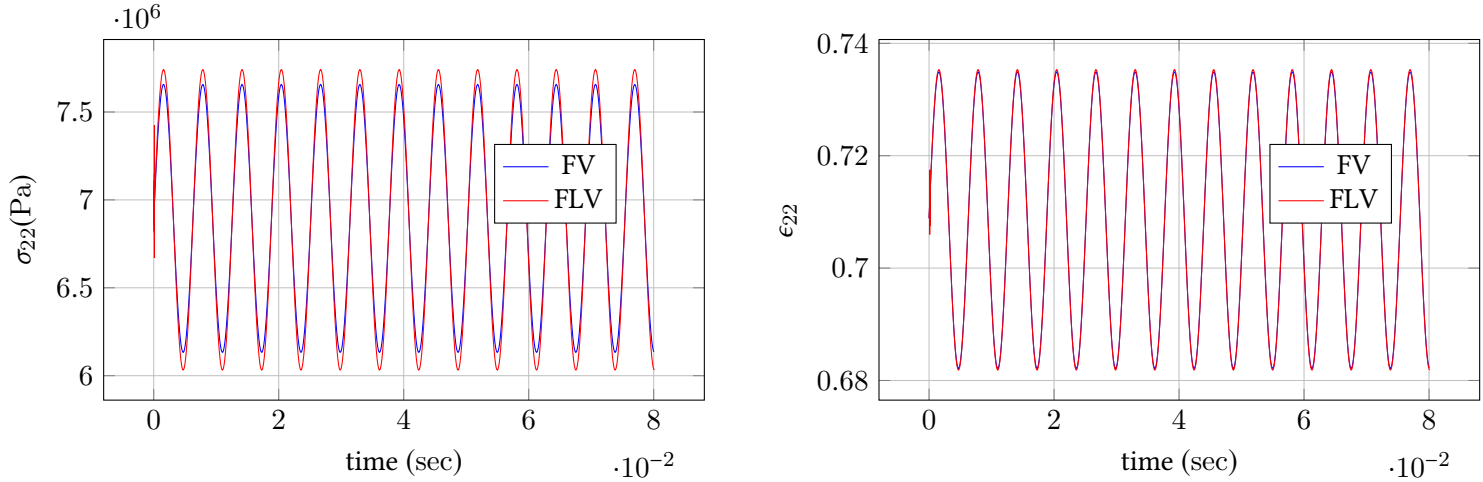


Figure 9.4:  $\sigma_{22}$  and  $\epsilon_{22}$  vs time for FLV and FV models. Small perturbations are imposed on large background strains.  $\epsilon_{22}$  is the 22 component of the logarithmic strain.

It can be seen from the figure 9.4 that the two models predict slightly different values of stresses at the same strain level. The FV model predicts a slightly smaller stress level than the FLV model.

The difference between the FLV and the FV models in this case can be seen by writing the FLV model for the case of small perturbations superposed on large background deformations. For this case, FLV model becomes

$$\mathbf{S}_{2d} \approx \hat{\mathbf{S}}_{2d}^{\infty} + \hat{\mathbf{S}}_{2d}^v. \quad (9.87)$$

In the above,  $\hat{\mathbf{S}}_{2d}^v \approx \int_{-\infty}^t g(t-s) \frac{\partial \hat{\mathbf{S}}^s}{\partial s} ds$ . It has been assumed for times  $t > t_1$ , where  $t_1$  is the time when the specimen is stretched to the target pre-stretch level (in this case  $5 \times 10^7$  s),  $\mathbf{F}(t)$  can be written as  $\mathbf{F}(t) = \mathbf{F}(t_1) \mathbf{F}_{rel}$ , where  $\mathbf{F}_{rel}$  is the relative deformation gradient. Since the perturbations imposed are infinitesimal,  $\mathbf{F}_{rel}$  has been assumed to be of the form  $\mathbf{I} + \epsilon$ , where the magnitude of  $\epsilon$  is much smaller than 1. Hence, the higher order terms in  $\epsilon$  have been neglected.  $\hat{\mathbf{S}}^s$  is computed according to the equation A.14 at time  $s$ . The evolution equations for the FV model remains same as that in the equation 9.80. Hence, it can be seen that the evolution equations differ for the FV and the FLV models in this case.

## 9.5 APPLICATION OF FV MODEL TO THE EXPERIMENTS

To compare the predictions of FLV and FV models when applied to large strains and large perturbations, the methodology employed in the chapter 7 will be used, where the crack speed is imposed on the model using the boundary conditions from the experiment. The FLV model has been used in that chapter and was ‘calibrated’

to match the observations from the experiments. Here, the same stiffness ratios and the relaxation times will be used for the FV model and the results will be compared to the predictions from FLV model.

The stiffness ratios in the chapter 7 are with respect to the *glassy* modulus of the material, while the stiffness ratios in the FV model are with respect to the *rubbery* modulus. Hence, they are scaled using the expression

$$(g_i)_{\text{rubbery}} = \frac{(g_i)_{\text{glassy}}}{1 - \sum_{i=1}^N (g_i)_{\text{glassy}}}. \quad (9.88)$$

The parameter  $\gamma_0$  in the equation 9.15 has been taken to be 1. The above model parameters were then used to perform some simulations to understand and compare the behaviors of FLV and FV models.

Table 9.1: FV model parameters with  $\gamma_0 = 1$ .

Branch(i)	1	2	3	4	5	6	7	8
Stiffness ratio, $(g_i)_{\text{rubbery}}$	2.11	21.178	1.0589	0.5298	0.157	0.121	0.128	0.05294
Relaxation time, $\tau_i$ (s)	1E-8	1E-7	1E-6	1E-5	1E-4	1E-3	1E-2	1E-1

The scaled parameters and the relaxation times can be seen in the table 9.1. The FV model with these parameters are then used to determine the displacement and velocity fields for the case of  $\lambda_y = 3.5$ , where the crack speed is about  $56 \text{ m s}^{-1}$ . The predictions from the model can be seen in the figures 9.5 and 9.6 (to be compared with figures 7.16 and 7.20a, respectively). The velocity profile can be seen to be sharper than that from the FLV model but blunter than in the hyperelastic case. Also, the horizontal displacements can be seen to be under predicted when compared to the experiments and the FLV model. However, the profile can be seen to have some resemblance with the hyperelastic case (see figure 7.12).

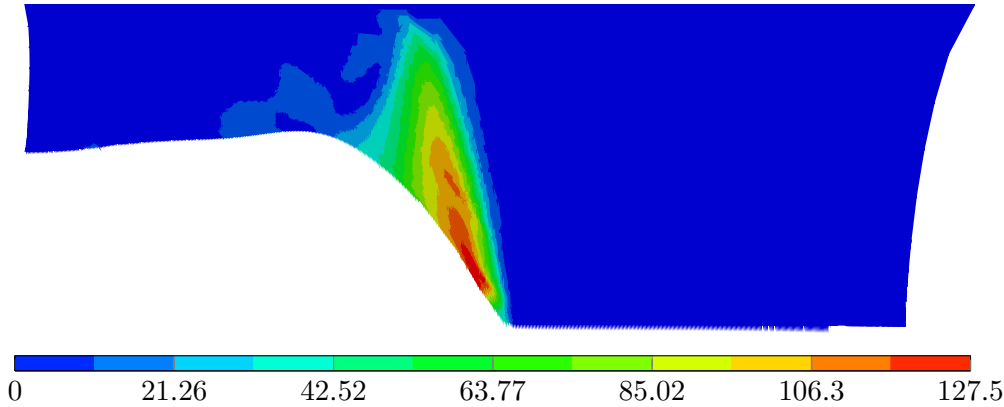


Figure 9.5: Particle velocity magnitude in  $\text{m s}^{-1}$  for  $\lambda = 3.5$  plotted on deformed configuration, FV model,  $\gamma_0 = 1$ .

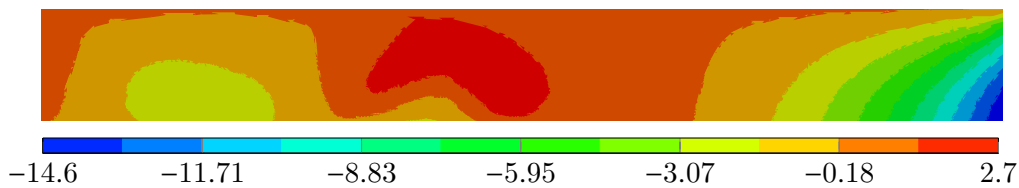


Figure 9.6: Horizontal displacement magnitude in mm for  $\lambda = 3.5$  plotted on undeformed configuration, FV model,  $\gamma_0 = 1$ .

As in the previous chapters, the variation of particle speeds at about 5 mm above the crack path has been extracted from the FE simulations and the result can

be seen together with the results from experiments, hyperelastic FE simulations, and FLV simulations in the figure 9.7.

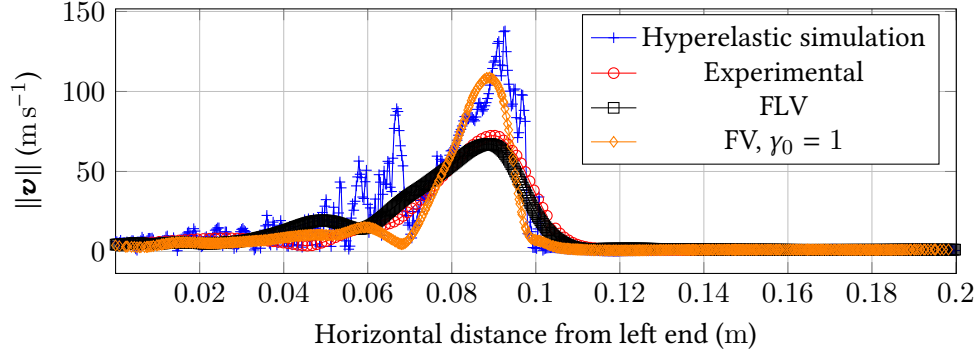


Figure 9.7: Velocity distribution along about 5 mm above the crack path for  $\lambda = 3.5$ ,  $\gamma_0 = 1$ .

It can be observed from the figures that the predictions from the FV model do not match the experiments or the results from the simulations with FLV model. In fact, the velocity magnitude can be seen to closely follow the hyperelastic case without any jumps. The fields can be seen to be continuous as opposed to the hyperelastic case.

### Further discussions

It can be seen from the above that the results from the FV model with  $\gamma_0 = 1$  are closer to the hyperelastic case, but without a shock front. In order to determine if the viscous effects are active in these simulations and the extent to which they are active, a *viscous indicator* parameter  $\beta$  is defined as follows.

$$\beta := \frac{\psi_\infty(\mathbf{b}) + \sum_{i=1}^N \psi_i(\mathbf{b}_e^{(i)})}{\psi_\infty(\mathbf{b})}. \quad (9.89)$$

$N$  denotes the number of viscous arms. The  $\psi_i$  s in the above equation indicate the strain energy densities in each of the viscous arms. It has been indicated that the  $\psi_i$  s depend on the corresponding  $\mathbf{b}_e^{(i)}$  s, the left Cauchy-Green tensor based on the corresponding elastic parts of the deformation gradient,  $\mathbf{F}_e^{(i)} \left( = \mathbf{F} \left( \mathbf{F}_v^{(i)} \right)^{-1} \right)$  s. Hence, the further the value of  $\beta$  from 1, the further is the material behavior from the hyperelastic case. A value of 1 for  $\beta$  indicates a purely hyperelastic behavior. For the result presented above for the case of  $\lambda_y = 3.5$ , the value of  $\beta$  in various regions of the body can be seen in the figure 9.8.

The scale has been truncated at 1.3 to bring out the features of the distribution. It can be seen that the value of  $\beta$  remains very close to 1 (about 1.0008) in front of the front-like region to the right of the crack. Its value then increases to about 1.2 and then behind another front-like feature, it again increases beyond 1.3. It shall be noted that the two front-like features in the figure 9.8 coincide with the shock front-like features observed for the particle velocities in the figure 7.21b. Hence, in the case of the simulations with FV model with the current parameters, it can be said that the viscous effects diffuse or blunten the shock front-like feature observed in the hyperelastic simulations (the velocity variations in figure 9.7 are closer to the hyperelastic simulations, but without the jumps) by increasing the stiffness of the material as a consequence of higher strain rates (like discussed in the chapter 7 and in Kamasamudram et al., 2021). The FV model is expected to displace the relaxation times to smaller values at higher strains. Hence, it can be

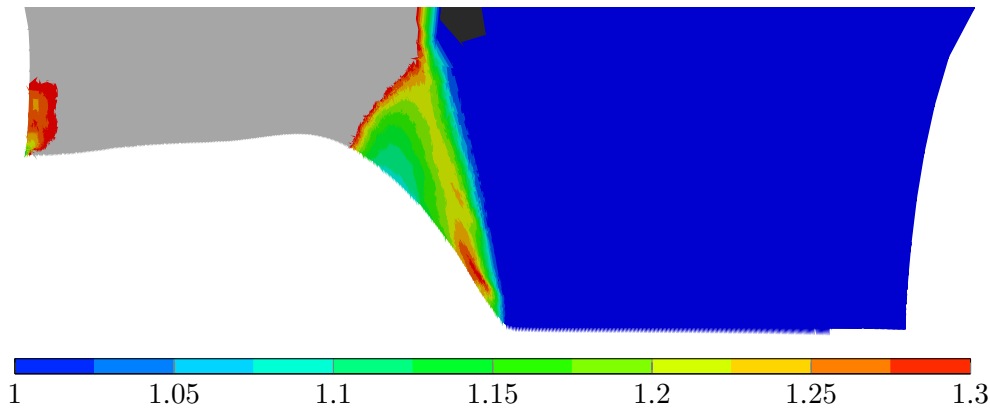


Figure 9.8: The viscous indicator parameter  $\beta$  for  $\lambda = 3.5$  plotted on deformed configuration, FV model,  $\gamma_0 = 1$ .

said that the viscous effects in the FV model with the current model parameters are ‘not high enough’ to bring the results closer to the experiments at  $\lambda = 3.5$ .

This is consistent with the predictions from Govindjee and Reese, 1997, where the relaxation functions of FLV and FV models are compared for different strain levels by subjecting a square object with a side of 1 mm to a certain displacement under plane strain conditions and observing the evolution of stress with time. The same numerical experiments will be performed for the models in plane stress conditions and the results will be presented in the appendix B. For the case of FLV model, the authors of Govindjee and Reese, 1997 comment

*As the strain of the loading is increased the curve shifts upward as an indication of the nonlinear stiffening of the material in the current (spatial) configuration. Note that the curves merely shift upwards and do not translate simultaneously along the time axis.*

While for the case of FV model,

*The curves simultaneously map left and upwards as the amount of strain increases. This mapping to the left is a result of the nonlinear structure of the viscoelasticity model itself and not due to the explicit incorporation of any shift-factors.*

The shift towards left of the relaxation curves at higher strain levels indicate the shift of relaxation times to smaller values with an increase in strain. This implies that the FLV model behaves in a stiffer (or more viscous) way when compared to the FV model at larger strains for a given strain rate.

In addition to the above, the activity of  $i^{\text{th}}$  viscous arm in different regions of the body can be examined using the ratio  $\frac{\psi_i}{\psi_\infty}$ , the ratio of strain energy density in the viscous arm to that of the energy in the hyperelastic arm. The ratios for the case of  $\lambda = 3.5$  can be seen in the figure 9.9. Activity can be seen along the shock-front-like features in multiple branches.

### 9.5.1 Model with adjusted parameters

As was observed in the simulations with the imposed crack speed, the predictions of the FLV and the FV model differ when applied for the stretch ratio of 3.5. This is the consequence of the shift in the relaxation times with the applied strain in the latter model. To counter this, the parameter  $\gamma_0$  in the equation 9.15 can be made less than 1. It shall be noted that the reducing  $\gamma_0$  from 1 has the same effect of increasing the relaxation times (moving the relaxation curves to the right in the sense of Govindjee and Reese, 1997). Hence, the model becomes *stiffer* than when  $\gamma_0 = 1$  at a given strain rate. After performing some simulations with various values of  $\gamma_0 < 1$ , it was found that choosing  $\gamma_0$  as  $\frac{1}{60}$ , while modifying one of the

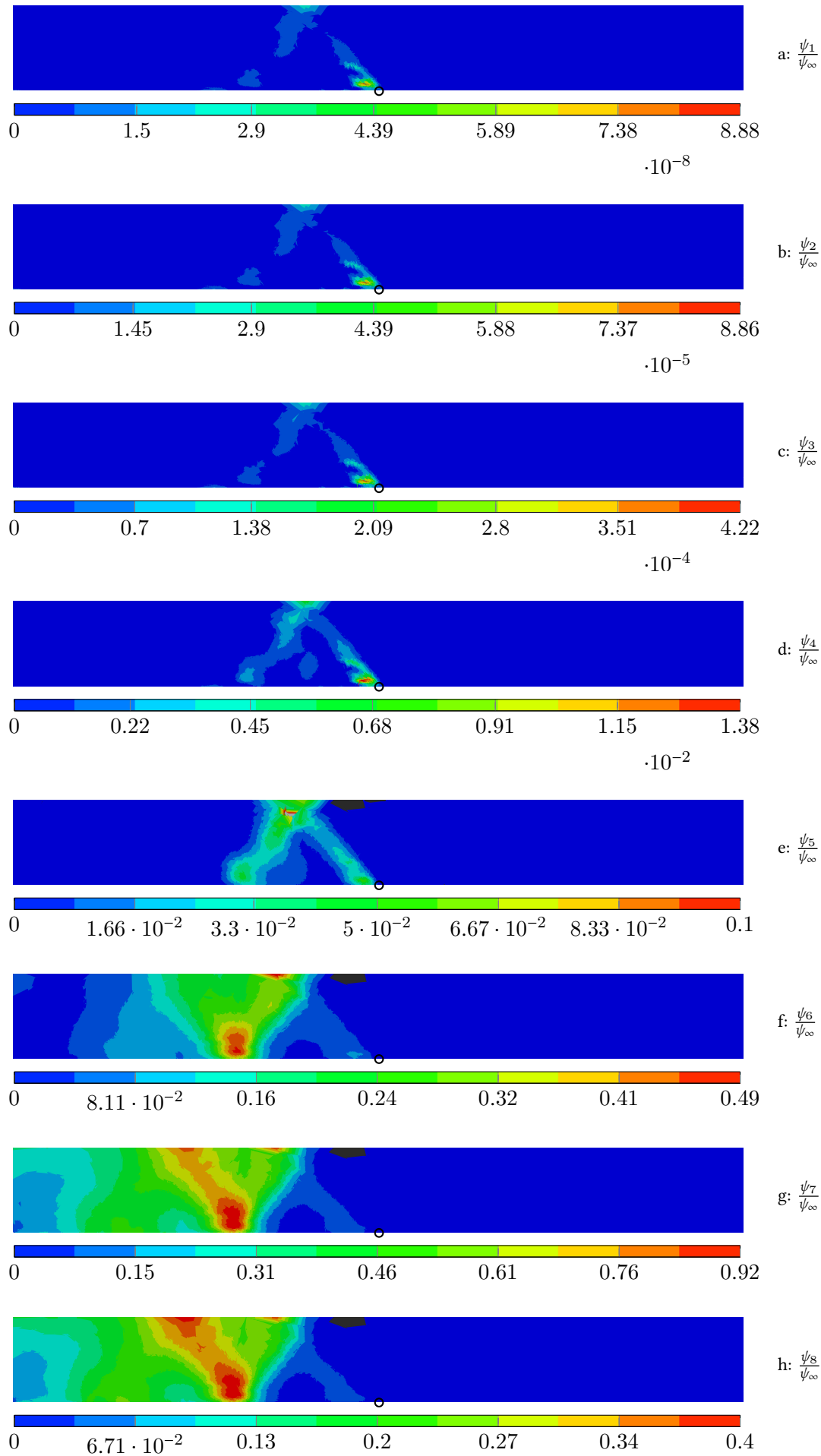


Figure 9.9:  $\frac{\psi_i}{\psi_\infty}$  for all the viscous branches ( $i = 1$  to 8) for  $\lambda = 3.5$  plotted on deformed configuration,  $\gamma_0 = 1$ . The position of crack tip is indicated by a circle.

stiffness ratios (corresponding to the relaxation time of  $1 \times 10^{-7}$  s) results in the predictions of the FV model matching the results from the experiment. The new model parameters can be found in the table 9.2. Only 7 viscous arms were found

Table 9.2: FV model parameters with  $\gamma_0 = \frac{1}{60}$ .

Branch(i)	1	2	3	4	5	6	7
Stiffness ratio, $(g_i)_{\text{rubbery}}$	1.9	1.1589	0.5298	0.157	0.121	0.128	0.05294
Relaxation time, $\tau_i(\text{s})$	1E-7	1E-6	1E-5	1E-4	1E-3	1E-2	1E-1

necessary (by examining the ratio  $\frac{\psi_i}{\psi_{\infty}}$ , any branches with values smaller than  $10^{-5}$  have been discarded) for the simulations with the new model parameters.

The simulations from the previous section are repeated with the new parameters and the predictions of the model can be seen in the figures 9.10 and 9.11.

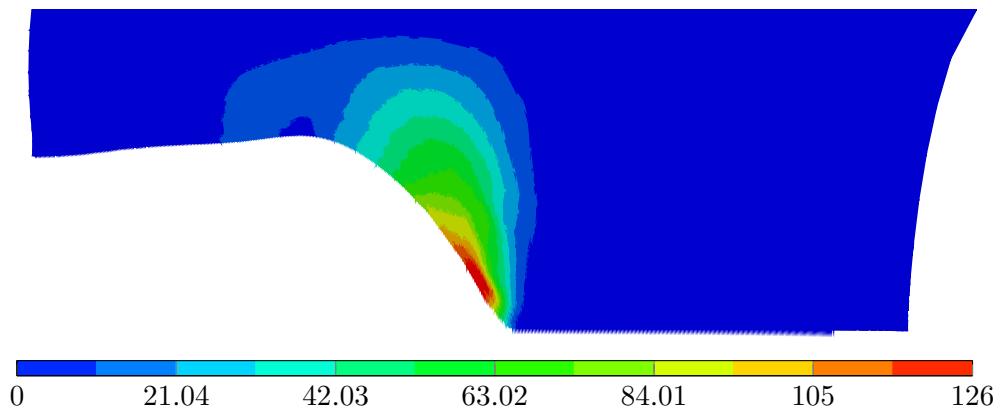


Figure 9.10: Particle velocity magnitude in  $\text{m s}^{-1}$  for  $\lambda = 3.5$  plotted on deformed configuration, FV model,  $\gamma_0 = 1/60$ .

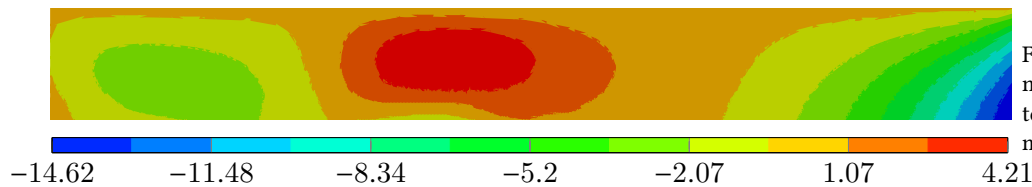


Figure 9.11: Horizontal displacement magnitude in mm for  $\lambda = 3.5$  plotted on undeformed configuration, FV model,  $\gamma_0 = 1/60$ .

The velocity profile in the figure 9.11 can be found to be blunter than in the case of  $\gamma_0 = 1$  (figure 9.6) and closer to the FLV result (figure 7.16). The horizontal displacement can also be seen to be closer to the experimental and the FLV results. However, FV model with  $\gamma_0 = 1/60$  slightly under predicts the displacements.

The variation of particle velocity magnitude at about 5 mm above the crack path can be seen in the figure 9.12 together with the results from the experiments, FLV model, and FV model with  $\gamma_0 = 1$ . It can be seen that the predictions of FV model with the new model parameters are close to that of the FLV model and the experiments.

The variation of parameter  $\beta$  that determines how much the viscoelastic effects are active can be seen in the figure 9.13. The scale has been truncated so that it can be compared to the results from the old model parameters (figure 9.8). The variation of  $\beta$  at about 5 mm above the crack path for both the cases can be seen in the figure 9.14. It can be seen that the viscous effects start to act further ahead in the material with  $\gamma_0 = 1/60$  than with  $\gamma_0 = 1$ . This is expected, since a value of less than 1 for  $\gamma_0$  moves the relaxation times to larger values which would result

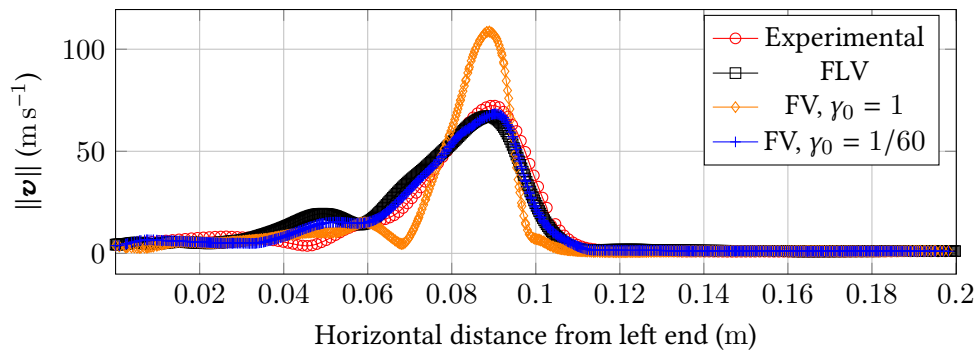


Figure 9.12: Velocity distribution along about 5 mm above the crack path for  $\lambda = 3.5$ , various cases.

in the viscous effects starting to act at smaller strain rates. The increase in  $\beta$  in the figure 9.13 is also more gradual. Also, the value of  $\beta$  exceeds 1.3 in the region just behind the tip than when compared to the previous case indicating more prevalent viscous effects in that region.

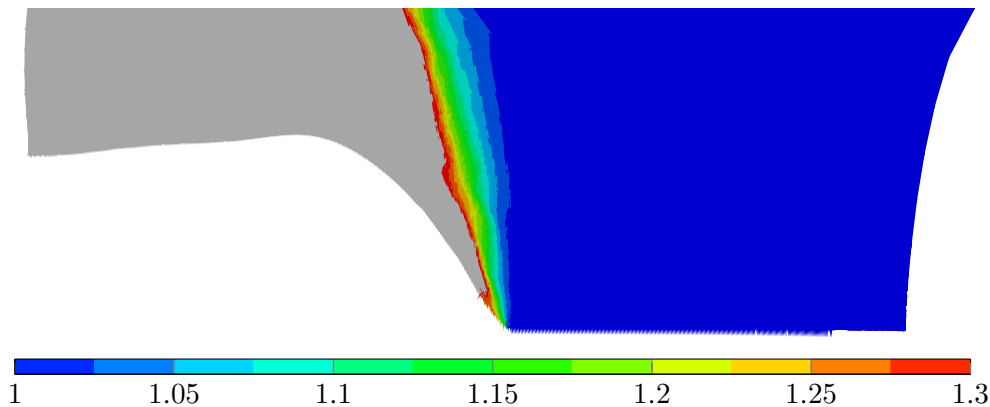


Figure 9.13: The viscous indicator parameter,  $\beta$  for  $\lambda = 3.5$ , plotted on deformed configuration, FV model,  $\gamma_0 = 1/60$ .

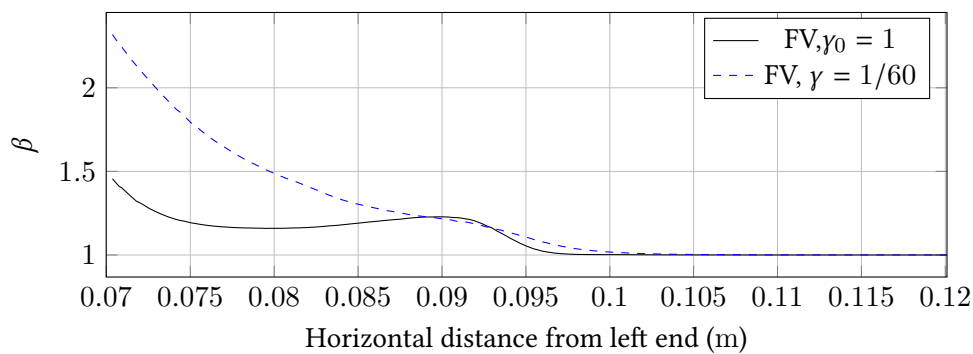


Figure 9.14: Variation of  $\beta$  about 5 mm above the crack path for  $\gamma_0 = 1$  and  $\frac{1}{60}$  when the crack is at the center of the specimen. Regions far ahead and behind the tip has been removed.

The same model parameters have then been used to simulate the case of  $\lambda = 2.5$  with imposed crack speed from the experiments. The resulting horizontal displacements can be seen in the figure 9.15. The displacements from the experiment for  $\lambda = 2.5$  can be seen in figure 9.16. Likewise, the velocity evolution at about 5 mm above the crack path, together with the results from the experiments and the FLV, can be seen in the figure 9.17.

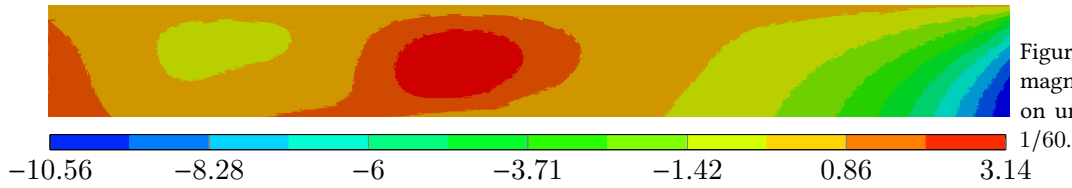


Figure 9.15: Horizontal displacement magnitude in mm for  $\lambda = 2.5$  plotted on undeformed configuration,  $\gamma_0 = 1/60$ .

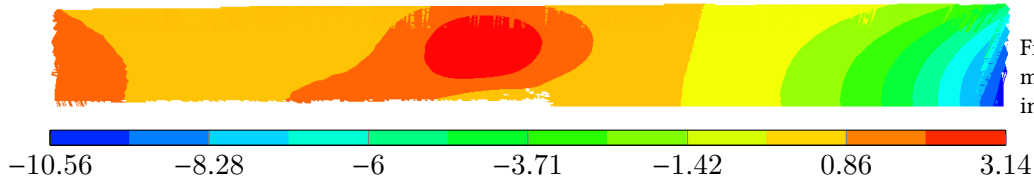


Figure 9.16: Horizontal displacement magnitude in mm for  $\lambda = 2.5$  obtained in the experiments.

### Further discussions

The FV model with the parameter  $\gamma_0 = 1/60$  and one adjusted stiffness ratio (to be called shifted FV model from hereon) can be seen to predict the velocity and displacement fields close to the experiments when compared to  $\gamma_0 = 1$ . Choosing the parameter  $\gamma_0$  less than 1 has the same effect of moving the relaxation times to higher values. In short, choosing  $\gamma_0 = 1/60$  has the same effect as retaining  $\gamma_0 = 1$  and multiplying each of the relaxation times by 60. One of the consequences of  $\gamma_0 \neq 1$  is that the FV model does not coincide with that of (finite) linear viscoelastic model at small strains and small perturbations. The relaxation times of the latter model are to be modified to make their predictions match at these conditions.

The shifted FV model can be seen to slightly under predict the displacements at  $\lambda = 3.5$  and slightly over predict them at  $\lambda = 2.5$ . This indicates that the viscoelastic model tends to get stiffer as the strains are reduced, as expected. However, the shifted FV model can be seen to predict the experimental results with a 'good enough' accuracy. Hence, energetic analysis of those experiments will be performed using this model in the next section.

## 9.6 ENERGY BUDGET IN VISCOELASTODYNAMIC FRACTURE

Since the shifted FV model was able to predict the displacements and velocities from the experiments of  $\lambda = 2.5$  and 3.5 with a good enough accuracy, it will be used to perform an energetic analysis of those experiments. The FLV model from the previous chapter could not be used to do so as a consequence of lack of an expression for the strain energy function and the energy dissipation in that model.

### 9.6.1 From the experiments

First, the energy balance will be performed for the case where the crack speed is imposed onto the FE model using the displacements from the experiments. It shall be noted that the analysis can also be performed directly on the displacements and velocities as done in Corre, 2018. The methodology is exactly the same as in the section 7.2, but with the FLV model in the bulk replaced by the shifted FV model.

For the cases of  $\lambda = 2.5$  and 3.5, the evolution of strain energy, kinetic energy, and the dissipation in the material with time have been extracted for the simulations presented in the previous section with the shifted FV model. Their evolution with time can be seen in the figures 9.18 and 9.19 once the initial transients have passed.

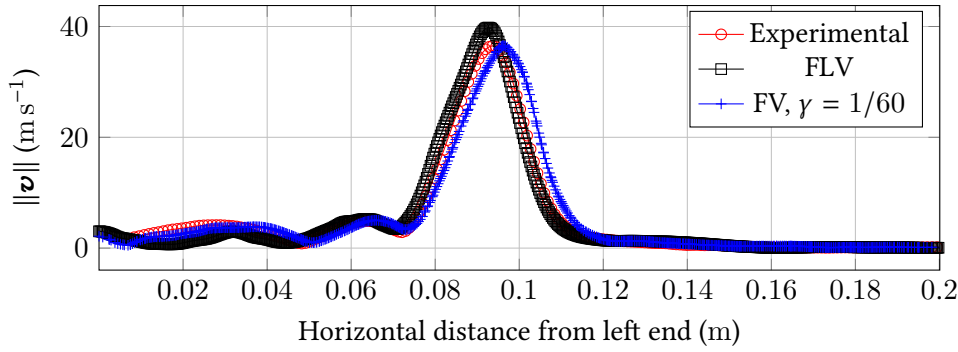


Figure 9.17: Velocity magnitude in  $\text{m s}^{-1}$  for  $\lambda = 2.5$  plotted on undeformed configuration.

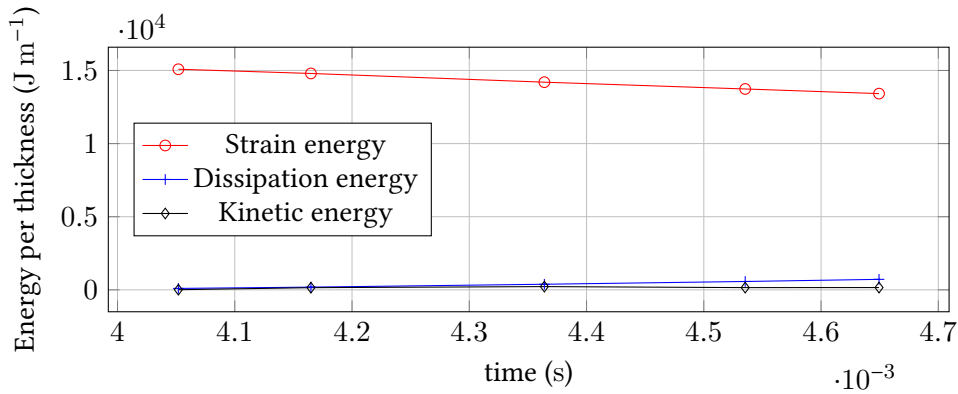


Figure 9.18: Energy evolution for the case of  $\lambda = 2.5$  with the shifted FV model. The crack is at about the center of the specimen at about 4.5 ms.

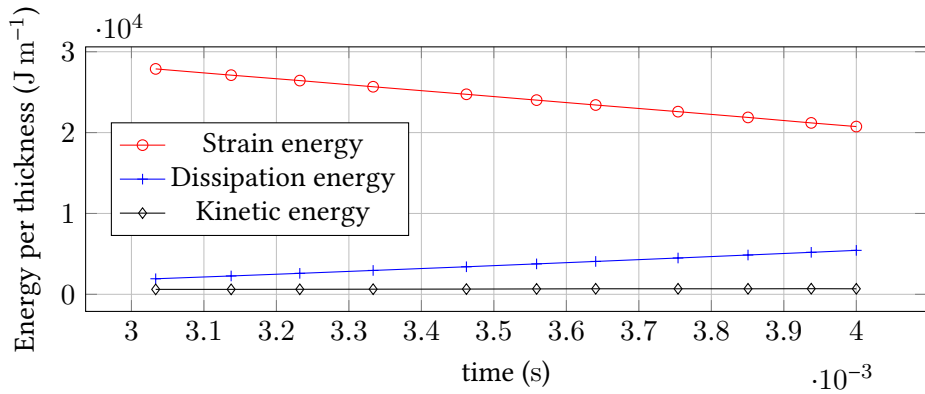


Figure 9.19: Energy evolution for the case of  $\lambda = 3.5$  with the shifted FV model. The crack is at about the center of the specimen at about 3.5 ms.

It shall be noted that only half of the specimen was used to obtain these results taking symmetry into account. Using this data, energy balance can be written as

$$P_{ext} = \frac{dSE}{dt} + \frac{dD}{dt} + \frac{dKE}{dt}, \quad (9.90)$$

where  $P_{ext}$  is the power of the external forces,  $SE$ ,  $D$ , and  $KE$  denote the strain energy, viscoelastic energy dissipation, and kinetic energy, respectively. In the current case, since only the part of material that is about 1 mm away from the crack path has been modeled,  $P_{ext}$  includes the power of external forces, the viscoelastic energy dissipation in the material that is not included, and the power dissipated during the fracture process.

The time derivative of the quantities for the case of  $\lambda = 2.5$  and 3.5 can be seen in the table 9.3. It shall be noted that the sign of  $P_{ext}$  is negative in both the cases. This indicates that the work has been extracted from the system or work has been done by the system during the crack propagation. As already mentioned, this work includes the work in the fracture process zone and the dissipation in the

Table 9.3: Energy rates with the shifted FV model in MJ m<sup>-1</sup> s<sup>-1</sup>.

$\lambda$	$\frac{dSE}{dt}$	$\frac{dD}{dt}$	$\frac{dKE}{dt}$	$P_{ext}$
2.5	-2.81	1.03	0.18	-1.6
3.5	-7.4	3.7	0.08	-3.62

material in the vicinity of the crack path that has been excluded.

Dividing  $-\frac{d(SE + KE)}{dt}$  by the crack speed gives *Energy release rate*, which is experimentally computed (usually) as  $\psi h_0$ , where  $\psi$  is the strain energy density is the material far ahead of the crack tip.  $h_0$  is the undeformed specimen height. In the current case, the strain energy behind the tip may not be zero as a consequence of viscous effects. Hence, the quantity  $[[\psi]]h_0 = (\psi(\infty) - \psi(-\infty))h_0$  (see figure 2.14) will have a different value from  $\psi h_0$ . In the current case,  $\psi(\infty)$  and  $\psi(-\infty)$  have been computed at about 50 mm in front of and behind the tip, respectively. All the computed quantities can be seen in the table 9.4.

Table 9.4: Energy release rates for the experiments in kJ/m<sup>2</sup>.

$\lambda$	$-\frac{2}{w_0} \frac{dSE}{dt}$	$\frac{2}{w_0} \frac{dD}{dt}$	$\frac{2}{w_0} \frac{dKE}{dt}$	$-\frac{2}{w_0} P_{ext}$	$\psi h_0$	$[[\psi]]h_0$
2.5	130	49	8.5	76	166	120
3.5	260	129	2.0	127	348	268

The factor 2 above has been used since only half of the specimen geometry has been used in the analysis. From the tables 9.3 and 9.4, and the figure 9.20, it can be observed that the majority (about half) of the strain energy is taken up by the dissipating material. The kinetic energy takes up very little energy when compared with the viscoelastic dissipation. The rest ( $P_{ext}$ ) is taken up by the material along and a little away from the crack path in the form of viscoelastic dissipation and the fracture processes at the crack tip. The quantities  $-\frac{2}{w_0} \frac{dSE}{dt}$  and  $[[\psi]]h_0$  are quite close to each other for both the cases presented. Again, it shall be noted that the strain energy behind the tip used in the computation of  $[[\psi]]$  is the total strain energy contained in the elastic as well as the viscous arms. When the above results are compared with that of the analysis performed in Corre, 2018 (see figures 6.7 and 6.8 of the cited reference), some differences can be noticed. The analysis in the cited reference uses a hyperelastic material to compute the evolution of the total energy.

The energy release rate (obtained by evaluating  $\frac{d(SE + KE)}{dt}$ , where the strain energy has only the elastic contribution) from that analysis can be seen to match the quantity  $\psi h_0$  in the same analysis as well as from the table 9.4. However, when viscous effects are included, some strain energy is locked in the viscous arms, which affects the computation of  $\frac{d(SE + KE)}{dt}$ . This quantity is hence smaller in the current study and it can be seen to match  $[[\psi]]h_0$ , rather than  $\psi h_0$ .

### 9.6.2 From the simulations with cohesive model

The previous sections analyze the experiments performed in Corre et al., 2020. However, as can be noted, only the material starting from about 1.5 mm above the

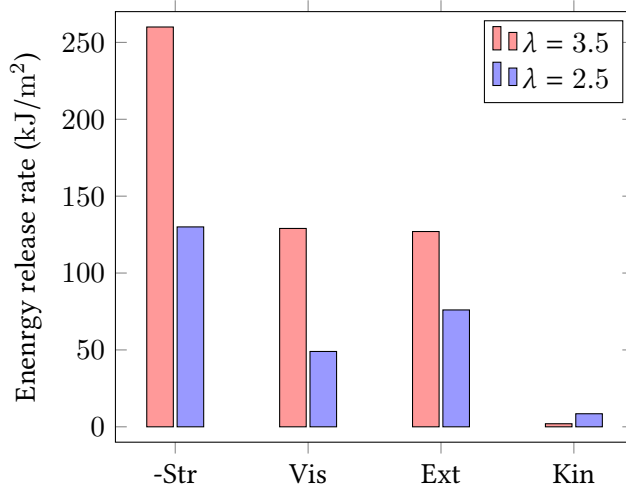


Figure 9.20: Strain (Str), Viscous (Vis), External work (Ext), and Kinetic (Kin) Energy release rates for the data from the experiments.

crack path has been modeled. Hence, the term  $P_{ext}$  included the viscous dissipation in the excluded material. In the simulations performed using the cohesive model using the FLV model presented in the previous chapter, this problem does not exist. Data can be extracted right along the crack path from those simulations which then can be imposed onto the current model, where the bulk material has been modeled by the FV model.  $P_{ext}$  computed this way will solely comprise of the work done in the cohesive zone and the dissipation,  $D$ , will include the total viscoelastic dissipation in the material. *It shall be noted that the crack propagation has not been modeled explicitly in this section. Only half of the bulk material has been used with the crack speeds imposed implicitly.*

This procedure has been followed for the case of  $\lambda = 2.5$  and 3.5. The results of energy evolution for both the cases can be seen in the figures 9.21 and 9.22.

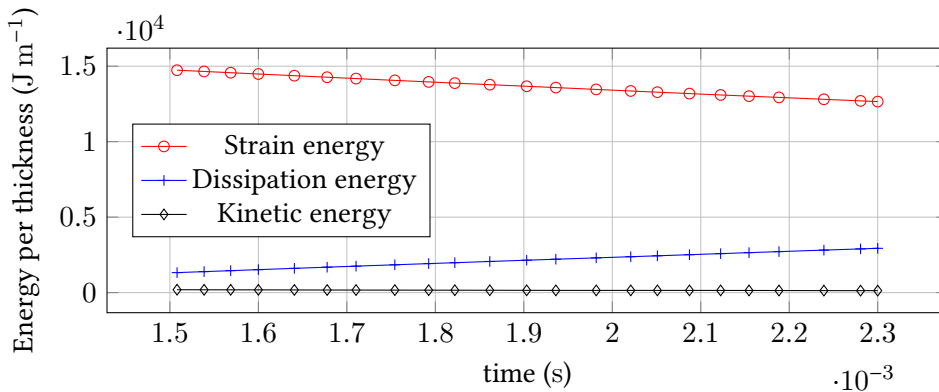


Figure 9.21: Energy evolution for the case of  $\lambda = 2.5$  with the shifted FV model. The crack is near the center of the specimen at about 2.2 ms.

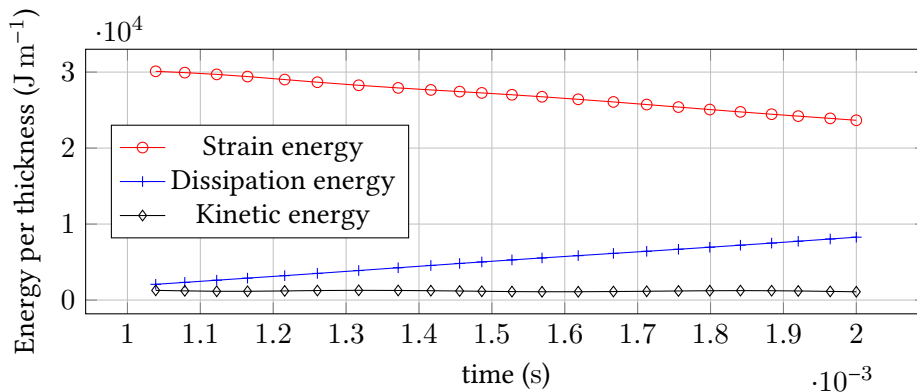


Figure 9.22: Energy evolution for the case of  $\lambda = 3.5$  with the shifted FV model. The crack is at about the center of the specimen at about 1.7 ms.

As earlier, the time derivatives of the quantities can be seen in the table 9.5. The

energy release rates can be computed and can be seen in the table 9.6, plotted in the figure 9.23.

Table 9.5: Energy rates with the shifted FV model for the FE simulations in  $\text{MJ m}^{-1} \text{s}^{-1}$ .

$\lambda$	$\frac{dSE}{dt}$	$\frac{dD}{dt}$	$\frac{dKE}{dt}$	$P_{ext} = P_{coh}$
2.5	-2.63	2.02	0.07	-0.54
3.5	-7.18	6.22	0.06	-0.9

Table 9.6: Energy release rates for the FE simulations in  $\text{kJ/m}^2$ .

$\lambda$	$-\frac{2}{w_0} \frac{dSE}{dt}$	$\frac{2}{w_0} \frac{dD}{dt}$	$\frac{2}{w_0} \frac{dKE}{dt}$	$G_{coh} = -\frac{2}{w_0} P_{ext}$	$\psi h_0$	$[[\psi]] h_0$
2.5	119	91	3.1	24	166	127
3.5	250	220	2	30	348	252

When comparing the results from the experiments, it can be seen that the strain energy release rate is about the same in both the cases. Viscoelastic dissipation is higher in the results from the simulations. This is expected, as the data in the case of FE simulations have been extracted right along the crack path and hence includes the material where higher dissipation takes place. The  $P_{ext}$  simply becomes  $P_{coh}$ , the energy spent during the fracture processes. Even in this case, the two parameters,  $-\frac{2}{w_0} \frac{dSE}{dt}$  and  $[[\psi]] h_0$  can be seen to be close. The computed value of  $G_{coh}$  can be compared with the area under the traction separation curves (figure 8.7) in the previous chapter. The areas under the traction separation curves can be approximately seen to be  $18.5 \text{ kJ/m}^2$  and  $21 \text{ kJ/m}^2$ , for  $\lambda = 2.5$  and  $3.5$ , respectively. The results from the shifted FV model can be seen to over predict these quantities (as  $24 \text{ kJ/m}^2$  and  $30 \text{ kJ/m}^2$ , respectively). Performing a FE simulation with the FV model in bulk together with the CZM may result in a more accurate estimate of this energy. However, that analysis has not been done as a result of higher computational cost involved.

The region of the body in which the viscoelastic dissipation takes place can be seen in the figure 9.24. Significant dissipation can be seen in the material that is within about 2 mm from the crack path. This can explain the differences in

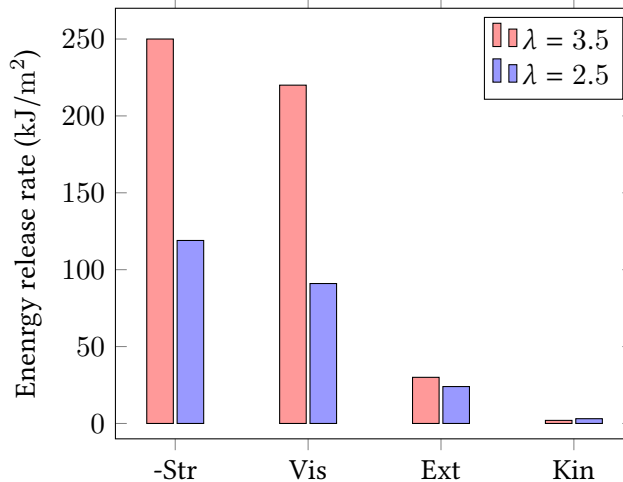


Figure 9.23: Strain (Str), Viscous (Vis), External work (Ext), and Kinetic (Kin) Energy release rates for the data from FLV simulations with cohesive zone.

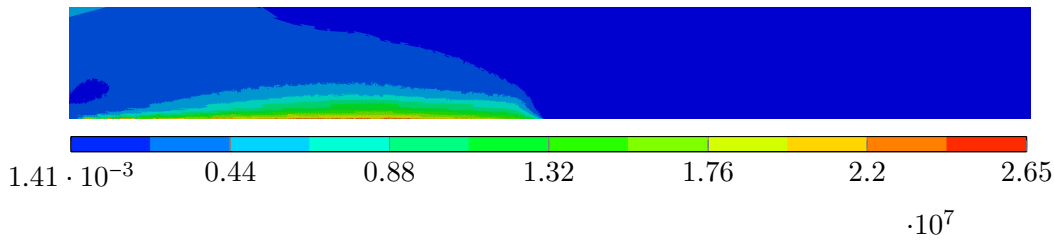


Figure 9.24: Viscoelastic energy dissipation density for  $\lambda = 3.5$ , crack speed imposed from CZM simulations.

the viscoelastic dissipation observed from the results in tables 9.4 and 9.6. Also, the temperature measurements made on the test samples from batch-2 revealed a significant increase in temperatures near the tip. Thus, the viscous dissipation region in the figure 9.24 can be seen to be a qualitative match to the experiment.

## 9.7 DISCUSSIONS

### FV vs FLV models

In this chapter, the plane stress version of the Finite Viscoelastic model of Reese and Govindjee, 1998 has been used to understand the energy budget during the viscoelastodynamic fracture. The model has been implemented into UMAT subroutine of Abaqus (Dassault, 2014). Initially, the analyses were performed using the same stiffness ratios and the relaxation times as that of the FLV model. It was observed that the velocity and displacement predictions from FV model did not match the experimental observations. The velocity raise was seen to be sharper than in the FLV case and the displacements were seen to be under predicted and closer to the hyperelastic case. There was, however, no shock-front-like feature in the results from FV model unlike for the hyperelastic case. Using the viscous indicator,  $\beta$ , which is defined as the ratio of the total strain energy to that in the hyperelastic branch, the regions in the body where the viscoelastic effects are active have been identified. It was observed that the value of  $\beta$  is very close to 1 in front of a front-like region. Its value increased to about 1.3 in the region behind another front-like region. The two front-like features observed in the figure 9.8 coincide with the shock-front-like features observed in the velocity profiles in the hyperelastic case. This, when combined with the velocity profiles, indicate that the effect of viscoelasticity is to blunten the shock-front-like feature in the velocity distributions observed in the hyperelastic case. The differences from FLV case can be attributed to the relaxation times shifting to the smaller values with an increase in the strain in the FV model.

The results from the FV model were then brought closer to the experiments by decreasing the value of the coefficient  $\gamma_0$  ( $= 1$  initially) to  $\frac{1}{60}$ . This can be viewed as multiplying the relaxation times by 60 to compensate for their decrease at higher strains. This, however, will lead to a difference in the predictions between the FV and the FLV models at small strains (FV model with  $\gamma_0 = 1/60$  will behave stiffer than the FLV model at small strains with the same stiffness ratios and relaxation times). But decreasing  $\gamma_0$  was seen to bring the results from simulations closer to the experiments. The velocity and displacement fields for  $\lambda = 3.5$  and 2.5 were seen to be closer to the experiments than when  $\gamma_0 = 1$ . Even with the reduced  $\gamma_0$ , the FV model can be seen to slightly under predict the displacements at  $\lambda = 3.5$  and over predict them at  $\lambda = 2.5$ . By making the model agree with the experiments at  $\lambda = 3.5$ , it was made to slightly stiffer than needed at 2.5.

One way to compensate this would be to make  $\gamma_0$  a decreasing function of either

$\mathbf{b}_e = \mathbf{F}_e \mathbf{F}_e^T$ , corresponding to the elastic part of  $\mathbf{F}$  or  $\mathbf{C}$ , the overall deformation tensor, such that  $\gamma_0(\mathbf{b}_e \text{ or } \mathbf{C} = \mathbf{I}) = 1$ . This is equivalent to slightly compensating for the shift in the relaxation times as a consequence of the non-linearity in the FV model. This will result in the model predicting the same results as that of FLV model at small strains and agreeing with the experimental results at higher strains. However, when  $\gamma_0$  is made a function of  $\mathbf{C}$  (its invariants, more precisely, as a consequence of isotropy), the viscous evolution equations then become

$$\epsilon_{1e} + \frac{\gamma_0(\mathbf{C})\Delta t}{2\eta_D} (\tau_1 + p) - (\epsilon_{1e})_{tr} = 0, \quad (9.91)$$

This poses no problem when solving for the  $\epsilon_{Ae}$  s in the local Newton iterations as  $\mathbf{C}$  does not change during those iterations and hence  $\gamma_0$  can be treated as a constant. However, when the global tangent is to be computed as a part of global Newton iterations,  $\gamma_0$  cannot be treated as a constant. The contribution of the viscous evolution equations to the global tangent comes in the form of the derivative  $\frac{\partial \epsilon_{Ae}}{\partial (\epsilon_{Be})_{tr}}$ . Since the overall deformation changes during the global iterations,  $\gamma_0(\mathbf{C})$  contributes to the tangent as well. An attempt can be made to evaluate the derivative by observing that  $\mathbf{C}^n = (\mathbf{F}^n)^T \mathbf{F}^n = (\mathbf{F}_v^{n-1})^T (\mathbf{C}_e)_{tr} \mathbf{F}_v^{n-1}$ . Since  $\mathbf{F}_v^{n-1}$  is constant during the global iterations,  $\gamma_0$  can be viewed as a function of  $(\mathbf{C}_e)_{tr}$  to evaluate the derivative  $\frac{\partial \epsilon_{Ae}}{\partial (\epsilon_{Be})_{tr}}$ . However, this requires the knowledge of  $\mathbf{F}_v^{n-1}$ , which is not known. Only  $\mathbf{C}_v^{n-1}$  is known and hence  $\mathbf{F}_v^{n-1}$  can be evaluated up to rigid body motions. One other alternate is to make  $\gamma_0$  a function of the invariants of  $\mathbf{b}$ . In this case,  $\mathbf{b}^n = \mathbf{F}^n (\mathbf{F}^n)^T = (\mathbf{F}_e)_{tr} (\mathbf{b}_v^{n-1})^T ((\mathbf{F}_e)_{tr})^T$ . Again, this requires the knowledge of  $(\mathbf{F}_e)_{tr}$ , which can be determined only up to a rigid body motion. Hence, this path was not explored further in this thesis. The other alternate is to make  $\gamma_0$  a function of  $\mathbf{b}_e$  like in Bergström and Boyce, 1998. However, the Bergström-Boyce model may lead to a faster decay of stresses in the relaxation tests than that of the Reese and Govindjee, 1998 model, which is equivalent to shift in the relaxation times further to the left.

The cohesive zone model used in the previous chapter is based on the use of convolution integrals, where the relaxation times and the stiffness have been chosen to be same as that of the bulk material. However, in the current chapter, it can be seen that the inclusion of non-linearity in the viscoelastic model shifts the relaxation times of the material with the applied strain. How this shift affects the relaxation times in the cohesive zone is currently not known. However, this shift can be included in the cohesive zone by using ‘strain clock’ models (Wineman, 2009), where  $t - s$  in the equation 8.4 is replaced by  $\xi(t) - \xi(s)$ , where  $\xi$  is a function of strain and possibly its history.

### Energy budget in viscoelastodynamic fracture

The shifted FV model can be seen to predict the displacements and velocities close to the experiments for  $\lambda = 2.5$  and  $3.5$ . Hence, it has been used to analyze the energy evolution for those experiments. The strain energy release rate was seen to match the quantity  $[\psi]h_0$  and smaller than  $\psi h_0$ . When compared with the computations from Corre, 2018, the value of  $-\frac{2}{w_0} \frac{dSE}{dt}$  in the current case can be seen to be smaller than what can be seen in the figure 6.8 of that study. This can be attributed to the viscoelastic effects included in the current study. Using a similar method, the results from the cohesive zone simulations performed in the previous

chapter have been analyzed as well. A significant portion of the strain energy can be seen to be dissipated by the viscoelastic effects in the material. The rest of the energy can be seen to be taken up by the fracture processes. The shifted FV model over predicts the energy dissipated by the fracture processes when compared with the results from the cohesive zone simulations from the previous chapter. Perhaps performing the simulations with the cohesive zone and the shifted FV model in the bulk will make in both the results to agree.

The region in the body where the viscoelastic dissipation takes place can be seen in the figure 9.24. The region near the crack path can be seen to dissipate the majority of the energy, while the dissipation in the material that is a bit far can be seen to be smaller. An element along the crack path and in the vicinity of the tip undergoes very high rates of deformation, which can be seen to result in higher dissipation. This can be seen as a reason for the difference in the viscoelastic dissipation computed in tables 9.3 and 9.5. Also, the temperature measurements from the experiments performed on the materials of different batch reveal a large increase in temperature along the crack faces (see figure 5.10). This is consistent with the regions where the viscous dissipation is concentrated in figure 9.24. A quantitative comparison of the temperature raise has not been made as the samples are from different batches.

#### SUMMARY

The plane stress version of the FV model has been presented and implemented in Abaqus. Using the relaxation times that are different from the FLV model, it was observed that the FV model was able to predict the results from the experiments reasonably well. The energy evolution during the crack propagation in the experiments from Corre, 2018 and the simulations with the cohesive zone from the previous chapter has been computed. The slope of the strain energy evolution vs time curve has been observed to match  $\llbracket \psi \rrbracket h_0$ , which stresses the importance of including the viscous effects in the analysis. Examining the parameter  $\beta$ , the viscous effects were seen to be active starting from the region just in front of the crack tip. The region along the crack faces behind the tip can be seen to dissipate considerable amount of total energy. This region is comparable to the region where there was a considerable temperature raise in the experiments.

# Conclusions and perspectives

## CONCLUSIONS

The analysis of dynamic fracture of elastomers has been made in the current thesis. First, regarding the origin of transonic cracks in elastomers, examining the velocity and strain fields from the experiments revealed no presence of shock fronts in the material. Simulations have been performed to explain this observation using the experimental data and implicitly imposing the cracks speeds. In one case, the bulk material has been assumed to be hyperelastic that exhibits an upturn in its stress strain response. The velocity fields obtained from this case were observed to contain jumps along a shock-front-like feature, which is absent in the experiments. When the bulk has been made viscoelastic, the shock-front-like features disappeared and the displacement, velocity and the strain fields resembled those from the experiments. The hyperelastic branch of the material still included the upturn in its stress-strain response. When it is replaced by a model that does not exhibit the upturn, the fields were still observed to be continuous, devoid of any shock-front-like features. Hence, it has been concluded that the observation of transonic cracks in polyurethane elastomers can be attributed to the viscoelastic stiffening of the material rather than the hyperelastic stiffening.

Experiments performed on natural rubber specimens of different geometries in literature revealed that the crack speeds were independent of the specimen geometry (specifically the height) beyond a certain threshold. Whether such a conclusion is valid for all the materials is not known. To address this, the current author performed more experiments on Polyurethane samples of different geometries. However, as a consequence of either defective material or the material with different properties from different batches, no conclusions could be drawn from the experiments performed along with the experiments from the literature. But, the crack speeds from batch-2 for different geometries seemed to settle down at a certain level starting from some stretch level, indicating that they became height independent.

The cohesive zone model has been used to predict the crack speeds observed in the experiments since the crack path is already known in advance if initiated at the middle of the specimen. Simulations have been performed with cohesive zone inserted all along the prospective crack path and the bulk material modeled by the Finite Linear Viscoelastic model. Rate dependence was found to be necessary in the cohesive zone to match the crack speeds observed in the simulations with that of the experiments. The rate dependence has been introduced in terms of convolution integrals with the relaxation times and stiffness ratios chosen to be same as that of the bulk material. Using this model, the crack speeds observed in the experiments at different stretches could be reproduced. The tractions in the cohesive zone and the energy expended in the cohesive zone have been found to be an increasing function of crack speed for the cases studied. Also, when the specimens of different heights were simulated, it has been observed that the crack speeds became independent of the height from a certain threshold like in the experiments from the literature.

In the next part, a Finite Viscoelastic model has been implemented in the

plane stress setting. Some differences have been observed in the predictions of the FV and the FLV models as a consequence of the non-linearity of the evolution equations in the former model. From the numerical relaxation tests performed, it has been observed that the relaxation times in the FV model are a function of strain as a consequence of the non-linearity of the model. For the FLV model, the stress vs time curves during the numerical relaxation tests at different strain levels were observed to just translate (upward along the stress axis) without any change in shape, indicating an independence of relaxation times on the strain level. The material parameters have been modified in the FV model so that the predictions of this model matches the observations from the experiments. Using this FV model, the strain energy evolution and the dissipation in the material during the propagation of crack has been studied. It has been found that the majority of the energy is consumed as the viscoelastic dissipation of the bulk material. A comparatively small portion is consumed in the cohesive zone. This has been the case for both the cases studied in this thesis. Whether the energy consumed in the cohesive zone can be computed directly from the experiments in any other way is not known at the moment.

#### **FUTURE PERSPECTIVES**

From the temperature measurements made from the experiments, a large raise in temperature has been observed in the material in the vicinity of the crack tip. This region also corresponds with the regions where the dissipation takes place, as identified by the FV model. The viscoelastic properties of the material are expected to be a function of temperature, which in turn affects the dissipation and possibly the crack speeds as well. Solving a fully coupled thermoviscoelastic problem will help gain insights into how these phenomena interact with each other. Also, the FV model used in this thesis has been calibrated using the data from the crack propagation experiments. As expected, some difference has been noticed between the predictions of the FLV and the FV models. However, whether the actual behavior of the material is closer to one model or the other is not known. Perhaps, performing simple relaxation tests like in the appendix B can help understand the behavior of the material. Once the model is calibrated to predict these experiments accurately, it can perhaps be further refined using the data from the crack propagation experiments.

The other aspect would be to consider the shift in relaxation times while modeling the behavior of the failing material. In the convolution integral type models used in this study, this can perhaps be achieved by using strain clock models, where the times in the relaxation functions are replaced by shifted times depending on the strain level. How this will affect the crack speeds and other observations from the simulations is not known.

One other aspect of interest would be to relate the surface roughness variations observed with the crack speed and the viscoelastic properties of the material. The role played by cavitation and the effects of viscoelasticity on cavitation has to be investigated. The effect of specimen thickness on the crack speeds and roughness in the high speed regime needs to be investigated as well.

# Bibliography

- Abraham, F., Walkup, R., Gao, H., Duchaineau, M., Diaz, T., Rubia, D. L., & Seager, M. (2002). Simulating materials failure by using up to one billion atoms and the world's fastest computer : Brittle fracture. *Proceedings of the National Academy of Sciences*, 99(9), 5777–5782. doi:10.1073/pnas.062012699
- Anderson, T. (2017). *Fracture mechanics: fundamentals and applications*. CRC press.
- Arruda, E. & Boyce, M. [Mary]. (1993). A three-dimensional constitutive model for the large stretch behavior of rubber elastic materials. *Journal of the Mechanics and Physics of Solids*, 41(2), 389–412.
- Atkinson, C. & Popelar, C. (1979). Antiplane dynamic crack propagation in a viscoelastic strip. *Journal of the Mechanics and Physics of Solids*, 27(5-6), 431–439. doi:10.1016/0022-5096(79)90024-3
- Barenblatt, G. I., Salganik, R. L., & Cherepanov, G. P. (1962). On the nonsteady propagation of cracks. *Journal of Applied Mathematics and Mechanics*, 26(2), 469–477. doi:10.1016/0021-8928(62)90076-X. arXiv: NIHMS150003
- Belytschko, T., Chen, H., Xu, J., & Zi, G. (2003). Dynamic crack propagation based on loss of hyperbolicity and a new discontinuous enrichment. *International Journal for Numerical Methods in Engineering*, 58(12), 1873–1905. doi:10.1002/nme.941
- Belytschko, T., Liu, W. K., & Moran, B. (2000). *Nonlinear finite elements for continua and structures*. Wiley.
- Bergström, J. & Boyce, M. (1998). Constitutive modeling of the large strain time-dependent behavior of elastomers. *Journal of the Mechanics and Physics of Solids*, 46(5), 931–954. doi:10.1016/S0022-5096(97)00075-6
- Bonet, J. (2001). Large strain viscoelastic constitutive models. *International Journal of Solids and Structures*, 38(17), 2953–2968. doi:10.1016/S0020-7683(00)00215-8
- Bonet, J. & Wood, R. (2008). *Nonlinear Continuum Mechanics for Finite Element Analysis*. Cambridge: Cambridge University Press. doi:10.1017/CBO9780511755446
- Bouchbinder, E., Goldman, T., & Fineberg, J. (2014). The dynamics of rapid fracture: instabilities, nonlinearities and length scales. *Reports on Progress in Physics*, 77(4), 46501. doi:10.1088/0034-4885/77/4/046501
- Bouchbinder, E., Livne, A., & Fineberg, J. (2008). Weakly nonlinear theory of dynamic fracture. *Physical Review Letters*, 101(26). doi:10.1103/PhysRevLett.101.264302. arXiv: 0807.4868
- Boulanger, P. & Hayes, M. (2001). *Finite-Amplitude Waves in Mooney-Rivlin and Hadamard Materials*. doi:10.1007/978-3-7091-2582-3
- Bourdin, B., Francfort, G. A., & Marigo, J.-J. (2000). Numerical experiments in revisited brittle fracture. *Article in Journal of the Mechanics and Physics of Solids*. doi:10.1016/S0022-5096(99)00028-9
- Broberg, K. B. (1999). *Cracks and fracture*. Elsevier.
- Buehler, M. J. (2008). *Atomistic modeling of materials failure*. Springer Science & Business Media.
- Buehler, M., Abraham, F., & Gao, H. (2003). Hyperelasticity governs dynamic fracture at a critical length scale. *Nature*, 426(6963), 141–146. doi:10.1038/nature02096

- Chen, C. H., Zhang, H. P., Niemczura, J., Ravi-Chandar, K., & Marder, M. (2011). Scaling of crack propagation in rubber sheets. *Epl*, 96(3). doi:10.1209/0295-5075/96/36009
- Christensen, R. M. (1979). A rate-dependent criterion for crack growth. *International Journal of Fracture*, 15(1), 3–21. doi:10.1007/BF00115904
- Coleman, B. & Gurtin, M. E. [Morton E]. (1967). Thermodynamics with internal state variables. *The Journal of Chemical Physics*, 47(2), 597–613.
- Coleman, B. & Noll, W. (1961). Foundations of Linear Viscoelasticity. *Rev. Mod. Phys.* 33(2), 239–249. doi:10.1103/RevModPhys.33.239
- Corigliano, A. & Ricci, M. (2001). Rate-dependent interface models: Formulation and numerical applications. *International Journal of Solids and Structures*, 38(4), 547–576. doi:10.1016/S0020-7683(00)00088-3
- Corre, T. (2018). *Rupture dynamique de membranes élastomères : étude expérimentale par mesure de champs* (Doctoral dissertation).
- Corre, T., Coret, M., Verron, E., Leblé, B., & Le Lay, F. (2020). Experimental full field analysis for dynamic fracture of elastomer membranes. *International Journal of Fracture*, 224(1), 83–100. doi:10.1007/s10704-020-00447-1
- Cotterell, B. & Rice, J. R. [J R]. (1980). Slightly curved or kinked cracks. *International Journal of Fracture*, 16(2), 155–169. doi:10.1007/BF0012619
- D’Amico, F., Carbone, G., Foglia, M. M., & Galietti, U. (2013). Moving cracks in viscoelastic materials: Temperature and energy-release-rate measurements. *Engineering Fracture Mechanics*, 98, 315–325. doi:https://doi.org/10.1016/j.engfracmech.2012.10.026
- Dal, H. & Kaliske, M. [Michael]. (2009). Bergström-Boyce model for nonlinear finite rubber viscoelasticity: Theoretical aspects and algorithmic treatment for the FE method. *Computational Mechanics*, 44(6), 809–823. doi:10.1007/s00466-009-0407-2
- Dally, J. W. (1979). Dynamic photoelastic studies of fracture. *Experimental Mechanics*, 19(10), 349–361.
- Dassault. (2014). ABAQUS/Standard User’s Manual, Version 6.14. Dassault Systems Simulia Corp.
- Deegan, R. D., Petersan, P. J., Marder, M., & Swinney, H. L. (2002). Oscillating fracture paths in rubber. *Physical review letters*, 88(1), 14304. doi:10.1103/PhysRevLett.88.014304
- Drapaca, C. S., Sivaloganathan, S., & Tenti, G. (2007). Nonlinear constitutive laws in viscoelasticity. *Mathematics and Mechanics of Solids*, 12(5), 475–501. doi:10.1177/1081286506062450
- Elmukashfi, E. & Kroon, M. (2012). Numerical analysis of dynamic crack propagation in rubber. *International Journal of Fracture*, 177(2), 163–178. doi:10.1007/s10704-012-9761-8
- Elmukashfi, E. & Kroon, M. (2014). Numerical analysis of dynamic crack propagation in biaxially strained rubber sheets. *Engineering Fracture Mechanics*, 124-125, 1–17. doi:10.1016/J.ENGFRACMECH.2014.04.025
- Erdogan, F. & Sih, G. C. (1963). On the crack extension in plates under plane loading and transverse shear.
- Eshelby, J. D. (1956). The Continuum Theory of Lattice Defects. In F. Seitz & D. B. T. .-. S. S. P. Turnbull (Eds.), (Vol. 3, pp. 79–144). Academic Press. doi:https://doi.org/10.1016/S0081-1947(08)60132-0
- Fineberg, J., Gross, S. P., Marder, M., & Swinney, H. L. (1992). Instability in the propagation of fast cracks. *Physical Review B*, 45(10), 5146–5154. doi:10.1103/PhysRevB.45.5146

- Fineberg, J. & Marder, M. (1991). Instability in dynamic fracture. *Physical Review Letters*, 67(4), 457–460. doi:10.1103/PhysRevLett.67.457. arXiv: arXiv:1305.0989v1
- Fisher, G. M. C. & Gurtin, M. E. [Morton E.]. (1965). Wave propagation in the linear theory of viscoelasticity. *Quarterly of Applied Mathematics*, 23(3), 257–263. doi:10.1090/qam/191196
- Freund, L. (1979). The mechanics of dynamic shear crack propagation. *Journal of Geophysical Research*, 84(B5), 2199. doi:10.1029/JB084iB05p02199
- Freund, L. (1990). *Dynamic fracture mechanics*. Cambridge: Cambridge University Press. doi:10.1142/6139
- Freund, L. & Hutchinson, J. (1985). High strain-rate crack growth in rate-dependent plastic solids. *Journal of the Mechanics and Physics of Solids*, 33(2), 169–191. doi:10.1016/0022-5096(85)90029-8
- Fuller, K. N. G., Fox, P. G., & Field, J. E. (1975). The temperature rise at the tip of fast-moving cracks in glassy polymers. *Proceedings of the Royal Society of London. A. Mathematical and Physical Sciences*, 341(1627), 537–557.
- Geißler, G. & Kaliske, M. [Michael]. (2010). Time-dependent cohesive zone modelling for discrete fracture simulation. *Engineering Fracture Mechanics*, 77(1), 153–169. doi:10.1016/J.ENGFRACMECH.2009.09.013
- Geißler, G., Kaliske, M., Nase, M., & Grellmann, W. (2007). Peel process simulation of sealed polymeric film computational modelling of experimental results. *Engineering Computations (Swansea, Wales)*, 24(6), 586–607. doi:10.1108/02644400710774798
- Gent, A. (1996a). A new constitutive relation for rubber. *Rubber chemistry and technology*, 69(1), 59–61.
- Gent, A. (1996b). Adhesion and Strength of Viscoelastic Solids. Is There a Relationship between Adhesion and Bulk Properties? †. *Langmuir*, 12(19), 4492–4496. doi:10.1021/la950887q
- Gent, A. & Marteny, P. (1982a). Crack velocities in natural rubber. *Journal of Materials Science*, 17(10), 2955–2960. doi:10.1007/BF00644675
- Gent, A. & Marteny, P. (1982b). The effect of strain upon the velocity of sound and the velocity of free retraction for natural rubber. *Journal of Applied Physics*, 53(9), 6069–6075. doi:10.1063/1.331558
- Germain, P., Nguyen, Q. S., & Suquet, P. (1983). Continuum thermodynamics. *Journal of Applied Mechanics, Transactions ASME*, 50(4), 1010–1020. doi:10.1115/1.3167184
- Geubelle, P., Danyluk, M. J., & Hilton, H. H. (1998). Dynamic mode III fracture in viscoelastic media. *International Journal of Solids and Structures*, 35(9-10), 761–782. doi:10.1016/S0020-7683(97)00084-X
- Geubelle, P. & Knauss, W. (1994). Finite strains at the tip of a crack in a sheet of hyperelastic material: I. Homogeneous case. *Journal of Elasticity*, 35(1-3), 61–98. doi:10.1007/BF00115539
- Goldstein, R. V. & Salganik, R. L. (1974). Brittle fracture of solids with arbitrary cracks. *Int. J. Fracture*, 10, 507.
- Gori, M., Rubino, V., Rosakis, A. J., & Lapusta, N. (2018). Pressure shock fronts formed by ultra-fast shear cracks in viscoelastic materials. *Nature communications*, 9(1), 4754. doi:10.1038/s41467-018-07139-4
- Govindjee, S. & Reese, S. (1997). A presentation and comparison of two large deformation viscoelasticity models. *Journal of Engineering Materials and Technology, Transactions of the ASME*, 119(3), 251–255. doi:10.1115/1.2812252

- Graham, G. A. C. & Walton, J. R. (1995). *Crack and contact problems for viscoelastic bodies*.
- Green, A. E. & Rivlin, R. S. [R. S.]. (1997). *The Mechanics of Non-Linear Materials with Memory* (G. I. Barenblatt & D. D. Joseph, Eds.). Springer New York. doi:10.1007/978-1-4612-2416-7\_70
- Greensmith, H. W. (1957). Rupture of Rubber. IV. Tear Properties of Vulcanizates Containing Carbon Black. *Rubber Chemistry and Technology*, 30(2), 584–595. doi:10.5254/1.3542707
- Greensmith, H. W. & Thomas, A. G. (1956). Rupture of Rubber. III. Determination of Tear Properties. *Rubber Chemistry and Technology*, 29(2), 372–381. doi:10.5254/1.3542533
- Griffith, A. A. (1921). The Phenomena of Rupture and Flow in Solids. *Philosophical Transactions of the Royal Society A: Mathematical, Physical and Engineering Sciences*, 221(582-593), 163–198. doi:10.1098/rsta.1921.0006
- Guo, G., Yang, W., & Huang, Y. (2003). Supersonic crack growth in a solid of upturn stress-strain relation under anti-plane shear. *Journal of the Mechanics and Physics of Solids*, 51(11-12), 1971–1985. doi:10.1016/j.jmps.2003.09.028
- Gurtin, M. E. [Morton E]. (2000). Configurational Forces as Basic Concepts of Continuum Physics. 137. doi:10.1007/b97847. arXiv: arXiv:1011.1669v3
- Halphen, B. & Nguyen, Q. S. (1975). Sur les matériaux standards généralisés. (January).
- Hilber, H. M., Hughes, T. J. R., & Taylor, R. L. (1977). Improved Numerical Dissipation For Time Integration Algorithms in Structural Dynamics. *Earthquake Engineering and Structural Dynamics*, 5(June 1976), 283–292.
- Holzappel, A. G. (2000). Nonlinear solid mechanics II.
- Holzappel, G. A. (2000). Nonlinear Solid Mechanics - A Continuum Approach for Engineering.
- Hussain, M. A., Pu, S. L., & Underwood, J. (1974). Strain Energy Release Rate for a Crack Under Combined Mode I and Mode II. In G. R. Irwin (Ed.), *Fracture analysis: Proceedings of the 1973 national symposium on fracture mechanics, part ii* (pp. 2–28). West Conshohocken, PA: ASTM International. doi:10.1520/STP33130S
- Hutchinson, J. W. & Tvergaard, V. (1992). The relation between crack growth resistance and fracture process parameters elastic-plastic solids. *Journal of the Mechanics and Physics of Solids*, 40(6), 1377–1397.
- Inglis, C. E. (1913). Stresses in a plate due to the presence of cracks and sharp corners. *Trans Inst Naval Archit*, 55, 219–241.
- Irwin, G. R. (1957). Analysis of stresses and strains near the end of a crack transversing a plate. *Trans. ASME, Ser. E, J. Appl. Mech.* 24, 361–364.
- Jagota, A., Bennison, S. J., & Smith, C. A. (2000). Analysis of a compressive shear test for adhesion between elastomeric polymers and rigid substrates. *International Journal of Fracture*, 104(2), 105–130. doi:10.1023/A:1007617102311
- Kadir, A. & Thomas, A. G. (1981). Tear behavior of rubbers over a wide range of rates.
- Kadir, A. & Thomas, A. G. (1984). Tearing of Unvulcanized Natural Rubber. *Journal of polymer science. Part A-2, Polymer physics*, 22(9), 1623–1634. doi:10.1002/pol.1984.180220906
- Kaliske, M. & Heinrich, G. (1999). An extended tube-model for rubber elasticity: statistical-mechanical theory and finite element implementation. *Rubber Chemistry and Technology*, 72(4), 602–632.
- Kamasamudram, V. (2021). <https://github.com/vasude1/UMAT>.

- Kamasamudram, V. & Coret, M. (2019a). Investigation of Dynamic Fracture of Elastomers - IIa. doi:<https://doi.org/10.5281/zenodo.4040507>
- Kamasamudram, V. & Coret, M. (2019b). Investigation of Dynamic Fracture of Elastomers - IIb. doi:<https://doi.org/10.5281/zenodo.4040619>
- Kamasamudram, V., Coret, M., & Moës, N. (2021). The role played by viscoelasticity in the bulk material during the propagation of a dynamic crack in elastomers. *International Journal of Fracture*, 231(1), 43–58. doi:10.1007/s10704-021-00561-8
- Knauss, W. G. & Losi, G. U. (1993). Crack propagation in a nonlinearly viscoelastic solid with relevance to adhesive bond failure. *Journal of Applied Mechanics, Transactions ASME*, 60(4), 793–801. doi:10.1115/1.2900985
- Knauss, W. (1970). *Delayed Failure - The Griffith problem for Linearly Viscoelastic Materials* (tech. rep. No. 1).
- Knauss, W. (2015). A review of fracture in viscoelastic materials. *International Journal of Fracture*, 196(1-2), 99–146. doi:10.1007/s10704-015-0058-6
- Knauss, W. & Mueller, H. (1971). Crack propagation in a linearly viscoelastic strip. *Journal of Applied Mechanics*, 38, 483–488. doi:10.1115/1.3408801
- Knowles, J. K. (1977). The finite anti-plane shear field near the tip of a crack for a class of incompressible elastic solids. *International Journal of Fracture*, 13(5), 611–639. doi:10.1007/BF00017296
- Kostrov, B. V. & Nikitin, L. V. (1970). Some General problems Of Mechanics Of Brittle Fracture. *Archiwum Mechaniki Stosowanej*, 22(6).
- Krishnan, V. R., Hui, C. Y., & Long, R. (2008). Finite strain crack tip fields in soft incompressible elastic solids. *Langmuir*, 24(24), 14245–14253. doi:10.1021/la802795e
- Kroon, M. (2014). Energy release rates in rubber during dynamic crack propagation. *International Journal of Solids and Structures*, 51(25-26), 4419–4426. doi:10.1016/j.ijsolstr.2014.09.010
- Kubair, D. & Geubelle, P. (2003). Comparative analysis of extrinsic and intrinsic cohesive models of dynamic fracture. *International Journal of Solids and Structures*, 40(15), 3853–3868. doi:10.1016/S0020-7683(03)00171-9
- Lake, G. J., Lawrence, C. C., & Thomas, a. G. (2000). High-Speed Fracture of Elastomers: Part I. *Rubber Chemistry and Technology*, 73(5), 801–817. doi:10.5254/1.3547620
- Lake, G. J., Thomas, A. G., & Lawrence, C. C. (1992). Effects of hydrostatic pressure on crack growth in elastomers. *Polymer*, 33(19), 4069–4074. doi:10.1016/0032-3861(92)90607-X
- Livne, A., Ben-David, O., & Fineberg, J. (2006). Oscillations in Rapid Fracture. doi:10.1103/PhysRevLett.98.124301. arXiv: 0609273 [cond-mat]
- Livne, A., Bouchbinder, E., & Fineberg, J. (2008). Breakdown of Linear Elastic Fracture Mechanics near the Tip of a Rapid Crack. *Physical Review Letters*, 101(26), 264301. doi:10.1103/PhysRevLett.101.264301
- Loew, P. J., Peters, B., & Beex, L. A. (2019). Rate-dependent phase-field damage modeling of rubber and its experimental parameter identification. *Journal of the Mechanics and Physics of Solids*, 127, 266–294. doi:10.1016/j.jmps.2019.03.022
- Lubliner, J. (1985). A model of rubber viscoelasticity. *Mechanics Research Communications*, 12(2), 93–99.
- Mai, T. T., Okuno, K., Tsunoda, K., & Urayama, K. (2020). Crack-Tip Strain Field in Supershear Crack of Elastomers. *ACS Macro Letters*, 9(5), 762–768. doi:10.1021/acsmacrolett.0c00213

- Marckmann, G. & Verron, E. (2006). Comparison of hyperelastic models for rubber-like materials. *Rubber chemistry and technology*, 79(5), 835–858.
- Marder, M. (2005). Shock-wave theory for rupture of rubber. *Physical Review Letters*, 94(4). doi:10.1103/PhysRevLett.94.048001. arXiv: 0407236 [arXiv: cond-mat]
- Marder, M. (2006). Supersonic rupture of rubber. *Journal of the Mechanics and Physics of Solids*, 54(3), 491–532. doi:10.1016/j.jmps.2005.10.002
- Marigo, J.-J., Maurini, C., & Pham, K. (2016). An overview of the modelling of fracture by gradient damage models An overview of the modelling of fracture by gradient damage models An overview of the modelling of fracture by gradient damage models. *Meccanica*, (12), 51. doi:10.1007/s11012-016-0538-4
- Marsden, J. E. & Hughes, T. J. R. (1994). *Mathematical foundations of elasticity*. Courier Corporation.
- Maugin, G. A. [Gérard A.]. (2016). *Configurational forces: thermomechanics, physics, mathematics, and numerics*. CRC Press.
- Maugin, G. A. [Gerard A.] & Muschik, W. (1994). Thermodynamics with internal variables part i. general concepts. *Journal of Non-Equilibrium Thermodynamics*, 19(3), 217–249. doi:10.1515/jnet.1994.19.3.217
- Mello, M., Bhat, H. S., Rosakis, A. J., & Kanamori, H. (2010). Identifying the unique ground motion signatures of supershear earthquakes: Theory and experiments. *Tectonophysics*, 493(3-4), 297–326. doi:10.1016/j.tecto.2010.07.003
- Miehe, C. [C.], Welschinger, F., & Hofacker, M. (2010). Thermodynamically consistent phase-field models of fracture: Variational principles and multi-field FE implementations. *International Journal for Numerical Methods in Engineering*, 83(10), 1273–1311. doi:10.1002/nme.2861
- Miehe, C. [Christian] & Schänzel, L. M. (2014). Phase field modeling of fracture in rubbery polymers. Part I: Finite elasticity coupled with brittle failure. *Journal of the Mechanics and Physics of Solids*, 65(1), 93–113. doi:10.1016/j.jmps.2013.06.007
- Miehe, C. [Christian], Schänzel, L. M., & Ulmer, H. (2015). Phase field modeling of fracture in multi-physics problems. Part I. Balance of crack surface and failure criteria for brittle crack propagation in thermo-elastic solids. *Computer Methods in Applied Mechanics and Engineering*, 294, 449–485. doi:10.1016/j.cma.2014.11.016
- Miller, O., Freund, L., & Needleman, A. (1999). Energy Dissipation in Dynamic Fracture of Brittle Materials. *Modelling and Simulation in Materials Science and Engineering*, 7(4), 573. doi:10.1088/0965-0393/7/4/307
- Moës, N., Stolz, C., Bernard, P. E., & Chevaugeon, N. (2011). A level set based model for damage growth: The thick level set approach. *International Journal for Numerical Methods in Engineering*, 86(3), 358–380. doi:10.1002/nme.3069
- Mooney, M. (1940). A theory of large elastic deformation. *Journal of applied physics*, 11(9), 582–592.
- Mott. (1948). Brittle Fracture in Mild-Steel Plates. *Engineering*, 165, 16–18.
- Moulinet, S. & Adda-Bedia, M. (2015). Popping Balloons: A Case Study of Dynamical Fragmentation. *Physical Review Letters*, 115(18). doi:10.1103/PhysRevLett.115.184301
- Musto, M. & Alfano, G. (2011). Aquasicontinuum methodology for multiscale analyses of discrete microstructural ... *Proceedings of the 2011 American Control Conference*, (February), 1885–1891. doi:10.1002/nme. arXiv: 1010.1724
- Needleman, A. (1999). An Analysis of Intersonic Crack Growth Under Shear Loading. *Journal of Applied Mechanics*, 66(4), 847. doi:10.1115/1.2791788

- Nguyen, N. & Waas, A. M. (2016). Nonlinear, finite deformation, finite element analysis. *Zeitschrift für Angewandte Mathematik und Physik*, 67(3), 1–24. doi:10.1007/s00033-016-0623-5
- Nguyen, T. D. & Govindjee, S. [S.]. (2006). Numerical study of geometric constraint and cohesive parameters in steady-state viscoelastic crack growth. *International Journal of Fracture*, 141(1-2), 255–268. doi:10.1007/s10704-006-0080-9
- Niemczura, J. & Ravi-Chandar, K. (2011). On the response of rubbers at high strain rates-III. Effect of hysteresis. *Journal of the Mechanics and Physics of Solids*, 59(2), 457–472. doi:10.1016/j.jmps.2010.09.009
- Ogden, R. W. (1972). Large deformation isotropic elasticity—on the correlation of theory and experiment for incompressible rubberlike solids. *Proceedings of the Royal Society of London. A. Mathematical and Physical Sciences*, 326(1567), 565–584.
- Özenc, K., Kaliske, M., Lin, G., & Bhashyam, G. (2014). Evaluation of energy contributions in elasto-plastic fracture: A review of the configurational force approach. *Engineering Fracture Mechanics*, 115, 137–153. doi:10.1016/J.ENGFRACMECH.2013.11.001
- Peerlings, R. H., De Borst, R., Brekelmans, W. A., & Geers, M. G. (2002). Localisation issues in local and nonlocal continuum approaches to fracture. *European Journal of Mechanics, A/Solids*, 21(2), 175–189. doi:10.1016/S0997-7538(02)01211-1
- Persson, B. N. J., Albohr, O., Heinrich, G., & Ueba, H. (2005). Crack propagation in rubber-like materials. *Journal of Physics Condensed Matter*, 17(44). doi:10.1088/0953-8984/17/44/R01
- Persson, B. N. & Brener, E. A. (2005). Crack propagation in viscoelastic solids. *Physical Review E - Statistical, Nonlinear, and Soft Matter Physics*, 71(3), 1–8. doi:10.1103/PhysRevE.71.036123
- Petersan, P. J., Deegan, R. D., Marder, M., & Swinney, H. L. (2004). Cracks in rubber under tension exceed the shear wave speed. *Physical Review Letters*, 93(1), 015504–1. doi:10.1103/PhysRevLett.93.015504. arXiv: 0311422 [cond-mat]
- Rahulkumar, P., Jagota, A., Bennison, S. J., & Saigal, S. (2000). Cohesive element modeling of viscoelastic fracture: Application to peel testing of polymers. *International Journal of Solids and Structures*, 37(13), 1873–1897. doi:10.1016/S0020-7683(98)00339-4
- Ravi-Chandar, K. & Knauss, W. (1984a). An experimental investigation into dynamic fracture: I. Crack initiation and arrest. *International Journal of Fracture*, 25(4), 247–262. doi:10.1007/BF00963460
- Ravi-Chandar, K. & Knauss, W. (1984b). An experimental investigation into dynamic fracture: III. On steady-state crack propagation and crack branching. *International Journal of Fracture*, 26(2), 141–154. doi:10.1007/BF01157550
- Ravi-Chandar, K. & Yang, B. (1997). On the role of microcracks in the dynamic fracture of brittle materials. *Journal of the Mechanics and Physics of Solids*, 45(4), 535–563. doi:10.1016/S0022-5096(96)00096-8
- Reese, S. & Govindjee, S. (1998). A theory of finite viscoelasticity and numerical aspects. *International Journal of Solids and Structures*, 35(26-27), 3455–3482. doi:10.1016/S0020-7683(97)00217-5
- Reese, S. & Wriggers, P. (1995). A finite element method for stability problems in finite elasticity. *International journal for numerical methods in engineering*, 38(7), 1171–1200.

- Rice, J. R. [J R]. (1968). A Path Independent Integral and the Approximate Analysis of Strain Concentration by Notches and Cracks. *Journal of Applied Mechanics*, 35(2), 379–386. doi:10.1115/1.3601206
- Rice, J. R. [James R.]. (1979). Mechanics of Quasi-Static Crack Growth. *IEEE Journal of Solid-State Circuits*, (July), 191–216.
- Rivlin, R. S. [R S]. (1948). Large elastic deformations of isotropic materials IV. Further developments of the general theory. *Philosophical Transactions of the Royal Society of London. Series A, Mathematical and Physical Sciences*, 241(835), 379–397.
- Rivlin, R. S. [R. S.] & Thomas, A. G. (1953). Rupture of Rubber. I. Characteristic Energy for Tearing. *Journal of Polymer Science*, 10(3), 291–318. doi:10.1007/978-1-4612-2416-7\_180
- Rivlin, R. S. [R. S.] & Thomas, A. G. (1997). Rupture of Rubber. I. Characteristic Energy for Tearing. *Collected Papers of R.S. Rivlin*, 10(3), 2615–2642. doi:10.1007/978-1-4612-2416-7\_180
- Rivlin, R. S. [Ronald S] & Saunders, D. W. (1951). Large elastic deformations of isotropic materials VII. Experiments on the deformation of rubber. *Philosophical Transactions of the Royal Society of London. Series A, Mathematical and Physical Sciences*, 243(865), 251–288.
- Rosakis, A. J. (2002). Intersonic shear cracks and fault ruptures. *Advances in Physics*, 51(4), 1189–1257. doi:10.1080/00018730210122328
- Rosakis, A. J., Samudrala, O., & Coker, D. (2000). Intersonic shear crack growth along weak planes. *Materials Research Innovations*, 3(4), 236–243. doi:10.1007/s100190050009
- Runesson, K., Larsson, F., & Steinmann, P. (2009). On energetic changes due to configurational motion of standard continua. *International Journal of Solids and Structures*, 46(6), 1464–1475. doi:10.1016/j.ijsolstr.2008.11.011
- Saccomandi, G. (2007). Finite amplitude waves in nonlinear elastodynamics and related theories: A personal overview. In *Cism international centre for mechanical sciences, courses and lectures* (Vol. 495, pp. 129–179). Vienna: Springer Vienna. doi:10.1007/978-3-211-73572-5\_5
- Schapery, R. A. (1975a). A theory of crack initiation and growth in viscoelastic media - I. Theoretical development. *International Journal of Fracture*, 11(1), 141–159. doi:10.1007/BF00034721
- Schapery, R. A. (1975b). A theory of crack initiation and growth in viscoelastic media - III. Analysis of continuous growth. *International Journal of Fracture*, 11(4), 549–562. doi:10.1007/BF00116363
- Schapery, R. A. (1975c). A theory of crack initiation and growth in viscoelastic media II. Approximate methods of analysis. *International Journal of Fracture*. doi:10.1007/BF00033526
- Sharon, E. & Fineberg, J. (1996). Microbranching instability and the dynamic fracture of brittle materials. *Physical Review B*, 54(10), 7128–7139. doi:10.1007/s11099-014-0033-x
- Sharon, E., Gross, S. P., & Fineberg, J. (1996). Energy dissipation in dynamic fracture. *Physical Review Letters*, 76(12), 2117–2120. doi:10.1103/PhysRevLett.76.2117
- Sih, G. C. (1973). Some basic problems in fracture mechanics and new concepts. *Engineering fracture mechanics*, 5(2), 365–377.
- Simha, N. K., Fischer, F. D., Shan, G. X., Chen, C. R., & Kolednik, O. (2008). J-integral and crack driving force in elastic-plastic materials. *Journal of the Mechanics and Physics of Solids*, 56(9), 2876–2895. doi:10.1016/j.jmps.2008.04.003

- Simha, N. K., Fischer, F., Kolednik, O., & Chen, C. (2003). Inhomogeneity effects on the crack driving force in elastic and elastic–plastic materials. *Journal of the Mechanics and Physics of Solids*, 51(1), 209–240. doi:10.1016/S0022-5096(02)00025-X
- Simo, J. C. (1987). On a fully three-dimensional finite-strain viscoelastic damage model: Formulation and computational aspects. *Computer Methods in Applied Mechanics and Engineering*, 60(2), 153–173. doi:10.1016/0045-7825(87)90107-1
- Simo, J. C. & Hughes, T. J. (1998). *Computational Inelasticity*.
- Steinmann, P. (2000). Application of material forces to hyperelastostatic fracture mechanics. I. Continuum mechanical setting. *International Journal of Solids and Structures*, 37(48–50), 7371–7391. doi:10.1016/S0020-7683(00)00203-1
- Stevenson, A. & Thomas, A. G. (1979). On the bursting of a balloon. *Journal of Physics D: Applied Physics*, 12(12), 2101–2109. doi:10.1088/0022-3727/12/12/012
- Suffis, A., Lubrecht, T. A., & Combescure, A. (2003). Damage model with delay effect analytical and numerical studies of the evolution of the characteristic damage length. *International Journal of Solids and Structures*, 40(13–14), 3463–3476. doi:10.1016/S0020-7683(03)00153-7
- Tarantino, A. M. (1999). On the finite motions generated by a mode I propagating crack. *Journal of Elasticity*, 57(2), 85–103. doi:10.1023/A:1007673212904
- Taylor, R. L., Pister, K. S., & Goudreau, G. L. (1970). Thermomechanical Analysis of Viscoelastic Solids. 2(February 1969), 45–59.
- Treloar, L. R. G. (1943). The elasticity of a network of long-chain molecules—II. *Transactions of the Faraday Society*, 39(0), 241–246. doi:10.1039/TF9433900241
- Tsunoda, K., Busfield, J. J., Davies, C. K., & Thomas, A. G. (2000). Effect of materials variables on the tear behaviour of a non-crystallizing elastomer. *Journal of Materials Science*, 35(20), 5187–5198. doi:10.1023/A:1004860522186
- Verron, E. (2018). Modèles hyperélastiques pour le comportement mécanique des élastomères. *Techniques de l'ingénieur, AM8210 V1(0)*, 28.
- VIC-2D, Correlated Solutions. (2019).
- Washabaugh, P. D. & Knauss, W. (1994). A reconciliation of dynamic crack velocity and Rayleigh wave speed in isotropic brittle solids. *International Journal of Fracture*, 65(2), 97–114. doi:10.1007/BF00032282
- Weber, G. & Anand, L. (1990). Finite deformation constitutive equations and a time integration procedure for isotropic, hyperelastic-viscoplastic solids. *Computer Methods in Applied Mechanics and Engineering*, 79(2), 173–202. doi:10.1016/0045-7825(90)90131-5
- Willis, J. (1967). Crack propagation in viscoelastic media. *Journal of the Mechanics and Physics of Solids*, 15(4), 229–240. doi:10.1016/0022-5096(67)90013-0
- Wineman, A. (2009). *Nonlinear Viscoelastic Solids—A Review*. doi:10.1177/1081286509103660
- Xu, D. B., Hui, C. Y., & Kramer, E. J. (1992). Interface fracture and viscoelastic deformation in finite size specimens. *Journal of Applied Physics*, 72(8), 3305–3316. doi:10.1063/1.352342
- Xu, X. P. & Needleman, A. (1994). Numerical simulations of fast crack growth in brittle solids. *Journal of the Mechanics and Physics of Solids*, 42(9), 1397–1434. doi:10.1016/0022-5096(94)90003-5
- Yavari, A. (2010). A geometric theory of growth mechanics. *Journal of Nonlinear Science*, 20(6), 781–830. doi:10.1007/s00332-010-9073-y. arXiv: 0911.4671
- Yin, B. & Kaliske, M. [Michael]. (2019). Fracture simulation of viscoelastic polymers by the phase-field method. *Computational Mechanics*. doi:10.1007/s00466-019-01769-1

- Zhang, H. P., Niemczura, J., Dennis, G., Ravi-Chandar, K., & Marder, M. (2009). Toughening effect of strain-induced crystallites in natural rubber. *Physical Review Letters*, *102*(24), 4–7. doi:10.1103/PhysRevLett.102.245503
- Zreid, I., Fleischhauer, R., & Kaliske, M. (2013). A thermomechanically coupled viscoelastic cohesive zone model at large deformation. *International Journal of Solids and Structures*, *50*(25-26), 4279–4291. doi:10.1016/j.ijsolstr.2013.08.031

PLANE STRESS VERSION OF  
FINITE LINEAR VISCOELASTIC  
MODEL



CONTENTS

A.1 Time integration . . . . . 147  
A.2 Computation of tangent . . . . . 148

The PK2 stress in Simo, 1987's model is given by

$$\mathbf{S} = -p\mathbf{J}\mathbf{C}^{-1} + \text{DEV}_t \left\{ \int_{-\infty}^t g(t-s) \frac{\partial}{\partial s} \text{DEV}_s \left\{ 2 \frac{\partial \psi}{\partial \mathbf{C}}(s) \right\} ds \right\}, \quad (\text{A.1})$$

where the first  $\text{DEV}_t \left\{ \bullet \right\}$  projector is evaluated at time  $t$  and the projector inside the integral is evaluated at time  $s$ . In this appendix, the plane stress version of the above model will be derived.

First, the above equation is simplified to move the time derivative from the  $\text{DEV} \left\{ \bullet \right\}$  to the first term by using integration by parts.

$$\begin{aligned} \int_{-\infty}^t g(t-s) \frac{\partial}{\partial s} \text{DEV}_s \left\{ 2 \frac{\partial \psi}{\partial \mathbf{C}} \right\} ds &= g(t-s) \text{DEV} \left\{ 2 \frac{\partial \psi}{\partial \mathbf{C}} \right\} \Big|_{-\infty}^t - \int_{-\infty}^t \frac{\partial}{\partial s} g(t-s) \text{DEV}_s \left\{ 2 \frac{\partial \psi}{\partial \mathbf{C}} \right\} ds \\ &= g(0) \text{DEV} \left\{ 2 \frac{\partial \psi}{\partial \mathbf{C}}(t) \right\} - \int_{-\infty}^t \frac{\partial}{\partial s} g(t-s) \text{DEV} \left\{ 2 \frac{\partial \psi}{\partial \mathbf{C}} \right\} ds, \end{aligned} \quad (\text{A.2})$$

where,  $\text{DEV} \left\{ 2 \frac{\partial \psi}{\partial \mathbf{C}}(-\infty) \right\} = \mathbf{O}$  has been used. Defining  $\tilde{\mathbf{S}} := 2 \frac{\partial \psi}{\partial \mathbf{C}}$ , the first equation becomes

$$\mathbf{S} = -p\mathbf{C}^{-1} + g(0) \text{DEV}_t \left\{ \tilde{\mathbf{S}}(t) \right\} - \text{DEV}_t \left\{ \int_{-\infty}^t h(t-s) \text{DEV}_s \left\{ \tilde{\mathbf{S}}^s \right\} ds \right\}, \quad (\text{A.3})$$

where  $h(t-s) := \frac{\partial}{\partial s} g(t-s)$  and  $\text{DEV}_t \left\{ \text{DEV}_t \left\{ \bullet \right\} \right\} = \text{DEV}_t \left\{ \bullet \right\}$ , since  $\text{DEV} \left\{ \bullet \right\}$  is a projector. A superscript has been added to indicate the time at which the quantity is evaluated. The deviatoric projector inside the integral can be evaluated as

$$\text{DEV}_s \left\{ \tilde{\mathbf{S}}^s \right\} = \tilde{\mathbf{S}}^s - \frac{1}{3} \text{tr}(\tilde{\mathbf{S}}^s \mathbf{C}^s) (\mathbf{C}^s)^{-1}. \quad (\text{A.4})$$

The integral hence becomes

$$\int_{-\infty}^t h(t-s) \text{DEV}_s \left\{ \tilde{\mathbf{S}}^s \right\} ds = \int_{-\infty}^t h(t-s) \tilde{\mathbf{S}}^s ds - \frac{1}{3} \int_{-\infty}^t h(t-s) \text{tr}(\tilde{\mathbf{S}}^s \mathbf{C}^s) (\mathbf{C}^s)^{-1} ds. \quad (\text{A.5})$$

It has been made clear that the quantities are to be evaluated at the time  $s$ . The deviator at time  $t$  can now be written as

$$\begin{aligned} \text{DEV}_t \left\{ \int_{-\infty}^t h(t-s) \text{DEV}_s \left\{ \tilde{\mathbf{S}}^s \right\} ds \right\} &= \\ &= \int_{-\infty}^t h(t-s) \tilde{\mathbf{S}}^s ds - \frac{1}{3} \int_{-\infty}^t h(t-s) \text{tr}(\tilde{\mathbf{S}}^s \mathbf{C}^s) (\mathbf{C}^s)^{-1} ds \\ &- \frac{1}{3} \int_{-\infty}^t h(t-s) \text{tr}(\tilde{\mathbf{S}}^s \mathbf{C}^s) (\mathbf{C}^s)^{-1} ds + \frac{1}{9} \int_{-\infty}^t h(t-s) \text{tr}(\tilde{\mathbf{S}}^s \mathbf{C}^s) \text{tr}((\mathbf{C}^s)^{-1} \mathbf{C}^t) (\mathbf{C}^t)^{-1} ds. \end{aligned} \quad (\text{A.6})$$

The 33 component of the above deviator is given by

$$\begin{aligned} & \left[ \text{DEV}_t \left\{ \int_{-\infty}^t h(t-s) \text{DEV}_s \left\{ \tilde{\mathbf{S}}^s \right\} ds \right\} \right]_{33} = \\ & \int_{-\infty}^t h(t-s) \tilde{S}_{33}^s ds - \frac{1}{3} \int_{-\infty}^t h(t-s) \text{tr}(\tilde{\mathbf{S}}^s \mathbf{C}^t) (\mathbf{C}_{33}^t)^{-1} ds \\ & - \frac{1}{3} \int_{-\infty}^t h(t-s) \text{tr}(\tilde{\mathbf{S}}^s \mathbf{C}^s) (\mathbf{C}_{33}^s)^{-1} ds + \frac{1}{9} \int_{-\infty}^t h(t-s) \text{tr}(\tilde{\mathbf{S}}^s \mathbf{C}^s) \text{tr}((\mathbf{C}^s)^{-1} \mathbf{C}^t) (\mathbf{C}_{33}^t)^{-1} ds. \end{aligned} \quad (\text{A.7})$$

It has been assumed that the strain tensors can be expressed in the form of A.10 to write the above equation. The expression for  $p$  can now be developed by using  $S_{33} = 0$ . This implies

$$p(\mathbf{C}_{33}^t)^{-1} = g(0) \left( \tilde{S}_{33}^t - \frac{1}{3} \text{tr}(\tilde{\mathbf{S}}^t \mathbf{C}^t) (\mathbf{C}_{33}^t)^{-1} \right) - \left[ \text{DEV}_t \left\{ \int_{-\infty}^t h(t-s) \text{DEV}_s \left\{ \tilde{\mathbf{S}}^s \right\} ds \right\} \right]_{33}. \quad (\text{A.8})$$

Hence,

$$\begin{aligned} p &= g(0) \left( \tilde{S}_{33}^t \mathbf{C}_{33}^t - \frac{1}{3} \text{tr}(\tilde{\mathbf{S}}^t \mathbf{C}^t) \right) - \int_{-\infty}^t h(t-s) \tilde{S}_{33}^s \mathbf{C}_{33}^t ds + \frac{1}{3} \int_{-\infty}^t h(t-s) \text{tr}(\tilde{\mathbf{S}}^s \mathbf{C}^t) ds \\ &+ \frac{1}{3} \int_{-\infty}^t h(t-s) \text{tr}(\tilde{\mathbf{S}}^s \mathbf{C}^s) (\mathbf{C}_{33}^s)^{-1} \mathbf{C}_{33}^t ds - \frac{1}{9} \int_{-\infty}^t h(t-s) \text{tr}(\tilde{\mathbf{S}}^s \mathbf{C}^s) \text{tr}((\mathbf{C}^s)^{-1} \mathbf{C}^t) ds. \end{aligned} \quad (\text{A.9})$$

As a consequence of the plane stress assumption, the deformation gradient can be written in a block form to be

$$\mathbf{F} = \begin{bmatrix} \mathbf{F}_{2d} & \mathbf{o} \\ \mathbf{o}^T & F_{33} \end{bmatrix}. \quad (\text{A.10})$$

The above form is assumed to be valid at all times. Now, the expression for  $\tilde{\mathbf{S}}$ , written in terms of 3D-strain invariants can be seen to be

$$\tilde{\mathbf{S}} = 2 \frac{\partial \psi}{\partial I_1} \mathbf{I} + 2 \frac{\partial \psi}{\partial I_2} [I_1 \mathbf{I} - \mathbf{C}], \quad (\text{A.11})$$

where  $I_1$  and  $I_2$  are the invariants of  $\mathbf{C}$ , since the material is incompressible. The inplane stress components can now be expressed in terms of the invariants of the in-plane strain tensor as

$$\tilde{S}_{2d} = 2 \frac{\partial \psi}{\partial I_1} I_{2d} + 2 \frac{\partial \psi}{\partial I_2} \left[ (I_1^{2d} + C_{33}) I_{2d} - C_{2d} \right], \quad (\text{A.12})$$

where  $C_{2d} = \mathbf{F}_{2d}^T \mathbf{F}_{2d}$ ,  $I_1^{2d} = \text{tr}(\mathbf{C}_{2d})$ ,  $C_{33} = 1/\det(\mathbf{C}_{2d})$ . Hence,

$$\tilde{S}_{33} = 2 \frac{\partial \psi}{\partial I_1} + 2 \frac{\partial \psi}{\partial I_2} I_1^{2d} \quad (\text{A.13})$$

Defining

$$\hat{\mathbf{S}} = 2 \frac{\partial \psi}{\partial \mathbf{C}_{2d}}, \quad (\text{A.14})$$

where  $\psi$  is the glassy strain energy density functional now expressed completely in terms of the invariants of  $\mathbf{C}_{2d}$ . The expression can be seen to be

$$\hat{\mathbf{S}} = 2 \frac{\partial \psi}{\partial I_1} \left( \mathbf{I} - \frac{1}{\det \mathbf{C}_{2d}} \mathbf{C}_{2d}^{-1} \right) + 2 \frac{\partial \psi}{\partial I_2} \left( I_1^{2d} \mathbf{I} - \frac{I_1^{2d}}{\det \mathbf{C}_{2d}} \mathbf{C}_{2d}^{-1} + \frac{1}{\det \mathbf{C}_{2d}} \mathbf{I} - \mathbf{C}_{2d} \right). \quad (\text{A.15})$$

The relation between the two stresses can be seen to be

$$\tilde{\mathbf{S}}_{2d}^s = \hat{\mathbf{S}}^s + \frac{\tilde{S}_{33}^s}{\det \mathbf{C}_{2d}^s} (\mathbf{C}_{2d}^s)^{-1} \quad \forall s \in [0, t]. \quad (\text{A.16})$$

The term  $\text{tr}(\tilde{\mathbf{S}}^s \mathbf{C}^s)$  can be computed as

$$\text{tr}(\tilde{\mathbf{S}}^s \mathbf{C}^s) = \text{tr}(\tilde{\mathbf{S}}_{2d}^s \mathbf{C}_{2d}^s) + \tilde{S}_{33}^s C_{33}^s = \text{tr}(\hat{\mathbf{S}}^s \mathbf{C}_{2d}^s) + 3\tilde{S}_{33}^s C_{33}^s \quad \forall s \in [0, t]. \quad (\text{A.17})$$

All the above can be combined to obtain the total stress. The terms with  $g(0)$  as coefficient can be evaluated as

$$\text{DEV}_t \left\{ \tilde{\mathbf{S}}^t \right\} - \left( \tilde{S}_{33}^t C_{33}^t - \frac{1}{3} \text{tr}(\tilde{\mathbf{S}}^t \mathbf{C}^t) \right) (\mathbf{C}^t)^{-1} = \tilde{\mathbf{S}}^t - \tilde{S}_{33}^t C_{33}^t (\mathbf{C}^t)^{-1}. \quad (\text{A.18})$$

The restriction of above equation to in-plane components will yield (from equation A.16)

$$\left[ \text{DEV}_t \left\{ \tilde{\mathbf{S}}^t \right\} - \left( \tilde{S}_{33}^t C_{33}^t - \frac{1}{3} \text{tr}(\tilde{\mathbf{S}}^t \mathbf{C}^t) \right) (\mathbf{C}^t)^{-1} \right]_{2d} = \tilde{\mathbf{S}}_{2d}^t - \tilde{S}_{33}^t C_{33}^t (\mathbf{C}_{2d}^t)^{-1} = \hat{\mathbf{S}}^t. \quad (\text{A.19})$$

The left over terms, after canceling the like terms, can be seen to be

$$\begin{aligned} (\mathbf{C}^t)^{-1} \int_{-\infty}^t h(t-s) \tilde{S}_{33}^s C_{33}^t ds - \frac{1}{3} (\mathbf{C}^t)^{-1} \int_{-\infty}^t h(t-s) \text{tr}(\tilde{\mathbf{S}}^s \mathbf{C}^s) (C_{33}^s)^{-1} C_{33}^t ds \\ - \int_{-\infty}^t h(t-s) \tilde{\mathbf{S}}^s ds + \frac{1}{3} \int_{-\infty}^t h(t-s) \text{tr}(\tilde{\mathbf{S}}^s \mathbf{C}^s) (\mathbf{C}^s)^{-1} ds ds. \end{aligned} \quad (\text{A.20})$$

Restricting to in-plane components,

$$\begin{aligned} (\mathbf{C}_{2d}^t)^{-1} \int_{-\infty}^t h(t-s) \tilde{S}_{33}^s C_{33}^t ds - \frac{1}{3} (\mathbf{C}_{2d}^t)^{-1} \int_{-\infty}^t h(t-s) \text{tr}(\tilde{\mathbf{S}}^s \mathbf{C}^s) (C_{33}^s)^{-1} C_{33}^t ds \\ - \int_{-\infty}^t h(t-s) \tilde{\mathbf{S}}_{2d}^s ds + \frac{1}{3} \int_{-\infty}^t h(t-s) \text{tr}(\tilde{\mathbf{S}}^s \mathbf{C}^s) (\mathbf{C}_{2d}^s)^{-1} ds \end{aligned} \quad (\text{A.21})$$

The term 2 of A.21 becomes

$$\begin{aligned} - \frac{1}{3} (\mathbf{C}_{2d}^t)^{-1} \int_{-\infty}^t h(t-s) \text{tr}(\tilde{\mathbf{S}}^s \mathbf{C}^s) (C_{33}^s)^{-1} C_{33}^t ds = \\ - \frac{1}{3} (\mathbf{C}_{2d}^t)^{-1} \int_{-\infty}^t h(t-s) \text{tr}(\hat{\mathbf{S}}^s \mathbf{C}_{2d}^s) (C_{33}^s)^{-1} C_{33}^t ds - (\mathbf{C}_{2d}^t)^{-1} \int_{-\infty}^t h(t-s) \tilde{S}_{33}^s C_{33}^t ds \end{aligned} \quad (\text{A.22})$$

The term 3 of A.21 becomes

$$\begin{aligned} - \int_{-\infty}^t h(t-s) \tilde{\mathbf{S}}_{2d}^s ds = \\ - \int_{-\infty}^t h(t-s) \hat{\mathbf{S}}^s ds - \int_{-\infty}^t h(t-s) \frac{\tilde{S}_{33}^s}{\det \mathbf{C}_{2d}^s} (\mathbf{C}_{2d}^s)^{-1} ds. \end{aligned} \quad (\text{A.23})$$

The term 4 of A.21 becomes

$$\begin{aligned} \frac{1}{3} \int_{-\infty}^t h(t-s) \text{tr}(\tilde{\mathbf{S}}^s \mathbf{C}^s) (\mathbf{C}_{2d}^s)^{-1} ds = \\ \frac{1}{3} \int_{-\infty}^t h(t-s) \text{tr}(\hat{\mathbf{S}}^s \mathbf{C}_{2d}^s) (\mathbf{C}_{2d}^s)^{-1} ds + \int_{-\infty}^t h(t-s) \tilde{S}_{33}^s C_{33}^s (\mathbf{C}_{2d}^s)^{-1} ds \end{aligned} \quad (\text{A.24})$$

Defining  $\text{DEV}_\alpha^{2D}\{\hat{\mathbf{S}}^s\} := \hat{\mathbf{S}}^s - \frac{1}{3} \text{tr}(\hat{\mathbf{S}}^s \mathbf{C}_{2d}^\alpha)(\mathbf{C}_{2d}^\alpha)^{-1}$  and combining the above equations, A.21 becomes

$$\text{A.21} = - \int_{-\infty}^t h(t-s) \left[ \text{DEV}_s^{2D}\{\hat{\mathbf{S}}^s\} \right] ds - \frac{1}{3} (\mathbf{C}_{2d}^t)^{-1} \int_{-\infty}^t h(t-s) \text{tr}(\hat{\mathbf{S}}^s \mathbf{C}_{2d}^s)(\mathbf{C}_{33}^s)^{-1} \mathbf{C}_{33}^t ds. \quad (\text{A.25})$$

Integrating the above by parts and realizing that  $h(t-s) = \frac{\partial}{\partial s} g(t-s)$ , the above equation becomes

$$\begin{aligned} & -g(0)\hat{\mathbf{S}}^t + \int_{-\infty}^t g(t-s) \frac{\partial}{\partial s} \left[ \text{DEV}_s^{2D}\{\hat{\mathbf{S}}^s\} \right] \\ & \quad + \frac{\mathbf{C}_{33}^t}{3} (\mathbf{C}_{2d}^t)^{-1} \int_{-\infty}^t g(t-s) \frac{\partial}{\partial s} \left[ \text{tr}(\hat{\mathbf{S}}^s \mathbf{C}_{2d}^s)(\mathbf{C}_{33}^s)^{-1} \right] ds. \end{aligned} \quad (\text{A.26})$$

Inserting all the above in equation A.3, the total stress can be obtained to be

$$\mathbf{S}_{2d} = \int_{-\infty}^t g(t-s) \frac{\partial}{\partial s} \left[ \text{DEV}_s^{2D}\{\hat{\mathbf{S}}^s\} \right] + \frac{\mathbf{C}_{33}^t}{3} (\mathbf{C}_{2d}^t)^{-1} \int_{-\infty}^t g(t-s) \frac{\partial}{\partial s} \left[ \text{tr}(\hat{\mathbf{S}}^s \mathbf{C}_{2d}^s)(\mathbf{C}_{33}^s)^{-1} \right] ds \quad (\text{A.27})$$

## Check

The correctness of the above equation can be checked by setting  $g(t) = g_\infty$ , which would be the case of a hyperelastic material.

$$\mathbf{S}_{2d} \Big|_{g(t)=1} = g_\infty \text{DEV}_t^{2D}\{\hat{\mathbf{S}}^t\} + \frac{g_\infty}{3} \text{tr}(\hat{\mathbf{S}}^t \mathbf{C}_{2d}^t)(\mathbf{C}_{2d}^t)^{-1} = g_\infty \hat{\mathbf{S}}^t, \quad (\text{A.28})$$

which is the result expected for a hyperelastic material.

## A.1 TIME INTEGRATION

The expression in equation A.27 can be integrated in time by using the semi-analytic technique in Taylor et al., 1970. Denoting the term inside the time derivative as  $\mathbf{h}$  and denoting the integral as  $\mathbf{H}$ , the time integral can be written as

$$\mathbf{H}(t) = \int_{-\infty}^t g(t-s) \frac{\partial}{\partial s} \mathbf{h}(s). \quad (\text{A.29})$$

The integration technique as in Taylor et al., 1970 will be used to integrate the above equation. Since  $g(t) = g_\infty + g_1 \exp(-\frac{t}{\tau})$ , the integration technique will be demonstrated on the exponential term. Defining  $\mathbf{I}(t) := \int_{-\infty}^t e^{-\frac{t-s}{\tau}} \frac{\partial}{\partial s} \mathbf{h}(s)$ ,

$$\mathbf{I}(t) = \int_t^{t-\Delta t} e^{-\frac{t-s}{\tau}} \frac{\partial}{\partial s} \mathbf{h}(s) + \int_{t-\Delta t}^t e^{-\frac{t-s}{\tau}} \frac{\partial}{\partial s} \mathbf{h}(s) \quad (\text{A.30})$$

$$= e^{-\frac{\Delta t}{\tau}} \mathbf{I}(t-\Delta t) + \int_{t-\Delta t}^t e^{-\frac{t-s}{\tau}} \frac{\partial}{\partial s} \mathbf{h}(s). \quad (\text{A.31})$$

The second term in the above equation will be integrated approximately.

$$\int_{t-\Delta t}^t e^{-\frac{t-s}{\tau}} \frac{\partial}{\partial s} \mathbf{h}(s) \approx \frac{\mathbf{h}(t) - \mathbf{h}(t-\Delta t)}{\Delta t} e^{-\frac{t}{\tau}} \int_{t-\Delta t}^t e^{\frac{s}{\tau}} ds \quad (\text{A.32})$$

$$\approx [\mathbf{h}(t) - \mathbf{h}(t-\Delta t)] \frac{1 - e^{-\Delta t/\tau}}{\Delta t/\tau}. \quad (\text{A.33})$$

Hence,

$$\mathbf{I}(t) = e^{-\frac{\Delta t}{\tau}} \mathbf{I}(t - \Delta t) + [\mathbf{h}(t) - \mathbf{h}(t - \Delta t)] \frac{1 - e^{-\Delta t/\tau}}{\Delta t/\tau}. \quad (\text{A.34})$$

The first term on the right hand side of A.27 is evaluated as (denoting it as  $T_1$ )

$$\begin{aligned} T_1(t) &= \int_{-\infty}^t e^{-\frac{t-s}{\tau}} \frac{\partial}{\partial s} \left[ \text{DEV}_s^{2D} \left\{ \hat{\mathbf{S}}^s \right\} \right] \approx \\ &e^{-\frac{\Delta t}{\tau}} T_1(t - \Delta t) + \frac{1 - e^{-\Delta t/\tau}}{\Delta t/\tau} \left[ \text{DEV}_t^{2D} \left\{ \hat{\mathbf{S}}^t \right\} - \text{DEV}_{t-\Delta t}^{2D} \left\{ \hat{\mathbf{S}}^{t-\Delta t} \right\} \right] \end{aligned} \quad (\text{A.35})$$

The second term on the right hand side of A.27 inside the integral is evaluated as (denoting it as  $T_2$ )

$$\begin{aligned} T_2(t) &= \int_{-\infty}^t e^{-\frac{t-s}{\tau}} \frac{\partial}{\partial s} \left[ \text{tr}(\hat{\mathbf{S}}^s \mathbf{C}_{2d}^s) (\mathbf{C}_{33}^s)^{-1} \right] \approx \\ &e^{-\frac{\Delta t}{\tau}} T_2(t - \Delta t) + \frac{1 - e^{-\Delta t/\tau}}{\Delta t/\tau} \left[ \text{tr}(\hat{\mathbf{S}}^t \mathbf{C}_{2d}^t) (\mathbf{C}_{33}^t)^{-1} - \text{tr}(\hat{\mathbf{S}}^{t-\Delta t} \mathbf{C}_{2d}^{t-\Delta t}) (\mathbf{C}_{33}^{t-\Delta t})^{-1} \right] \end{aligned} \quad (\text{A.36})$$

The entire integral can hence be evaluated as

$$\begin{aligned} \mathbf{S}_{2d} &= e^{-\frac{\Delta t}{\tau}} T_1(t - \Delta t) + \frac{1 - e^{-\Delta t/\tau}}{\Delta t/\tau} \left[ \text{DEV}_t^{2D} \left\{ \hat{\mathbf{S}}^t \right\} - \text{DEV}_{t-\Delta t}^{2D} \left\{ \hat{\mathbf{S}}^{t-\Delta t} \right\} \right] + \\ &\frac{\mathbf{C}_{33}^t}{3} (\mathbf{C}_{2d}^t)^{-1} \left( e^{-\frac{\Delta t}{\tau}} T_2(t - \Delta t) + \frac{1 - e^{-\Delta t/\tau}}{\Delta t/\tau} \left[ \text{tr}(\hat{\mathbf{S}}^t \mathbf{C}_{2d}^t) (\mathbf{C}_{33}^t)^{-1} - \text{tr}(\hat{\mathbf{S}}^{t-\Delta t} \mathbf{C}_{2d}^{t-\Delta t}) (\mathbf{C}_{33}^{t-\Delta t})^{-1} \right] \right) \end{aligned} \quad (\text{A.37})$$

The terms  $T_1$  and  $T_2$  are updated as per equations A.35 and A.36.

## A.2 COMPUTATION OF TANGENT

The tangent is computed as  $\mathfrak{C} = 2 \frac{\partial \mathbf{S}_{2d}}{\partial \mathbf{C}_{2d}}$ . It involves the computation of the derivative of the deviatoric projector.

$$\begin{aligned} \frac{\partial}{\partial \mathbf{C}_{2d}} \text{DEV}_t^{2D} \left\{ \hat{\mathbf{S}}^t \right\} &= \frac{\partial}{\partial \mathbf{C}_{2d}} \left[ \hat{\mathbf{S}}^t - \frac{1}{3} \text{tr}(\hat{\mathbf{S}}^t \mathbf{C}_{2d}^t) (\mathbf{C}_{2d}^t)^{-1} \right] \\ &= \frac{\partial \hat{\mathbf{S}}^t}{\partial \mathbf{C}_{2d}} - \frac{1}{3} \left[ \text{tr}(\hat{\mathbf{S}}^t \mathbf{C}_{2d}^t) \mathbf{i} + (\mathbf{C}_{2d}^t)^{-1} \otimes \frac{\partial}{\partial \mathbf{C}_{2d}} \text{tr}(\hat{\mathbf{S}}^t \mathbf{C}_{2d}^t) \right]. \end{aligned} \quad (\text{A.38})$$

In the above equation,  $\mathbf{i} = \frac{\partial (\mathbf{C}_{2d})^{-1}}{\partial \mathbf{C}_{2d}}$ , where  $i_{ijkl} = -\frac{(\mathbf{C}_{2d})_{ik}^{-1} (\mathbf{C}_{2d})_{jl}^{-1} + (\mathbf{C}_{2d})_{il}^{-1} (\mathbf{C}_{2d})_{jk}^{-1}}{2}$ .

$\frac{\partial}{\partial (\mathbf{C}_{2d})_{ij}} (\hat{\mathbf{S}}_{pq}^t (\mathbf{C}_{2d})_{qp}) = \frac{\partial \hat{\mathbf{S}}_{pq}^t}{\partial (\mathbf{C}_{2d})_{ij}} (\mathbf{C}_{2d})_{qp} + \hat{\mathbf{S}}_{pq}^t \frac{\partial (\mathbf{C}_{2d})_{qp}}{\partial (\mathbf{C}_{2d})_{ij}}$ . So,  $\frac{\partial}{\partial \mathbf{C}_{2d}} \text{tr}(\hat{\mathbf{S}}^t \mathbf{C}_{2d}^t) = \mathbf{C}_{2d} : \frac{\partial \hat{\mathbf{S}}^t}{\partial \mathbf{C}_{2d}} + \hat{\mathbf{S}}^t : \mathfrak{I}$ . Here,  $\mathfrak{I} = \frac{\partial \mathbf{C}_{2d}}{\partial \mathbf{C}_{2d}}$  is the fourth order identity tensor. The derivative of the second term involves the computation of

$$\frac{\partial \det \mathbf{C}_{2d}}{\partial \mathbf{C}_{2d}} = -\frac{1}{\det \mathbf{C}_{2d}} (\mathbf{C}_{2d})^{-1}, \quad (\text{A.40})$$

and

$$\frac{\partial (\det \mathbf{C}_{2d})^{-1}}{\partial \mathbf{C}_{2d}} = \frac{1}{(\det \mathbf{C}_{2d})^3} (\mathbf{C}_{2d})^{-1}. \quad (\text{A.41})$$

# ADDITIONAL RESULTS FOR FINITE VISCOELASTIC MODEL



## CONTENTS

B.1	Stress components for the hyperelastic case . . . . .	150
B.2	Comparison of relaxation tests between FLV and FV . . . . .	150
B.2.1	Analysis . . . . .	152

Here, additional results for the plane stress version of the FV model in chapter 9 will be presented.

### B.1 STRESS COMPONENTS FOR THE HYPERELASTIC CASE

In section 9.4.1, only the 22 component of stress has been compared between the UMAT and Abaqus for the hyperelastic case. Here, the other stress components will be presented. From the figures B.1 and B.2, it can be seen that the stress distributions are exactly the same between the UMAT and the Abaqus's internal implementation.

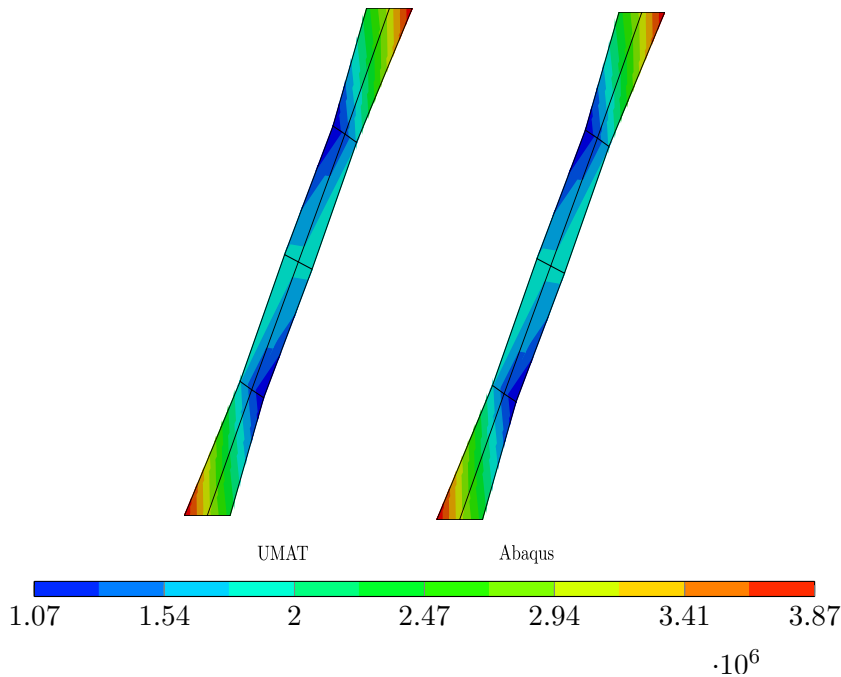


Figure B.1:  $\sigma_{11}$  (in Pa) predicted by UMAT and the polynomial model from Abaqus.

### B.2 COMPARISON OF RELAXATION TESTS BETWEEN FLV AND FV

Similar to what has been done in Govindjee and Reese, 1997, a comparison has been made between the FLV and FV models using a relaxation type test. A similar setup as in Govindjee and Reese, 1997 has been used, except that the plane stress conditions are assumed to prevail as opposed to that study. A square sample of dimensions  $1 \text{ mm} \times 1 \text{ mm}$  is held fixed at the bottom and a displacement of  $\delta$  has been applied in the  $y$ -direction to the top face in a span of  $0.01 \text{ s}$ . It is then held there for  $30 \text{ s}$ . The evolution of  $yy$ -component of the cauchy stress tensor has been monitored. The relaxation function is defined as  $E(t) := \sigma(t)/\ln(1 + \delta/L)$ , where  $L = 1 \text{ mm}$ . The effect of applied stretch on the relaxation function has been studied. The relaxation test can be considered to come under the case of large strains and large perturbations, since the strains in the viscous arms are equal to the applied strain at the end of first step.

The material has been taken to be incompressible. The hyperelastic and the viscoelastic branches have been assumed to be represented by a Neo-Hookean model. This is achieved by taking  $N = 1$  and  $C_{01} = 0$  in the polynomial model.  $C_{01}$  has been taken to be  $10 \text{ MPa}$ .  $C_{01}$  for the viscous branch has been taken to be

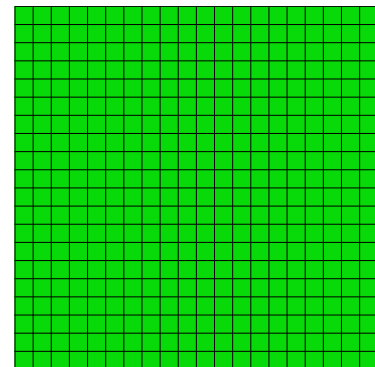


Figure B.3: Square of side 1 mm with mesh.

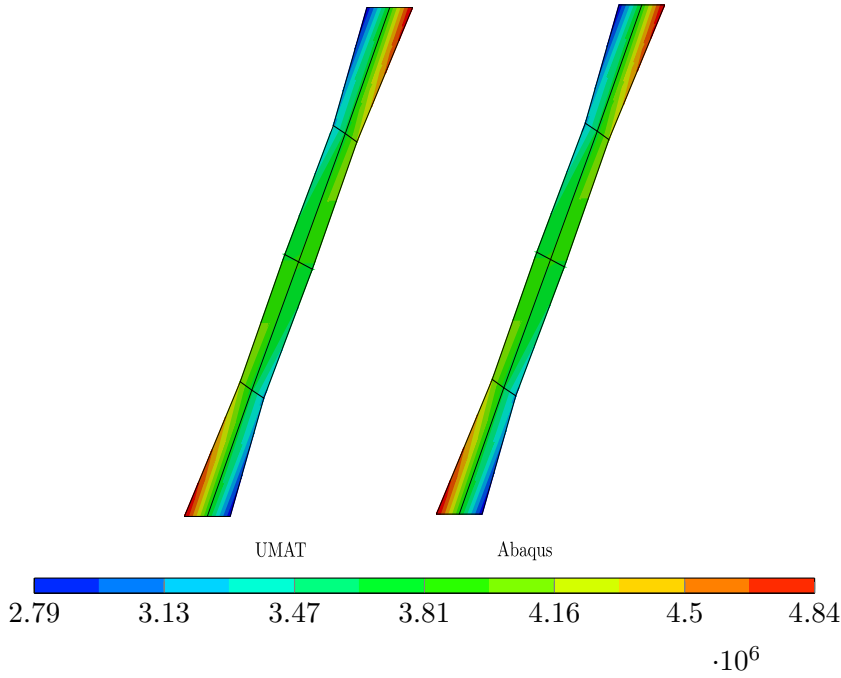


Figure B.2:  $\sigma_{12}$  (in Pa) predicted by UMAT and the polynomial model from Abaqus.

equal to that of the hyperelastic branch. The relaxation time has been chosen to be 1 s.  $\gamma_0 = 1$ . The results of the predictions for  $\delta = [2 \text{ mm}, 1 \text{ mm}, 0.01 \text{ mm}]$  from FLV and FV models can be seen in the figure B.4. It can be observed from figure

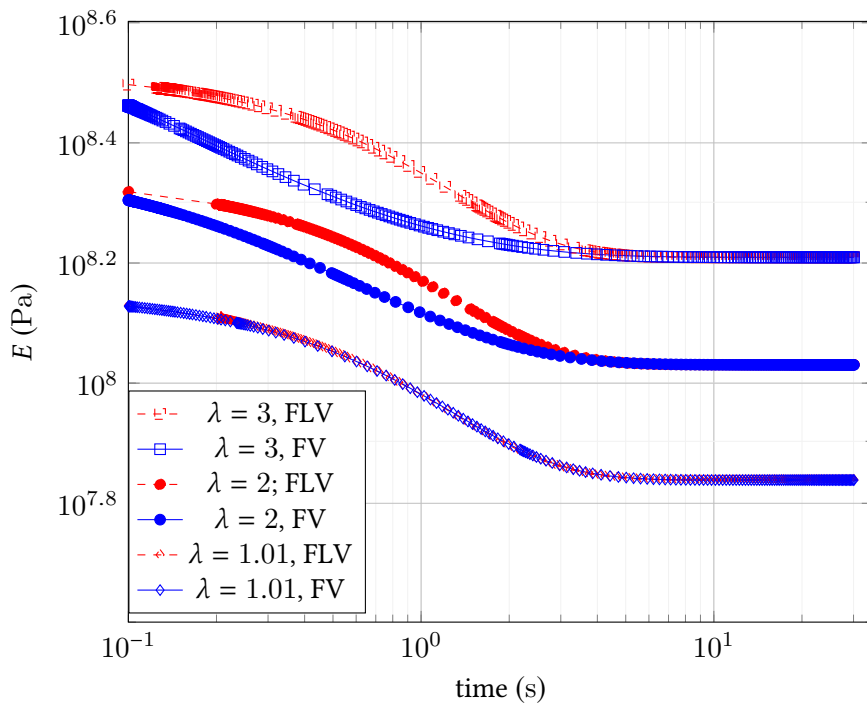


Figure B.4:  $E$  vs time for FLV and FV models for various stretches. Results for FLV model are in red dashed lines and the results for FV model are in blue solid lines.

B.4 that the modulus,  $E$ , decays faster for larger strains in the case of FV model when compared to the FLV model. As the strains are reduced, the gap between the two models decreases as well. In the case of infinitesimal strain, the models can be seen to predict almost same results. This is a consequence of the shift in

relaxation times to smaller values at larger strains in the case of FV model. Also, the shapes of the curves at various stretch levels can be seen to be similar in the case of FLV model. The relaxation times can be seen to be not affected in this case. This observation is in coherence with what was presented in Govindjee and Reese, 1997 (see figure 4.3 of the reference).

### B.2.1 Analysis

The results from the relaxation test above can be analyzed as follows. In the case of FLV model, the stress can be written as

$$\mathbf{S}_{2d} = \int_{-\infty}^t g(t-s) \frac{\partial}{\partial s} \left[ \text{DEV}_s^{2D} \left\{ \hat{\mathbf{S}}^s \right\} \right] + \frac{C_{33}^t}{3} (C_{2d}^t)^{-1} \int_{-\infty}^t g(t-s) \frac{\partial}{\partial s} \left[ \text{tr}(\hat{\mathbf{S}}^s C_{2d}^s) (C_{33}^s)^{-1} \right]. \quad (\text{A.27})$$

where  $g(s) = g_\infty + \sum_{i=1}^N g_i \exp(-s/\tau_i)$  and

$$\hat{\mathbf{S}} = 2 \frac{\partial \psi}{\partial \mathbf{C}_{2d}}, \quad (\text{A.14})$$

$g_\infty + \sum_{i=1}^N g_i = 1$ .  $\psi$  is the glassy strain energy density functional. Defining  $\psi^\infty := g_\infty \psi$  to be the rubbery strain energy functional, the above expression for stress can be simplified as

$$\begin{aligned} \mathbf{S}_{2d} = & \hat{\mathbf{S}}_{2d}^\infty + \sum_{i=1}^N \int_{-\infty}^t g_i \exp(-(t-s)/\tau_i) \frac{\partial}{\partial s} \left[ \text{DEV}_s^{2D} \left\{ \hat{\mathbf{S}}^s \right\} \right] \\ & + \frac{C_{33}^t}{3} (C_{2d}^t)^{-1} \sum_{i=1}^N \int_{-\infty}^t g_i \exp(-(t-s)/\tau_i) \frac{\partial}{\partial s} \left[ \text{tr}(\hat{\mathbf{S}}^s C_{2d}^s) (C_{33}^s)^{-1} \right]. \quad (\text{B.1}) \end{aligned}$$

The loading can be divided into two steps, where in the first step, the body is rapidly loaded to the target strain level and in the second step, it is held at that strain level. The strain ( $\mathbf{C}$  tensor) is assumed to be increased from  $\mathbf{I}$  to  $\mathbf{C}^{t_1}$  in a span  $t_1$  that is much smaller than the corresponding relaxation time,  $\tau$ , in the first step. Assuming only one viscous branch for convenience, this step corresponds to the glassy material behavior. This can be seen from the fact that  $\frac{t-s}{\tau} \rightarrow 0 \quad \forall \quad t, s \leq t_1 \ll \tau$  and so, the exponential term will almost be equal to 1. The integrals can hence be evaluated directly. The total stress at the end of first step can be written as

$$\mathbf{S}_{2d} = \hat{\mathbf{S}}_{2d}^\infty|_{t=t_1} + g_1 \text{DEV}_{t_1}^{2D} \left\{ \hat{\mathbf{S}}^{t_1} \right\} + \frac{g_1}{3} \text{tr}(\hat{\mathbf{S}}^{t_1} C_{2d}^{t_1}) (C_{2d}^{t_1})^{-1} = \hat{\mathbf{S}}_{2d}|_{t=t_1}, \quad (\text{B.2})$$

since  $g_\infty + g_1 = 1$ . Hence, it can be written that

$$\begin{aligned} \int_{-\infty}^{t_1} g_1 \exp(-(t-s)/\tau) \frac{\partial}{\partial s} \left[ \text{DEV}_s^{2D} \left\{ \hat{\mathbf{S}}^s \right\} \right] &= g_1 \text{DEV}_{t_1}^{2D} \left\{ \hat{\mathbf{S}}^{t_1} \right\}, \quad \text{and} \quad (\text{B.3}) \\ \frac{C_{33}^{t_1}}{3} (C_{2d}^{t_1})^{-1} \int_{-\infty}^{t_1} g_1 \exp(-(t-s)/\tau) \frac{\partial}{\partial s} \left[ \text{tr}(\hat{\mathbf{S}}^s C_{2d}^s) (C_{33}^s)^{-1} \right] &= \frac{g_1}{3} \text{tr}(\hat{\mathbf{S}}^{t_1} C_{2d}^{t_1}) (C_{2d}^{t_1})^{-1}. \quad (\text{B.4}) \end{aligned}$$

In the second step, the strain is held constant and the evolution of total stress is studied in the intervals of  $\Delta t$ . For this step, the two integrals in the stress term

(B.1) can be written as

$$\begin{aligned} & \int_{-\infty}^{t_1+\Delta t} \exp(-(t_1 + \Delta t - s)/\tau) \frac{\partial \bullet}{\partial s} ds = \\ & \exp(-\Delta t/\tau) \int_{-\infty}^{t_1} \exp(-(t_1 - s)/\tau) \frac{\partial \bullet}{\partial s} ds + \int_{t_1}^{t_1+\Delta t} \exp(-(t_1 + \Delta t - s)/\tau) \frac{\partial \bullet}{\partial s} ds, \end{aligned} \quad (\text{B.5})$$

where  $\bullet$  denotes the terms in the first and the second integral. It shall be noted that for all times bigger than  $t_1$ ,  $\frac{\partial \bullet}{\partial s} = 0$ , since the total strain is held constant and the terms inside the derivative are functions of the total strain only. The first integral on the RHS in the equation B.5 can be recognized as either of B.3 or B.4. Hence, using the above recursively at time steps  $2\Delta t, 3\Delta t, \dots, n\Delta t$ ,

$$\int_{-\infty}^{t_1+n\Delta t} \exp(-(t_1 + n\Delta t - s)/\tau) \frac{\partial \bullet}{\partial s} ds = \exp(-n\Delta t/\tau) \bullet|_{t=t_1}. \quad (\text{B.6})$$

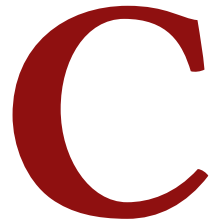
The total stress for all times greater than  $t_1$  can then be written as

$$S_{2d} = \left[ 1 + \frac{g_1}{1-g_1} \exp(-n\Delta t/\tau) \right] \hat{S}_{2d}^\infty|_{t=t_1}. \quad (\text{B.7})$$

$g_\infty + g_1 = 1$  has been used. When  $n = 0$ ,  $t = t_1$  and the above expression becomes  $S_{2d} = \frac{1}{1-g_1} \hat{S}_{2d}^\infty|_{t=t_1} = \hat{S}_{2d}|_{t=t_1}$ , which is equation B.2. As  $n \rightarrow \infty$ ,  $\exp(-n\Delta t/\tau) \rightarrow 0$  and so,  $S_{2d} \rightarrow \hat{S}_{2d}^\infty|_{t=t_1}$ , the fully relaxed state. Hence, for the FLV model, the relaxation times can be seen to be ‘independent of the strain level’. The curves in the figure B.4 for the FLV model hence merely translate upward for different strain levels.

In the case of FV model, in the first step, when  $\Delta t < t_1 \ll \tau$ , the term  $\frac{y_0 \Delta t}{2\eta_D} (\tau_1 + p)$  in the equation 9.44 tends to 0. So,  $\epsilon_{Ae} = (\epsilon_{Ae})_{tr} = \epsilon_A$ . Hence, the strain in the viscous arms will be equal to the total strain, which implies the glassy state. During the second step, the evolution of the strain in the viscous arms is governed by the evolution equations 9.44 and 9.45. However, since the strains in the viscous arms are no longer small, the evolution equations do not condense to the ones in the equation 9.79 and hence are non-linear. Hence, it can be seen to be different from the equation B.7 and so the observed differences in the figure B.4.

C++ IMPLEMENTATION OF THE  
UMAT



**THE FILE USUBLIB\_PS.CPP**

```

#include <stdio.h>
#include <iostream>
#include <aba_for_c.h>
#include <Eigen/Dense>

#include "Parser_ps.h"
#include "Material_ps.h"
#include "viscous_branch_ps.h"

using namespace Eigen;
using namespace std;

// SDV format - 0 to 4 - C.i-I , 5-psi/psi.hyper similarly for all
// the branches.
// The last , of SDV are follows - Strain energy of hyperelastic
// branch, ratio of sum of SE of all viscous arm to hyper branch,
// xy component of PK1, yy component of PK1, temperature increment
// (in K)
extern "C"
void FOR_NAME(umat)(double* STRESS, double* STATEV, double* DDSDD,
double* SSE, double* SPD, double* SCD, double* RPL, double* DDSDDT,
double* DRPLDE, double* DRPLDT, double* STRAN, double* DSTRAN,
double* TIME, double* DTIME, double* TEMP, double* DTEMP, double*
PREDEF, double* DPRED, char* CMNAME, int& NDI, int& NSHR, int& NTENS
, int& NSTATV, double* PROPS, int& NPROPS, double* COORDS, double*
DROT, double* PNEWDT, double* CELENT, double* DFGRD0, double*
DFGRD1, int& NOEL, int& NPT, int& LAYER, int& KSPT, int& JSTEP, int&
KINC)
{
int number_branches =2; // User input for the no. of visc.
branches
int left=0;
MatrixXd F = MatrixXd::Zero(2,2);
MatrixXd F_old = MatrixXd::Zero(2,2);
parse_deformation_variables(DFGRD0,DFGRD1,F,F_old);
MatrixXd C = F.transpose()*F;
MatrixXd b = F*F.transpose();
MatrixXd C_inv = C.inverse();

double stiff_ratio[number_branches];
double relaxation_time[number_branches];
parse_material_properties(PROPS, stiff_ratio, relaxation_time,
number_branches);
Matrix2d ivar[number_branches];
parse_internal_variables(STATEV, ivar, number_branches);
viscous_branch branch[number_branches+1];
Matrix2d tau[number_branches+1];
Matrix3d tangent[number_branches+1];
double _SSE[number_branches+1];
double _SCD[number_branches+1];
Matrix2d tau_final = MatrixXd::Zero(2,2);
Matrix3d tangent_final = MatrixXd::Zero(3,3);

#pragma omp parallel num_threads(number_branches+1) //
Parallelization for viscous branches
{
#pragma omp for
for(int i=left; i<number_branches+1; ++i)
{
if(i==number_branches)

```

```

{
(branch+i)->delta_t = *DTIME;
(branch+i)->Material::set_material(1.0,1E16);
(branch+i)->set_inelastic_strain(MatrixXd::Identity(2,2));
(branch+i)->compute_be_tr(F);
(branch+i)->update_intervar_newton_principal(F);
*(tau+i) = (branch+i)->compute_stress_tau();
*(tangent+i) = (branch+i)->rotate_mat_tan(1);
*(STATEV+5*i) = *(_SSE+i) = (branch+i)->compute_strain_energy(
    branch[i].be);
*( _SCD+i) = (branch+i)->compute_dissipation();
}
else
{
(branch+i)->delta_t = *DTIME;
(branch+i)->Material::set_material(stiff_ratio[i],relaxation_time[
    i]);
(branch+i)->set_inelastic_strain(*(ivar+i));
(branch+i)->compute_be_tr(F);
*(ivar+i)=(branch+i)->update_intervar_newton_principal(F);
*(tau+i) = (branch+i)->compute_stress_tau();
*(tangent+i) = (branch+i)->rotate_mat_tan(0);
*(STATEV+5*i+4) = *(_SSE+i) = (branch+i)->compute_strain_energy(
    branch[i].be);
*( _SCD+i) = (branch+i)->compute_dissipation();
}
}
}
double SCD_rate;
add_all(&tau_final,&tangent_final,SSE,&SCD_rate,tau,tangent,_SSE,
    _SCD,number_branches+1,left);
*SCD += SCD_rate>(*DTIME);
deviatoric_projector_tangent(tau_final,&tangent_final);
Matrix2d PK1 = tau_final*((F.transpose()).inverse());
*(STATEV+5*number_branches+2)=PK1(0,1);
*(STATEV+5*number_branches+3)=PK1(1,1);
*(STATEV+5*number_branches+4) += 0.9*SCD_rate>(*DTIME)
    /1100.0/1760.0; // 0.9*D*delta_t/rho/C_v
return_stress(STRESS,tau_final);
return_tangent(DDSDDE,tangent_final);
return_intervar(STATEV,ivar,number_branches);
return;
};

```

### THE FILE PARSER\_PS.H

```

void parse_deformation_variables(double* DFGRD0,double* DFGRD1,
    MatrixXd& F,MatrixXd& F_old){
F(0,0) = *DFGRD1;
F(1,0) = *(DFGRD1+1);
F(0,1) = *(DFGRD1+3);
F(1,1) = *(DFGRD1+4);
// F_old not implemented as it is not needed
};

void parse_material_properties(double* props, double* stiff_ratio,
    double* relax, int number_branches){
for(int i=0;i<number_branches;++i){
stiff_ratio[i]=props[2*i];
relax[i]=props[2*i+1];
}};

```

```

void parse_internal_variables(double* STATEV, Matrix2d* ivar, int
    number_branches){
for (int i=0; i<number_branches; ++i){
*(ivar+i) << *(STATEV+5*i), *(STATEV+5*i+1), *(STATEV+5*i+2),
*(STATEV+5*i+3);
*(ivar+i) += MatrixXd::Identity(2,2);
}};

void deviatoric_projector_tangent(Matrix2d tau, Matrix3d* tangent){
VectorXd tau_row(3);
tau_row << tau(0,0), tau(1,1), tau(0,1);
(*tangent)(0,0) += 2*tau_row(0);
(*tangent)(1,1) += 2*tau_row(1);
(*tangent)(2,2) += 0.5*(tau_row(0)+tau_row(1));
(*tangent)(2,0) += tau_row(2);
(*tangent)(2,1) += tau_row(2);
(*tangent)(0,2) += tau_row(2);
(*tangent)(1,2) += tau_row(2);
};

void return_stress(double* stress, MatrixXd tau){
*(stress) = tau(0,0);
*(stress+1) = tau(1,1);
*(stress+2) = tau(0,1);
};

void return_tangent(double* DDSDDDE, MatrixXd tangent){
*(DDSDDDE+0) = tangent(0,0);
*(DDSDDDE+1) = tangent(1,0);
*(DDSDDDE+2) = tangent(2,0);
*(DDSDDDE+3) = tangent(0,1);
*(DDSDDDE+4) = tangent(1,1);
*(DDSDDDE+5) = tangent(2,1);
*(DDSDDDE+6) = tangent(0,2);
*(DDSDDDE+7) = tangent(1,2);
*(DDSDDDE+8) = tangent(2,2);
};

void return_internalvar(double* STATEV, Matrix2d* ivar, int
    number_branches){
Matrix2d temp;
for (int i=0; i<number_branches; ++i){
temp = *(ivar+i)-MatrixXd::Identity(2,2);
*(STATEV+5*i) = temp(0,0);
*(STATEV+5*i+1) = temp(0,1);
*(STATEV+5*i+2) = temp(1,0);
*(STATEV+5*i+3) = temp(1,1);
}
double total_SE = 0.0;
for (int i=0; i<number_branches; ++i){
total_SE += *(STATEV+5*i+4);
}
total_SE += *(STATEV+5*number_branches);
*(STATEV+5*number_branches+1) = total_SE / (*(STATEV+5*
    number_branches));
for (int i=0; i<number_branches; ++i){
*(STATEV+5*i+4) /= *(STATEV+5*number_branches);
}};

void add_all(Matrix2d* tau_final, Matrix3d* tangent_final, double*
    SSE, double* SCD_rate, Matrix2d* tau,
Matrix3d* tangent, double* _SSE, double* _SCD, int branches, int left
    ){

```

```

*SSE = 0.0;
*SCD_rate = 0.0;
for(int i=left;i< branches; ++i)
{
*tau_final = *tau_final + *(tau+i);
*tangent_final = *tangent_final + *(tangent+i);
*SSE += *(_SSE+i);
*SCD_rate += *(_SCD+i);
}};

```

**THE FILE MATERIAL\_PS.H**

```

#ifndef MATERIAL_H
#define MATERIAL_H
#include <iostream>
class Material
{
public:
double c[9] =
    {1044000.0,0.0,-22730.0,0.0,0.0,336.0,124.0,0.0,0.0};
double relaxation_time;
double stiff_ratio;
void set_material(double _stiff_ratio , double _relaxation_time);
};
#endif

```

**THE FILE MATERIAL\_PS.CPP**

```

#include <iostream>
#include <cmath>
#include <Eigen/Dense>
#include "Material_ps.h"
using namespace Eigen;
using namespace std;
void Material::set_material(double _stiff_ratio , double
    _relaxation_time){ //Constructor
stiff_ratio = _stiff_ratio;
relaxation_time = _relaxation_time;
for(int i=0;i<9;++i){
c[i] *= stiff_ratio;
}};

```

**THE FILE VISCOUS\_BRANCH\_PS.H**

```

#ifndef VISCOUS_BRANCH_H
#define VISCOUS_BRANCH_H
#include <iostream>
#include <cmath>
#include <Eigen/Dense>
using namespace Eigen;
using namespace std;
#include "Material_ps.h"

typedef Matrix<double , 6, 6> Matrix6d;

class viscous_branch: public Material
{
Matrix2d C_i,be_tr,be,be_inverse;
Vector2d res_principal,eigs,eigs_tr;
Vector2d epsilon;
Matrix2d Stiff_principal,Tangent_principal,C_alg,pressure_tangent;

```

```

Matrix2d tau;
Vector2d tau_principal, epsilon, epsilon_tr, tau_dev;
Matrix3d mat_tan;
Matrix3d mat_tan_vol;
Matrix3d Rotation_mat;
Matrix3d Rotation_mat_transp;
double lambda_A, lambda_B, lambda_C, eta, p;
Vector2d vo, v1, v2, vo_, v1_, v2_;
double invar[2];
double derivative[2];
double second_derivative[2][2];
double I1, I2, dW_dI1, dW_dI2, d2W_dI1I1, d2W_dI1I2, d2W_dI2I1,
    d2W_dI2I2, gamma_o;
double dI1_dA, dI2_dA, dI1_dB, dI2_dB, d2AI1_dAdA, d2AI1_dAdB,
    d2AI2_dAdA, d2AI2_dAdB, d2BI1_dBdA, d2BI1_dBdB, d2BI2_dBdA,
    d2BI2_dBdB;
double delta_t;

viscous_branch();
void set_inelastic_strain(MatrixXd);
void compute_be_tr(MatrixXd);
void compute_invar(MatrixXd, bool);
void compute_derivative();
void compute_second_derivative();
void compute_stress_tau_principal();
MatrixXd compute_stress_tau();
double compute_strain_energy(MatrixXd);
double compute_dissipation();
void compute_tangent_principal();
void compute_tangent_pressure();
void compute_tangent_nr_principal();
void compute_residual_principal();
void mat_tan_principal(bool);
MatrixXd rotate_mat_tan(bool);
MatrixXd mat_tan_volu();
MatrixXd update_intervar_newton_principal(MatrixXd);

friend void convert_matrix_to_vector(MatrixXd&, MatrixXd&);
friend void convert_vector_to_matrix(MatrixXd&, MatrixXd&);
};

template <typename number>
number sq( number n ) {
return (n*n);
}
template <typename number>
number cu( number n ) {
return (n*n*n);
}
#endif

```

#### THE FILE VISCOUS\_BRANCH\_PS.CPP

```

#include <iostream>
#include <cmath>
#include <Eigen/Dense>
#include "Material_ps.h"
#include "viscous_branch_ps.h"
using namespace Eigen;
using namespace std;

viscous_branch::viscous_branch() { //Constructor

```

```

mat_tan = MatrixXd::Zero(3,3);
mat_tan_vol = MatrixXd::Zero(3,3);
Rotation_mat = MatrixXd::Zero(3,3);
}

void viscous_branch::set_inelastic_strain(MatrixXd _C_i){
gamma_o = 60.0; //User input
C_i = _C_i;
eta = 2.0*relaxation_time*c[0]*gamma_o;
};

void viscous_branch::compute_be_tr(MatrixXd F){
be_tr = F*(C_i.inverse()*F.transpose());
EigenSolver<Matrix2d> es(be_tr);
vo_ = es.eigenvectors().col(0).real()(seq(0,1),0);
v1_ = es.eigenvectors().col(1).real()(seq(0,1),0);
vo = es.eigenvectors().row(0).real()(0,seq(0,1));
v1 = es.eigenvectors().row(1).real()(0,seq(0,1));
eigs_tr(0) = es.eigenvalues()(0,0).real();
eigs_tr(1) = es.eigenvalues()(1,0).real();
Rotation_mat(0,0) = vo(0)*vo(0);
Rotation_mat(1,0) = v1(0)*v1(0);
Rotation_mat(2,0) = vo(0)*v1(0);

Rotation_mat(0,1) = vo(1)*vo(1);
Rotation_mat(1,1) = v1(1)*v1(1);
Rotation_mat(2,1) = vo(1)*v1(1);

Rotation_mat(0,2) = 2.0*vo(0)*vo(1);
Rotation_mat(1,2) = 2.0*v1(0)*v1(1);
Rotation_mat(2,2) = vo(0)*v1(1)+vo(1)*v1(0);

Rotation_mat_transp = Rotation_mat.transpose();
};

void viscous_branch::compute_invar(MatrixXd C, bool a){
if(a){
double c33 = 1.0/C.determinant();
I1 = invar[0] = C(0,0) + C(1,1) + c33;
Matrix2d CC = C*C;
I2 = invar[1] = 0.5*(invar[0]*invar[0]-(CC(0,0)+CC(1,1)+c33*c33));
}
if(!a){
double c33 = 1.0/C(0)/C(1);
I1 = invar[0] = C(0)+ C(1) + c33;
I2 = invar[1] = C(0)*C(1)+C(1)*c33+c33*C(0);
lambda_A = C(0);
lambda_B = C(1);
lambda_C = 1.0/c33;
}};

void viscous_branch::compute_derivative(){
I1 = invar[0];
I2 = invar[1];
derivative[0]= c[0]+2.0*c[2]*(I1-3)+3.0*c[5]*sq(I1-3)+2.0*c[6]*(I1-3)*(I2-3);
derivative[1]= c[6]*sq(I1-3);
dI1_dA = 1.0-1.0/sq(lambda_A)/lambda_B;
dI1_dB = 1.0-1.0/sq(lambda_B)/lambda_A;
dI2_dA = lambda_B-1.0/sq(lambda_A);
dI2_dB = lambda_A-1.0/sq(lambda_B);
};

```

```

void viscous_branch::compute_second_derivative() {
I1 = invar[0];
I2 = invar[1];
second_derivative[0][0] = 2*c[2] + 6*c[5]*(I1-3)+2.0*c[6]*(I2-3);
second_derivative[0][1] = 2.0*c[6]*(I1-3);
second_derivative[1][0] = 2.0*c[6]*(I1-3);
second_derivative[1][1] = 0.0;

d2AI1_dAdA = 1.0+1.0/sq(lambda_A)/lambda_B;
d2AI1_dAdB = 1.0/sq(lambda_B)/lambda_A;

d2BI1_dBdB = 1.0+1.0/sq(lambda_B)/lambda_A;
d2BI1_dBdA = 1.0/sq(lambda_A)/lambda_B;

d2AI2_dAdA = lambda_B+1.0/sq(lambda_A);
d2AI2_dAdB = lambda_A;

d2BI2_dBdB = lambda_A+1.0/sq(lambda_B);
d2BI2_dBdA = lambda_B;
};

void viscous_branch::compute_stress_tau_principal() {
dW_dI1 = derivative[0];
dW_dI2 = derivative[1];
tau_principal(0) = 2.0*(dW_dI1*dI1_dA+dW_dI2*dI2_dA)*lambda_A;
tau_principal(1) = 2.0*(dW_dI1*dI1_dB+dW_dI2*dI2_dB)*lambda_B;
p = -(tau_principal(0)+tau_principal(1))/3.0;
};

MatrixXd viscous_branch::compute_stress_tau() {
tau = tau_principal(0)*vo_*vo_.transpose()+tau_principal(1)*v1_*
v1_.transpose();
return tau;
};

double viscous_branch::compute_strain_energy(MatrixXd _be) {
double psi = 0.0;
compute_invar(_be,1);
I1 = invar[0];
I2 = invar[1];
psi += c[0]*(I1-3)+c[1]*(I2-3)+c[2]*sq(I1-3)+c[3]*(I1-3)*(I2-3);
psi += c[4]*sq(I2-3)+c[5]*cu(I1-3)+c[6]*sq(I1-3)*(I2-3);
psi += c[7]*(I1-3)*sq(I2-3)+c[8]*cu(I2-3);
return psi;
};

double viscous_branch::compute_dissipation() {
double psi = 0.0;
psi = tau_dev.transpose()*tau_dev+p*p;
psi /= 2.0*eta;
return psi;
};

void viscous_branch::compute_tangent_principal() {
compute_second_derivative();
I1 = invar[0];
I2 = invar[1];
dW_dI1 = derivative[0];
dW_dI2 = derivative[1];

d2W_dI1I1 = second_derivative[0][0];
d2W_dI1I2 = second_derivative[0][1];
d2W_dI2I2 = second_derivative[1][1];
};

```

```

d2W_dI2I1 = d2W_dI1I2;

Stiff_principal(0,0) = 2.0*dW_dI1*d2AI1_dAdA + 2.0*lambda_A*dI1_dA*(
    d2W_dI1I1*dI1_dA + d2W_dI1I2*dI2_dA);
Stiff_principal(0,0) += 2.0*dW_dI2*d2AI2_dAdA + 2.0*lambda_A*dI2_dA*(
    d2W_dI2I1*dI1_dA + d2W_dI2I2*dI2_dA);
Stiff_principal(0,0) *= 2*lambda_A;
Stiff_principal(0,1) = 2.0*dW_dI1*d2AI1_dAdB + 2.0*lambda_A*dI1_dA*(
    d2W_dI1I1*dI1_dB + d2W_dI1I2*dI2_dB);
Stiff_principal(0,1) += 2.0*dW_dI2*d2AI2_dAdB + 2.0*lambda_A*dI2_dA*(
    d2W_dI2I1*dI1_dB + d2W_dI2I2*dI2_dB);
Stiff_principal(0,1) *= 2*lambda_B;

Stiff_principal(1,1) = 2.0*dW_dI1*d2BI1_dBdB + 2.0*lambda_B*dI1_dB*(
    d2W_dI1I1*dI1_dB + d2W_dI1I2*dI2_dB);
Stiff_principal(1,1) += 2.0*dW_dI2*d2BI2_dBdB + 2.0*lambda_B*dI2_dB*(
    d2W_dI2I1*dI1_dB + d2W_dI2I2*dI2_dB);
Stiff_principal(1,1) *= 2*lambda_B;
Stiff_principal(1,0) = 2.0*dW_dI1*d2BI1_dBdA + 2.0*lambda_B*dI1_dB*(
    d2W_dI1I1*dI1_dA + d2W_dI1I2*dI2_dA);
Stiff_principal(1,0) += 2.0*dW_dI2*d2BI2_dBdA + 2.0*lambda_B*dI2_dB*(
    d2W_dI1I2*dI1_dA + d2W_dI2I2*dI2_dA);
Stiff_principal(1,0) *= 2*lambda_A;
};

void viscous_branch::compute_tangent_pressure() {
pressure_tangent(0,0) = -1.0/3.0*(Stiff_principal(0,0)+
    Stiff_principal(1,0));
pressure_tangent(0,1) = -1.0/3.0*(Stiff_principal(0,1)+
    Stiff_principal(1,1));

pressure_tangent(1,0) = pressure_tangent(0,0);
pressure_tangent(1,1) = pressure_tangent(0,1);
};

void viscous_branch::compute_tangent_nr_principal() {
compute_tangent_pressure();
Tangent_principal = delta_t/2.0/eta*(Stiff_principal+
    pressure_tangent)+MatrixXd::Identity(2,2);
};

void viscous_branch::compute_residual_principal() {
compute_invar(eigs,0);
compute_derivative();
compute_stress_tau_principal();
I1 = invar[0];
I2 = invar[1];
dW_dI1 = derivative[0];
dW_dI2 = derivative[1];
tau_dev = tau_principal.array()+p;
res_principal = epsilon + delta_t/2.0/eta*tau_dev - epsilon_tr;
};

void viscous_branch::mat_tan_principal(bool elastic) {
C_alg = Stiff_principal*(Tangent_principal.inverse());
mat_tan(seq(0,1),seq(0,1)).array() = C_alg - 2.0*Matrix2d(
    tau_principal.asDiagonal());

if (eigs_tr(0)==eigs_tr(1)) {
mat_tan(2,2) = 0.5*(C_alg(0,0)-C_alg(1,0))-tau_principal(0);
}
else {
mat_tan(2,2) = (tau_principal(0)*eigs_tr(1) - tau_principal(1)*

```

```

    eigs_tr(0))/(eigs_tr(0) - eigs_tr(1));
  }};

MatrixXd viscous_branch::rotate_mat_tan(bool elastic){
  mat_tan_principal(elastic);
  mat_tan = Rotation_mat*(mat_tan*Rotation_mat_transp);
  return mat_tan;
};

MatrixXd viscous_branch::update_intervar_newton_principal(MatrixXd
  F){
  eigs = eigs_tr;
  epsilon_tr = 0.5*log(eigs_tr.array());
  epsilon = epsilon_tr;
  do {
    compute_residual_principal();
    compute_tangent_principal();
    compute_tangent_nr_principal();
    depsilon = Tangent_principal.householderQr().solve(res_principal);
    epsilon = epsilon - depsilon;
    eigs = exp(2.0*epsilon.array());
  }
  while (res_principal.norm() > 1E-5);
  compute_residual_principal();
  compute_tangent_principal();
  compute_tangent_nr_principal();
  be = eigs(0)*vo_*vo_.transpose()+eigs(1)*v1_*v1_.transpose();
  be_inverse = 1.0/eigs(0)*vo_*vo_.transpose()+1.0/eigs(1)*v1_*v1_.
    transpose();
  C_i = F.transpose()*(be_inverse*F);
  return C_i;
};

```

**Titre :** Étude de la rupture dynamique des élastomères: sur le rôle joué par la viscoélasticité

**Mots clés :** Rupture dynamique, Élastomères, Fissures transsoniques, Zone cohésive, Viscoélasticité

**Résumé :** Cette thèse s'intéresse à la propagation d'une fissure dynamique à travers une membrane en élastomère. La propagation des fissures dans un élastomère en polyuréthane ont été étudiés expérimentalement au cours d'une étude précédente. Dans cette étude, sous certaines conditions de chargement, la vitesse de propagation des fissures dépasse la vitesse des ondes de cisaillement. De telles fissures sont appelées fissures transsoniques. Deux hypothèses principales ont été avancées dans littérature pour expliquer l'observation des fissures transsoniques. L'une d'elles repose sur la rigidification hyperélastique du matériau au voisinage de la pointe de fissure, tandis que l'autre repose sur le raidissement viscoélastique. Cette étude examine ces deux hypothèses et détermine que le raidissement viscoélastique est l'ingrédient nécessaire (et suffisant). La viscoélasticité

linéaire finie a été utilisée en premier lieu. Dans un second temps, un modèle cohésif dépendant de la vitesse a été utilisé pour prédire la vitesse de propagation de la fissure. La vitesse de fissure s'est avérée indépendante de la hauteur de l'éprouvette au-delà d'un certain seuil. Un modèle viscoélastique non linéaire a également été mis en œuvre en supposant des conditions de contraintes planes. En utilisant cela, l'énergie dissipée dans le matériau en raison des effets viscoélastiques et l'énergie consommée par les processus de rupture ont été calculées explicitement. Les résultats montrent que la majorité de l'énergie de déformation est consommée sous forme de dissipation viscoélastique dans le matériau. L'énergie restante est consommée par les processus de rupture.

**Title :** Investigation of dynamic fracture of elastomers: On the role played by viscoelasticity

**Keywords :** Dynamic fracture, Elastomers, Transonic cracks, Cohesive zone, Viscoelasticity

**Abstract :** This study aims to investigate the propagation of a dynamic crack through an elastomer membrane. The crack propagation in polyurethane elastomers was studied experimentally in an earlier study. Under certain loading conditions, crack speeds in that study were found to exceed the shear wave speed. Such cracks are called transonic cracks. Two main hypotheses were put forward in literature to explain the observation of Transonic cracks. One of them relies on the hyperelastic stiffening of the material in the vicinity of the tip, while the other relies on the viscoelastic stiffening. This study examines these two hypotheses and determines that viscoelastic stiffening is the necessary (and sufficient) ingredient. Finite Linear viscoelasticity has been used in the first instance.

Once this has been established, a rate-dependent cohesive model has been used to predict the crack propagation speed. The crack speed has been found to be independent of the specimen height starting from a certain threshold. A nonlinear viscoelastic model has also been implemented assuming plane stress conditions to prevail. Using this, the energy dissipated in the bulk because of viscoelastic effects and the energy consumed by the fracture processes has been explicitly computed. The majority of the strain energy has been observed to be consumed as the viscoelastic dissipation in the bulk material. The rest is taken up by the fracture processes.